ABSTRACT

Title of Dissertation: MULTI-LAYERED, VARIABLE POROSITY SOLID-STATE LITHIUM-ION ELECTROLYTES: RELATIONSHIP BETWEEN MICROSTRUCTURE AND LITHIUM-ION BATTERY PERFORMANCE

Tanner Ray Hamann, Doctor of Philosophy, 2019

Dissertation directed by: Professor Eric Wachsman
Department of Materials Science and Engineering

The global drive to create safer, higher capacity energy storage devices is increasingly focused on the relationship between the microstructures of electrochemically-active materials and overall battery performance. The advent of solid-state electrolytes with multi-layered, variable porosity microstructures opens new avenues to creating the next generation of rechargeable batteries, while creating new challenges for device integration and operation. In this dissertation, microstructures of solid-state Li-ion conducting electrolytes were characterized to identify the primary limiting factors on electrolyte performance and identify structural changes to improve porous electrolyte performance in dense-porous bilayer systems.

LLZO-based garnet electrolytes were fabricated with varied porosity and characterized using 3D Focused Ion Beam (FIB) Tomography, enabling digital reconstructions of the underlying 3D microstructures. Ion transport through the microstructures was analyzed using M-factors, which identified garnet volume fraction and

bottlenecks as primary limiters on effective conductivity, followed by geometric tortuosity. Notably, a template-based porous microstructure displayed a low tortuosity plane and a high tortuosity direction, as opposed to the more homogenous tape-cast porous microstructures. To evaluate the performance of these microstructures in Li symmetric cells, dense-porous bilayers were digitally constructed using the FIB Tomography microstructures as porous layers with fully infiltrated Li-metal electrodes, and equilibrium electric potentials were simulated. The bilayers had area-specific resistance (ASR) values similar to the ASR value of the dense layer alone. The bilayer ASR also decreased as porous layer porosity increased, due to ion transport occurring primarily through the dense layer-electrode interface and higher porosity creating higher interfacial area. Artificial bilayers were created with porous layers composed of columns for a range of column diameters/particle sizes, porous layer porosities, and porous layer thicknesses. The bilayer ASR decreased with increasing porosity and decreasing column diameter, similar to the FIB Tomography bilayers. However, bilayer ASR dramatically increased when only partially infiltrated with electrodes, and instead increased with increasing porosity and decreasing column diameter. The simulation results showed that fabricating solid-state bilayer symmetric cells with low ASR required high porosity porous microstructures with small particle sizes, and electrodes completely infiltrated to the dense layer.

MULTI-LAYERED, VARIABLE POROSITY SOLID-STATE LITHIUM-ION ELECTROLYTES: RELATIONSHIP BETWEEN MICROSTRUCTURE AND LITHIUM-ION BATTERY PERFORMANCE

by

Tanner Ray Hamann

Dissertation submitted to the Faculty of the Graduate School of the
University of Maryland, College Park in partial fulfillment
of the requirements for the degree of
Doctor of Philosophy
2019

Advisory Committee:
Professor Eric Wachsman, *Chair/Advisor*
Assistant Professor Paul Albertus
Associate Professor Liangbing Hu
Professor Kenneth Kiger, *Dean's Representative*
Assistant Professor Yifei Mo
Professor Lourdes G. Salamanca-Riba

Dedication:

To my family, those who are here to see me graduate and those who have passed on.

I thank you for always believing in me and helping me become who I am today.

Acknowledgement

The research described in this dissertation was supported by funding from the Department of Energy (DOE) through the Advanced Research Projects Agency – Energy (ARPA-E, Contract No. DE-AR0000787) and the Office of Energy Efficiency and Renewable Energy (EERE, Contract No. DE-EE0007807).

I want to thank my advisor Dr. Eric Wachsman. Being a part of your research group helped me learn the current state of energy research in the world and allowed me to join a larger community working to solve the energy challenges facing the future. I am grateful for the many opportunities to learn new practical research skills and techniques, including complex characterization approaches such as 3D Focused Ion Beam (FIB) Tomography and equilibrium electric potential simulations. I also appreciate your guidance when choosing the direction of my dissertation research and your advice to focus on studying several key topics extensively to produce high quality research results.

I want to thank Dr. Jiancun Rao, Dr. Sz-Chian Liou, and Dr. Wen-An Chiou of the UMD AIMLab for training me to use the Tescan XEIA and GAIA focused ion beam-scanning electron microscope (FIB-SEM) instruments, both of which proved invaluable for my dissertation research. I am grateful for your patience when answering my many questions about instrument operation, as well as working with me to identify effective solutions to issues I encountered during SEM imaging, sample preparation, or 3D FIB Tomography imaging. Overall, I want to acknowledge the support of the Maryland NanoCenter and its AIMLab for providing access to its facilities and instrumentation.

I want to thank my colleagues in battery research: Dr. Gregory Hitz, Dr. Dennis McOwen, Dr. Yunhui Gong, Dr. Lei Zhang, Griffin Godbey, Jack Gritton, Dr. Zhezhen

Fu, Dr. Yaoyu Ren, Matt Limpert, and Jon O'Neill. I also want to thank my colleagues in the research laboratory as a whole: Dr. Yi-Lin Huang, Mann Sakbodin, Dr. Patrick Stanley, Dr. Alireza Pesaran, Ian Robinson, Eugene Ostrovskiy, and Zixiao Liu. Working with you in the lab to understand the structure and performance of the garnet electrolyte taught me many lessons about the practical implementation of cutting-edge research. I also enjoyed and greatly benefitted from the many discussions about notable papers in the literature, the mechanisms underlying the mechanical and electrochemical properties we observed in our own research, and how best to use what we knew to further ongoing research and identify new research topics.

I want to thank Dr. Joshua Taillon, who's notes on sample preparation and 3D FIB Tomography, publicly available FIJI shade correction plugin, and personal correspondence helped me quickly learn the fundamentals of 3D FIB Tomography, image set processing, and analysis of geometric tortuosity.

I want to thank Dr. Lourdes Salamanca-Riba, who helped answer my questions on 3D FIB Tomography, image set processing, and analysis of geometric tortuosity.

I want to thank Christopher Klingshirn, who helped answer my questions on FIB milling/polishing and helped me apply non-local means filters to the 3D FIB Tomography image sets.

I want to thank Dr. Peter Zavalij and the Teaching Assistants of the UMD X-ray Crystallographic Center, who oversaw my x-ray diffraction (XRD) training and assisted my analysis of XRD scan results for garnet samples. XRD has been an invaluable tool during my graduate research for studying how sintering conditions and dopants affected the final crystal structure of the garnet electrolyte.

I want to thank John Abrahams, Jonathan Hummel, and the rest of the Fablab staff for training me on Fablab cleanroom procedures and the Fablab SEM, BET, and atomic layer deposition (ALD) systems. These instruments allowed me to learn the fundamentals of characterizing the garnet electrolyte microstructure, as well as contribute to the fabrication of high conductivity, low resistance solid-state batteries.

I want to thank Dr. Kathleen Hart, who I could always come to with questions about registering for classes, important deadlines, billing issues, and the requirements of the Materials Science and Engineering Department and the Engineering Graduate Program.

Last but not least, I want to thank my family and friends, who continuously supported me through my graduate experience and helped me stay focused on my ultimate goal. And I am especially grateful to my parents and my sister, who have been the foundation of my life through all its the challenges and successes.

Table of Contents:

List of Tables:

List of Figures:

List of Abbreviations and Symbols:

α	Tilt angle between Euclidean/straight path across porous microstructure and travel pathway through porous electrolyte (for derivation of geometric tortuosity)
A	Travel pathway cross-sectional area
$A_{bottleneck}$	Cross-sectional area of bottlenecks
$A_{particle}$	Cross-sectional area of particles
ALD	Atomic layer deposition
AOI	Area-of-interest
ASR	Area-specific resistance
$\vec{b}$	List of boundary condition values in 3D simulation
β	Constriction factor of electrolyte/phase being analyzed
BSE	Back scattered electron
c-PSD	Continuous particle size distribution
Δl	Length of travel pathways through porous microstructure
Δx	Euclidean/straight path distance across porous microstructure
$d_{bottleneck}$	Circular diameter of bottlenecks
$d_{particle}$	Circular diameter of particles
$D_{final,\ full}$	Maximum width between the 2 angled sides of the 3D FIB Tomography thickness reference mark triangle for final cross-section image
$D_{initial,\ full}$	Maximum width between the 2 angled sides of the 3D FIB Tomography thickness reference mark triangle for initial cross-section image
$D_{final,half}$	Half of maximum width between the 2 angled sides of the 3D FIB Tomography thickness reference mark triangle for final cross-section image
$D_{initial,half}$	Half of maximum width between the 2 angled sides of the 3D FIB Tomography thickness reference mark triangle for initial cross-section image
$D_{sim,dense}$	Diffusivity used in simulation of dense electrolyte
$D_{sim,porous}$	Diffusivity calculated from simulation of porous electrolyte
DLS	Dynamic light scattering
DMC	Dimethyl carbonate
$\vec{E}$	Electric field vector
EC	Ethylene carbonate
EIS	Electrochemical Impedance Spectroscopy
f	Volume fraction of electrolyte/phase being analyzed
FIB	Focused ion beam
FIB-SEM	Focused ion beam-scanning electron microscope
FIB Tomography	Focused Ion Beam Tomography
IA	Interfacial area
$\vec{J}$	Current density vector
l_x	Voxel size along x-axis
l_y	Voxel size along y-axis
l_z	Voxel size along z-axis
L	Projected Euclidean/straight path across porous microstructure from travel pathway length
L_{final}	Distance between apex/top vertex of 3D FIB Tomography thickness reference mark triangle and final cross-section
$L_{initial}$	Distance between apex/top vertex of 3D FIB Tomography thickness reference mark triangle and initial cross-section
$L_{thickness}$	Total thickness milled
LCO	$LiCoO_2$
Li	Lithium
LLCZN	$Li_7La_{2.75}Ca_{0.25}Zr_{1.75}Nb_{0.25}O_{12}$

LLTO	Lithium lanthanum titanate
LLZO	$Li_7La_3Zr_2O_{12}$
LFMO	Lithium iron manganese oxide
$\widehat{M}$	Square matrix encoding relationships between neighboring updatable voxels in 3D simulation
M	M-factor/microstructure factor
MIP-PSD	Mercury intrusion porosimetry particle size distribution
$\vec{n}$	Vector normal to surface of electrolyte in 3D simulation
N	Number of entries in square matrix M
N	Number of 3D FIB Tomography images
$N_{phase,connected}$	Total number of chosen phase voxels that were contiguous and connected to 1 of the boundary planes of the 3D image region
$N_{phase,total}$	Total number of chosen phase voxels in the 3D image region
φ	Electric potential of voxel in 3D simulation
$\vec{\Phi}$	List of potentials of all updatable voxels in 3D simulation
P	Percolation factor of electrolyte/phase being analyzed
PMMA	Poly-(methyl methacrylate)
$R_{straight}$	Resistance of un-tilted travel pathway
R_{tilt}	Resistance of tilted travel pathway
RGB	Red-green-blue
σ	Conductivity of voxel in 3D simulation
$\sigma_{effective}$	Effective conductivity of porous electrolyte
$\sigma_{intrinsic}$	Intrinsic conductivity of electrolyte material
$\sigma_{pathway,effective}$	Effective conductivity of tilted travel pathway through porous microstructure
$\sigma_{pathway,intrinsic}$	Intrinsic conductivity of electrolyte
$\sigma_{sim,dense}$	Conductivity of dense electrolyte in diffusive tortuosity simulation
$\sigma_{sim,porous}$	Conductivity calculated for porous electrolyte in diffusive tortuosity simulation
SA	Surface area
SA/V	Surface area-to-volume
SD	Standard deviation
SE	Secondary electron
SEI	Solid electrolyte interface
SEM	Scanning electron microscope
SIFT	Scale Invariant Feature Transform
SIMS	Secondary ion mass spectroscopy
SOFC	Solid oxide fuel cell
τ	Tortuosity
$\tau_{characteristic}$	Characteristic tortuosity
τ_{geo}, $\tau_{geometric}$	Geometric tortuosity
$\tau_{diffusive}$	Diffusive tortuosity
θ	Angle between sides of 3D FIB Tomography thickness reference mark triangle and triangle centerline
TEM	Transmission electron microscope
TOF	Time-of-flight
$Voxel_{z\text{-}axis}$	Average Z-axis voxel size
WEKA	Waikato Environment for Knowledge Analysis
XRD	X-ray diffraction
YSZ	Yttrium-stabilized zirconia

1. Lithium-Ion Batteries:

At a fundamental level, secondary/rechargeable batteries are simple in operation: oxidation and reduction reactions are split between two electrodes, with ions traveling between the electrodes through an intermediate electrolyte and electrons directed through an external circuit. Charging builds a potential difference across the battery to store energy, while discharging consumes that potential difference to produce external current that powers devices. In the 150 years since secondary batteries were first demonstrated, these fundamental principles remained unchanged even as the components and basic chemistry at work have undergone many revisions (Figure 1.1).[1] Today, lithium-ion (Li-ion) batteries are among the most prevalent in the world due to their widespread utilization in consumer electronics and increasing applications in transportation and, potentially, in large-scale energy infrastructure. With a wide range of battery materials under study, the next generation of rechargeable batteries could range from simple improvements of existing designs to radically new operational approaches.

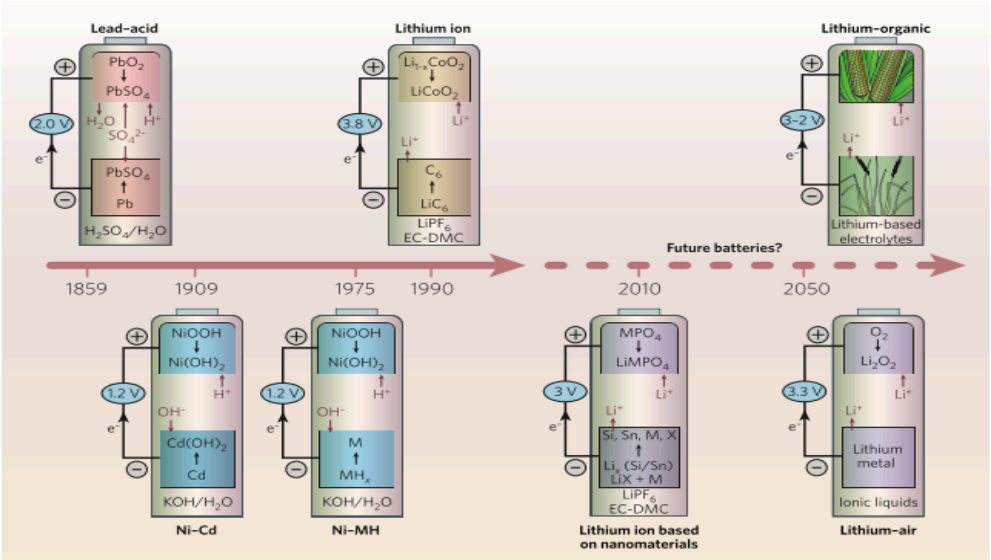

Figure 1.1: Leading secondary battery chemistries over the years.[1]

1.1. Liquid Organic Electrolytes:

1.1.1. Background:

First commercialized by Sony in the 1990's, secondary Li-ion batteries using a $LiCoO_2$ | liquid organic electrolyte | graphite architecture have dominated energy storage in consumer electronics for many years and remain the standard for modern Li-ion batteries.[2] The liquid electrolyte is typically a mixture of ethylene carbonate (EC) and the linear carbonate dimethyl carbonate (DMC), into which a lithium salt, such as $LiPF_6$, is dissolved to provide ionic conductivity.[3] This particular liquid electrolyte chemistry demonstrated both a high Li-ion conductivity (~10^{-3} S/cm) and the ability to form a stable solid electrolyte interface (SEI) that passivated the electrolyte-graphite interface, radically slowing deleterious side reactions that caused performance decay.[3] Even as academia and industry continue to find ways to improve Li-ion technology, most commercially available rechargeable batteries still rely heavily on liquid organic electrolytes and designs similar to the original Sony battery.[3]

1.1.2. Material Challenges:

One of the biggest issues facing Li-ion batteries utilizing liquid organic electrolytes is the formation of Li-metal dendrites that bridge the electrodes and short-circuit the battery.[4] Under ideal operational conditions, a porous separator prevents physical contact between the electrodes while still allowing the liquid organic electrolyte to pass through and move Li-ions through the battery.[5] However, cycling the battery at high current densities can cause the Li-ions to plate onto the electrode surface and create Li-metal dendrite protrusions (Figure 1.2a), which will grow each cycle and reduce battery

performance by decreasing the distance between electrodes (Figure 1.2b).[6] If a dendrite extends across the entire battery and connects the electrodes directly, the resulting short circuit allows large electrical currents to flow through the thin metal dendrite and release significant heat. If this heat initiates a thermal runaway reaction, it can ignite the flammable liquid organic electrolyte or produce enough gas to rupture the battery.[7–9] This safety concern for batteries using Li-metal anodes drove Sony's decision to abandon high capacity Li-metal anodes (3861 mAhr/g) in favor of low capacity graphite anodes (372 mAhr/g) that better resist dendrite formation.[10] Even with safer graphite anodes, Li-metal dendrites still can form if battery charge/discharge current densities are too high, particularly at low temperatures where the liquid electrolyte conductivity is significantly reduced.[10,11]

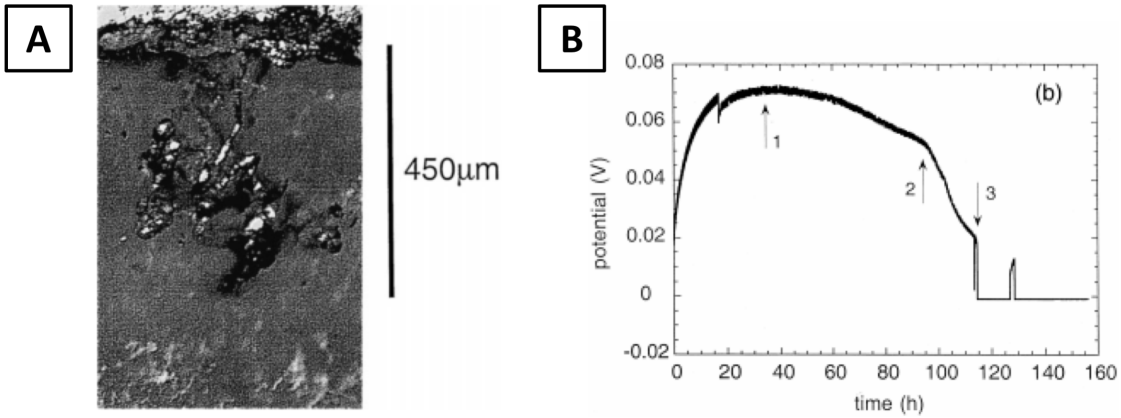

Figure 1.2: A) lithium dendrite growing through PEO electrolyte from lithium metal anode and B) observed degradation of battery voltage while polarized. Dendrite growth reduced the cathode-anode distance, decreasing battery voltage until final failure by short circuit.[6]

A variation of the Li dendrite issue is the formation of "dead lithium" at the electrodes, especially for Li-metal anodes.[12] During operation, the Li-ions are reduced at the Li-metal anode and plate to the surface of the electrode. However, subsequent cycles formed an SEI layer on the surface of the plated Li-metal, consuming part of the cycled Li-

ions in the process.[13] While dendrite growth is stalled by this SEI, repeated plating and SEI formation continuously consume more Li-ions and isolate parts of the plated Li-metal from the bulk electrode, creating the "dead lithium." Alternatively, Li-dendrites extending from the surface of the Li-metal anode can break away and become electrically isolated. As a consequence, the charge/discharge capacity of the battery decays quickly with time as more of the available Li-ions became trapped in SEI layers or are rendered inert.

Using liquid organic electrolyte also precludes the use of many high-performance electrodes and even limits the performance of electrodes compatible with the electrolyte. On the cathode side, liquid electrolytes decompose into potentially combustible products when cycled above 4.5 V (vs. Li/Li^+), prohibiting the use of promising high voltage cathode materials (e.g., $LiMn_{1.5}Ni_{0.5}O_4$, $LiNiPO_4$, and $LiCoPO_4$) that could significantly increase battery energy density and power density.[7,14,15] Sulfur, one of the highest capacity cathodes currently known (1672 mAhr/g), is not yet utilized in commercial batteries due to the dissolution of polysulfide compounds into the liquid electrolyte that leads to the so-called "polysulfide shuttle effect".[16,17] Li-rich, Mn-rich layered oxide cathodes also received significant interest due to high Li-ion capacity (> 250 mAhr/g) and improved cycling behavior when compared to typical $LiCoO_2$ (LCO) cathodes (140 mAhr/g).[18] However, Li-rich, Mn-rich layered oxide cathodes also suffer from metal-ion dissolution into the liquid electrolyte or internal structural transformations when cycled above 4.4 V, causing the cathode to irreversibly transition to low capacity phases.[19,20] Limiting the voltage range would preserve the material microstructure, but at the cost of utilizing only a fraction of the capacity of the Li-rich, Mn-rich layered oxide cathodes.

Despite these limitations, the capabilities of Li-ion batteries are being pushed as far as possible to satisfy demand for increasingly long-lasting and fast-charging batteries for consumer electronics, as well as future applications in automobiles, air travel, and large-scale energy infrastructure.[15] Still, the limits of the liquid organic electrolytes continue to result in low energy density and low power density battery systems, leading to bulky battery packs that require extensive thermal maintenance and can still suffer catastrophic failures.[8,21–24] Clearly, Li-ion batteries need a breakthrough, and replacing the liquid electrolyte is the key.

1.2. Solid-State Lithium-Ion Electrolytes:

1.2.1. Background:

A novel approach within the last two decades was to replace the liquid organic electrolyte with a solid-state electrolyte.[25] Both solid-state electrolytes and liquid organic electrolytes conduct Li-ions through the battery, but solid electrolytes have a number of unique properties that make them ideal for battery use. A key advantage is that solid electrolytes act as a physical barrier separating the electrodes. If sufficiently hard and possessing minimal surface defects, even solid electrolytes composed of organic materials could prevent lithium dendrite growth and short circuits, eliminating a major safety concern for Li-ion batteries.[26,27] This safety function is further augmented in metal oxide solid electrolytes, since the oxide is completely non-flammable due to the incorporation of oxygen into the chemical structure.[28] In terms of battery performance, some solid electrolytes have shown wider electrochemical stability windows than liquid electrolytes, allowing for the use of high voltage cathodes that are incompatible with liquid electrolytes.[29] Additionally, solid electrolytes cannot dissolve lithium polysulfide compounds, preventing the "polysulfide shuttle effect" and thereby making sulfur a viable cathode material.[30] Given these clear benefits, solid electrolytes are the subject of intense study in recent years, with investigations including gel polymers, Li-ion conducting polymers, plastic crystals, perovskite materials, garnet-like ceramics, glasses, and composite materials.[31–34]

Two key aspects of an electrolyte's ability to conduct Li-ions are the ionic conductivity and the transference number (i.e., the ratio of Li-ions transferred to total ions transferred). Solid-state electrolytes generally have relatively low ionic conductivities at

room temperature compared to carbonate-based liquid organic electrolytes with conductivities up to 10^{-2} S-cm^{-1}.[35–37] As such, extensive research was focused on synthesizing a wide variety of solid electrolyte compositions with the ultimate goal of achieving higher room temperature ionic conductivity (Figure 1.3).[35]

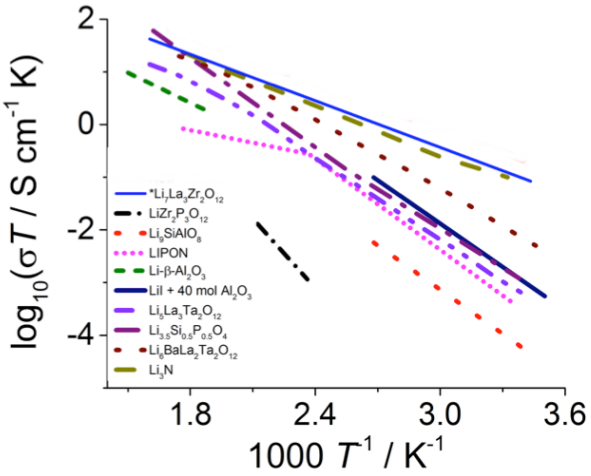

Figure 1.3: Comparison of Li^+ ionic conductivities for solid-state Li-ion electrolytes [adapted from Murugan, *et al.*].[35]

1.2.2. LLZO and LLCZN:

Murugan, *et al*, was the first to synthesize a particularly intriguing solid-state electrolyte with the chemical composition $Li_7La_3Zr_2O_{12}$, known as LLZO.[35] This electrolyte was the latest in a series of Li-ion conducting metal oxides that adopted garnet-like crystal structures, with previous iterations having Li_5 and then Li_6 compositions.[35,38,39] LLZO displayed a room temperature tetragonal phase with relatively low ionic conductivity (~10^{-6} S-cm^{-1}) and a high temperature cubic phase with high ionic conductivity (~10^{-4} S-cm^{-1}).[40] Crucially, LLZO demonstrated good stability in the presence of lithium metal and electrochemical stability up to 7 V (vs. Li/Li^+), making it compatible with both high capacity lithium metal anodes and high voltage cathodes.[35,41] While other

solid-state electrolytes such as perovskite-type lithium lanthanum titanate (LLTO) have even higher ionic conductivities (~10^{-3} S-cm^{-1}), they are unstable when in contact with lithium metal anodes and can only be used with lower capacity graphite anodes.[31,35]

Early studies revealed that LLZO leached Al from the Al_2O_3 crucibles during calcination and the Al-doping stabilized the cubic phase at room temperature.[42] Since then, additional dopants were investigated and also found to stabilize the cubic phase, as well as change the conductivity of the doped LLZO (Figure 1.4).[43–46] When the Zr-site was doped with Nb, the resulting $Li_{7-x}La_3Zr_{2-x}Nb_xO_{12}$ displayed a maximum ionic conductivity of $8x10^{-4}$ S-cm^{-1} for x=0.25 (Figure 1.5a) and electrochemical stability up to 9 V (vs. Li/Li^+).[47] Based on these results, the La and Zr sites were simultaneously doped with Ca and Nb, respectively, to form $Li_7La_{2.75}Ca_{0.25}Zr_{1.75}Nb_{0.25}O_{12}$ or LLCZN.[48] LLCZN showed slightly reduced ionic conductivity compared to Nb-doped LLZO (Figure 1.5b), but adding Ca reduced the final sintering temperature, which is useful from a processing perspective.[48] As such, LLCZN appears to be a better candidate for use in Li-ion batteries than LLZO.

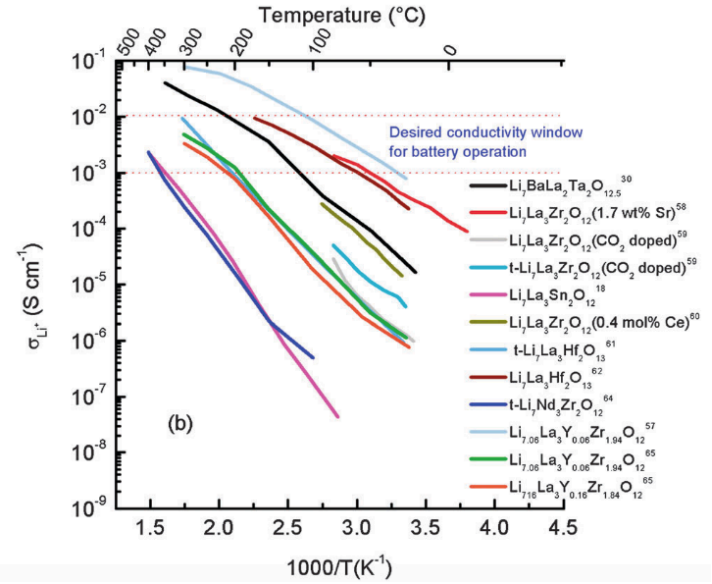

Figure 1.4: Ionic conductivities of doped LLZO.[46]

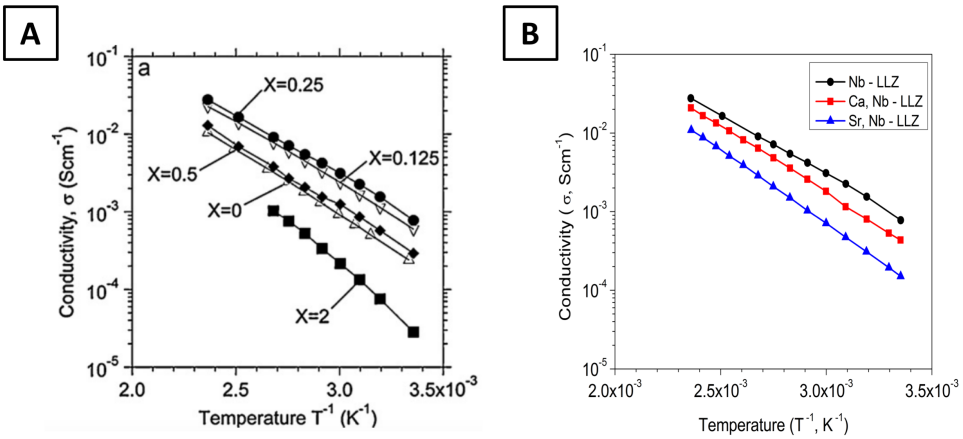

Figure 1.5: A) conductivity of $Li_{7-x}La_3Zr_{2-x}Nb_xO_{12}$ for varying Nb doping,[47] and B) x = 0.25 Nb in LLZO, Ca/Nb doped LLZO (LLCZN), and Sr/Nb doped LLZO [adapted from Kihira, *et al.*].[48]

1.2.3. Challenges in Adopting Solid-State Li-ion Electrolytes:

The advantages of solid-state electrolytes are accompanied by unique disadvantages. Perhaps the single most pressing issue for solid electrolytes is the high interfacial impedance associated with the electrolyte-electrode interface.[28] This generally arises from having poor ion transport across the interface, possibly due to insulating surface coatings that arise from undesirable side reactions at the electrolyte or electrode, or due to poor electrolyte-electrode physical contact.[25,49] When exposed to humid air, the LLZO/LLCZN reacts with H_2O to produce a surface coating of $LiOH*H_2O$ (due to proton exchange with Li-ions in the bulk). The $LiOH*H_2O$ then reacts with CO_2 to form a surface coating of Li_2CO_3 and $LiOH*H_2O$.[50] The Li_2CO_3 and $LiOH*H_2O$ coating has poor Li-ion conductivity, acting as an insulating layer between the LLZO/LLCZN and the electrode. The formation of these surface contaminants also extracts Li-ions from the LLZO, affecting Li-concentrations and ionic conductivity near the surface.[45] As to physical contact between the electrolyte and electrodes, the rigid nature of both materials makes it difficult to achieve highly conformal solid-solid interfaces.[51] This limits the amount of electrolyte-electrode

interfacial area, increasing the current density at the few contact points and thus increasing the overall interfacial resistance. In contrast, liquid organic electrolytes are able to fully wet the surfaces of the electrodes, so do not have this physical contact issue.

To address high impedance surface contaminants, many studies deliberately established a new, stable, Li^+-conducting layers on the surface of the electrode or electrolyte to protect against undesirable secondary reactions.[51–54] Depending on the electrode material, it is also possible to achieve a more conformal electrolyte-electrode interface by pressing or melting the electrode onto the surface of the electrolyte.[49,55] For LLCZN, applying an ultrathin Al_2O_3 layer via atomic layer deposition (ALD) prevents the formation of insulating $LiOH*H_2O$ and Li_2CO_3 surface contaminants, and improved the LLCZN-lithium interface (Figure 1.6a).[51] The improved interface results from the molten lithium reacting with the insulating Al_2O_3 layer to form a Li-ion conducting Li-Al-O layer. This Li-Al-O layer in turn causes the remaining molten lithium to readily wet the ALD-coated LLCZN. Figure 1.6b shows secondary electron (SE) scanning electron microscope (SEM) images of garnet pellets with and without ALD coatings, demonstrating how the ALD coating made the garnet-Li metal interface significantly more conformal. Electrochemical Impedance Spectroscopy (EIS) showed the area-specific resistance (ASR) of the LLCZN-lithium interface dropped significantly for samples with the ALD coating compared to samples without the ALD coating (Figure 1.7). Over 50 cycles on lithium symmetric cells and LFMO | LLCZN | Li-metal full cells showed consistent cycling voltage plateaus and discharge capacities, respectively, indicating the Li-Al-O interfacial layer was stable long term. These results further demonstrated how controlling the surface chemistry of interfaces can reduce sources of high interfacial resistance.

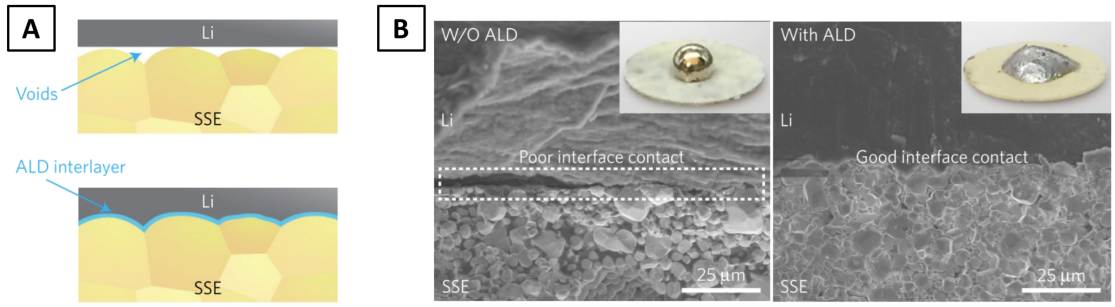

Figure 1.6: A) schematic and B) SEM images of LLCZN-lithium interface without and with ALD layer.[51]

Table 1 | Electrochemical impedance and d.c. ASR for Li/LLCZN/Li cells with and without ALD coating on both sides of garnet SSE.

Li/LLCZN/Li symmetric cell	Bulk/high-frequency ASR (Ω cm^2)	GB/interface ASR (Ω cm^2)	Total EIS ASR (Bulk+GB/interface) (Ω cm^2)	Interfacial EIS ASR* (Ω cm^2)	d.c. ASR (Ω cm^2)	Interfacial d.c. ASR* (Ω cm^2)
W/O ALD	28	3,500	3,528	1,710	N/A	N/A
ALD	26	150	176	34	110	1

*Interfacial EIS and d.c. ASR calculated by subtracting total garnet ASR (108 Ω cm^2) from total EIS and d.c. ASR, respectively, and dividing by interfacial area. GB, grain boundary. Garnet ASR (108 Ω cm^2) was obtained from the EIS garnet conductivity measurement of the Au/garnet/Au symmetric cells.

Figure 1.7: ASR associated with Li-ion conduction through the bulk, grain boundary, and LLCZN-Li electrode interface of LLCZN pellets without and with ALD layer.[51]

Another major challenge facing solid-state electrolytes is the higher amount of electrolyte mass in the final battery due to the higher density of the solid electrolyte vs. a liquid organic electrolyte. From an energy and power density perspective, electrolytes are essentially "dead weight," increasing the battery's mass and weight without contributing to Li-ion storage. As solid electrolytes are up to 4x as dense as liquid electrolytes, a higher performance battery requires as little solid electrolyte as possible to maximize battery energy density. In addition, even the best solid electrolytes still have lower ionic conductivities than liquid electrolytes, resulting in higher electrolyte resistances and ohmic losses. The combined impedance sources in the battery increase the total battery resistance and over-potential during cycling, reducing the battery energy density. Decreasing the solid-state electrolyte thickness provides some mitigation by eliminating "unnecessary" mass not contributing to Li-ion storage while also reducing ohmic resistance in the battery. The resistance and ASR of the electrolyte layer are expected to be linear with layer

thickness (Equation 1.1), so thinner solid electrolytes should have reduced ASR. EIS measurements of LLCZN samples with varying dense layer thicknesses support this, with dense layers less than 100 μm demonstrating lower ASR than ideal commercial cells (Figure 1.8).

$$ASR\ (\Omega\ cm^2) = R * A = \rho * L = {}^{L}/_{\sigma} \tag{1.1}$$

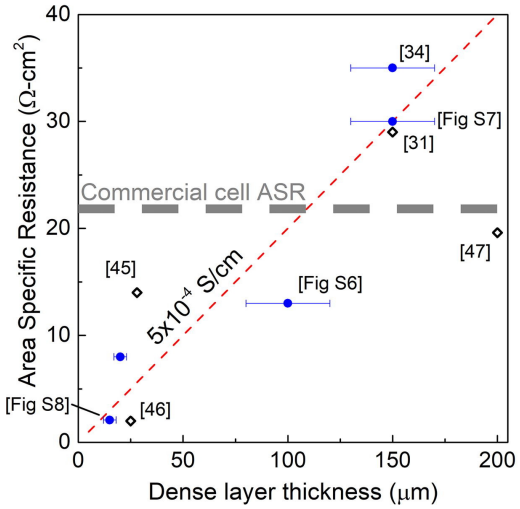

Figure 1.8: ASR of LLCZN samples as a function of dense layer thickness.[56]

However, reducing the solid electrolyte thickness also reduces its mechanical strength. As solid electrolytes function as both Li-ion conductor and electrode separator, the electrolyte must be strong enough to survive battery assembly and stresses during battery operation. This implies a minimum thickness is required, that, in turn, establishes an upper limit on the performance of batteries using solid electrolytes. Overcoming this limit is possible with a new battery structure. For example, replacing the dense, single layer, planar structure with a porous-dense-porous multilayer structure, wherein the thin dense layer separates the electrodes and the thicker porous layers provides the mechanical support (and increased contact area with the electrodes) (Figure 1.9).[56] The performance

advantages of a thin electrolyte and the mechanical strength of a thick electrolyte are achieved simultaneously with this “trilayer” structure.

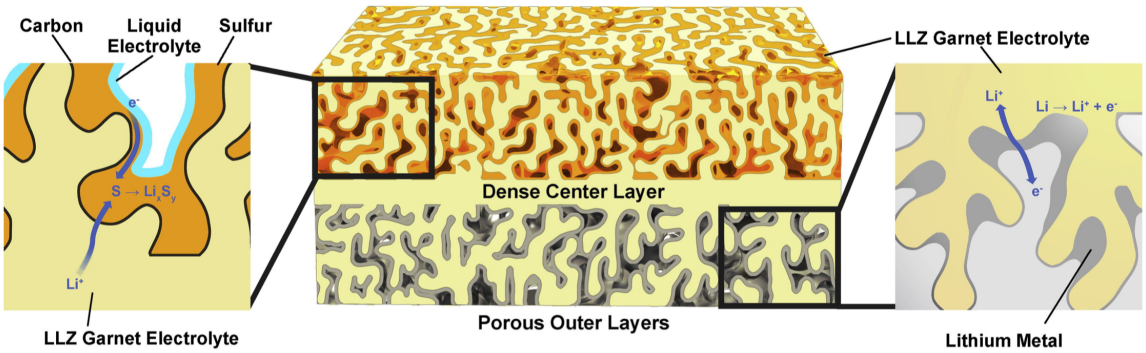

Figure 1.9: Schematic of solid-state electrolyte with porous-dense-porous trilayer microstructure, with cathode and anode material infiltrated into the networks of pores.[56]

1.3. Research Objective: Understanding Porous Solid-State Li-ion Electrolyte Performance:

Radically altering the garnet electrolyte structure carries the potential to both improve performance and magnify the effects of microstructural limitations. Thus far, the results for batteries employing LLCZN "trilayers" and "bilayers" were highly promising, showing lower ASR values while achieving higher electrode loading than planar electrolyte structures.[57–59] This suggests the potential structural limitations of the porous LLCZN layers did not pose a significant issue for these configurations. However, this may change if the porosity, thickness, or microstructure of the porous layer is further modified, therefore, a better understanding of the porous layer's role in overall electrolyte performance is crucial.[60–62]

This dissertation reflects a study of key microstructural parameters that directly affect porous electrolyte effective conductivity via a microstructure factor, or M-factor (Equation 1.2).[63,64] The M-factor was determined by calculating the conductive phase volume fraction (f), the geometric tortuosity (τ_{geo}), the percolation factor (P), and the constriction factor (β), and combining these values in Equation 1.3. These parameters were evaluated for 3D reconstructions of porous LLZO-based electrolytes to help determine the relative importance of each parameter on effective conductivity. Simulations of equilibrium electric potential distributions in bilayer symmetric cells were run to study the electric fields, current densities, and bilayer ASR values within the porous electrolyte microstructures and to determine the optimal microstructure for battery applications.

$$\sigma_{effective} = \sigma_{intrinsic} * M \tag{1.2}$$

$$M = \frac{f*P*\beta}{(\tau_{geo})^2} \tag{1.3}$$

2. 3D Focused Ion Beam (FIB) Tomography:

The bulk device properties of batteries, solid oxide fuel cells (SOFC), and other electrochemically-active devices depend heavily on the intrinsic properties of the constituent materials and on the overall device microstructure. This understanding has long guided the development of SOFC's, where oxidation/reduction efficiencies and ionic/electronic transport properties were connected to tortuosity and triple-phase boundary lengths.[65–74] In recent years, battery research groups developed a similar focus as studies connected performance degradation to changes in electrode microstructure, including particle fracture, transition metal distribution, surface reconstruction, and elemental dissolution.[20,75–77] The advent of solid-state electrolytes for Li-ion batteries dramatically increased the importance of understanding battery microstructures due to the rigid morphology of the solid electrolyte introducing new challenges to cell operation.[35,46,78–80] Thus, the battery research community has steadily embraced the use of 3D imaging techniques (focused ion beam tomography, x-ray computed tomography) to study electrode microstructures.[81–86] Research for this dissertation used 3D Focused Ion Beam tomography (3D FIB Tomography for short) to create 3D image sets of the porous electrolyte samples and reconstruct the full 3D microstructures.

2.1. Background:

Focused ion beam (FIB) systems utilize similar technology as electron microscopes to accelerate and focus a beam of ionically charged particles towards a sample.[87] Due to the large mass of the ions, the ion beam carries significant momentum and will ablate material from the sample surface when interacting with the sample.[88] FIB systems can

therefore physically alter samples on the scale of hundreds of nanometers up to hundreds of microns. Initially, FIB systems were prohibitively expensive and thus limited to niche applications such as circuit modification and repair at semiconductor manufacturing facilities.[87,89] Subsequent researchers developed approaches to utilize the fine milling control of FIB systems to greatly reduce transmission electron microscope (TEM) sample preparation time, resulting in a wider use of FIB systems.[90]

Like the electron beam in a SEM, a FIB generates secondary electrons from the sample by transferring momentum from the accelerated ions to the outer electrons of the sample atoms.[88] Thus, FIB systems can scan and image sample surfaces in much the same way as an SEM, though at the cost of sputtering material from the sample surface being imaged. The destructive nature of FIB imaging can also help gain elemental information about the sample through secondary ion mass spectroscopy (SIMS).[91,92] Here, some of the sputtered atoms from the sample become ionized by the ion beam and these secondary ions are detected by quadrupole, sector, or time-of-flight (TOF) mass analyzers.[93] Crucially, SIMS is capable of detecting light elements such as Li, making it possible to identify the presence/distribution of Li in Li-containing electrolytes, cathodes, or anodes.[94]

Today, the most common use of the FIB is in dual beam FIB-SEM systems, where a FIB is mounted at an angle to an SEM such that the ion beam and electron beam intersect inside the vacuum chamber at the sample surface (Figure 2.1).[95,96] The FIB-SEM has the distinct advantage of combining all the normal SEM imaging modes with the additional characterization techniques available through the FIB. The FIB-SEM also enables 3D FIB Tomography, whereby the FIB repeatedly mills into the sample to expose new cross-sections of the sample microstructure while the SEM takes images of each cross-section.[97]

The resulting image sets are processed to reconstruct the 3D microstructure of the sample, providing invaluable insight not attainable through normal 2D imaging techniques.

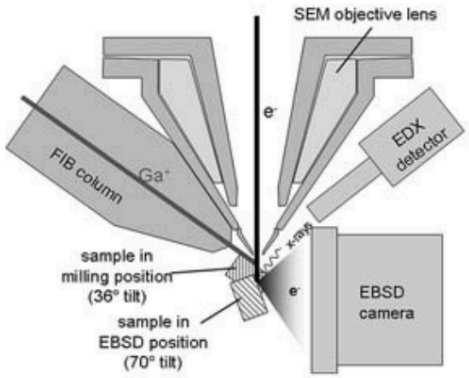

Figure 2.1: Diagram of a dual-beam FIB-SEM, with the FIB attached at an angle to the SEM so the electron and ion beams intersect at the sample.[96]

A number of artifacts can manifest during a 3D FIB Tomography imaging run that make later analysis difficult or potentially impossible. One of the easier artifacts to address is the "pore-back effect", wherein the back of unfilled pores is visible in the SEM image before the polished cross-section has reached the pore back.[98,99] The result is pores that should appear dark instead have contrast similar to the sample at the polished cross-section (Figure 2.2a). Preventing the "pore-back" artifact is done by infiltrating a low contrast material into the sample pores during sample preparation that later solidifies, such as epoxy. Another common artifact is curtaining artifacts (Figure 2.2b), wherein variable or incomplete milling across the polished cross-section creates vertical stripes that can alter contrast across homogenous phases.[68] FIB Tomography samples are typically coated with a layer of platinum at the top of the polished cross-section to protect the region from excess milling and to help reduce the severity of the curtain artifacts.[100,101] In addition, longer milling times with lower ion beam currents can also reduce the size of the curtains, but drastically increases the total FIB Tomography run time. Alternatively, mathematical

filters applied to the image sets can attempt to isolate the artifacts, but the results may vary dramatically.[102–105] Sample charging can also become a significant issue when using SE mode due to the sample often being an insulating ceramic surrounding by an insulating filling material. Most commonly, this facilitates negative charge buildup due to the electron beam scanning across the polished cross-section surface, which then deflects the electron beam during later scanning and creates patches of variable contrast (Figure 2.2c). Lower electron beam currents or alternate imaging modes can reduce the problem. A positive charging artifact can also occur due to positive ions from the ion beam implanting in and around the polished cross-section surface, which reduces the amount of secondary/backscatter electrons that leave the sample resulting in global dimming of the SEM image.[106] Periodically exposing the charged surface to low energy electrons from a "flood gun" can negate the positive charge buildup.[107]

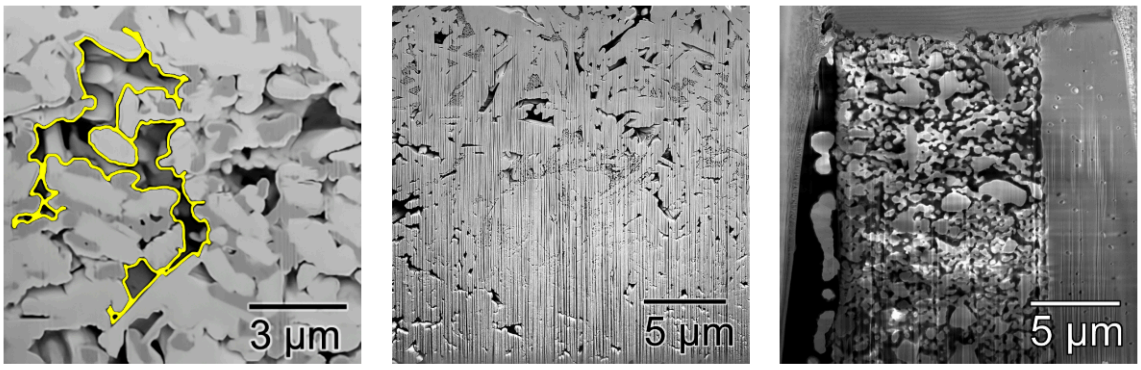

Figure 2.2: A) pore-back effect (highlighted in yellow), B) curtaining artifact, and C) charging artifact.[98]

2.2. Sample Preparation:

Porous LLCZN samples (Figure 2.3a) were infiltrated with Allied EpoxyBond 110, placed under vacuum for 10 minutes to remove air pockets, and cured at 70 °C for 12 hours. The epoxy-filled samples were cut to expose a cross-section of the sample and embedded into a disc of Allied EpoxySet, then cured at room temperature for 12 hours (Figure 2.3b). The epoxy disc surface was polished with 240, 400, 600, and 1200 grit silicon carbide abrasive discs (LECO), followed by further polishing with 9 µm, 6 µm, 1 µm, and 0.25 µm diamond particle suspensions (LECO). Copper tape was applied to the epoxy disc near the polished sample cross-section to prevent charging during SEM imaging and on the sides/bottom of the disc to provide an electrical contact to the sample holder. A thin coating of gold-palladium was plasma-sputtered onto the epoxy disc using an Anatek Hummer X Sputter System in order to prevent charging during SEM imaging. The coated epoxy disc was secured in a multi-purpose specimen mount (Ted Pella, Inc.) by set screws to minimize sample movement (Figure 2.3c). The cross-section of the epoxy-filled samples was imaged in secondary electron (SE) and back-scatter electron (BSE) modes in a Tescan XEIA3 FIB-SEM (Figure 2.3d).

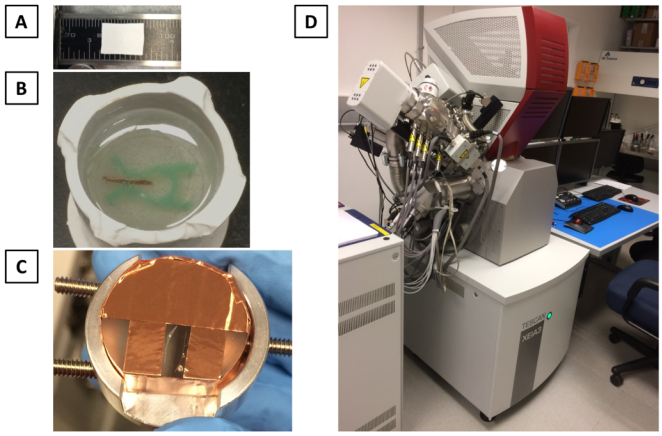

Figure 2.3: A) initial porous LLCZN sample, followed by B) infiltration with Allied EpoxyBond and then Allied EpoxySet epoxies, and finally C) secured in the Ted Pella, Inc., specimen mount. D) specimen mount was then inserted into the Tescan XEIA3 FIB-SEM, available through the UMD AIM Lab.

2.3. SEM/3D FIB Tomography Image Acquisition:

The mechanically polished cross-section of the epoxy-filled samples was imaged in secondary electron (SE) and back-scatter electron (BSE) modes in a Tescan XEIA3 FIB-SEM (Figure 2.4a). Based on these images, several samples with different amounts of porosity were selected for 3D FIB Tomography. The sample was placed into the Tescan XEIA3 FIB-SEM and a representative area-of-interest (AOI) was identified in the SEM images. The xenon-plasma focused ion beam (FIB) and the gas injection system (GIS) were used to deposit platinum on top of the AOI to prevent excessive ion beam milling (Figure 2.4b). A U-shaped trench was milled around the AOI to expose an internal cross-section of the porous microstructure and to prevent re-deposition of sputtered material onto the exposed cross-section (Figure 2.4c). For this reason, the sides of the trench were made with 50 microns of clearance from the sides of the cross-section and the front of the trench was made approximately twice as long as the trench was deep.

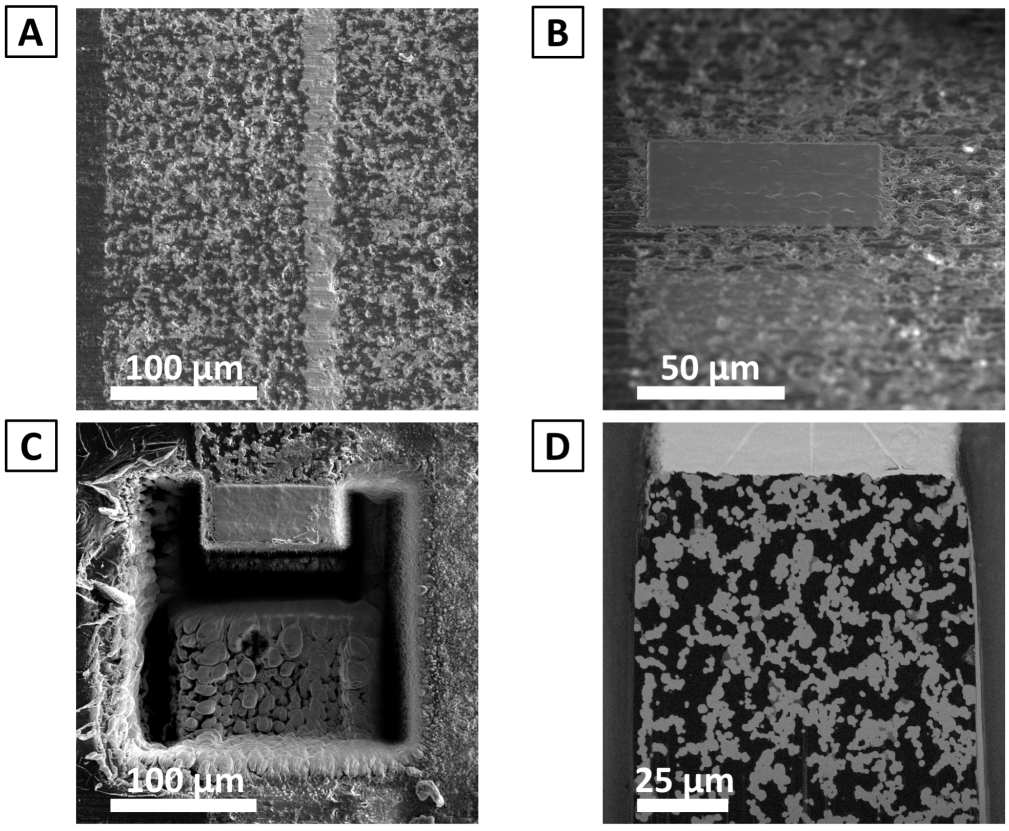

Figure 2.4: A) SEM image of the polished surface of trilayer LLCZN sample prior to ion milling. B) deposition of platinum protection layer. C) milling of U-shaped trench. D) FIB Tomography cross-section after final polishing in the GAIA3, with angled thickness reference marks visible on the platinum layer at the top of the image.

The cross-section was polished by the xenon-plasma FIB with progressively lower ion beam currents, with each step polishing away defects created by the previous polishing step. The sample was then transferred to a Tescan GAIA3 FIB-SEM for final polishing with the gallium-ion FIB (Figure 2.4d). A circle-and-cross-shaped reference mark was milled near the sample to help the GAIA3 minimize pattern drift during later serial milling-and-imaging. The sides and centerline of a triangle were milled into the top of the platinum protection layer (visible in Figure 2.4d) to calculate the average FIB slice thickness during post-analysis. The GAIA3 FIB-SEM was set to automatically mill ~100 nm thick slices through the AOI with a 10 nA beam current, then take SE and BSE images of each newly

exposed cross-section at resolutions of 50-60 nm/pixel. During each milling step, milling was automatically paused every few minutes to update the displayed image of the cross-section and confirm that the process was proceeding correctly. Total milling-and-imaging times were 40-60 hours and produced ~200 images that were 80-100 μm x 80-100 μm. The built-in "Geometric Transformation" function was set to "follow cross-section," which automatically corrected the SEM images to compensate for the 55° angle between the electron beam and the polished cross-section.

2.3.1. Global Signal Loss Due to Positive-Ion Charging:

Early runs of 3D FIB-tomography on porous layer samples primarily focused on determining the optimum parameters for bulk sample preparation, trench and cross-section preparation, and 3D acquisition. During one test run, both the SE and BSE images recorded during the 3D acquisition became increasingly darker as the run continued, and more images were collected (Figure 2.5). The issue became so severe that only the platinum protection layer was visible in late-stage images. Attempts to correct the issue by running the "Automated Brightness-and-Contrast" routine in the SEM control window failed to improve image quality, suggesting the problem originated from the sample and not an imaging setting. Without a clear way to correct the issue, the run was aborted prematurely to avoid unnecessary costs.

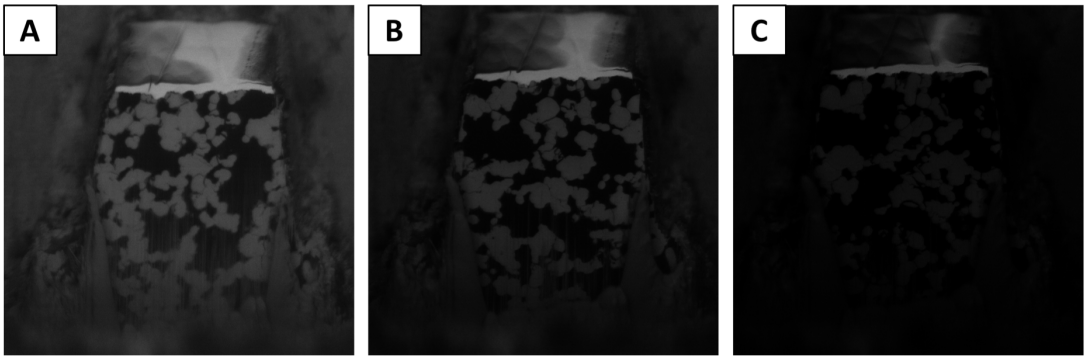

Figure 2.5: A) image 9, B) image 19, and C) image 29 in a BSE image set generated during a 3D FIB-Tomography run, with later images showing increasing signal loss across the entire image region.

Since the images became progressively darker with run time, it was thought positive charging from ion implantation was a likely cause. As noted earlier, the positive-charge ion utilized for the FIB (in this case, Ga^+ ions) both sputters material from the sample surface and implants into the near-surface bulk of the sample. The buildup of Ga^+ ions embedded in the cross-section, and especially in the trench floor around the cross-section, would create an increasing positive charge at the sample surface. This would weaken the SE and BSE signals detected by the SEM, causing the sample surface to appear increasingly dark. This scenario plausibly explains the global darkening of the 3D acquisition images.

As further corroboration, other 3D acquisition test runs did not display this global darkening. The key difference was the successful runs utilized the "FIB Observer" option in FIB-SEM software while the run that suffered from global darkening did not utilize this option. When enabled, the "FIB Observer" option added pauses in the FIB milling step at regular intervals (interval length was user-defined) and the SEM automatically scanned over the sample cross-section to update the SEM image on the monitor. If the sample was slowly accumulating positive-charge from an increasing amount of embedded Ga^+ ions, then regularly scanning the sample surface with the SEM electron beam exposed the

sample to a negative charge, negating the excess positive-charge. This is similar to using a "flood gun" to produce electrons to neutralize excess positive-charge on a sample surface. It was therefore concluded that the "FIB Observer" option was acting as an electron "flooding" step during ion milling that preventing the embedded Ga^{+} from interfering with sample imaging. All subsequent 3D FIB-Tomography runs that utilized the "FIB Observer" option did not suffer from global darkening.

2.4. Image Processing:

Following the acquisition of SEM images by the milling-and-imaging run during 3D FIB Tomography, the resulting image set was processed to replace the signal-based intensity of the original images with material-based intensity in the final segmented images (so each intensity value corresponded to a unique material). To accomplish this, the image set must undergo 3 steps: 1) Pre-Processing, where noise, shading, and other artifacts in the raw images were removed; 2) Segmentation, where a classification program groups together neighboring pixels of similar signal-intensities into a unified phase both within each image and between adjacent images in the image set; and 3) Post-Processing, where errors in the Segmentation step were removed.

2.4.1. Pre-Processing:

2.4.1.1 Image Registration:

The SE images showed charging artifacts not present in the BSE images, so the BSE images were used for the segmentation procedure and the SE images were used as references. For the BSE image set, pre-processing began by aligning the individual images using the "Linear stack alignment with SIFT" plug-in available in the image processing and analysis software, FIJI, with the "Rigid" option selected.[108–110] This plug-in utilized the Scale Invariant Feature Transform (SIFT) algorithm to identify unique features present across adjacent images and then shifted/rotated the images to correct for any image drift. The image set was then cropped to remove black areas on the image edges artificially created by the alignment process, excess parts of the image that extended beyond the

polished cross-section, and areas at the bottom of the image that had too many artifacts to be correctly segmented.

2.4.1.2. Shade Correction:

The aligned-and-cropped BSE image set then underwent the application of a "shade correction" plugin created by Dr. Taillon and run in FIJI.[98,111] The shading artifact is visible in Figure 2.6a, where the bottom quarter of the image appears darker than the rest of the image (brightness/contrast were adjusted to emphasize shading). This is also seen in the histograms of the top 300 rows and bottom 300 rows, showing that all pixels in the bottom of the image were shifted to lower intensity values (Figure 2.6c). The shading artifact originated from less signal escaping from the bottom of the cross-section as compared to the top due to the walls of the U-shaped trench blocking part of the signal.

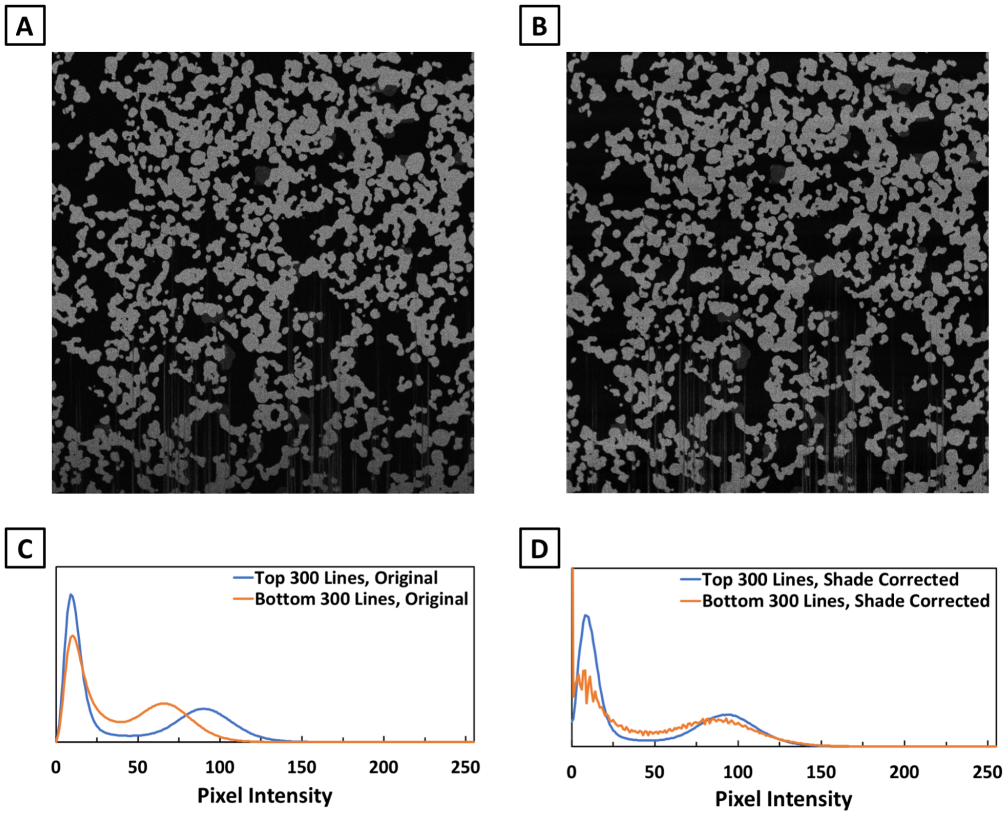

Figure 2.6: A) BSE image after cropping and alignment. Shading artifact clear visible in the bottom section of the image. B) BSE image after shade correction, showing greater homogeneity across the entire image. Histogram for different parts of C) the pre-correction BSE image and D) post-correction BSE image, clearly showing the effects of the shading artifact and the changes introduced by the shade-corrections.

Dr. Taillon's plugin implements a solution originally reported for data analysis of satellite images of Earth.[111] It was observed that a satellite image with sufficiently numerous and pseudo-random features has an approximately Gaussian distribution in the pixel intensity histogram. When uneven lighting/signal caused shadowing of part of the image, the "true" Gaussian distribution in that shaded region was shifted and dilated/compressed but still retained an approximately Gaussian distribution (Equation 2.1). When attempting to correct this shading, if the Gaussian distribution of the shadowed pixels was normalized then the distribution was fully described by its mean and standard deviation. Therefore, the changes in the "true" Gaussian distribution of the image due to shadowing are undone by simply adjusting the mean and standard deviation of the Gaussian

distribution of the shadowed pixels to best match the original, un-shadowed image. In practice, the shade correction plugin split each image into rows of pixels, combined the corresponding rows of all images in the image set, and calculated a pixel intensity histogram for each row of the combined image set as a function of distance from the top of the image set. The plugin used the histograms from the top rows as a reference for the "unshaded image", and then adjusted the mean and standard deviation of the histograms for all other rows in order to best match the reference (Equation 2.2). The final shade corrected image had a noticeably more uniform illumination of the garnet pixels (Figure 2.6b). While the shade-corrected rows in the image set showed increased noise at lower pixel intensity values (shown in Figure 2.6d), the pixel intensity of LLCZN particles across the entire image became more uniform and helped to improve the accuracy of later segmentation.

$$\frac{(I_{new}-\mu_{new})}{\sigma_{new}} = \frac{(I_{old}-\mu_{old})}{\sigma_{old}} \tag{2.1}$$

$$I_{new} = \frac{\sigma_{new}}{\sigma_{old}} * (I_{old} - \mu_{old}) + \mu_{new} \tag{2.2}$$

2.4.1.3. De-noising:

The aligned and shadow-corrected BSE image set was then opened in the 3D analysis software Avizo (FEI Visualization Sciences Group) and a "Non-local means filter" applied to the image set to remove pixel noise.[112] Pixel noise noise appeared to be completely random and caused pixels within ideally homogenous image regions to have intensities above or below the "true" intensity of that region, visible as "salt-and-pepper" noise. This proved especially problematic for segmentation because the noise-affected pixels were assigned to incorrect phases. Simple methods to remove this random noise

involve “local means filters” that replace the value of a given pixel with the average of the surrounding pixels. Since random noise should give equally high and low values, this greatly reduces pixel noise, but at the cost of blurring edges between discrete phases. In contrast, “non-local means filters” identify areas in the image similar to the area around the pixel being corrected and take the average of those areas, thereby reducing pixel noise while maintaining feature edges, but at the cost of substantially increased computation time.[112] For these reasons, the “non-local means filter” was used for image pre-processing in this work.

2.4.2. Segmentation:

The de-noised BSE images were segmented into discrete phases (pore, LLCZN) in FIJI using the 3D Trainable WEKA (Waikato Environment for Knowledge Analysis) plugin, with “secondary” and “gold” phases included when necessary.[113] The de-noised image set was loaded into the 3D Trainable WEKA plugin, the user drew lines across examples of each phase in the images, and each line was assigned by the user to one of the pre-defined phases. The 3D Trainable WEKA program was then “trained” on these lines by using the pattern of pixels intensities across each line to generate rules for assigning pixels to a given phase, and then applied those rules to all images. Based on how accurately the segmentation captured the image feature morphology, the user then assigned additional lines to the pre-defined phases and the Trainable WEKA program was “trained” again with the expanded data set. This process was repeated until a satisfactory segmentation was achieved, at which point the results were exported as red-green-blue (RGB) images and converted to grey scale in FIJI. Given that any gold particles present in the sample were

physically occupying pore volume, gold voxels (3D pixels) in the segmented image set were relabeled as pore voxels.

2.4.3. Post-Processing:

Two main types of artifacts were present in the segmented images: an “interface” artifact and a “curtaining” artifact. The interface artifact consisted of incorrectly labeled pixels at the interfaces between two phases due to the pixel intensity gradient of the interface resulting in pixels with the same intensity as additional segmented phase. This resulted in a coating of secondary phase pixels at the pore-LLCZN interfaces and a double coating of secondary phase and LLCZN pixels at the gold-pore boundaries. The interface artifact could also manifest on the image preceding the appearance of a LLCZN particle or on the image immediately after a particle disappears, essentially bookending the particle. Altogether, the interface artifact only slightly affected the volume fractions of each phase, but significantly affected surface areas. The curtaining artifact consisted of vertical stripes of incorrectly labeled phases in the bottom third of most images, resulting from the ion beam failing to polish perfectly flat cross-sections. This artifact was most common in the pore phase and would artificially increase the LLCZN phase volume while also altering the segmented LLCZN microstructure as compared to the true microstructure. Both artifacts were visible in Figure 2.7, where pore phase was black, secondary phase was dark grey, and LLCZN phase was light grey.

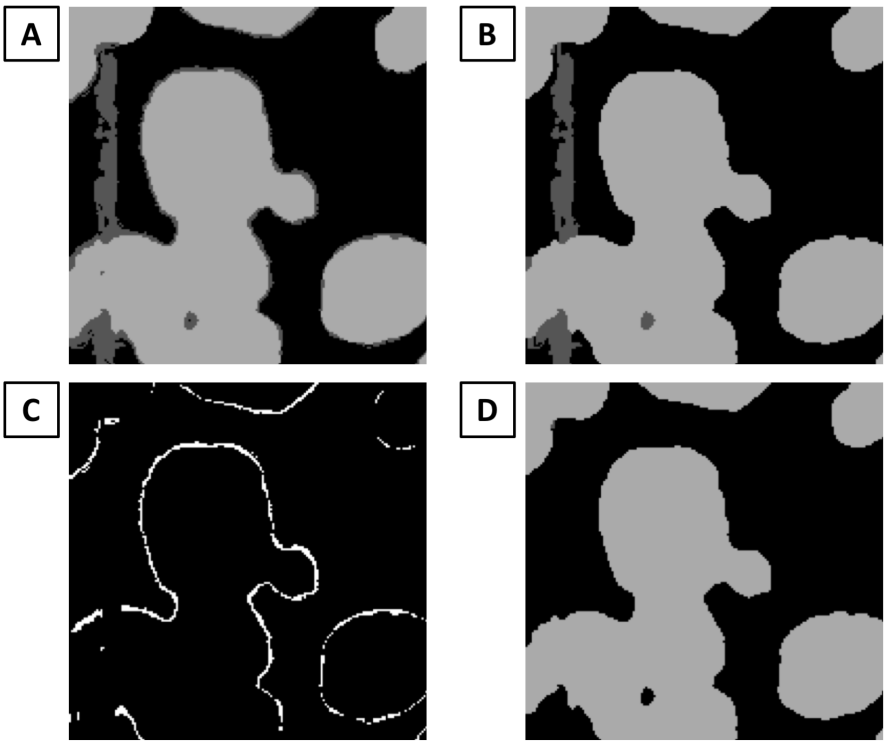

Figure 2.7: A) segmented images with pore phase as black, secondary phase as dark grey, and LLCZN phase as light grey. Both secondary phase "interface artifacts" and "curtaining artifacts" are present. B) segmented image after post-processing by artifact-removal MATLAB code. The interface artifacts were successfully removed but most of the curtaining artifacts remained. C) difference between segmented image before and after application of artifact-removal MATLAB code, showing the removed interface artifacts and curtaining artifacts. D) segmented image after manual clearing of curtaining artifacts with FIJI followed by second application of artifact-removal MATLAB code. All interface and curtaining artifacts now removed.

To remove the two types of artifacts, the segmented image set was post-processed by a custom artifact-removal code written in MathWorks MATLAB (given in Appendix A) that consisted of two parts: coating removal, followed by curtaining removal. The coating removal portion identified contiguous rows/columns of secondary phase pixels, identified what phases bordered the ends of the row/column, then removed the secondary phase pixels based on this and whether the contiguous row/column was smaller than a user-defined value. The curtaining removal portion identified all 3D contiguous secondary phase regions, filtered out 3D regions smaller than a user-defined size, and examined neighboring 2D images of the remaining 3D regions to determine if the secondary phase

smoothly transitioned between images. If this was the case, the secondary phase in question was likely a real secondary phase particle. If the secondary phase showed significant irregularity between neighboring images, then the secondary phase was likely a curtaining artifact unique to each image and was removed. Figure 2.7b shows the segmented image after application of the artifact-removal MATLAB code and Figure 2.7c shows the parts of the image removed by the code. The vast majority of changes remove interface artifacts, with only minor removal of curtaining artifacts in this area. The remaining curtaining artifacts were manually removed using the image adjustment tools in FIJI, with the original BSE images continuously consulted to ensure that only artifacts were removed. The "cleared" 3D image set was post-processed again with the artifact-removal MATLAB code to remove any small secondary artifacts that remained. The final "post-process-complete" 3D image set was used for all later structural analysis Figure 2.7d.

2.5. Mechanical Polishing/FIB Induced Cracking:

For the sample with the highest LLCZN volume fraction, cracks were observed in the top 20 μm of all images acquired during serial milling-and-imaging. In many instances, the cracks completely isolated the uppermost LLCZN particles from the rest of the LLCZN network. If these cracks existed in the original sample, then EIS measurements would give a low effective bulk conductivity for the sample. However, EIS measurements instead gave a relatively high effective bulk conductivity for the sample, in agreement with the high LLCZN volume fraction. Therefore, the cracks visible in the 3D image set were likely artifacts introduced to the sample by the mechanical polishing or by FIB milling/polishing. This was further substantiated by similar cracks appearing in the dense layer of mechanically polished trilayer cross-sections and a previous 3D FIB Tomography run on a trilayer sample, where cracks disconnected the porous layer from the dense layer. Moreover, 2D images of trilayer samples that were fractured without polishing showed well-connected porous layers and dense layers without any visible cracks. To remove the crack artifacts and prevent errors in later analysis, the image adjustment tools in FIJI were used to manually paint over cracks between LLCZN particles that appeared formerly connected, while retaining any clearly identifiable closed or open pores.

2.6. 2D SEM Image Analysis:

2.6.1. Area, Area Fraction, and Perimeter:

Using FIJI, the sample thickness/electrode-electrode distance was measured at several positions across each image and was re-measured for all images of a given sample. The mean and standard deviation was calculated from the resulting list of thicknesses to give a single value for each sample. The BSE images were then pre-processed, segmented, and post-processed with a combination of Avizo, FIJI, and MATLAB (described in Section 2.4). From these segmented images, the 2D area fraction of each phase visible in the BSE images was determined. A custom MATLAB code (given in Appendix B) was created to determine the 2D perimeter of each phase (the 2D analogue to 3D surface area) and the 2D perimeter/2D area ratio (the 2D analogue to 3D surface area-to-volume ratio). The results of all images for a given sample were averaged to give a single value representing each sample, with standard deviations also calculated.

2.7. 3D FIB Tomography Image Analysis:

2.7.1. Volume, Volume Fraction, and Surface Area:

Analyzing the 3D image region starts with first determining the dimensions of the image region, which requires calculating the X-, Y-, and Z-axis voxel dimensions. The voxel dimensions along the X-axis (horizontal axis) and the Y-axis (vertical axis) are always equal, being manually designated by the user when setting the resolution for SEM images collected during the serial milling-and-imaging process. In contrast, the user also designates a nominal Z-axis voxel dimension (along the milling direction) in the form of the ideal slice thickness, but the actual slice thickness will vary during a given run for a number of reasons. These reasons can include the accuracy of the mechanical and software controls for the sample stage, consistency in the FIB current and beam size over time, variation in sample microstructure within each slice and between different slices, and glitches that occur during process operation.

To calculate the actual Z-axis voxel dimension (i.e., actual milled slice thickness), measurements were made using the thickness reference marks milled into the top surface of the platinum protection layer to determine the total milling distance. The reference marks formed the sides and centerline of a triangle, with the angled sides intersecting at a point away from the platinum protection layer. The other ends of the angled sides of the triangle terminated at the milled cross-section, forming the "bottom" side of the triangle (Figure 2.8). This "bottom" side was key to calculating the total milling distance because its "width" would continuously decrease as more of the sample was milled during the serial milling-and-imaging process. Since the angle between the two angled sides of the triangle and the centerline (θ) was known, the change in width of the "bottom" side could be

directly correlated with the change in triangle height, which was equal to the total milling distance.

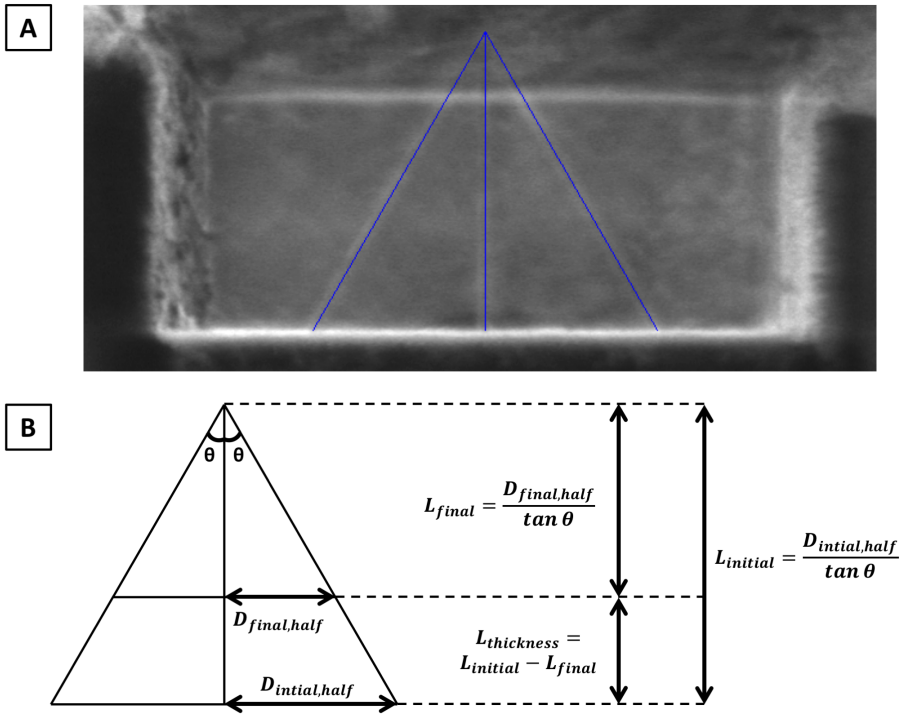

Figure 2.8: A) FIB image of Pt protection layer with overlaid pattern for milling the thickness reference marks (blue lines). B) diagram of relevant dimensions for calculating thickness milled based on images before and after 3D FIB Tomography run.

Using FIJI and the known X-axis voxel dimension, the side-to-side width of the full triangle "bottom" side was measured for the first image of the image set ($D_{initial,\ full}$) and for the final image ($D_{final,\ full}$). The half-widths of the triangle "bottom" sides were then calculated for the first image ($D_{initial,half}$) and the final image ($D_{final,half}$) by dividing the full widths by 2. These half-widths were then combined with the intersection angle between the two angled sides of the triangle and the centerline (θ) to calculate the distance from the intersection point to "bottom" side of the triangle on the first image ($L_{initial}$) and the final image (L_{final}). The total thickness milled ($L_{thickness}$) was calculated from the difference between $L_{initial}$ and L_{final}.

$$D_{intial,half} = {}^{D_{intial,full}}/_{2} \qquad D_{final,half} = {}^{D_{final,full}}/_{2}$$

$$L_{initial} = \frac{D_{intial,half}}{\tan\theta} \qquad L_{final} = \frac{D_{final,half}}{\tan\theta}$$

$$L_{thickness} = L_{initial} - L_{final}$$

The actual Z-axis voxel dimension ($Voxel_{Z\text{-}axis}$) was calculated from the total thickness milled ($L_{thickness}$) and the number of images in the image set (N) with Equation 2.3. "N – 1" was used instead of "N" due to the fact that if the image set was composed of two images, then there was only one milling slice separating them; if there were three images, then there were only two milling slices; if there were four images, then there were only three milling slices; and so on.

$$Voxel_{Z-axis} = \frac{L_{thickness}}{N-1} \tag{2.3}$$

Once the voxel dimensions were known, proper analysis of the data could begin. The total volume of the 3D image region was easily calculated by multiplying the number of pixels or images by the corresponding voxel dimension. The volume of each unique phase was determined by counting the number of voxels of each phase and multiplying by the volume of one voxel. The volume fraction was calculated from the volume of each phase divided by the total volume, or more simply the number of voxels of each phase divided by the total number of voxels. These calculations were performed with MATLAB. Surface areas calculations required specialized software that converted the voxel-based structures in the 3D image region into objects with surface meshes composed of polygons. The surface area of each phase was then determined from the sum of the surface mesh area associated with the objects of that phase. These calculations were performed with the Dragonfly visualization and analysis software (Object Research Systems). The surface

area-to-volume ratio (SA/V) was calculated by dividing the surface area of a given phase by the volume of the same phase.

The Dragonfly software does not have the capability to calculate the interfacial area between adjacent phases, but those areas can be determined from the surface areas calculated for each phase. If only two phases are present (i.e. pore and ceramic), then the surface areas of both phases are equal to each other and are equal to the pore-ceramic interfacial area. If there are three phases present (i.e. pore, secondary, and ceramic), then the surface areas of each phase will be different from each other and different from the interfacial areas associated with that phase. In actuality, the surface area of one phase (i.e. secondary) will be equal to the sum of the other two surface areas (i.e. ceramic and pore) minus 2 times the interfacial area between those two phases (since any interfacial area will be counted 2 times in the sum, once for one phase [i.e. ceramic] and once for the other phase [i.e. pore]).

$$SA_{secondary} = SA_{ceramic} + SA_{pore} - 2 * IA_{\text{ceramic–pore}}$$

Thus, the interfacial areas for all interfaces between three phases (i.e. pore, secondary, and ceramic) will be as follows:

$$IA_{\text{ceramic–pore}} = \frac{1}{2}\left(SA_{ceramic} + SA_{pore} - SA_{secondary}\right)$$

$$IA_{\text{ceramic–secondary}} = \frac{1}{2}\left(SA_{ceramic} + SA_{secondary} - SA_{pore}\right)$$

$$IA_{\text{secondary–pore}} = \frac{1}{2}\left(SA_{secondary} + SA_{pore} - SA_{ceramic}\right)$$

2.7.2. Tortuosity:

Travel paths through porous materials are always longer than travel paths in single phase materials because single phase materials facilitate direct routes, while porous microstructures only offer indirect routes (Figure 2.9).[114] As a consequence, the longer travel paths in porous microstructures result in lower conductivity/diffusivity, greater ohmic losses and higher ASR values. To quantify this behavior, the parameter "tortuosity" (τ) was defined as the lengths of travel pathways through a porous region (Δl) divided by the length of a Euclidean/straight path (Δx) across the same region, described in Equation 2.4. By this definition, any deviation from a straight path will result in a tortuosity greater than 1 regardless of the dimensions of the region being analyzed.

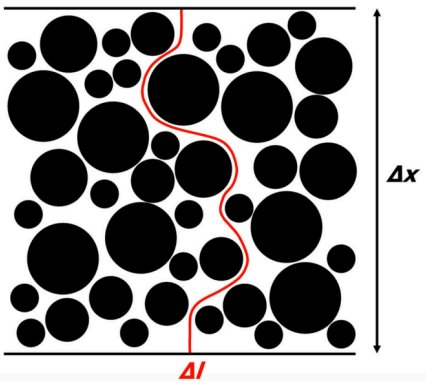

Figure 2.9: Tortuosity is defined as the ratio of the pathway length (Δl) to the straight/Euclidean path length (Δx).[114]

$$\tau_{geometric} = \lim_{l \to \infty} \frac{\Delta l}{\Delta x} \tag{2.4}$$

Multiple approaches exist within the literature for calculating the tortuosity of a 3D porous microstructure.[115] Experimentally, tortuosity can be measured by performing EIS on porous samples, calculating the effective conductivity, and comparing to the intrinsic conductivity of the conducting material.[116,117] Computationally, tortuosity can be calculated by analyzing 3D image sets of actual porous microstructures generated by 3D

FIB tomography[65] or x-ray computed tomography.[67] These calculations tend to follow two approaches: 1) distance-based/geometric tortuosity ($\tau_{geometric}$) and 2) simulation-based/diffusive tortuosity ($\tau_{diffusive}$). The distance-based/geometric tortuosity is defined as the calculated lengths of conduction pathways through the 3D image region divided by the external dimensions of the 3D image region, which follows directly from the original interpretation of tortuosity shown in Equation 2.4. Calculation approaches include the Fast Marching Method, which simulates a wave propagating through the 3D image region (Figure 2.10a).;[118,119] the pore centroid method, which tracks the mean pore centroid between 2D images (Figure 2.10b).;[66] and identification of minimum length paths via the Dijkstra algorithm (Figure 2.10c).[120,121]

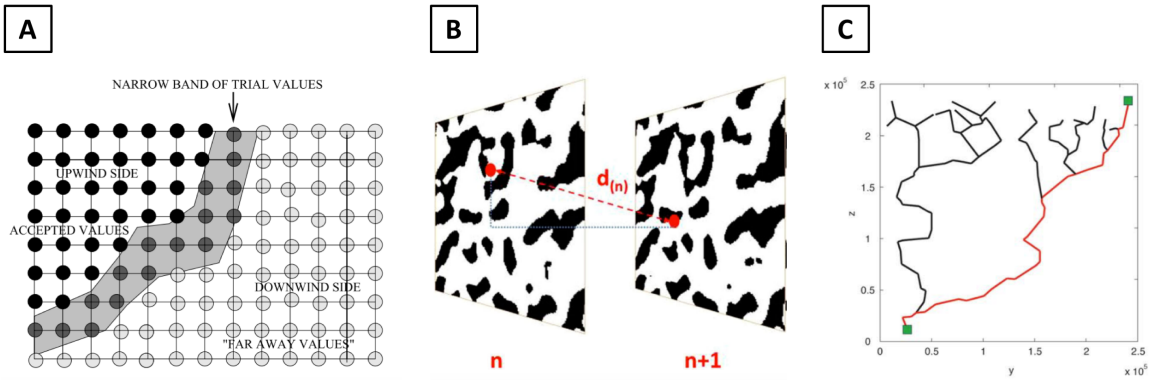

Figure 2.10: Visualizations of the A) Fast Marching method,[118] B) the pore centroid method,[114] and C) the identification of minimum path lengths via the Dijkstra algorithm.[120]

Simulation-based/diffusive tortuosity is defined as the intrinsic conductivity/diffusivity of the conducting phase in the simulation ($\sigma_{sim,dense}$ or $D_{sim,dense}$) multiplied by the conductive phase volume fraction (f) and divided by the conductivity/diffusivity of the porous microstructure as determined by simulations ($\sigma_{sim,porous}$ or $D_{sim,porous}$), as shown in Equation 2.5.[122] The simulation-based approaches include heat/electric current flow simulations via computational fluid dynamics software[123]

(Figure 2.11a); solving the Laplace equation[122]; and diffusivity calculations via random walk simulations (Figure 2.11b).[124]

$$\tau_{diffusive} = \frac{\sigma_{sim,intrinsic}*f}{\sigma_{sim,porous}} = \frac{D_{sim,intrinsic}*f}{D_{sim,porous}} \quad (2.5)$$

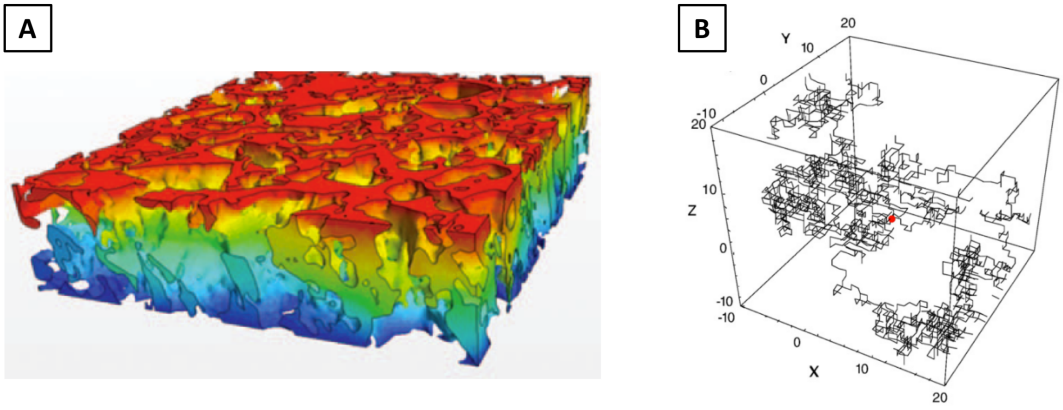

Figure 2.11: Visualizations of A) the computational fluid dynamics heat transfer simulation[123] and B) the random walk simulation.[124]

While different implementations are inherently expected to produce slightly different results, EIS-based tortuosity values are usually the highest, geometric tortuosity values are usually the lowest, and diffusive tortuosity values are usually intermediate.[125–127] This variation is generally attributed to geometric tortuosity approaches treating all paths through the 3D image region as equal contributors to the flow of ionic/electronic current.[128] In reality, not all pathways contribute equally because bottlenecks exist within the 3D microstructure that restrict current flow.[63,120] The effects of these bottlenecks were automatically probed by EIS measurements and diffusion simulations, so the EIS-based and diffusive tortuosity values were actually a convolution of tortuosity and bottleneck effects and thus gave higher values than the distance-based tortuosity.[120,127]

Moreover, theoretical and empirical measurements have shown the effective conductivity of the porous microstructure ($\sigma_{effective}$) is proportional to $(\tau_{geometric})^{-2}$ (Equation 2.6), while the same effective conductivity is proportional to $(\tau_{diffusive})^{-1}$ (Equations 2.7).[64,67,122,124,129,130] This further explains why diffusive and EIS tortuosity values were always higher than geometric tortuosity for the same microstructure. The use of the (-1) exponent for the diffusive tortuosity originates directly from Equation 2.5, where diffusive tortuosity is defined explicitly by the diffusivity/conductivity. In contrast, the geometric tortuosity is defined in terms of physical lengths of pathways through the material (Equation 2.4), so additional work is required to relate this to the diffusivity/conductivity in order to understand the origin of the (-2) exponent.

$$\frac{\sigma_{effective}}{\sigma_{intrinsic}} \sim \left(\tau_{geometric}\right)^{-2} \tag{2.6}$$

$$\frac{\sigma_{effective}}{\sigma_{intrinsic}} \sim \left(\tau_{diffusive}\right)^{-1} \tag{2.7}$$

Adapted from van Brakel, *et al*, consider a diffusive pathway segment that is parallel to the straight axis across a porous microstructure (i.e. a pathway segment with a tortuosity of 1.0).[63] The segment has a constant cross-sectional area (A), length (L), and an intrinsic conductivity ($\sigma_{pathway,intrinsic}$), shown in Figure 2.12. Now consider that same pathway segment is tilted by a constant angle (α) relative to the original straight pathway segment, also shown in Figure 2.12. The tilt will extend the segment length from L to L/cosα (note: the tube "height" along the vertical direction is still L). At the same time, the segment cross-sectional area will decrease from A to Acosα (note: the tube area when intersecting a horizontal plane is still A, so the tube volume is unchanged despite the tilt). If considering electrical flow, the result is the tilted pathway segment has a higher resistance (R_{tilt}) than the original straight pathway segment ($R_{straight}$), as shown in Equations

2.6 and 2.7. When the resistance of the tilted segment is calculated based on the cross-sectional area A and the length of the original straight pathway segment L, an effective conductivity is used ($\sigma_{pathway,effective}$) instead of the intrinsic conductivity.

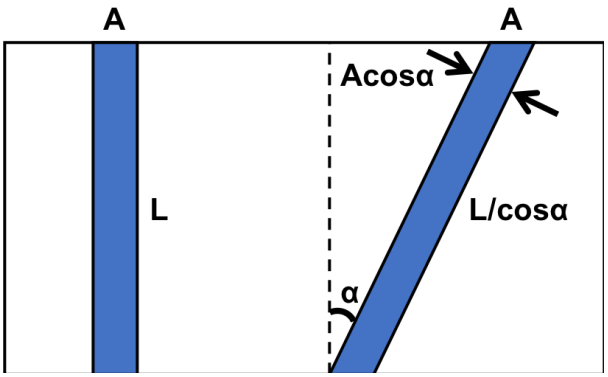

Figure 2.12: Diagram of relevant dimensions for calculating the exponent relating geometric tortuosity to conductivity.

$$R_{tilt} = \frac{L}{\sigma_{pathway,effective} * A} \tag{2.6}$$

$$R_{straight} = \frac{L}{\sigma_{pathway,intrinsic} * A} \tag{2.7}$$

Alternatively, the resistance of the tilted pathway segment can be calculated using the actual cross-sectional area and actual length of the tilted segment, in which case the intrinsic conductivity is used (Equation 2.8).

$$R_{tilt} = \frac{L/cos\alpha}{\sigma_{pathway,intrinsic} * Acos\alpha} = \frac{L}{\sigma_{pathway,intrinsic} * A(cos\alpha)^2} \tag{2.8}$$

Combining Equation 2.8 with Equation 2.6, we observe that the ratio of the effective conductivity to the intrinsic conductivity of the pathway segment is equal to the dimensionless quantity $(cos\alpha)^2$, as shown in Equation 2.9.

$$\frac{\sigma_{pathway,effective}}{\sigma_{pathway,intrinsic}} = (cos\alpha)^2 \tag{2.9}$$

Referring to the definition of geometric tortuosity (Equation 2.4) and substituting L/cosα for the pathway segment length, we observe that geometric tortuosity equaled 1/cosα (Equation 2.10).

$$\tau_{geometric} = \frac{L_{pathway}}{L_{straight}} = \frac{L/cos\alpha}{L} = \frac{1}{cos\alpha} \tag{2.10}$$

Substituting Equation 2.10 into Equation 2.9, we therefore confirm that the ratio of the effective conductivity to the intrinsic conductivity of the pathway segment is equal to the geometric tortuosity with a (-2) exponent (Equation 2.11). This relationship holds after averaging over all pathway segments in the porous microstructure. It is important to note that Equation 2.11 can be extended to describe the conductivity ratio of the porous microstructure if the conductive phase volume fraction and a parameter describing the effects of bottlenecks are included.

$$\frac{\sigma_{pathway,effective}}{\sigma_{pathway,intrinsic}} = \frac{1}{(\tau_{geometric})^2} = (\tau_{geometric})^{-2} \tag{2.11}$$

In this study, the geometric tortuosity of the LLCZN and pores phases was calculated using the Fast-Marching Method (FMM), which modeled a wave propagating from one boundary plane of the 3D image region (the "Starting Plane") through all contiguous voxels of the chosen phase to the opposing parallel boundary plane (the "Ending Plane"). As the wave propagated, minimum travel path lengths were assigned to the chosen phase voxels as they were encountered by the wave, and those distances were then converted to cumulative geometric tortuosity values. When assigning distances, calculations considered all 26 neighbor voxels sharing a face, edge, or corner with each voxel of interest, which produces more accurate distance results than considering only the six face-sharing/nearest neighbors.[131] Tortuosity values were calculated along the

"forward" and "reverse" directions of each of the X-, Y-, and Z-axes for a total of 6 separate tortuosity values, with the forward and reverse directions averaged together to give a single direction-averaged tortuosity value. To make comparing different samples easier, the X-, Y-, and Z-axes direction-averaged geometric tortuosity values were then combined into a single characteristic geometric tortuosity using Equation 2.12.[127] A detailed description of the MATLAB implementation of this tortuosity calculation approach is given in Appendix C.

$$\tau_{characteristic} = \frac{3}{\frac{1}{\tau_x}+\frac{1}{\tau_y}+\frac{1}{\tau_z}} \tag{2.12}$$

2.7.3. Percolation Factor:

When examining either conductive solids with multiple long-range phases or insulating porous solids filled with a conductive fluid, the effective conductivity/diffusivity of the conductive phase is affected by how much of the conductive phase is connected to the electrodes. This is critically important for the electrodes in SOFC's, where isolated pores or solid phase limit the triple phase boundary length and lower performance (Figure 2.13).[67,68,132,133] Similarly, the active material in electrodes of Li-ion batteries need to be connected to both the Li-ion conducting electrolyte and the electronically conducting phase.[134,135]

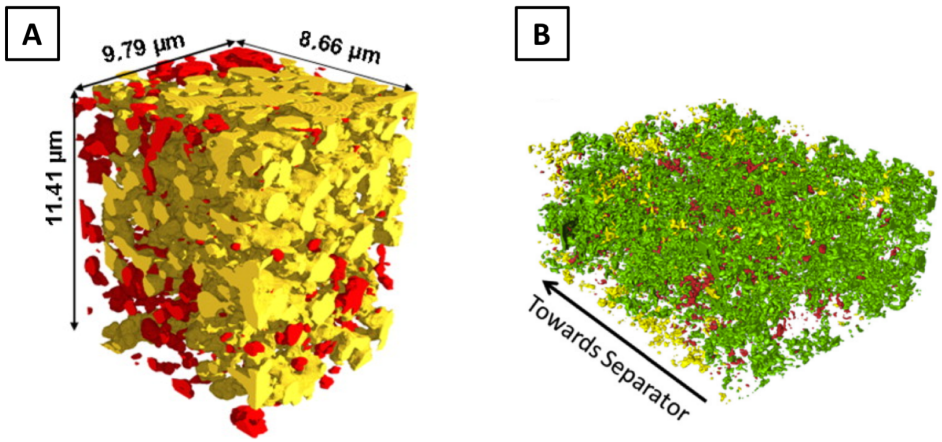

Figure 2.13: A) map of percolated Ni-phase (yellow) and isolated Ni-phase (red) in a Ni–8YSZ anode for an SOFC.[132] B) map of percolation in carbon black phase in $LiFePO_4$ composite electrode, divided into fully percolated to (green), potentially percolated (yellow), or fully isolated regions (red).[134]

The overall connectivity of the conductive phase in a porous sample can be expressed by the "percolation factor" (*P*), defined as the ratio of the volume of connected/percolated conductive phase to the total volume of conductive phase (Equation 2.13). This parameter is easily extracted from 3D image sets obtained by tomography techniques, since modern analysis software makes it simple to identify all conductive phase voxels that are contiguously connected to one of the six boundary planes of the 3D image region. As a result, it is also possible to identify anisotropy in the percolation factor for the given 3D image region.

$$P = \frac{N_{phase,connected}}{N_{phase,total}} \tag{2.13}$$

2.7.4. Continuous Particle Size Distribution (c-PSD), Mercury Intrusion Porosimetry PSD (MIP-PSD), and Constriction Factor:

The constriction factor is defined as the mean cross-sectional area of bottlenecks in the porous microstructure divided by the mean cross-sectional area of the particles (assuming a conductive solid), as shown by the middle parts of Equation 2.14.[130] The

bottlenecks and particles are commonly assumed to have circular cross-sections, so the constriction factor can also be determined from the mean minimum particle diameter (or mean bottleneck diameter) and mean maximum particle diameters, as shown in Figure 2.14a and the right part of Equation 2.14.

$$\beta = \frac{A_{bottleneck}}{A_{particle}} = \left(\frac{d_{bottleneck}}{d_{particle}}\right)^2 \tag{2.14}$$

The concept of using a constriction factor to capture the effects of bottlenecks in porous media was proposed many years ago by several researchers.[63,130,136,137] At the time, no experimental techniques existed to directly image porous microstructures, so instead the researchers studied the effects of pre-defined bottlenecks in theoretical microstructures. The advent of tomography techniques removed this limitation and constriction factors can be readily calculated for real microstructures. Münch, *et al*, created a practical way to determine the mean bottleneck and particle diameters by using the concept of a continuous particle size distribution (c-PSD).[138] Here, the chosen phase in the 3D image region was systematically filled with test spheres of identical diameters D, the volume fraction of the phase covered by spheres was determined, and the calculations were repeated for a series of increasing test sphere diameters (Figure 2.14b).[139] The default c-PSD cumulative coverage vs. sphere diameter curves described the distribution of particle sizes in the 3D image region, and the mean particle diameter was taken to be the diameter corresponding to 50% coverage (Figure 2.14d). To measure the mean bottleneck diameter, the c-PSD was used to simulate mercury intrusion porosimetry (MIP), a physical measurement approach wherein liquid mercury was infiltrated into a porous sample and the average pore bottleneck size was determined due to the inkbottle effect.[140] To accomplish this, the c-PSD approach was modified to reject any regions covered by test spheres that were not

contiguous with one of the six boundary plans of the 3D image region (Figure 2.14c).[138] From the resulting MIP-PSD cumulative coverage vs. sphere diameter curves, the mean bottleneck diameter was taken to be the diameter corresponding to 50% coverage (Figure 2.14d). With the c-PSD and MIP-PSD 50% coverage diameters, Equation 2.14 was then modified to give Equation 2.15. Detailed descriptions of the MATLAB implementation of the c-PSD and MIP-PSD calculation approaches are given in Appendix D and E, respectively.[141]

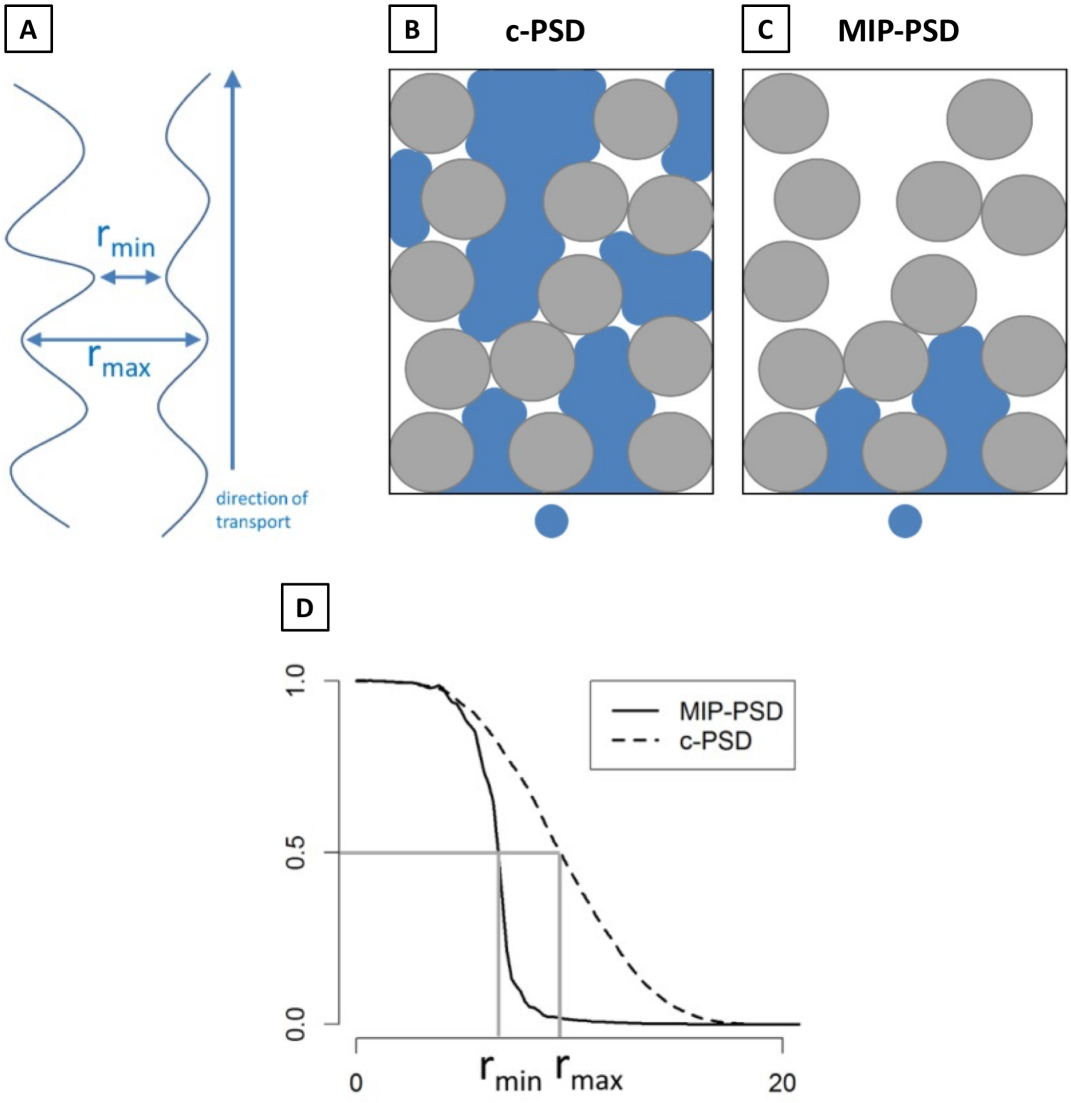

Figure 2.14: A) solid-phase particle size varies across 3D microstructures, creating small diameter particles (r_{min}) that act as bottlenecks and limit transport through larger diameter particles (r_{max}). Visualization of the sphere fitting approach for calculating B) the c-PSD, C) the MIP-PSD, and D) estimating minimum and maximum average particle diameters from 50% MIP-PSD and c-PSD coverage values, respectively.[139]

$$\beta = \frac{A_{bottleneck}}{A_{particle}} = \left(\frac{d_{MIP-PSD,50\%}}{d_{c-PSD,50\%}}\right)^2 \tag{2.15}$$

2.7.5. M-factor:

A long-term goal of microstructure researchers was to connect measured diffusion or electrochemical properties with parameters that uniquely define the underlying microstructure. Conceptually, this is accomplished by modifying the intrinsic conductivity/diffusivity of the dense sample ($\sigma_{intrinsic}$) by a microstructure factor, or M-factor (M), to calculate the effective conductivity/diffusivity of the porous sample ($\sigma_{effective}$), as shown in Equation 1.2. The most general form of the M-factor uses the conductive/diffusive phase volume fraction (f), the percolation factor (P), and the tortuosity (τ), as shown in Equation 2.16.[63,64]

$$\sigma_{effective} = M * \sigma_{intrinsic} \tag{1.2}$$

$$M = \frac{f*P}{\tau} \tag{2.16}$$

For EIS-based tortuosity and diffusive tortuosity, Equation 2.16 is sufficient. For geometric tortuosity, Equation 2.16 has to be modified to include the constriction factor (β) and a -2 exponent for the tortuosity, shown in Equation 2.17. Additional studies investigated many different artificial microstructures to determine the optimum exponents for the terms in the M-factor equation, though these studies also showed that the baseline form of the M-factor in Equation 2.17 provided good agreement with the calculated effective conductivities.[139,142,143]

$$M = \frac{f*P*\beta}{\left(\tau_{geometric}\right)^2} \tag{2.17}$$

3. Solid-State Li-Ion Electrolyte with Tape-Cast Porous Microstructure:

The dense-porous-dense multi-layered trilayer garnet structures reported in literature were fabricated with several methods, the most common approach being tape-casting of the separate layers. This allowed the composition of each tape and the resulting layer of the trilayer to be independently varied and optimized. Tape-casting was also compatible with production scale up by virtue of the ability to dramatically increase the sizes of individual tapes to meet size or throughput requirements. As such, this study used tape casting to create porous garnet microstructures with varying amounts of porosity.

3.1. Methods and Characterization:

3.1.1. Porous LLCZN Fabrication:

Precursor powders of $LiOH*H_2O$ (Alfa Aesar, 98%) or Li_2CO_3 (GFS Chemicals), La_2O_3 (GFS Chemicals, 99.9%) (dried at 800 °C in air for several hours), ZrO_2 (Inframat Advanced Materials, 99.9%), Ca_2CO_3 (Carolina), and Nb_2O_5 (Alfa Aesar, 99.9%) were weighed out to form the nominal composition of $Li_{6.75}La_{2.75}Ca_{0.25}Zr_{1.5}Nb_{0.5}O_{12}$ (LLCZN). 10 wt. % excess of the Li-containing precursor was added to account for losses during calcination. The powders were ball milled in isopropanol with yttrium-stabilized zirconia (YSZ) milling media (Inframat Advanced Materials) for 24 hours. The powders were sieved, dried at 100 °C in air, ground in a mortar-and-pestle, and pressed into pellets. The pellets were calcined on MgO plates at 900 °C for 6 hours in air, after which the pellets were ground again in a mortar and pestle. Dynamic light scattering (DLS) or laser diffraction were used to analyze the calcined LLCZN powder, reporting a mean particle size >5 microns and a wide particle size distribution. The LLCZN powder was again ball

milled in isopropanol, this time for several days. DLS/laser diffraction showed the resulting powder was composed of ~1 micrometer diameter particle, referred to as "micron powder" for the remainder of this study.

The calcined LLCZN "micron powder" was then mixed into tape-casting slurries with toluene (Fisher Chemical, HPLC Grade), isopropanol (Pharmco, 99% ACS/USP/NF Grade), benzyl butyl phthalate (Tape Casting Warehouse, Inc.), polyvinyl butyral (Tape Casting Warehouse, Inc.), menhaden fish oil (Tape Casting Warehouse, Inc.), polyalkylene glycol (Tape Casting Warehouse, Inc.), and poly-(methyl methacrylate) or PMMA (Soken Chemical and Engineering Company, Ltd.). To create sintered samples with varying porosities, different slurries had different LLCZN-PMMA pore former volume ratios and different mixtures of multiple PMMA sizes. The slurries were cast and dried, and sections of the resulting tapes were cut out and laminated to make green tape stacks. The stacks were sintered at 1050 °C on MgO plates in a tube furnace under flowing oxygen. The sintered porous samples were stored in a glovebox under argon.

3.1.2. Impedance Measurements:

Gold conductive paste (Heraeus Electronics) was painted onto the top and bottom surfaces of each porous sample and a silver wire was pressed against the gold paste. One of the gold electrodes was made smaller than the other gold electrode to act as a limiting electrode. The paste was dried at 100 °C in air, and then annealed at 700 °C for 1 hour in a tube furnace while flowing oxygen. The annealed samples were stored under argon in a glovebox. Room temperature (~25 °C) impedance measurements were performed in the glovebox using a Solartron 1260 Gain and Impedance Analyzer over the range of 15 MHz

to 1 Hz, with sample temperature measured by an IR gun. After completing the impedance measurements, both sides of the sample were photographed next to a ruler to determine the area of the limiting gold electrode. Using the image analysis program FIJI, the photograph was filtered with a color threshold to isolate the pixels of the gold electrode, the number of electrode pixels was determined, and the pixel count was converted to gold electrode area in cm^2 by using the image of the ruler as a reference.[108]

3.1.3. X-ray Diffraction:

The crystalline phases present in several samples were characterized via x-ray diffraction (XRD) using a Bruker C2 Discover with 2D Detector operated at 40 kV and 40 mA. Phase identification was performed with Diffrac.Eva (Version 4, Bruker AXS) and lattice parameters were calculated using Topas (Version 5, Bruker AXS).

3.2. Results and Discussion: LLCZN Phase:

Four samples were selected for imaging and reconstruction through 3D FIB Tomography, shown in Figure 3.1 (yellow for LLCZN, red for secondary phase). The first sample was the porous layer from a porous-dense-porous trilayer sample, referred to as "Trilayer 1". The remaining three samples were from entirely porous samples fabricated with different amounts of pore former, resulting in different amounts of porosity in the sintered samples. These three porous layer samples are referred to as "Porous 1", "Porous 2", and "Porous 3". For all four samples, the horizontal axis of the 3D image region was defined as the X-axis, the vertical axis was defined as the Y-axis, and the axis into the page (aka parallel to the milling direction) was defined as the Z-axis. For reference, the X-axis was normal to the gold electrodes applied to the external surfaces of the sample.

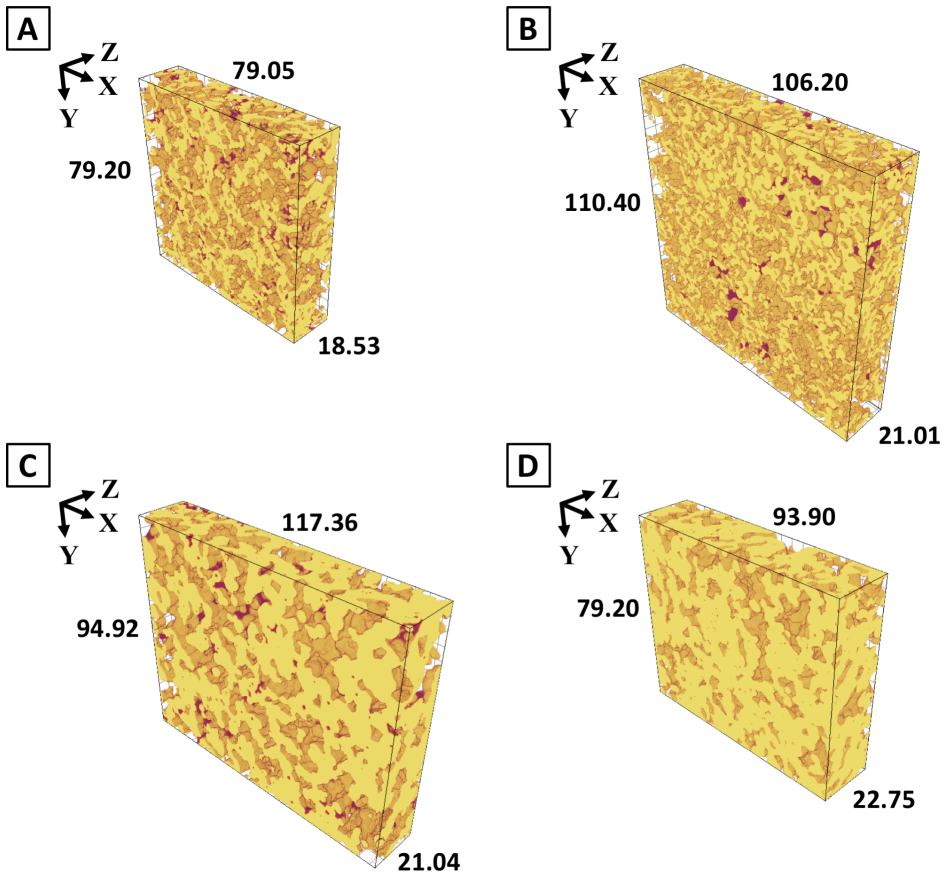

Figure 3.1: 3D reconstruction of A) Trilayer 1; B) Porous 1; C) Porous 2; and D) Porous 3 samples. LLCZN phase is yellow and any secondary phase is red. Reconstruction dimensions were in µm.

3.2.1. Volume, Volume Fraction, and Surface Area:

Table 3.1 shows the volume, volume fraction, surface area, and surface-area-to-volume (SA/V) ratio for each phase in each sample analyzed with 3D FIB Tomography. The Trilayer 1 and Porous 1 samples had similar microstructures, resulting in near identical porosity of 56.03% and 56.67%, respectively. Porous 2 displayed a lower porosity of 40.58%, and Porous 3 displayed the lowest porosity of 26.45%. The SA/V ratios of the LLCZN phase generally decreased as the LLCZN phase fraction increased, with a similar pattern observed for the pore phase. The secondary phase showed significantly higher SA/V ratios and no clear trend with secondary phase fraction. Prior EDS maps of the

secondary phase showed significantly less La and more Ca than the surrounding LLCZN, strongly suggesting it was not LLCZN and therefore not a Li-conducting material.

Table 3.1: Characterization of the 3D FIB Tomography image regions of the tape-cast LLCZN microstructures.

	Dimensions (µm)	**Material**	**Phase Volume Fraction (%)**	**Volume V (µm^3)**	**Surface Area SA (µm^2)**	**SA/V (1/µm)**
Trilayer 1	79.05	LLCZN	42.30	49,068.16	102,313.09	2.0851
	79.20	Secondary	1.67	1934.90	16,545.42	8.5510
	18.53	Pore	56.03	64,986.91	95,476.55	1.4692
Totals			*100.00*	*115,989.97*	*214,335.06*	
Porous 1	106.20	LLCZN	42.58	104,919.80	263,917.03	2.5154
	110.40	Secondary	0.75	1844.15	10,122.49	5.4890
	21.01	Pore	56.67	139,621.09	263,254.13	1.8855
Totals			*100.00*	*246,385.05*	*537,293.66*	
Porous 2	117.36	LLCZN	57.51	134,801.56	142,046.41	1.0537
	94.92	Secondary	1.91	4474.28	25,264.77	5.6467
	21.04	Pore	40.58	95,102.88	129,981.86	1.3667
Totals			*100.00*	*234,378.72*	*297,293.03*	
Porous 3	93.90	LLCZN	73.55	124,437.15	106,694.63	0.8574
	79.20	Secondary	0.00	0.00	0.00	
	22.75	Pore	26.45	44,748.18	106,694.63	2.3843
Totals			*100.00*	*169,185.33*	*213,389.26*	

Table 3.2 shows the interfacial areas for the LLCZN-pore, LLCZN-secondary, and secondary-pore interfaces. In all cases, the interfacial area was either equal to or less than the surface area of each of the phases associated with that interface, as expected. Despite this, the interfacial areas were relatively close in value to the associated surface area values, so the same trends were observed in both types of areas with regards to porosity. Focusing on the LLCZN surface, the interface with the secondary phase accounted for 11.43%, 2.04%, 13.14%, and 0% of the total LLCZN surface area for Trilayer 1, Porous 1, Porous 2, and Porous 3, respectively. Presuming the secondary phase was Li-blocking, this means that 88.57%, 97.96%, 86.86%, and 100%, respectively, of the total LLCZN surface was exposed to the pores and therefore accessible by infiltrated electrodes. Examining the total solid volume in the image region (i.e. LLCZN and secondary phase), Trilayer 1 was 3.79%

secondary phase, Porous 1 was 1.73% secondary phase, Porous 2 was 3.21% secondary phase, and Porous 3 was 0% secondary phase (Figure 3.2). No clear trend with sample porosity was present, but Figure 3.2 clearly shows the increasing amount of secondary phase in the solid part of the image region was directly correlated with higher amounts of LLCZN surface obscured by the secondary phase. While the secondary phase accounted for less than 4% of the total solid volume, it decreased the accessible LLCZN surface area, sometimes substantially, highlighting the importance of synthesizing LLCZN with 100% phase purity.

Table 3.2: Characterization of the interfacial areas in the 3D FIB Tomography image regions of the tape-cast LLCZN microstructures.

	Interface	Interfacial Area (μm^2)	% LLCZN Surface Contacting Secondary Phase	% Solid Volume Composed of Secondary Phase
Trilayer 1	LLCZN-pore LLCZN-secondary Secondary-pore	90,622.11 11,690.98 4854.44	11.43	3.79
Porous 1	LLCZN-pore LLCZN-secondary Secondary-pore	258,524.34 5392.69 4729.79	2.04	1.73
Porous 2	LLCZN-pore LLCZN-secondary Secondary-pore	123,381.75 18,664.66 6600.11	13.14	3.21
Porous 3	LLCZN-pore LLCZN-secondary Secondary-pore	106,694.63 0.00 0.00	0.00	0.00

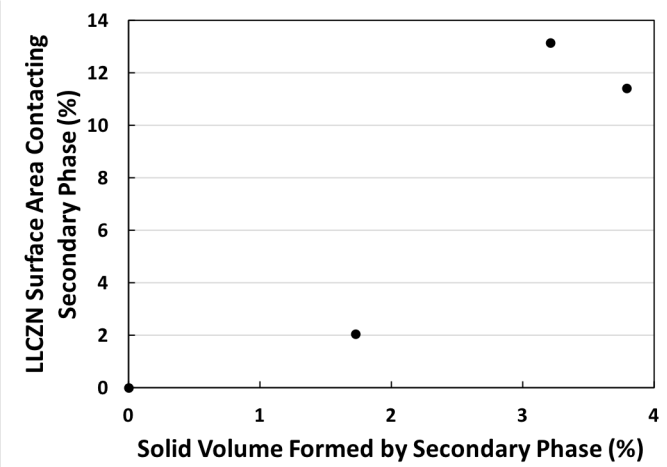

Figure 3.2: % of LLCZN surface area contacting secondary phase vs. % of solid volume in image region formed by secondary phase.

Examining the phase volume fractions at different points along the X-, Y, and Z-axes of the samples identified distinct behavior for each axis (Figure 3.3). Along the Z-axis, there was very little variability in the volume fractions across the sample, and the values at each position were very close to the sample-wide average values. Along the Y-axis, there were relatively moderate-sized, high-frequency oscillations around the average, but the volume fraction values at each position still were relatively close to the average values. Additionally, the shape of the Y-axis volume fraction curves appeared very similar throughout. In contrast, the X-axis showed both the high frequency oscillations visible for the Y-axis and low frequency oscillations that caused long-range changes in the phase volume fractions. As such, the X-axis volume fraction curves had multiple regions with distinct trends in phase volume fractions. This distinctive behavior possibly indicated pore collapse during sintering or garnet settling during the tape-casting process. The X-axis was parallel to the "vertical" axis of the sample during sintering, so any pore collapse would occur preferentially along the X-axis and cause the LLCZN phase to be aligned more along the YZ-plane than the X-axis. This suggested relatively large regions of alternating high

and low pore volume fraction should be visible along the X-axis, with more homogenous distributions along the Y- and Z-axes. The volume fraction variations could also result from the tape-casting process, where there was a time lag between casting the tape slurry and fully drying the tape, during which the randomly distributed garnet and pore former particles would settle. This would have similar microstructural effects as pore collapse and also be reflected in large volume fraction variations along the X-axis, with more homogenous distributions along the Y- and Z-axes. The results in Figure 3.3 show these expected trends almost perfectly.

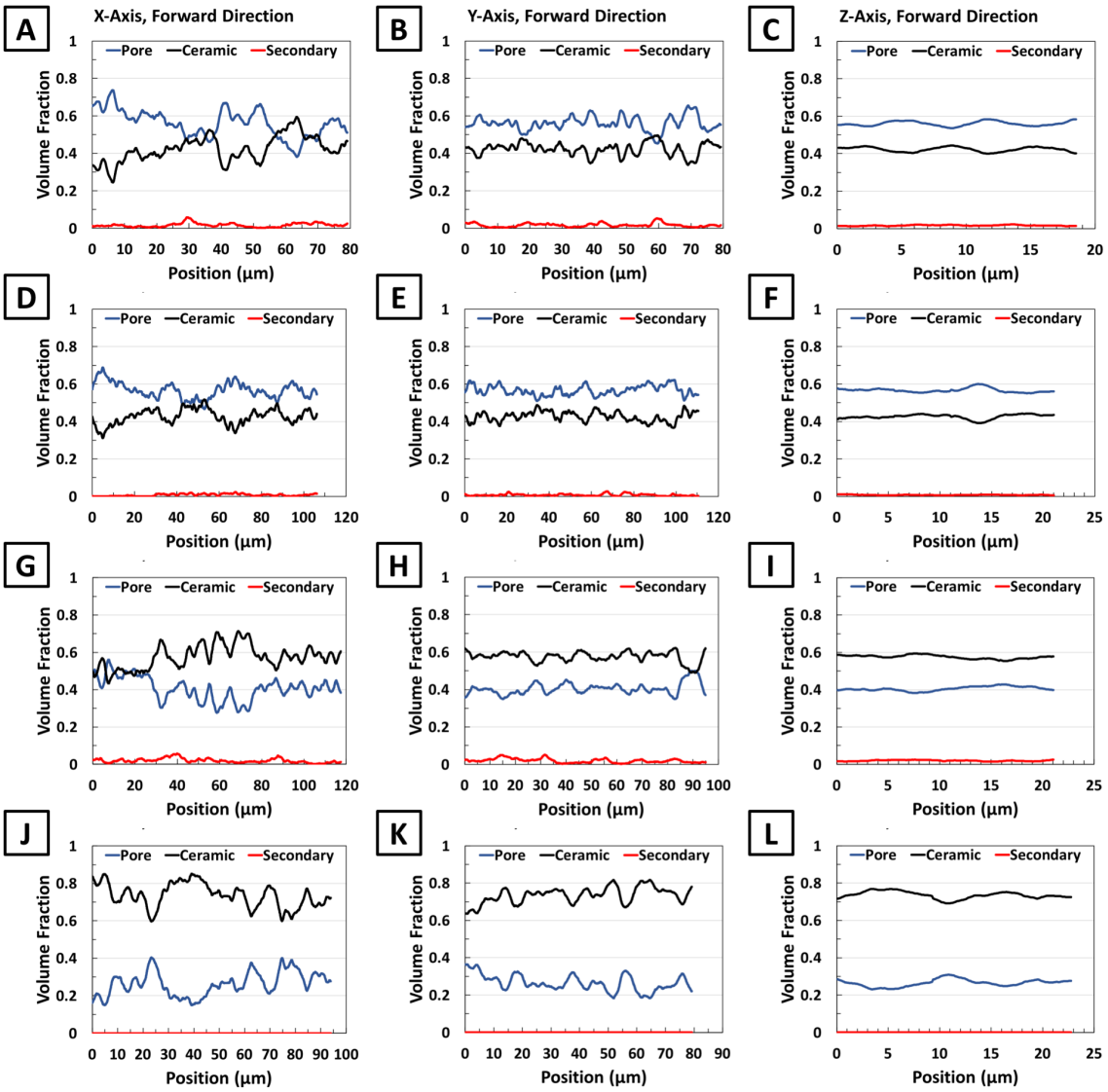

Figure 3.3: Phase volume fraction distributions along the X-, Y-, and Z-axes of the Trilayer 1 (A-C), Porous 1 (D-F), Porous 2 (G-I), and Porous 3 (J-L) samples. Pore phase volume fraction is blue, ceramic volume fraction is black, and secondary phase volume fraction is red.

3.2.2. Geometric Tortuosity:

Figure 3.4 shows 3D visualizations of the LLCZN phase cumulative geometric tortuosity calculated along the forward directions of the X-, Y-, and Z-axes for the four FIB Tomography samples, with arrows denoting the calculation direction. In all cases, the initial tortuosity value was 1.0 (blue color), with early deviations from straight paths resulting in tortuosity values quickly increasing above 1.5 (red color). As calculations

progressed across the 3D image region, the cumulative geometric tortuosity decreased, becoming more homogenous as local variations were smoothed over by the global properties of the 3D image region. This homogenization was more pronounced for the X- and Y-axes due to the large number of voxels along those axes (1300+) as compared to the Z-axis (170+). The Z-axis consistently had the lowest tortuosity values, the X-axis had the highest values, and the Y-axis had intermediate values.

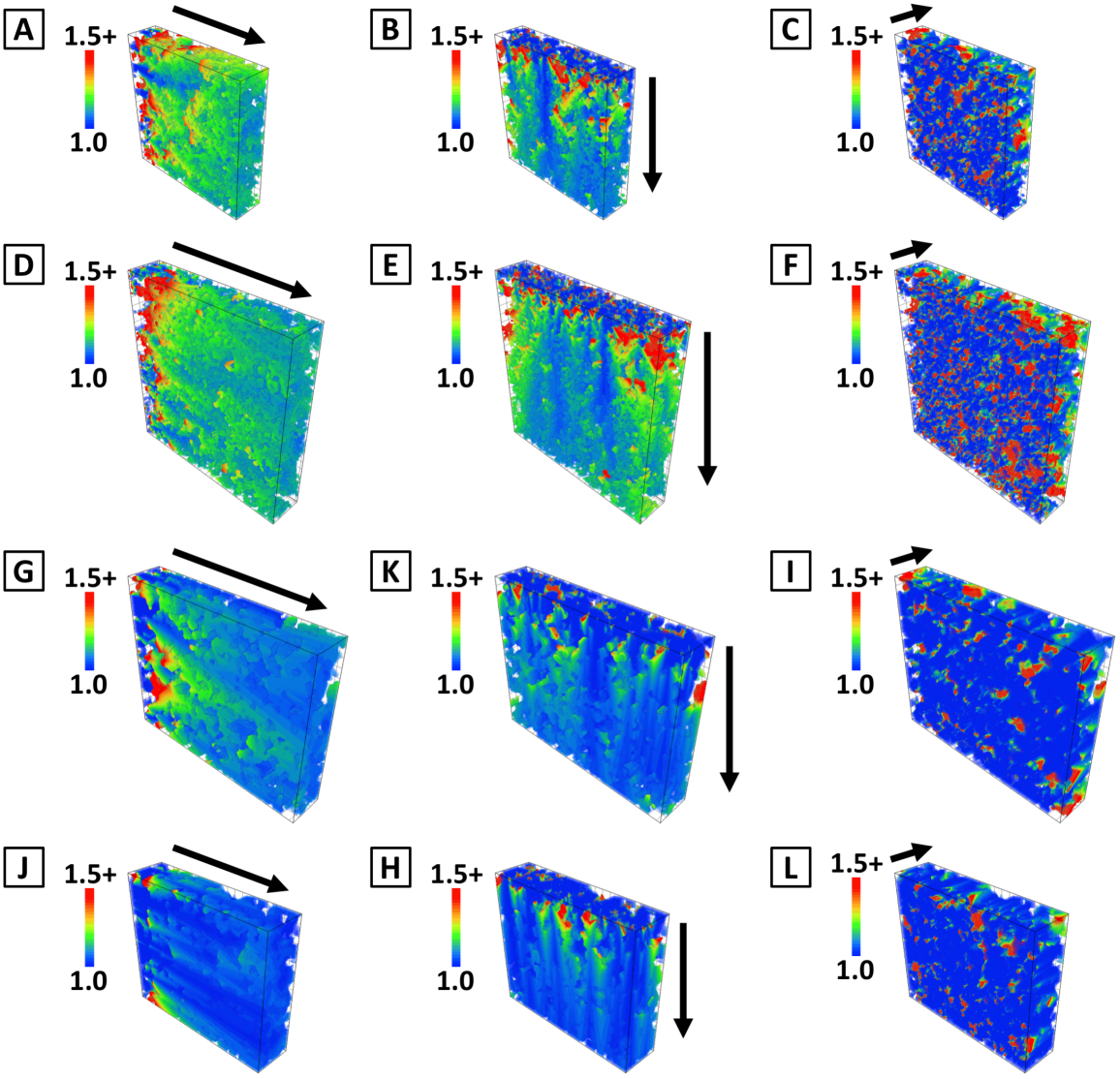

Figure 3.4: 3D visualization of the LLCZN phase cumulative geometric tortuosity along the forward directions for the X-, Y-, and Z-axes of the Trilayer 1 (A-C), Porous 1 (D-F), Porous 2 (G-I), and Porous 3 (J-L) samples.

The Trilayer 1 and Porous 1 samples had very similar microstructures and therefore showed very similar tortuosity distributions. Since the Trilayer 1 sample had a smaller volume than the Porous 1 sample, LLCZN pathways in the Trilayer 1 sample were less likely to encounter obstructions and should show lower tortuosity values along all axes. In reality, the Trilayer 1 sample had a somewhat higher X-axis tortuosity and somewhat lower Y-axis tortuosity than the Porous 1 sample, with the Z-axis tortuosity appearing very similar. Interestingly, low tortuosity pathways (i.e., close to 1.0) did extend quite far into the image region, especially along the Y-axis, despite the high porosity of the samples. For the Porous 2 sample, the lower porosity of the sample resulted in lower tortuosity for all axes. The low tortuosity pathways appeared more prevalent, though it was difficult to tell if they extend appreciably further into the image region. These trends continued for the Porous 3 sample, where even lower porosity resulted in significantly decreased tortuosity overall and many low tortuosity pathways.

The details of the tortuosity distribution were more apparent when plotting the average and standard deviation of the cumulative geometric tortuosity in each "slice" vs. Euclidean propagation distance (Figure 3.5). The same trends of high X-axis tortuosity and low Z-axis tortuosity were observed, as well as decreasing tortuosity when going from high porosity (Trilayer 1, Porous 1) to medium porosity (Porous 2) to low porosity (Porous 3). The effects of homogenization of geometric tortuosity were also seen, with high cumulative averages and large standard deviations at low propagation distances that steadily decreased as the propagation distance increased. The X- and Y-axes also tended to show more variability in the cumulative average compared to the Z-axis, with small but frequent increases and decreases.

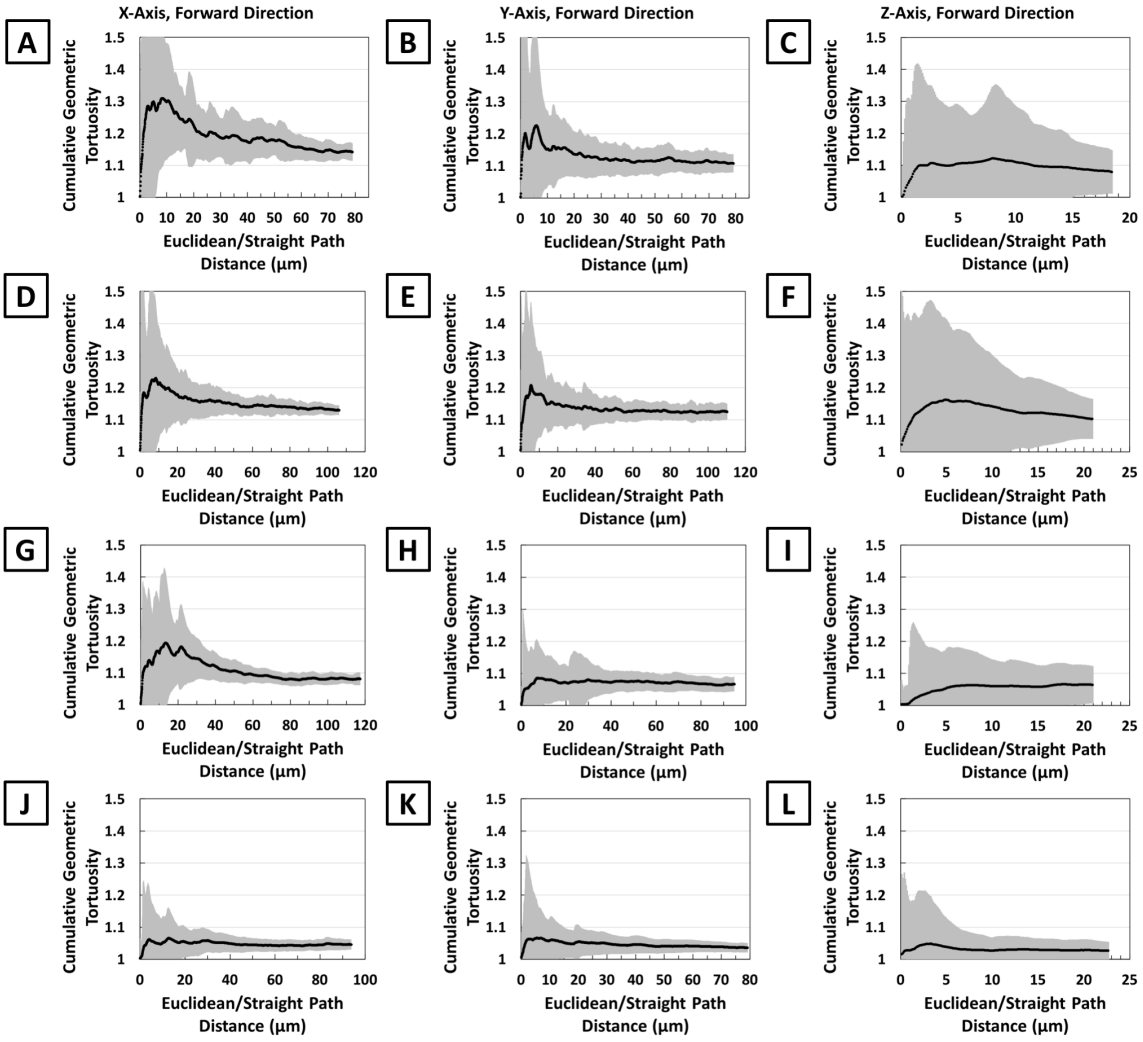

Figure 3.5: Average LLCZN phase cumulative geometric tortuosity and SD for the forward directions for the X-, Y-, and Z-axes of the Trilayer 1 (A-C), Porous 1 (D-F), Porous 2 (G-I), and Porous 3 (J-L) samples.

While tortuosity can theoretically be very large, it can only have a minimum value of 1.0 based on the definition of tortuosity. However, the lower standard deviation bars often dipped below 1.0 for the different directions. This indicated the distribution of tortuosity values within each "slice" was asymmetric about the mean, with a wide distribution above the mean and a narrow distribution below the mean (i.e., between the mean and the minimum of 1.0). As a result, the single standard deviation calculated and

plotted in Figure 3.5 underestimates the distribution width for higher tortuosity values and overestimates the width for lower tortuosity values.

As shown quantitatively in Figure 3.5, the X-axis had the highest tortuosity values, the Z-axis had the lowest tortuosity values, and the Y-axis was intermediate. The different tortuosity values of each axis may originate from one of two possible sources, or a mixture of both. In the first case, the differences in tortuosity reflected real anisotropy in the microstructure, which could be the result of pore collapse during sintering or from the tape-casting process. The X-axis was parallel to the "vertical" axis of the sample during sintering, so any pore collapse would occur preferentially along the X-axis and cause the LLCZN phase to be aligned more along the YZ-plane than the X-axis. This would be reflected in a higher X-axis tortuosity. During the tape-casting process, there was a time lag between casting the tape slurry and fully drying the tape, during which the randomly distributed garnet and pore former particles would settle. This would have similar microstructural effects as pore collapse and also be reflected in a higher X-axis tortuosity. In the second case, the differences in tortuosity resulted from the different aspect ratios of the 3D image region when viewed along each axis. The Z-axis (the milling direction) had the smallest number of images/voxels along the Z-axis and the largest cross-sectional area, while the X- and Y-axes had the largest numbers of voxels and the smallest cross-sectional areas. As a result, a given 3D feature could occupy more of the "slice" cross-sectional area along the X- and Y-axes as compared to the Z-axis, resulting in more tortuous paths and higher tortuosity. If correct, this suggested the 3D image region was too small relative to the microstructural features and was likely not representative of the sample.

To test this, sub-volumes from 10% to 90% of the full 3D image volume were extracted and the geometric tortuosity calculations repeated for each sub-volume. If the 3D image volume was large enough relative to the features imaged, then the tortuosity values for the different axes should stabilize as the sub-volume size increased towards 100% volume, but before reaching 100% volume. If the tortuosity failed to stabilize by the 100% volume, then the features were too large relative to the image volume and the image region was likely not representative of the overall sample microstructure. Figure 3.6 shows the direction-averaged results for each axis for the 3D FIB Tomography samples for different sub-volume sizes. Small sub-volumes showed significant variability in average tortuosity as well as large standard deviations that transitioned to more consistent values and smaller standard deviations as the sub-volume size increased. Between the 100% volume tortuosity and the 90% sub-volume tortuosity values, the X-, Y-, and Z-axes showed differences of 0.12%, 0.06%, and 0.14% for Trilayer 1; differences of 0.04%, 0.07%, and 0.06% for Porous 1; differences of 0.08%, 0.03%, and 0.28% for Porous 2; and differences of 0.10%, 0.01%, and 0.05% for Porous 3, respectively. For comparison, Tjaden, *et al*, observed differences of 7% between their 100% volume tortuosity and their 90% sub-volume tortuosity values and concluded their 3D image volume was large enough to be representative.[128] Accordingly, the Trilayer 1 image region was deemed as representative of the overall sample. Sub-volume checks for Porous 1, Porous 2, and Porous 3 showed similar behavior and were also deemed as representative of the corresponding samples. The X-, Y-, and Z-axes direction-averaged geometric tortuosity values were used to calculate the characteristic geometric tortuosity and the results plotted as a function of sub-volume size in Figure 3.6h. The characteristic tortuosity showed significantly less variability

compared to the direction-averaged tortuosity values as sub-volume size increased, further supporting the earlier conclusion that the 3D image regions were representative.

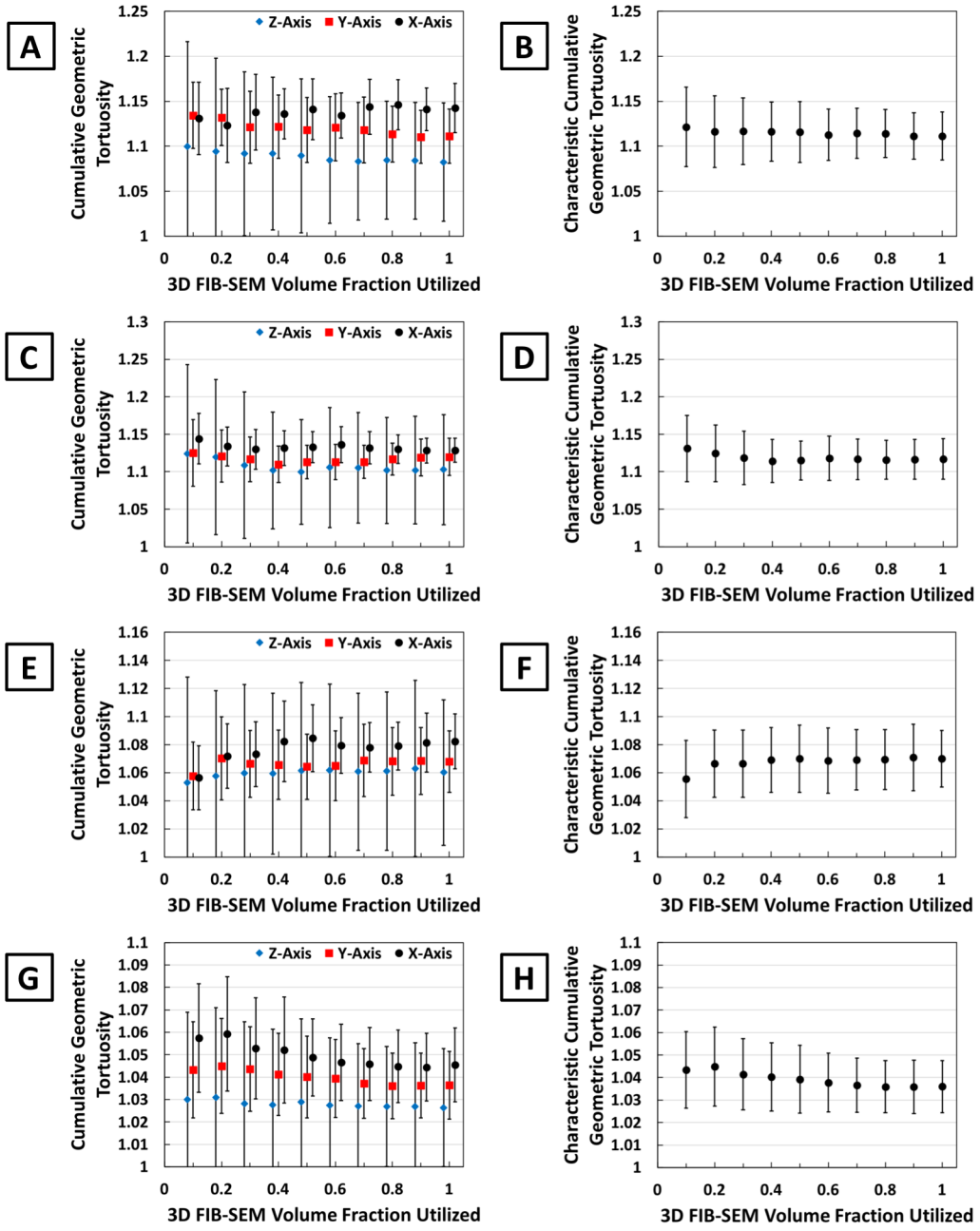

Figure 3.6: Average LLCZN phase cumulative geometric tortuosity and SD for the direction-averaged X-, Y-, and Z-axes, as well as overall cumulative tortuosity and SD, of the Trilayer 1 (A-B), Porous 1 (C-D), Porous 2 (E-F), and Porous 3 (G-H) samples.

The characteristic geometric tortuosity values for each 3D FIB Tomography sample were plotted vs. 3D sample porosity in Figure 3.7a. By the definition of tortuosity, 0% porosity corresponded with a tortuosity of 1.0, so an additional point was added at (0,1). A 2nd order curve was fitted to the results, with the fit forced to go through (0,1) to prevent physically impossible projections at low porosity values. The Trilayer 1 (56.03% porosity, 1.1114 tortuosity) and Porous 1 samples (56.67% porosity, 1.1170 tortuosity) showed near identical results and significant standard deviation (SD) bar overlap due to similar microstructures. Porous 2 (40.58% porosity, 1.0700 tortuosity) and Porous 3 (26.45% porosity, 1.0360 tortuosity) showed lower tortuosity values consistent with the lower LLCZN volume fraction of each sample. Despite the complex structures visible in Figure 3.1, the relatively low tortuosity values made it clear even the most porous sample examined here only suffered a 11.7% increase in overall conductive path length.

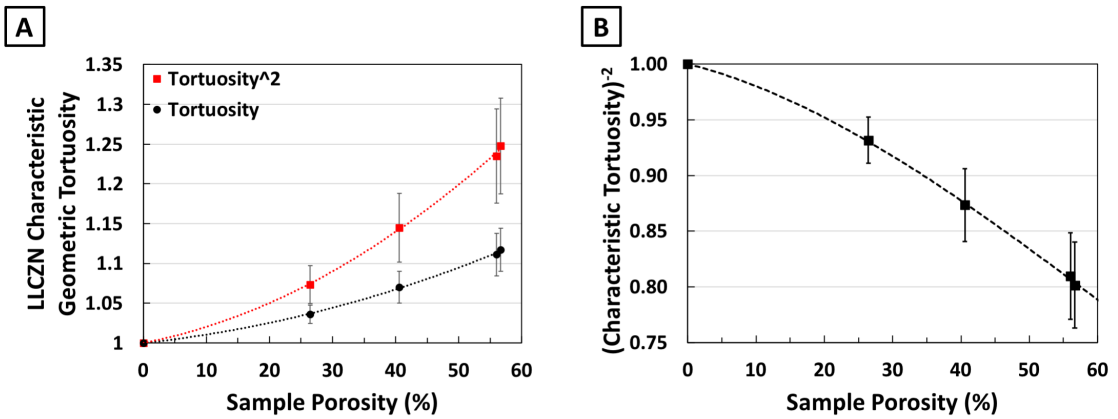

Figure 3.7: A) LLCZN phase characteristic geometric tortuosity (black markers) and tortuosity squared (red markers), as well as SD, for each of the 3D FIB Tomography samples. The broken lines represent 2nd order fits. B) inverse characteristic tortuosity squared, with broken line calculated from fit for characteristic tortuosity squared.

Since Equation 1.3 utilized the inverse tortuosity squared to calculate the M-factor, the characteristic geometric tortuosity squared was plotted vs. 3D sample porosity in Figure 3.7a and the inverse characteristic geometric tortuosity squared was plotted vs. 3D sample

porosity in Figure 3.7b. The highest tortuosity of 1.1170 corresponded to a tortuosity squared of 1.2477 and an inverse tortuosity squared of 0.8015, which reduced the effective conductivity by 19.85%. For reference, the sample in question (Porous 1) was 42.58% LLCZN, so the effective conductivity was reduced by 57.42% solely due to the reduced LLCZN volume fraction in the sample. This indicated the effect of tortuosity was relatively minor compared to the conductive phase volume fraction, even for the highest tortuosity value in this study.

3.2.3. Percolation Factor:

All LLCZN voxels contiguous with one of the six boundary planes of the 3D image region were identified and the percolation factor for the corresponding propagation direction was calculated. The direction-averaged percolation factor for the X-, Y-, and Z-axes were shown for different sub-volume utilization sizes for the 3D FIB Tomography samples (Figure 3.8a, c, e, g). Percolation factors for all samples and sub-volumes were above 0.995, with 100% volumes producing values above 0.998. Given the percolation factors were very close to 1.0, it was likely the remaining "unconnected LLCZN" reflected a combination of small spots of mislabeled LLCZN in the pore phase and real particles connected to the LLCZN microstructure at locations beyond the 3D image region boundaries. This was consistent with the LLCZN phase being the only long-range solid present in the samples, so any truly isolated LLCZN particles would separate from the bulk sample prior to epoxy infiltration. The X-, Y-, and Z-axes direction-averaged percolation factors were averaged into an overall percolation factor and plotted as a function of sub-volume size in Figure 3.8b, d, f, and h. Similar to the overall geometric tortuosity, the

overall percolation factor showed less variability and lower SD values than the direction-averaged percolation factors.

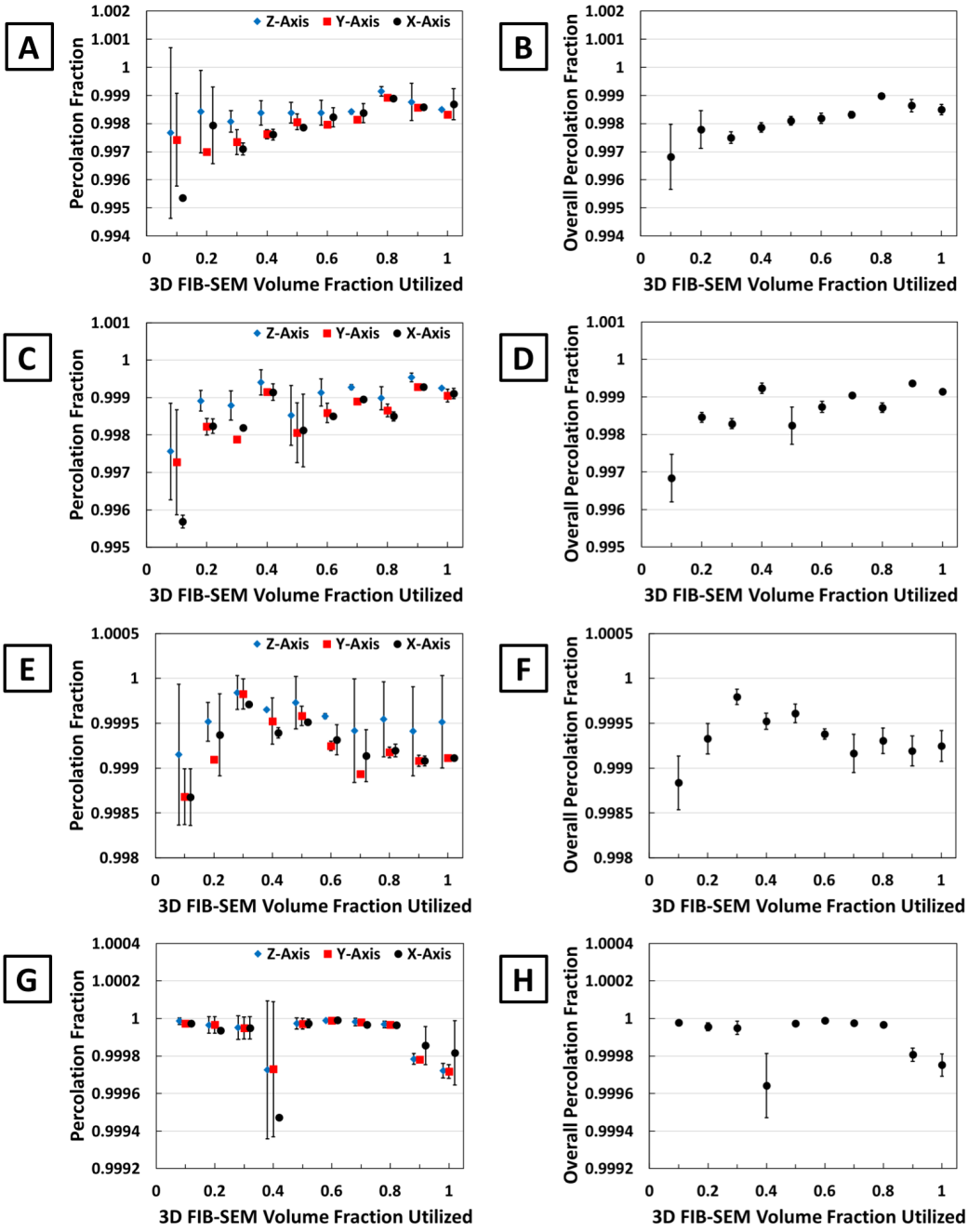

Figure 3.8: A) LLCZN phase percolation factor and SD for the direction-averaged X-, Y-, and Z-axes, as well as overall sample percolation factor and SD, of the Trilayer 1 (A-B), Porous 1 (C-D), Porous 2 (E-F), and Porous 3 (G-H) samples.

The overall LLCZN percolation factors for each 3D FIB Tomography sample were plotted vs. 3D sample porosity in Figure 3.9. By the definition of percolation factor, 0% porosity corresponded to a percolation factor of 1.0, so an additional point was added at (0,1). A 1st order curve was fitted to the results and forced to go through (0,1) to prevent physically impossible projections at low porosity values. Generally, the percolation factor decreased with increasing sample porosity, though even the lowest percolation factor was still above 0.9985, corresponding to an effective conductivity reduction of 0.15%. This indicated the percolation factor had virtually no effect on the effective conductivity of the porous LLCZN within the porosity range examined here.

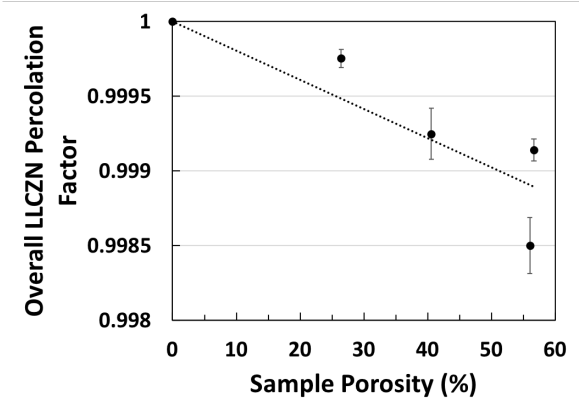

Figure 3.9: Overall sample LLCZN percolation factor and SD for all 3D image regions plotted vs. 3D sample porosity. The broken line represents a 1st order fit.

3.2.4. C-PSD, MIP-PSD, and Constriction Factor:

The cumulative coverage fraction c-PSD and average MIP-PSD results for the LLCZN phase in each 3D FIB Tomography samples were plotted together in Figure 3.10a, with the c-PSD results as a solid line and the corresponding MIP-PSD results as a dashed line. The starting test sphere diameter was 100 nm and was increased by 100 nm for each step. For all curves, the cumulative coverage fraction of LLCZN decreased as test sphere diameter increased and showed three distinct stages: an initial stage of high cumulative

coverage fraction and near 0 slope; a “breakthrough” stage where the cumulative coverage fraction rapidly decreased; and a final stage of low cumulative coverage fraction and near 0 slope. The MIP-PSD curves decreased more drastically in the “breakthrough” stage than the c-PSD curves, reflecting how the bottlenecks quickly choked off access to the LLCZN structure. When the cumulative coverage fraction was converted to instantaneous coverage fraction (shown in Figure 3.10b), this behavior translated to narrow MIP-PSD peaks and broad c-PSD peaks. The MIP-PSD curves displayed peaks at smaller test sphere diameters than the corresponding c-PSD curves, consistent with the bottlenecks representing the narrowest parts of the contiguous LLCZN microstructure. In both sets of distributions, the peaks became broader as the center of the peak shifted to higher diameters.

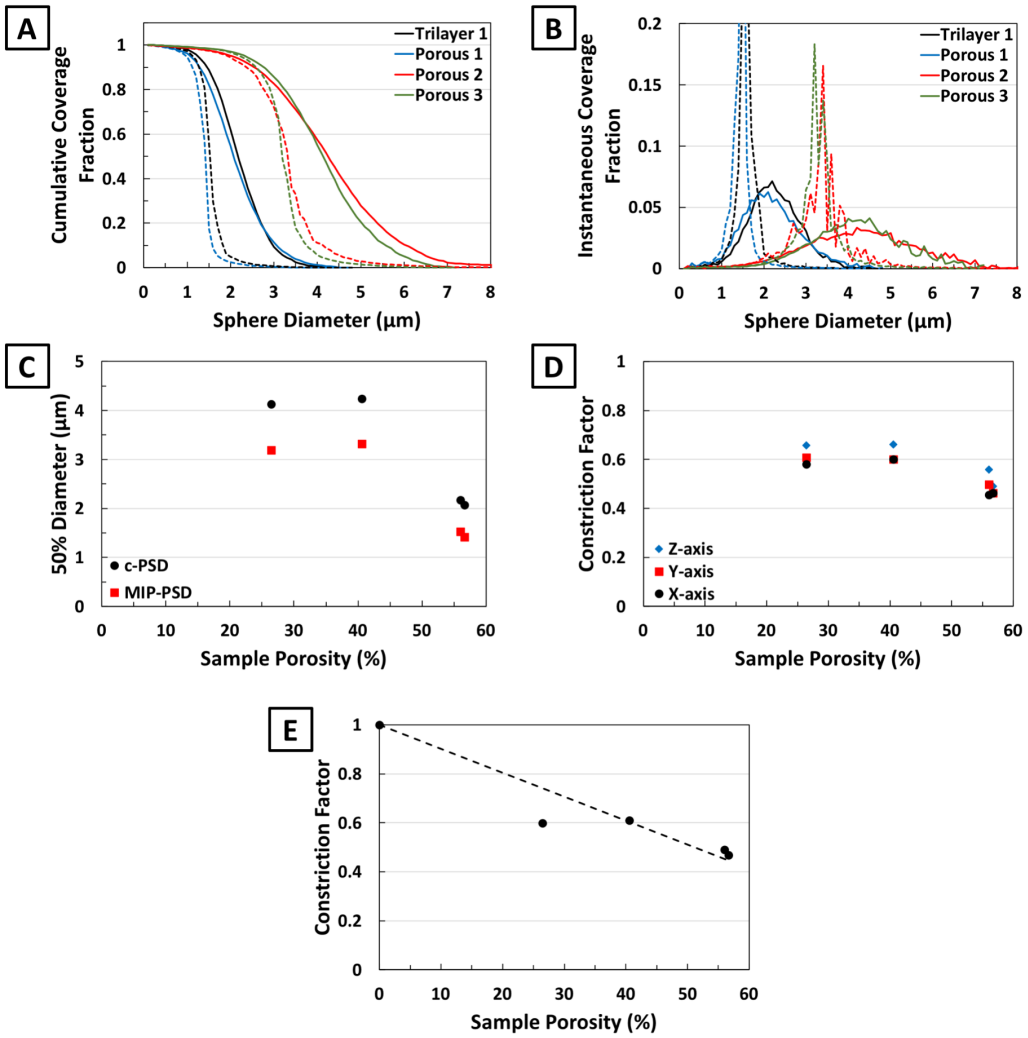

Figure 3.10: A) LLCZN phase c-PSD (solid lines) and average MIP-PSD (dashed lines) for the 4 FIB Tomography samples. B) instantaneous coverage distributions for c-PSD (solid lines) and average MIP-PSD (dashed lines). C) 50% sphere diameters for c-PSD (black circles) and for average MIP-PSD (red squares). D) constriction factors for the 4 FIB Tomography samples, with a linear fit plotted. E) constriction factors calculated for the X-, Y-, and Z-axes based on the direction-averaged MIP-PSD.

Figure 3.10c shows the corresponding 50% diameter values for the c-PSD and average MIP-PSD distributions for the 3D FIB Tomography samples. The Trilayer 1 (56.03% porosity) and Porous 1 samples (56.67% porosity) had the lowest particle and bottleneck diameters, consistent with having the highest porosity values. Porous 2 (40.58% porosity) had higher particle and bottleneck sizes, consistent with having a lower porosity value. In contrast, Porous 3 (26.45% porosity) had the lowest porosity yet showed lower

particle and bottleneck sizes than Porous 2, behavior expected for a higher porosity sample. Examining the 3D image set for Porous 3, sub-micron pores were observed throughout the LLCZN phase, likely reducing the LLCZN particle and bottleneck diameters despite the higher LLCZN volume fraction. This incomplete consolidation was likely due to the micron-sized LLCZN particles in the pre-sintered green tapes, an effect consistent with reports in the literature that using sub-micron pre-sintered particles decreased sintering temperatures and improved ceramic densities.[144,145]

The X-, Y-, and Z-axes constriction factors were calculated and plotted vs. 3D sample porosity in Figure 3.10d, where the X-axis displayed the lowest value and the Z-axis displayed the highest value. This was similar to the high X-axis tortuosity and low Z-axis tortuosity values previously discussed, since both sets of results describe greater difficulty moving along the X-axis of the 3D image region. As before, the differences were likely due to sample settling along the X-axis during sintering or tape-casting, though some effects from the non-cubic dimensions of the 3D image region were also possible. In the case of the constriction factor, the difference between the constriction factors for the different axes was extremely minor. The average constriction factor was calculated from the 50% diameter values for the c-PSD and overall MIP-PSD distributions and plotted vs. 3D sample porosity in Figure 3.10e. By the definition of constriction factor, 0% porosity corresponded to a constriction factor of 1.0, so an additional point was added at (0,1). The constriction factor had a nearly constant value of 0.6 between 26.45% porosity (Porous 3) and 40.58% porosity (Porous 2) and began to decrease further as porosity continued to increase to 56.67% porosity (Trilayer 1, Porous 1). A 1st order curve was fit to the results, with the fit forced to go through (0,1) to prevent physically impossible projections at low

porosity values. The fitted curve provided a very good fit to samples at or above 40.58% porosity (Trilayer 1, Porous 1, and Porous), but failed to properly capture sample behavior at 26.45% porosity (Porous 3). Due to use of micron-sized LLCZN particles, it was unknown if lower porosity samples would also have a constriction factor of 0.6 or if the constriction factor would begin to increase towards 1.0.

3.2.5. M-Factor:

Rearranging the M-factor equation terms (Equation 2.17) so each microstructural parameter took on values between 0.0 and 1.0 (Equation 3.1) made it possible to discern the relative importance of each parameter in reducing the conductivity/diffusivity of the porous LLCZN.

$$M = f * P * \beta * \frac{1}{(\tau_{geo})^2} \tag{3.1}$$

The overall results for each microstructural term and the corresponding curves of fit were plotted on a linear scale in Figure 3.11a and on a logarithmic scale in Figure 3.11b vs. 3D sample porosity. Looking at individual data points, the LLCZN volume fraction and the constriction factor were the most important components of the M-factor, with the geometric tortuosity being the 3rd most important, and the percolation factor playing almost no role at all. Some variation was present, with constriction factor being more important than LLCZN volume fraction for Porous 3 (26.45% porosity), while the remaining samples showed LLCZN volume fraction being as important as or slightly more important than the constriction factor. This indicated a transition in the primary limitation on Li-ion transport occurred between 26.45% and 40.58% porosity, with bottlenecks being the primary limitation below this transition, and conductive phase fraction/bottlenecks

being equally important above this transition. The combined M-factor was also plotted in Figure 3.11 and decreased exponentially as porosity increased, with a porosity increase of 56.67% corresponding to a ~1 order of magnitude reduction in M-factor. This was unexpected given that 1st and 2nd order curves used to fit the individual microstructural terms, and the constriction factor deviated from the fitted 1st order curve at low porosity. Based on the M-factors, increasing the LLCZN porosity to 26.45%, 40.58%, 56.03%, and 56.67% would result in LLCZN effective conductivities that were 41.0%, 30.6%, 16.8%, and 16.0% of the LLCZN intrinsic conductivity, respectively.

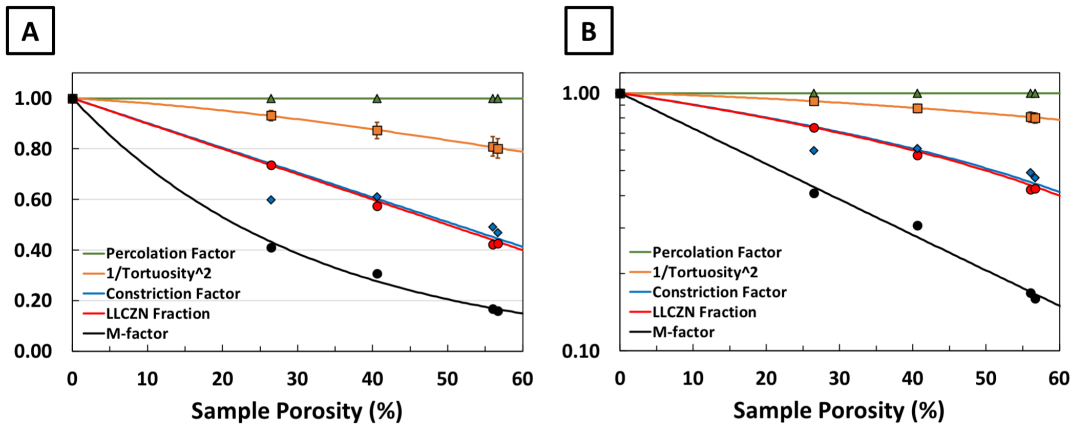

Figure 3.11: Overall sample LLCZN phase microstructure reduction terms plotted together for the 4 FIB Tomography samples, as well as the combined M-factor (black markers), A) on a linear vertical scale and B) on a logarithmic vertical scale. Curves of fit are plotted for each parameter.

3.2.6. 3D EIS Analysis:

The three porous layer samples (Porous 1, Porous 2, and Porous 3) were also measured with EIS prior to analysis with 3D FIB Tomography. The Trilayer 1 sample was excluded due to the issue of separating the effects of the dense layer from the porous layers in conductivity measurements. Based on the EIS results, the limiting gold electrode area calculated from camera images, the mean sample thickness calculated from SEM cross-section images, and the 3D porosity determined by 3D FIB Tomography, the measured

effective bulk conductivity was calculated for the three porous samples and plotted vs. 3D porosity in Figure 3.12a (black circles). In addition, results for several dense samples were included to provide baseline values for 0% porosity. SD bars for the conductivity values were based on the SD of the sample thickness, and an assumed 10% SD for the resistance and electrode area. The results in Figure 3.12a showed the measured effective bulk conductivity exponentially decreased as the porosity increased, consistent with the trend in the M-factor in Figure 3.11b. To support this observation, an exponential trendline was added (dashed line) and showed reasonable fit to the trend in the measured data. While effective conductivity was expected to decrease somewhat as sample porosity increased, the measured effective conductivity decreased more drastically than anticipated, reaching a minimum value of 2.03×10^{-6} S/cm for the maximum porosity of 56.67%.

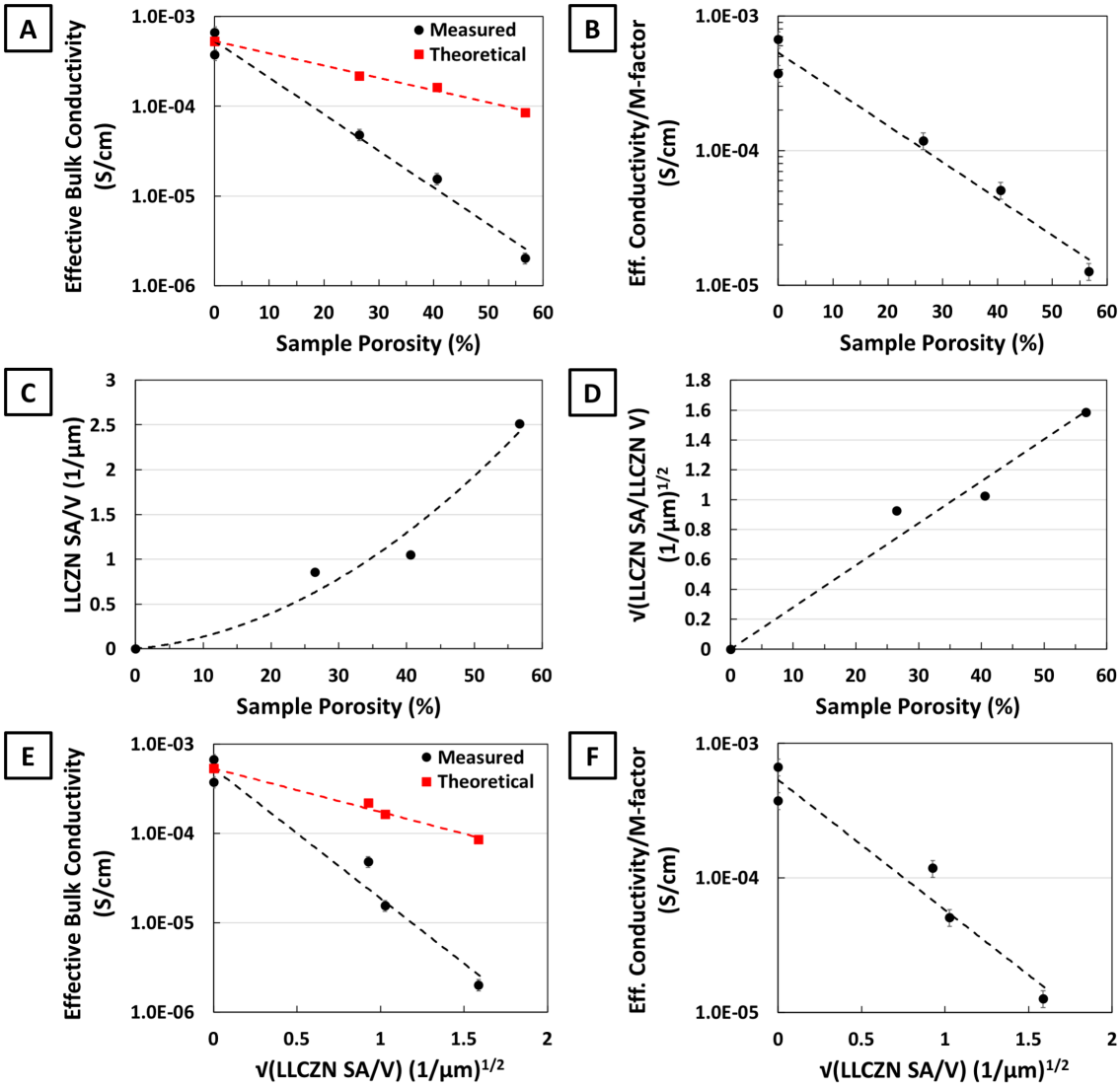

Figure 3.12: A) measured and theoretical effective bulk conductivity, and B) bulk conductivity (derived from effective conductivity/M-factor) vs. porosity. C) 3D LLCZN SA/V ratios vs. porosity. D) 3D LLCZN $(SA/V)^{1/2}$ ratios vs. porosity. E) Measured and theoretical effective bulk conductivity, and F) bulk conductivity (derived from effective conductivity/M-factor), vs. 3D LLCZN $(SA/V)^{1/2}$ ratios.

Using the exact M-factors previously calculated and Equation 3.1, the theoretical effective bulk conductivity was calculated for the Porous 1, Porous 2, and Porous 3 samples. The nominal intrinsic conductivity of the LLCZN was taken to be the 0% porosity intercept of the exponential curve fitted to the measured effective bulk conductivity (5.35 x 10^{-4} S/cm). The theoretical effective bulk conductivity for each sample (red squares) were plotted vs. 3D porosity in Figure 3.12a alongside the measured effective bulk conductivity.

Comparing the theoretical and measured results, two things became apparent: 1) both the theoretical and measured results decreased exponentially as porosity increased, and 2) the theoretical results were consistently higher than the measured results. The consistent discrepancy suggested an additional factor besides the LLCZN microstructure may be affecting the measured effective bulk conductivity. Referring to Equation 1.2, the only non-structural parameter that could affect the measured effective bulk conductivity was the bulk conductivity. Through Equation 1.2, the measured effective bulk conductivities and the corresponding exact M-factors were used to derive the bulk conductivity of each of the LLCZN samples. The results were plotted vs. 3D porosity in Figure 3.12b and showed the derived bulk conductivity decreased exponentially as porosity increased, although at a slower rate than the measured effective bulk conductivity. The lowest derived bulk conductivity calculated was 1.26×10^{-5} S/cm at 56.67% porosity, over an order of magnitude smaller than the initial bulk conductivity value of 5.35×10^{-4} S/cm for the 0% porosity samples.

One potential explanation for the decrease in LLCZN bulk conductivity was the implicit assumption of identical sintering behavior for all porous samples was incorrect. Recalling that LLCZN and similar electrolytes suffer Li-loss through the surfaces of electrolyte particles during high temperature sintering, samples with higher surface area would experience more Li-loss. Simultaneously, smaller electrolyte particle sizes (corresponding to higher SA/V ratios) would decrease the distance from the particle surface to all points within the particle bulk, so Li-loss would affect more of the total electrolyte volume. While studies have shown that Li-ion vacancies are key to stabilizing the high conductivity cubic phase in LLZ and related materials, too much Li-loss inevitably

degrades performance and ultimately decomposes the cubic phase into non-conductive phases.[40,42,146,147] Thus, the bulk conductivity of LLCZN and other Li-containing metal oxide electrolytes would be tied to the SA/V ratio of the sintered electrolyte. Since the SA/V ratio also increased as sample porosity increased, it appears the LLCZN bulk conductivity was affected by sample porosity despite SA/V ratio being the underlying cause.

To determine if this was plausible, the 3D LLCZN SA/V ratio was plotted vs. 3D porosity in Figure 3.12c, which showed the SA/V ratio appeared to be a 2nd order function of 3D porosity. To simplify analysis, the 3D LLCZN $(SA/V)^{1/2}$ ratio was plotted vs. 3D porosity in Figure 3.12d to give a linear relationship to porosity. The measured and theoretical effective bulk conductivity were then plotted as functions of $(SA/V)^{1/2}$ in Figure 3.12e, and the derived bulk conductivity was plotted vs. $(SA/V)^{1/2}$ in Figure 3.12f. Observing all conductivity figures, the logarithm of the conductivities appeared to be proportional to $(SA/V)^{1/2}$ and the conductivities consistently decreased as $(SA/V)^{1/2}$ increased. While this did not prove the SA/V ratio was the underlying cause of the bulk conductivity decrease, the similar trends in the plots of conductivity vs. $(SA/V)^{1/2}$ and in the plots of conductivity vs. 3D porosity indicated this mechanism was a viable possibility.

3.2.7. 2D EIS Analysis:

To determine if the trends observed from the 3D FIB Tomography results could be replicated in larger sample batches, a large number of porous LLCZN samples were characterized for effective conductivity, derived bulk conductivity, and for structural properties. Due to the expense of the 3D FIB Tomography process, these additional

samples did not have 3D porosity, percolation factor, constriction factors, tortuosity values, or M-factor values directly calculated for each. Instead, cross-sectional SEM images of the samples were used to determine the sample porosity (referred to as 2D porosity) and a M-factor was extrapolated for each sample based on the fitted curves for the exact M-factor results. Given the nominal electrolyte composition and fabrication approach remained consistent between all samples, such an extrapolation should provide a reasonable approximation.

Figure 3.13a-c show BSE images for several LLCZN samples with different porosities, where the epoxy-filled pores appeared dark, the LLCZN particles appeared grey, and the gold particles appeared bright grey/white. Any secondary phase present had pixel intensities intermediate to the epoxy-filled pores and the LLCZN particles. The images showed the gold electrodes maintained good contact with the porous LLCZN samples and very minimally infiltrated into the pores, meaning the majority of the LLCZN structure was probed by the impedance spectroscopy measurements. The final segmented images are shown in Figure 3.13d-f, where the segmented images more clearly display the different microstructures of the porous LLCZN samples.

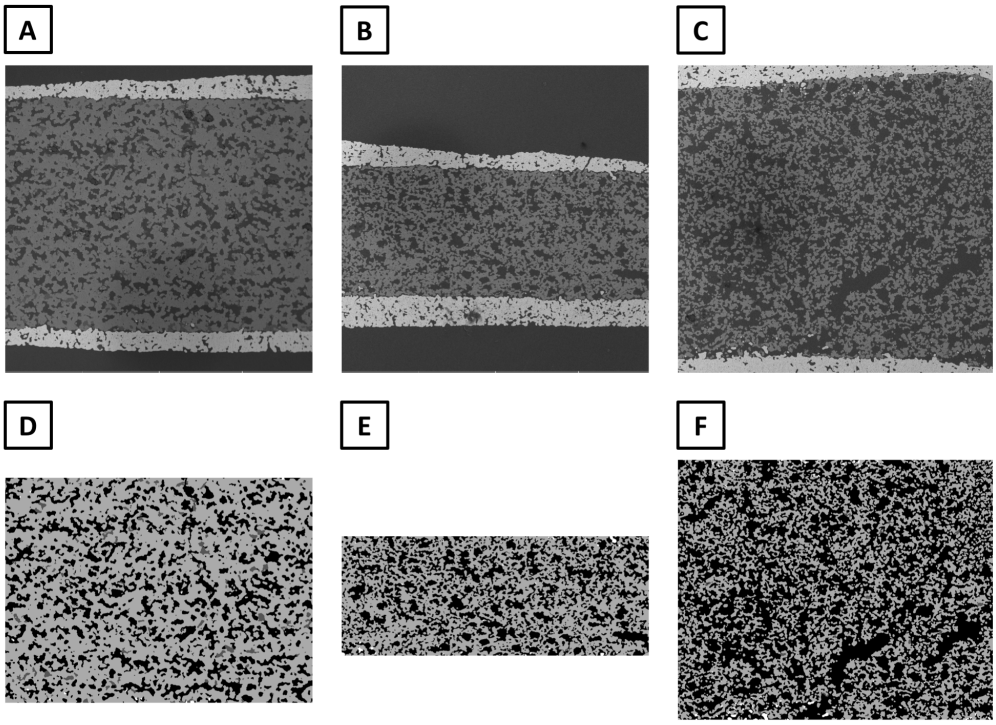

Figure 3.13: A-C) BSE images taken of several LLCZN samples with different porosity values, and D-F) the corresponding post-processed segmented images.

For the overall data set, the effective bulk conductivity values were calculated for all measured samples and plotted vs. 2D porosity in Figure 3.14a. This data set included the porous samples analyzed by 3D FIB Tomography (Porous 1, Porous 2, and Porous 3) and the dense samples included in earlier conductivity plots (Figure 3.12). SD bars for the conductivity values were based on the SD of the sample thickness, and an assumed 10% SD for the resistance and electrode area. The porosity error for the average 2D porosity value was taken to be the SD of the individual 2D porosity values derived from the set of SEM cross-sectional images associated with each sample. Figure 3.14a showed the effective bulk conductivity exponentially decreased as 2D porosity increased, consistent with trends observed from the 3D results.

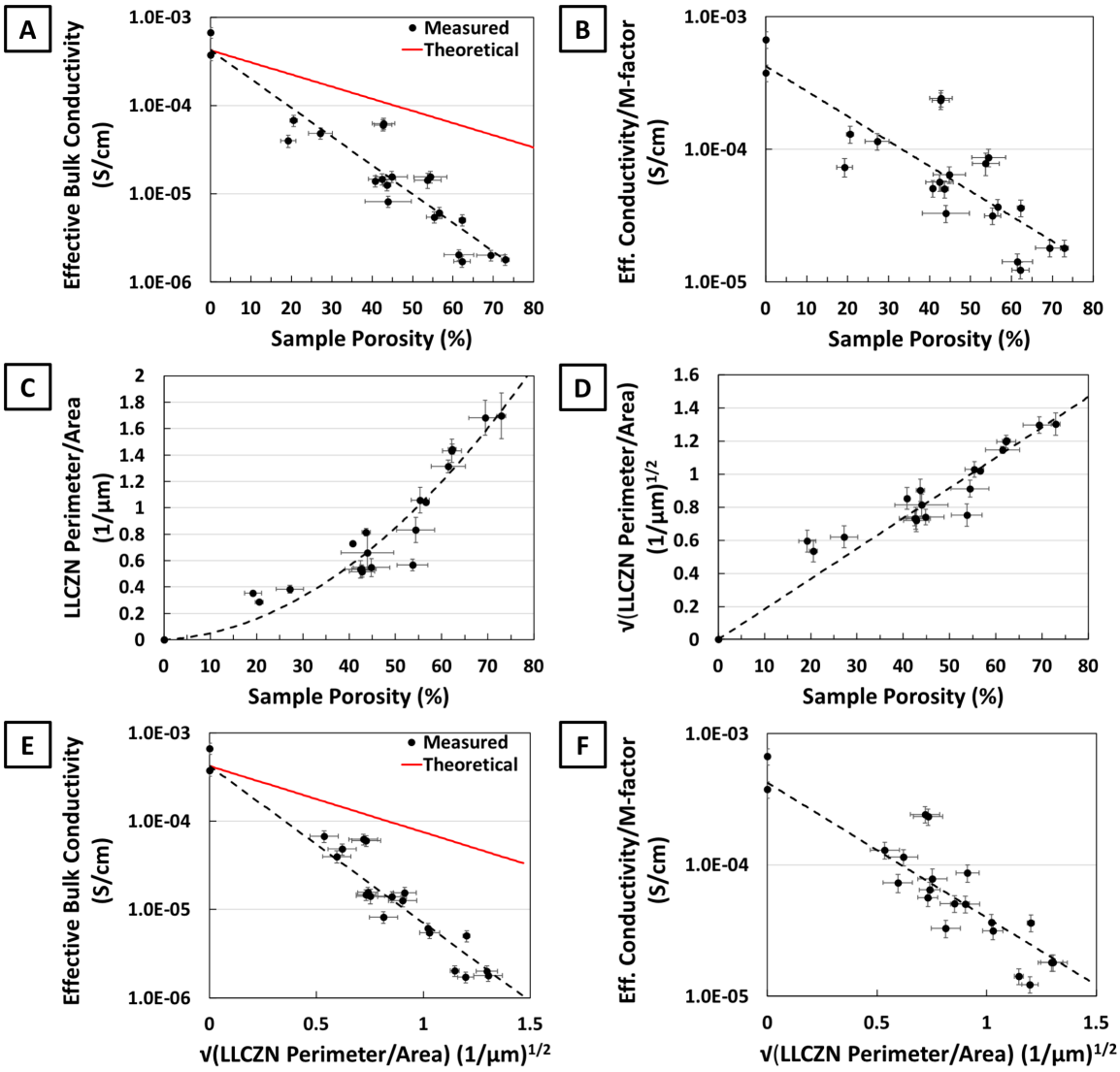

Figure 3.14: A) measured and theoretical effective bulk conductivity, and B) bulk conductivity (derived from effective conductivity/M-factor) vs. 2D porosity. C) 2D LLCZN perimeter/area ratios vs. porosity. D) 2D LLCZN (perimeter/area ratios)$^{1/2}$ vs. porosity. E) Measured and theoretical effective bulk conductivity, and F) bulk conductivity (derived from effective conductivity/M-factor), vs. 2D LLCZN (perimeter/area)$^{1/2}$ ratios.

The nominal intrinsic conductivity of the LLCZN was taken to be the 0% porosity intercept of the exponential curve fitted to the measured effective bulk conductivity (4.22 x 10^{-4} S/cm), similar to the value of 5.35 x 10^{-2} S/cm derived from the 3D results. This was combined with the exponential curve fitted to the M-factor to calculate the theoretical effective bulk conductivity as a function of 2D porosity in Figure 3.14a (red solid line).

Comparing the theoretical and measured results, the theoretical curve consistently overestimated the measured effective bulk conductivities, as also seen with the 3D results. The derived bulk conductivity necessary to reconcile the experimental and theoretical data was calculated and plotted vs. 2D porosity in Figure 3.14b, where an exponential decrease was observed, similar to the 3D results.

The 2D LLCZN perimeter/area ratio was plotted vs. 2D porosity in Figure 3.14c with a 2^{nd} order curve best fitting the results, just as with the 3D results. To simplify analysis, the LLCZN (2D perimeter/2D area)$^{1/2}$ ratio was plotted vs. porosity in Figure 3.14d to give a linear relationship to porosity. All three conductivities were then plotted as functions of (2D perimeter/2D area)$^{1/2}$ in Figure 3.14e-f, which showed a similar relationship as the 3D results. In contrast to the 3D results, all conductivity data points showed less scatter when viewed as functions of (2D perimeter/2D area)$^{1/2}$ than as functions of the 2D porosity. It was unclear whether this represented a meaningful trend not captured by the limited number of 3D samples or was due to variability in how accurately the 2D perimeter/area ratio approximated the 3D SA/V ratio. Regardless, it was concluded that the results determined from the 3D samples could be replicated and were indicative of a real trend.

3.2.9. XRD Results:

Figure 3.15 shows the XRD results for several of the 2D analysis samples. All samples showed nearly pure cubic phase patterns, with occasional weak secondary phase signals (+) and gold signals (*), the latter from the gold electrodes. Amongst the samples, there were clear shifts in the peak positions at higher angles indicating the lattice parameter

of the samples was slightly different. These lattice parameters were calculated and plotted in Figure 3.16 vs. the 2D porosity of the corresponding sample, showing significant scatter that caused some higher porosity samples to have lattice parameters similar to lower porosity samples. Analyzing the overall distribution, there may be a weak underlying trend of increasing lattice parameter with increasing porosity, though substantially more data points are needed to rigorously confirm this relationship.

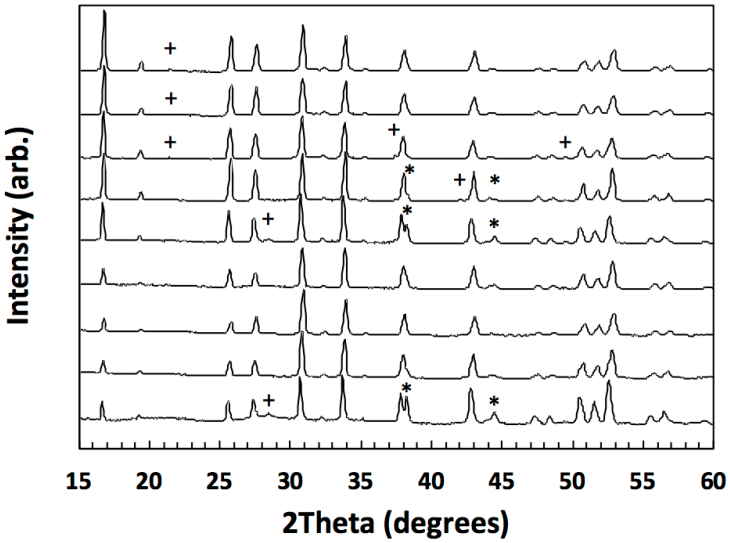

Figure 3.15: XRD patterns for several porous LLCZN samples. All samples were high purity cubic phase LLCZN, with minor impurities (+) or gold from the electrodes (*) in some cases.

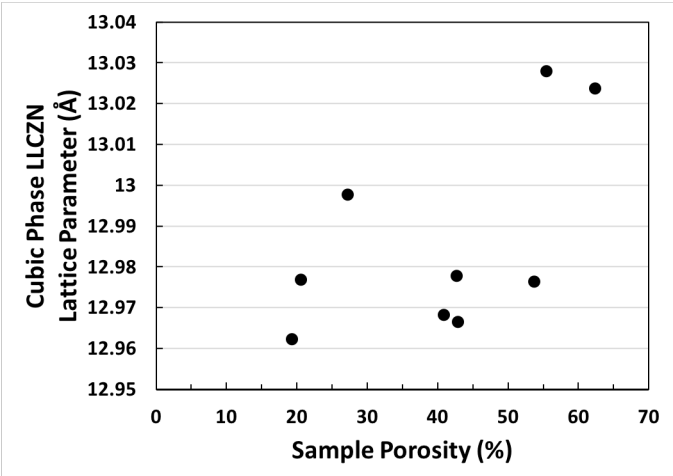

Figure 3.16: Cubic phase LLCZN lattice parameter vs. 2D porosity.

3.2.10. Comparison of 2D and 3D Structural Parameters:

The 3D FIB Tomography samples (Porous 1, Porous 2, and Porous 3) were represented in both the 2D and 3D results, making it possible to compare microstructural properties calculated in both dimensions and determine how accurately the 2D results captured true 3D behavior. Given that tortuosity, percolation factor, and constriction factor were 3D-only parameters, the comparable structural parameters were limited to the phase fractions and the SA/V ratios (2D perimeter/2D area ratios for the 2D analysis). The corresponding values from the 2D and 3D analysis were shown in Table 3.3, with structural parameters separated into LLCZN, secondary, and pore phases.

Table 3.3: Comparing 2D and 3D analyses of tape-cast LLCZN microstructures.

	Material	**2D Area Fraction (%)**	**2D L/A (1/μm)**	**3D Volume Fraction (%)**	**3D SA/V (1/μm)**
Porous 1	LLCZN	38.56 +/- 3.69	1.3138 +/-0.0470	42.58	2.5154
	Secondary	0.00		0.75	5.4890
	Pore	61.44 +/- 3.71	0.8239 +/- 0.1027	56.67	1.8855
Porous 2	LLCZN	54.55 +/- 3.48	0.5475 +/- 0.0690	57.51	1.0537
	Secondary	0.61 +/- 0.23	2.4301 +/- 0.4221	1.91	5.6467
	Pore	44.84 +/- 3.91	0.6647 +/- 0.0169	40.58	1.3667
Porous 3	LLCZN	70.50 +/- 2.42	0.3845 +/- 0.0298	73.55	0.8574
	Secondary	2.30 +/- 0.70	1.7963 +/- 0.2106	0.00	
	Pore	27.20 +/- 2.93	0.9012 +/- 0.0381	26.45	2.1336

Examining the phase fractions, the 2D and 3D analysis produced very similar results for the LLCZN and pore phases. The secondary phase was much less comparable, but this phase was non-conductive and did not play a meaningful role in electrolyte performance, so the differences were acceptable. Focusing on the LLCZN phase, the 3D volume fractions were consistently higher than the 2D area fractions, showing a difference of +4.02%, +2.99%, and +3.05% for the Porous 1, Porous 2, and Porous 3 samples, respectively. Compared to the 2D LLCZN area fraction SD's of 3.69%, 3.48%, and 2.42%,

the 3D LLCZN volume fractions were either within the SD ranges or just barely outside them. Focusing on the pore phase, the 3D volume fractions were consistently lower than the 2D area fractions, showing a difference of -4.77%, -4.26%, and -0.75% for the Porous 1, Porous 2, and Porous 3 samples, respectively. Compared to the 2D pore area fraction SD's of 3.71%, 3.91%, and 2.93%, the 3D pore volume fractions were either within the SD ranges or just barely outside them. This comparison indicated the 2D phase area fractions can successfully approximate the actual 3D volume fractions, provided an extra margin of +/- 1% is added to the existing SD of the 2D area fractions.

Examining the 3D SA/V ratios and the 2D perimeter/area ratios, the 3D and 2D analyses produced very different results. In all cases, the 3D SA/V ratio for the LLCZN and pore phases was larger than the corresponding 2D perimeter/area ratio by a factor of 1.9 to 2.4. However, the relatively narrow range in the ratio of the 3D-to-2D values suggested the 2D perimeter/area ratio could still capture trends in the 3D SA/V ratio. This was supported by Figure 3.12 and Figure 3.14 showing that 2D perimeter/area ratio vs. 2D porosity appeared very similar to the corresponding 3D SA/V ratio vs. 3D porosity. This comparison indicated the 2D perimeter/area ratios were useful proxies for the 3D SA/V ratios.

3.3. Results and Discussion: Pore Phase:

The performance of porous layers in the bilayer or trilayer architectures depended on both the ion-transport behavior of the LLCZN phase and on electrode infiltration behavior of the pore phase. If the electrodes failed to appreciably infiltrate into the pores and instead remained confined to the top surface of the porous layer, then the bilayer/trilayer would perform worse than a dense pellet of equivalent thickness. This does not significantly affect wetting electrodes (i.e., molten Li-metal or dissolved poly-sulfides). However, most electrodes will remain solid during infiltration and any limitations in the pore network will affect the electrode infiltration. Fortunately, using the M-factor it is possible to study effective diffusivity as well as conductivity, so the M-factor of the pore phase was analyzed to examine the diffusive behavior of the network.

3.3.1. Geometric Tortuosity:

Figure 3.17 shows 3D visualizations of the pore phase cumulative geometric tortuosity calculated along the forward directions of the X-, Y-, and Z-axes for the four FIB Tomography samples, with arrows denoting the calculation direction. Like the LLCZN phase, pore phase tortuosity was consistently lowest along the Z-axis consistently, highest along the X-axis, and intermediate along the Y-axis. For the high porosity samples (Trilayer 1 and Porous 1), the tortuosity visualizations clearly showed the pore phase tortuosity was significantly more homogenous and lower in value than the LLCZN tortuosity for the same samples. The Porous 2 sample had similar LLCZN and pore phase tortuosity values, and the low porosity Porous 3 sample had significantly higher pore phase tortuosity than LLCZN phase tortuosity.

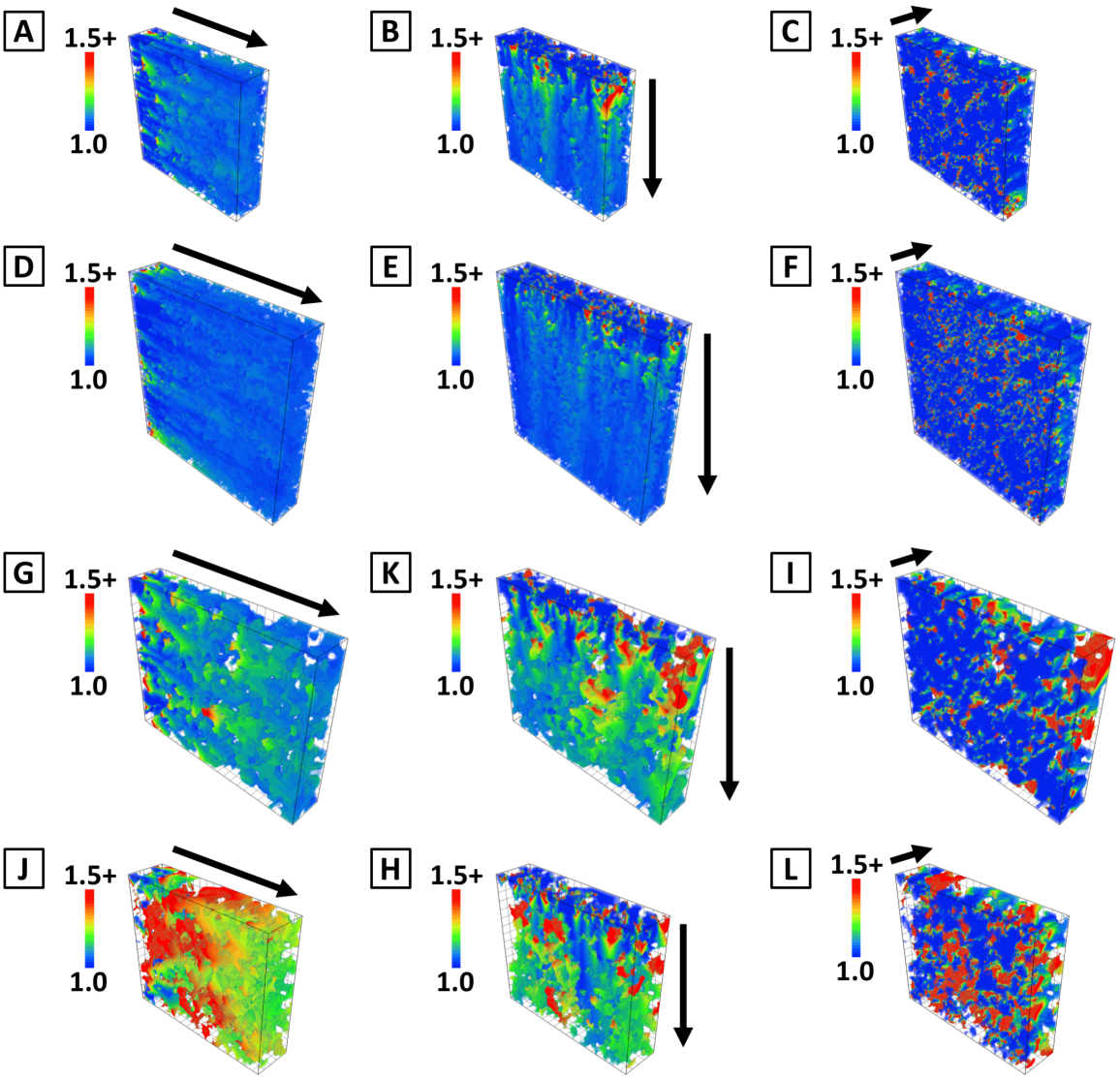

Figure 3.17: 3D visualization of the pore phase cumulative geometric tortuosity along the forward directions for the X-, Y-, and Z-axes of the Trilayer 1 (A-C), Porous 1 (D-F), Porous 2 (G-I), and Porous 3 (J-L) samples.

Examining the average and standard deviation of the cumulative geometric tortuosity in each "slice" as a function of Euclidean propagation distance (Figure 3.18), the pore phase tortuosity increased consistently as porosity decreased, as expected. As a result, the LLCZN phase tortuosity was substantially higher than the pore phase tortuosity for the highest porosity samples (Trilayer 1 and Porous 1), the LLCZN and pore phase tortuosity were similar for the medium porosity sample (Porous 2), and the pore phase tortuosity was substantially higher than the LLCZN phase tortuosity for the lowest porosity sample

(Porous 3). Similar to the LLCZN phase, the X-axis tortuosity tended to be the highest and the Z-axis tortuosity tended to be the lowest, and the cumulative tortuosity across each "slice" became more homogenous as more of the 3D image region was analyzed. Notable differences between the LLCZN and pore phase results were observed when focusing on the Porous 2 and Porous 3 samples. For the Porous 2 sample, the pore phase tortuosity values for the three axes were nearly identical, whereas the other 3 samples showed different pore phase tortuosity values depending on which axis was examined. For comparison, all samples showed different tortuosity values for the LLCZN phase of each axis. For the Porous 3 sample, the pore phase Y-axis tortuosity was found to be lowest rather than the Z-axis tortuosity. Given that the Porous 3 sample had the lowest porosity in the set of samples (26.45% porosity), the high LLCZN density might have changed the sample's sintering behavior and altered the formation of the pore network. It was unclear if a similar effect was the cause for the deviations observed for the Porous 2 sample, which had an intermediate porosity value in the set of samples.

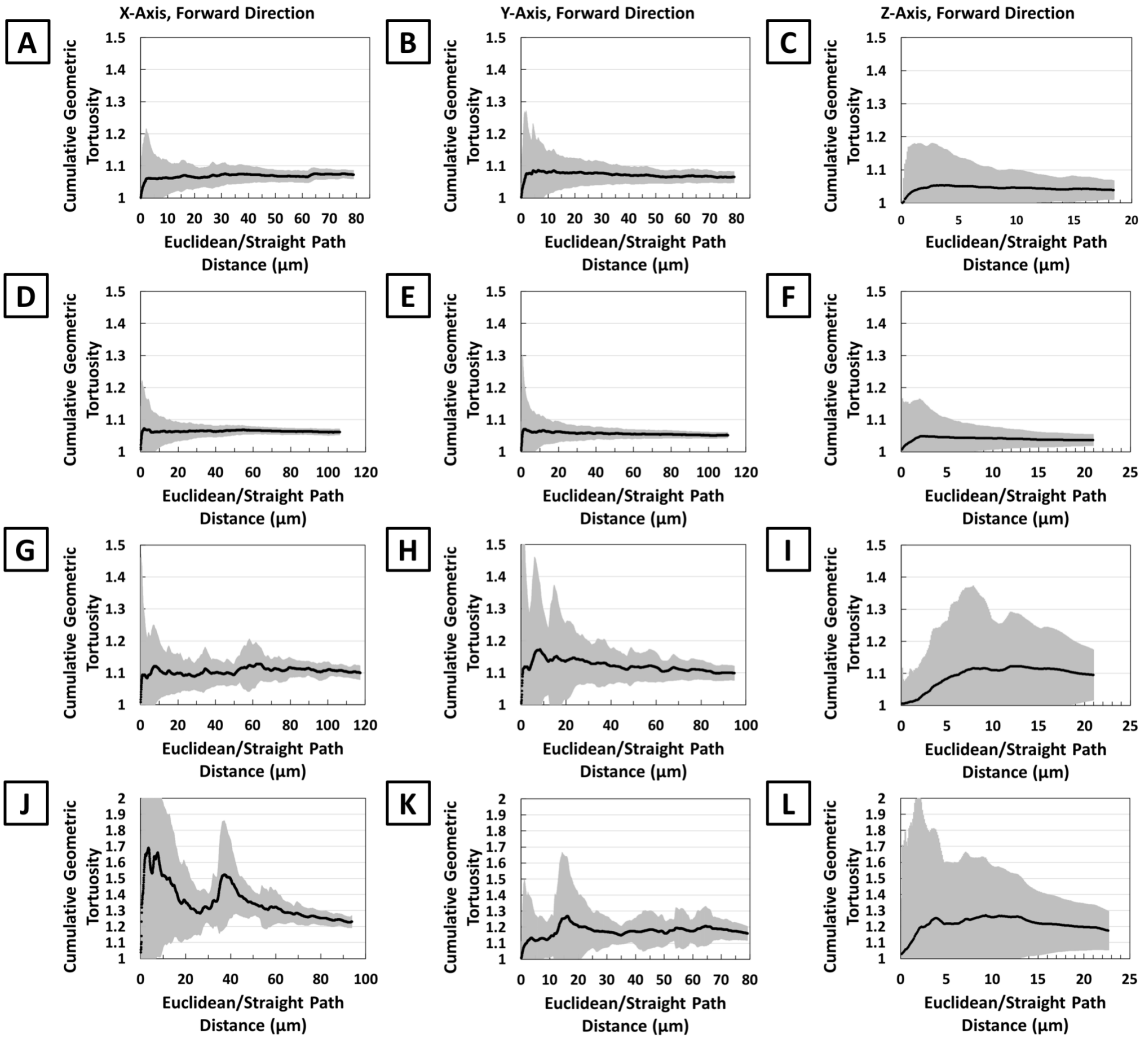

Figure 3.18: Average pore phase cumulative geometric tortuosity and SD for the forward directions for the X-, Y-, and Z-axes of the Trilayer 1 (A-C), Porous 1 (D-F), Porous 2 (G-I), and Porous 3 (J-L) samples.

As the porosity decreased from the Trilayer 1 (56.03% porosity) and Porous 1 samples (56.67% porosity) to the Porous 2 sample (40.58% porosity) and decreased further to the Porous 3 sample (26.45% porosity), the average and standard deviation of the pore phase cumulative geometric tortuosity increased. This was consistent with the corresponding behavior in the LLCZN phase, where the average and standard deviation of the LLCZN cumulative geometric tortuosity increased as the volume fraction of LLCZN decreased. However, the highest pore phase tortuosity values (for the Porous 3 sample)

were significantly higher than the highest LLCZN tortuosity values (for the Porous 1 sample). This difference may stem from the lowest sample porosity being 26.45% while the lowest LLCZN volume fraction was 42.30%, indicating the pore network with the least pore volume fraction was not directly comparable to the LLCZN network with the least LLCZN volume fraction and thus the networks had dissimilar tortuosity values.

Sub-volumes from 10% to 90% of the full 3D image volume were extracted and the pore phase geometric tortuosity calculations repeated for each sub-volume, with the results shown in Figure 3.19a, c, e, and g. Small sub-volumes showed significant variability in average tortuosity as well as large standard deviations that transitioned to more consistent values and smaller standard deviations as the sub-volume size increased. This was consistent with similar calculations performed for the LLCZN phase. Between the 100% volume pore phase tortuosity and the 90% sub-volume pore phase tortuosity values, the X-, Y-, and Z-axes showed differences of 0.06%, 0.05%, and 0.17% for Trilayer 1; differences of 0.01%, 0.05%, and 0.03% for Porous 1; differences of 0.05%, 0.08%, and 0.31% for Porous 2; and differences of 0.51%, 0.56%, and 0.45% for Porous 3, respectively. Based on this, all the 3D FIB tomography image regions were deemed as representative of the sample pore network, though the highest differences observed for the pore phase were all higher than the highest differences observed for the LLCZN. The X-, Y-, and Z-axes direction-averaged pore phase geometric tortuosity values were combined into a single characteristic pore phase geometric tortuosity that was plotted as a function of sub-volume size in Figure 3.19b, d, f, and h. The characteristic pore phase tortuosity showed significantly less variability compared to the direction-averaged tortuosity values

as sub-volume size increased, further supporting the earlier conclusion that the 3D image regions were representative of the pore network.

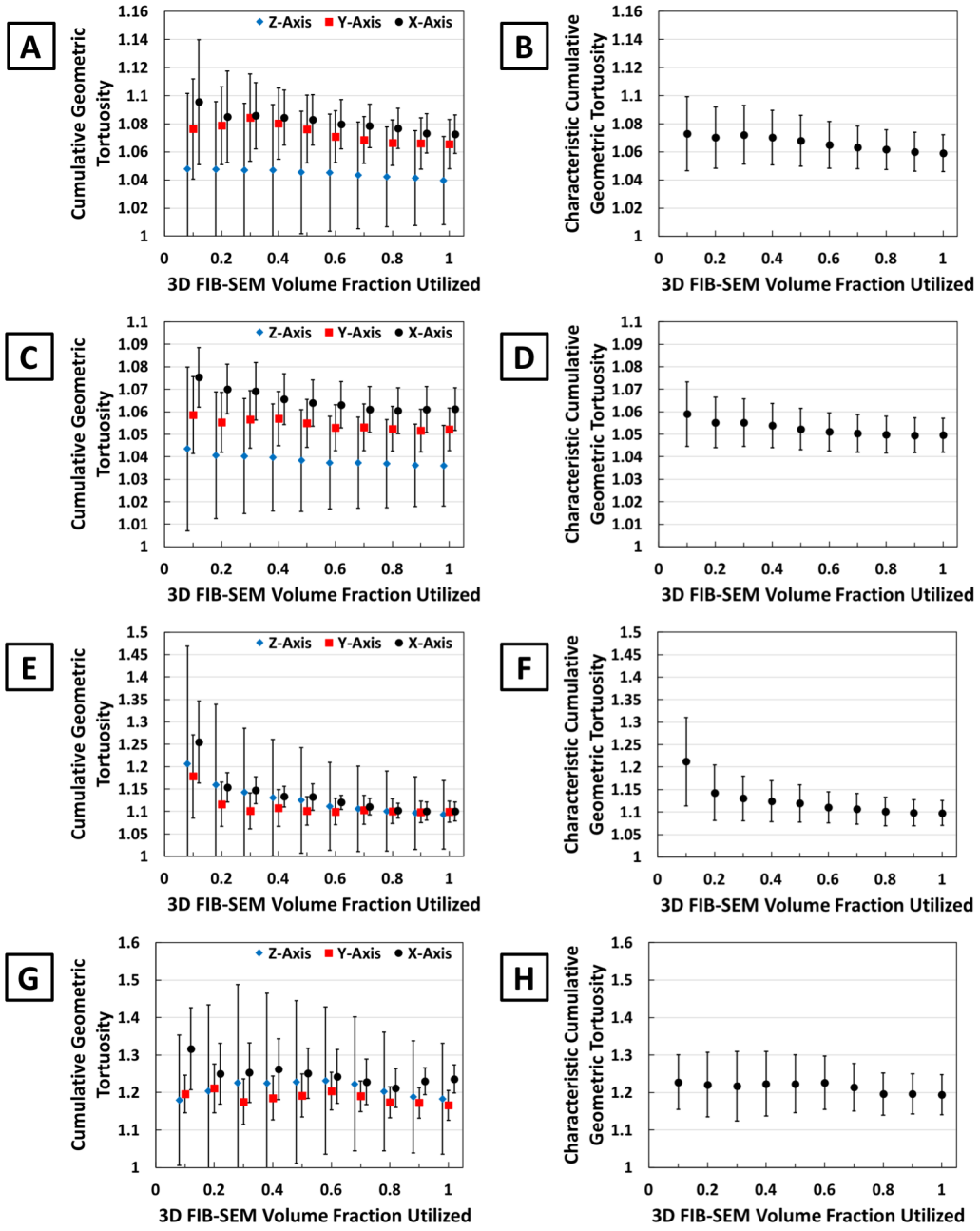

Figure 3.19: Average pore phase cumulative geometric tortuosity and SD for the direction-averaged X-, Y-, and Z-axes, as well as overall cumulative tortuosity and SD, of the Trilayer 1 (A-B), Porous 1 (C-D), Porous 2 (E-F), and Porous 3 (G-H) samples.

The characteristic geometric tortuosity (black line) and tortuosity squared (red line) for the pore phase in each of the 3D FIB Tomography samples were plotted vs. sample porosity in Figure 3.20. By the definition of tortuosity in the pore phase, 100% porosity corresponded with a tortuosity of 1.0, so an additional point was added at (100,1). A 2nd order curve was fitted to the results, with the fit forced to go through (100,1) to prevent physically impossible projections at high porosity values. The Trilayer 1 (56.03% porosity, 1.0590 tortuosity) and Porous 1 samples (56.67% porosity, 1.0496 tortuosity) showed near identical results, similar to the results for the LLCZN phase. Porous 2 (40.58% porosity, 1.0976 tortuosity) and Porous 3 (26.45% porosity, 1.1943 tortuosity) showed higher tortuosity values in line with the lower porosity of each sample. Despite following the expected trends, the pore phase tortuosity results showed good agreement with the 2nd order fit while the LLCZN tortuosity results had shown excellent agreement. This difference may be due to the LLCZN fit extending over a smaller range (from 0% to 56.67% porosity) compared to the range of the pore phase fit (from 100% to 26.45% porosity), making it easier to fit the LLCZN results. Alternatively, the formation behavior of the pore network may have become fundamentally different at low porosity values as discussed earlier. The inverse characteristic geometric tortuosity was plotted vs. sample porosity in Figure 3.20b and showed that diffusivity was reduced by 29.89% for the lowest porosity sample. For comparison, the effective conductivity of the LLCZN phase was reduced by a maximum of 19.85% for the highest porosity sample, suggesting that diffusion through the pore phase may be more susceptible to changes in porosity than the effective conductivity of the LLCZN phase. Alternatively, the lowest sample porosity observed was 26.45% while the lowest LLCZN volume fraction was 42.58%, and since tortuosity increased as the phase

volume fraction decreased, the LLCZN tortuosity might become similar to the highest pore phase tortuosity if the LLCZN volume fraction was also reduced to 26.45%.

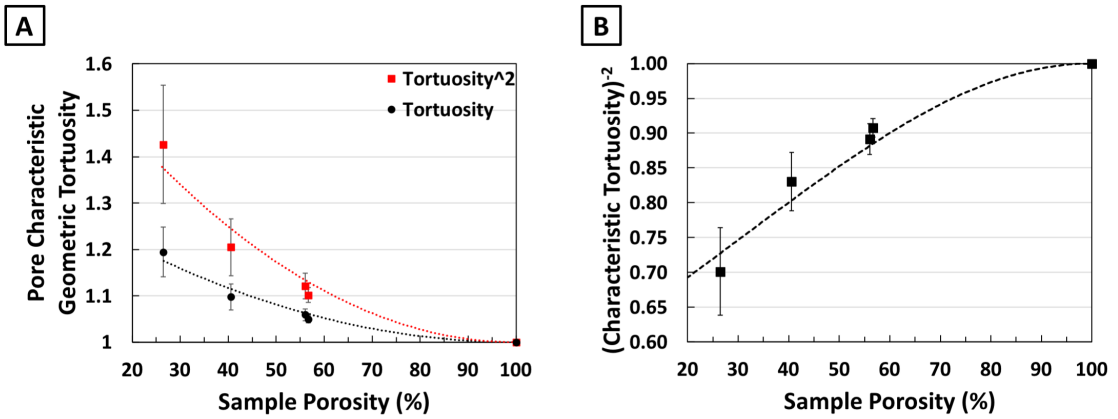

Figure 3.20: A) pore phase characteristic geometric tortuosity (black markers) and tortuosity squared (red markers), as well as SD, for each of the 3D FIB Tomography samples. The broken lines represent 2nd order fits. B) inverse characteristic tortuosity squared, with broken line calculated from fit for characteristic tortuosity squared.

3.3.2. Percolation Factor:

The pore phase direction-averaged percolation factor for the X-, Y-, and Z-axes were shown for different sub-volume utilization sizes for the 3D FIB Tomography samples (Figure 3.21a). All percolation factors for all samples and sub-volumes were above 0.98. Higher percolation factors were also observed for the 100% volumes for the Trilayer 1 and Porous 1 samples. Interestingly, the percolation factors for the 100% volumes for the Porous 2 and Porous 3 were lower than percolation factors for other sub-volume sizes for those samples, and the 100% volume values for the Porous 3 sample were almost the lowest observed for that sample. This was in contrast to the LLCZN phase, where the percolation factors almost always increased as the sub-volume size increased. One possible explanation was the low porosity samples (Porous 2 and especially Porous 3) had increasing numbers of closed pores proportional to the decreasing sample porosity that were not accessible by the pore phase tortuosity calculations. The X-, Y-, and Z-axes direction-averaged

percolation factors were averaged into an overall pore phase percolation factor and plotted as a function of sub-volume size in Figure 3.21b. Similar to the overall pore phase geometric tortuosity, the overall pore phase percolation factor showed less variability and lower SD values than direction-averaged percolation factors.

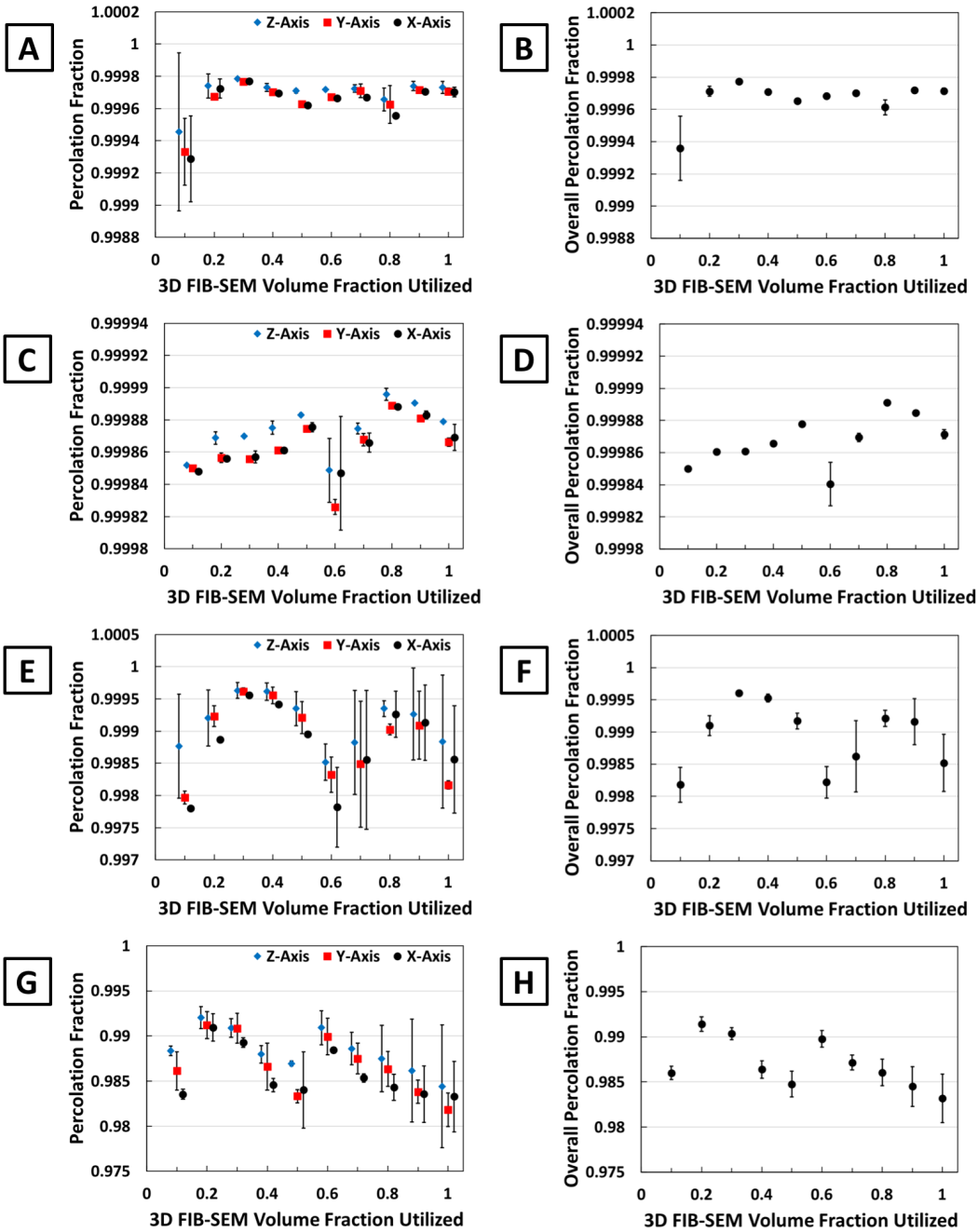

Figure 3.21: A) pore phase percolation factor and SD for the direction-averaged X-, Y-, and Z-axes, as well as overall sample percolation factor and SD, of the Trilayer 1 (A-B), Porous 1 (C-D), Porous 2 (E-F), and Porous 3 (G-H) samples.

The overall pore phase percolation factors for each of the 3D FIB Tomography samples were plotted vs. sample porosity in Figure 3.22. By the definition of percolation factor in the pore phase, 100% porosity corresponded to a percolation factor of 1.0, so an

additional point was added at (100,1). A 2nd order curve fitted to the results, with the fit forced to go through (100,1) to prevent physically impossible projections at low porosity values. Generally, the pore phase percolation factor increased with increasing sample porosity, though data points showed significant scatter around the 2nd order fit. In comparison, the LLCZN percolation factor results showed significant scatter around the 1st order fit used for that data. Even so, the lowest pore phase percolation factor observed was still above 0.98. Based on this, the percolation factor was deemed to have virtually no effect on transport behavior through the pore phase within the porosity range examined here.

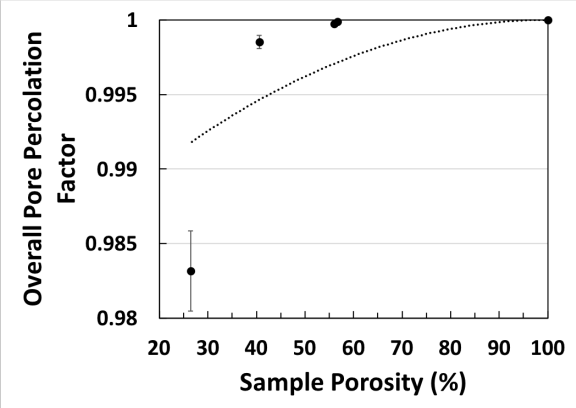

Figure 3.22: Overall sample pore percolation factor and SD for all 3D image regions plotted vs. 3D sample porosity. The broken line represents a 2nd order fit.

3.3.3. C-PSD, MIP-PSD, and Constriction Factor:

The cumulative coverage fraction c-PSD and average MIP-PSD results for the LLCZN phase in each of the 3D FIB Tomography samples were plotted together in Figure 3.23a, with the c-PSD results as a solid line and the corresponding MIP-PSD results as a dashed line. Immediately, significant differences were noted between the pore phase results and the LLCZN results. The LLCZN results for the Trilayer 1 and Porous 1 samples were very similar due to both samples having similar microstructure. In contrast, the pore phase results for the Trilayer 1 and Porous 1 samples showed significant differences, with the c-

PSD curve for the Trilayer 1 sample displaying a gradual drop while the c-PSD curve for the Porous 1 sample displayed an initial drop and long declining tail. Converting to instantaneous coverage fraction (Figure 3.23b), this behavior corresponded to both samples having different bimodal distributions in the pores. The Trilayer 1 sample had a near uniform distribution of pore sizes between 0.1 μm (minimum examined here) and 3.0 μm, with an increased number of pores between 4.0 μm and 6.0 μm. The Porous 1 sample had most pore sizes between 0.1 μm and 4.0 μm, with a clear peak at 2.0 μm, and another grouping of pore sizes between 8.0 μm and 9.0 μm. The MIP-PSD curves were more similar in appearance, although the Trilayer 1 sample had more peaks in the instantaneous coverage fraction at higher pore sizes than the Porous 1 sample, with one major peak at a lower pore size. Examining the 3D visualizations of the LLCZN and secondary phase in Figure 3.1, the Trilayer 1 sample does appear to have larger and more uniform pore sizes than the Porous 1 sample, supporting the c-PSD and MIP-PSD assessments. Still, it was surprising how much a difference could exist between the pore networks of samples with very similar LLCZN microstructures. The Porous 2 and Porous 3 samples showed curves with similar shapes, with the curves of the lower porosity Porous 2 sample being shifted to smaller pore sizes, as expected.

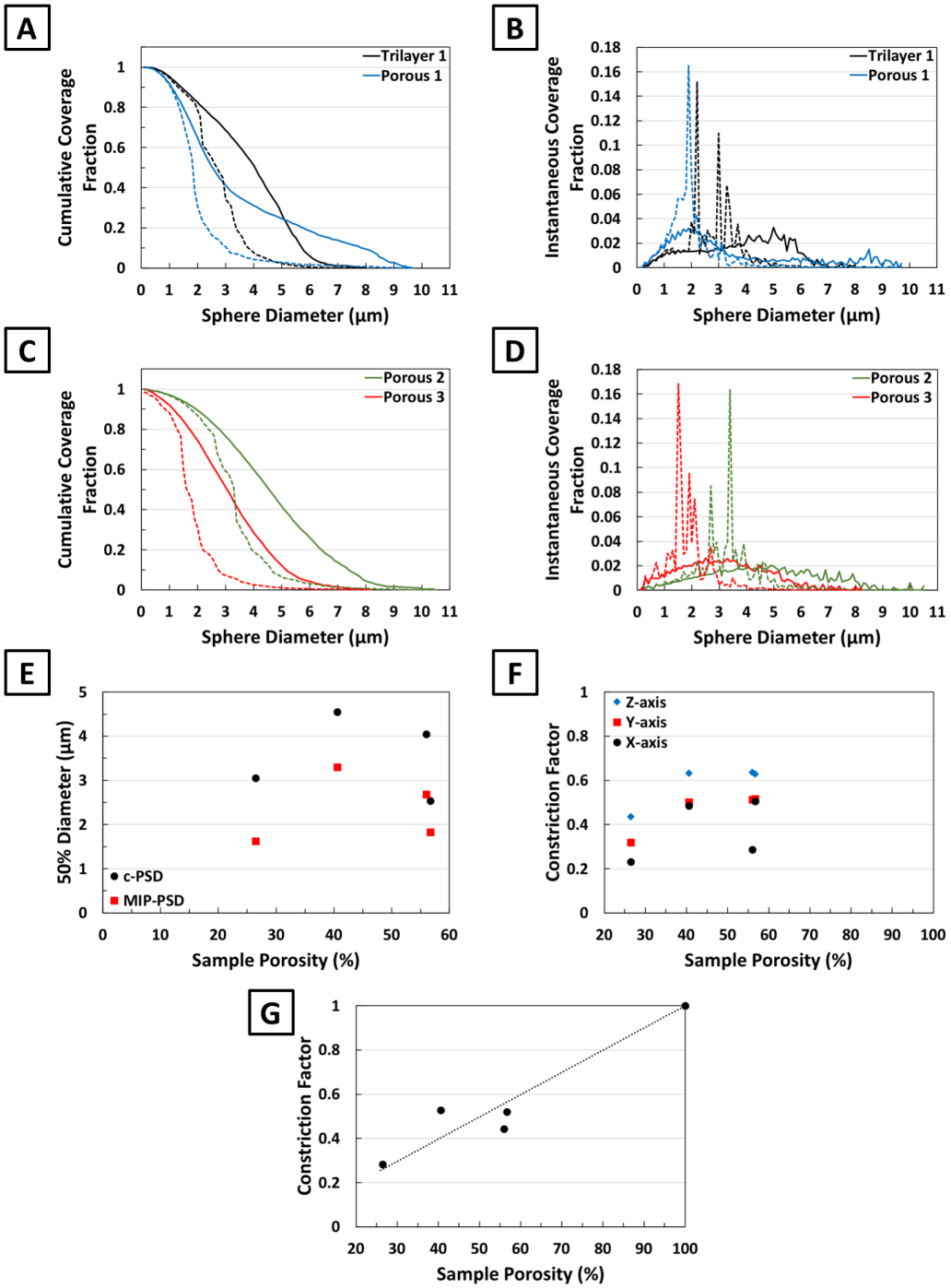

Figure 3.23: A) pore phase c-PSD (solid lines) and average MIP-PSD (dashed lines) for the 4 FIB Tomography samples. B) instantaneous coverage distributions for c-PSD (solid lines) and average MIP-PSD (dashed lines). C) 50% sphere diameters for c-PSD (black circles) and for average MIP-PSD (red squares). D) constriction factors for the 4 FIB Tomography samples, with a linear fit plotted. E) constriction factors calculated for the X-, Y-, and Z-axes based on the direction-averaged MIP-PSD.

Examining the 50% diameter values (Figure 3.23c) showed another major difference between the pore phase and the LLCZN phase. For the LLCZN, the c-PSD and MIP-PSD 50% diameter values were constant when increasing sample porosity from the Porous 3 sample (26.45% porosity) to the Porous 2 sample (40.58% porosity), then the 50% diameters decreased as porosity increased further to the Trilayer 1 (56.03% porosity) and Porous 1 samples (56.67% porosity). Here, the Trilayer 1 and Porous 1 samples had near identical results for the LLCZN. For the pore phase, the 50% diameter values increased when increasing sample porosity from the Porous 3 sample (26.45% porosity) to the Porous 2 sample (40.58% porosity), then the 50% diameters decreased somewhat as porosity increased further to the Trilayer 1 (56.03% porosity). However, the Porous 1 sample (56.67% porosity) showed significantly lower 50% diameter values than the Trilayer 1 sample, a result of the different pore size distributions discussed earlier.

Moving to the direction-averaged pore phase constriction factors (Figure 3.23d), we observed significant variation between the X-, Y, and Z-axes constriction factors. While the LLCZN phase also showed some variation between axes, the amount of variation for the pore phase was significantly larger, which suggested the pore network was more anisotropic than the LLCZN microstructure. Moreover, most samples followed the same trend as the LLCZN phase with regards to the X-axis constriction factor being the lowest and the Z-axis constriction being the highest. This was in line with expectations of sample settling along the X-axis and potential effects of the different dimensions of the 3D image region along the different axes. Unlike the pore phase 50% diameter values, the Trilayer 1 and Porous 1 samples had near identical Z- and Y-axes pore phase constriction factors, reminiscent of the similar constriction factors for the LLCZN phase in these two samples.

The major difference was in the X-axis, with a much lower pore phase constriction factor for the Trilayer 1 sample. The overall pore phase constriction factor was plotted vs. 3D sample porosity in Figure 3.23e. By the definition of constriction factor in the pore phase, 100% porosity corresponded to a constriction factor of 1.0, so an additional point was added at (100,1). A 1st order curve was fit to the results, with the fit forced to go through (100,1) to prevent physically impossible projections at high porosity values. The fitted curve provided a rough fit to the overall behavior of the pore phase constriction factors, which generally increased as sample porosity increased. However, the pore phase constriction factors were more scattered around the fitted curve than the LLCZN constriction factors.

3.3.4. M-Factor:

The overall results for each pore phase microstructural term and the corresponding curves of fit were plotted on a linear scale in Figure 3.24a and on a logarithmic scale in Figure 3.24b vs. 3D sample porosity. Looking at individual data points, the pore phase volume fraction and the constriction factor were the most important components of the M-factor, with the geometric tortuosity being the third most important and the percolation factor playing almost no role at all. While there was variation in whether the pore phase volume fraction or the constriction factor were most important, there was no discernable pattern amongst the samples. The combined M-factor was also plotted (Figure 3.24) and decreased exponentially as porosity decreased, with a porosity value of 26.45% corresponding to a porosity decrease of 73.55% and a ~1.5 order of magnitude reduction in M-factor. This was similar to the LLCZN M-factor when viewed as a function of LLCZN

volume fraction, though the pore phase M-factor data points showed more scatter about the exponential fit. Based on the M-factor, increasing the LLCZN porosity to 26.45%, 40.58%, 56.03%, and 56.67% would result in diffusion of non-wetting electrodes through the pore network being 5.2%, 17.7%, 22.1%, and 26.7% as effective as that of a fully open, unobstructed pore, respectively.

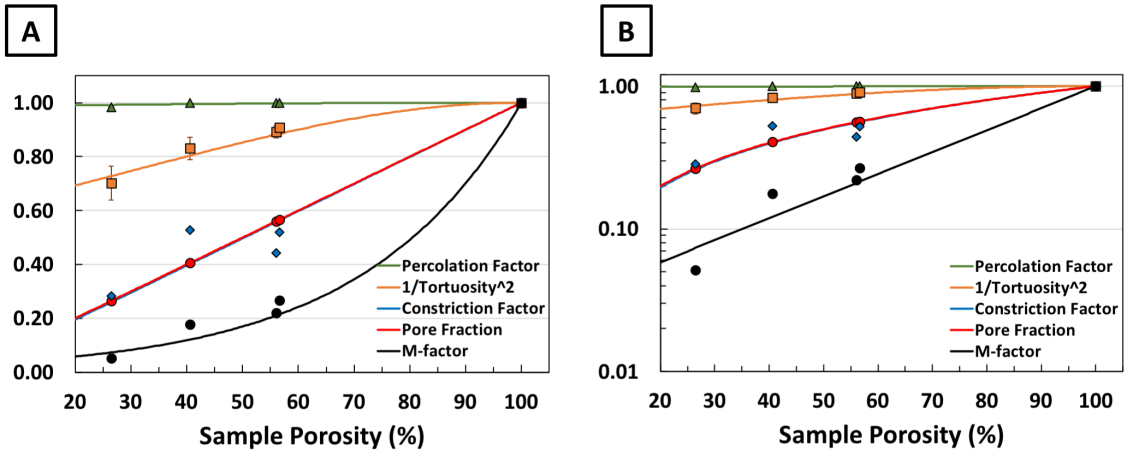

Figure 3.24: Overall sample pore phase microstructure reduction terms plotted together for the 4 FIB Tomography samples, as well as the combined M-factor (black markers), A) on a linear vertical scale and B) on a logarithmic vertical scale. Curves of fit are plotted for each parameter.

3.4. Implications for Batteries Utilizing Bilayer/Trilayer Garnet Electrolytes:

3D FIB Tomography was used to examine tape-cast porous LLCZN microstructures ranging from ~26% porosity to ~57% porosity, with the results of the LLCZN and pore phases summarized in Table 3.4. Over this range, the LLCZN M-factor reached a minimum of 0.160 for the highest porosity sample and a maximum of 0.410 for the lowest porosity sample, while the corresponding pore phase M-factor reached a maximum of 0.267 and a minimum of 0.052. This immediately demonstrated that creating an optimal porous LLCZN microstructure was a balancing act between achieving a high LLCZN M-factor (and thus a high effective Li-ion conductivity) to minimize porous layer ASR, while also achieving a high pore phase M-factor to ensure effective electrode infiltration. The relatively low values of the pore phase M-factor compared to the LLCZN M-factor suggested that diffusion through the pore network was more easily affected by changes to the sample microstructure. While this would only slightly improve the infiltration of wetting electrodes such as Li-metal (when melted) or sulfur (when melted or infiltrated as polysulfide), widely used particle-based electrodes (LCO, NMC, graphite, etc.) would greatly benefit from easier diffusion through the pore network. This then suggested that maximizing the pore phase M-factor by increasing sample porosity would provide greater gains due to better infiltrated electrodes than the losses due to lower LLCZN effective conductivity and higher ASR. This was reinforced by the fact that higher sample porosity would allow for more electrode loading while reducing electrolyte mass and thus facilitate higher battery energy density. At the same time, the potential influence of higher sample surface area on the bulk conductivity of the LLCZN emphasized the

importance of carefully investigating and maintaining optimum sintering conditions when fabricating solid-state Li-ion electrolytes with significant porosity.

Table 3.4: Summary of microstructural parameters for the LLCZN phase and pore phase of all tape-cast LLCZN samples.

	Trilayer 1		**Porous 1**		**Porous 2**		**Porous 3**	
	LLCZN	**Pore**	**LLCZN**	**Pore**	**LLCZN**	**Pore**	**LLCZN**	**Pore**
M-factor	0.168	0.221	0.160	0.267	0.306	0.177	0.410	0.052
Phase Volume Fraction	0.4230	0.5603	0.4258	0.5667	0.5751	0.4058	0.7355	0.2645
Characteristic Geometric Tortuosity	1.1114	1.0590	1.1170	1.0496	1.0700	1.0976	1.0360	1.1943
(Characteristic Geometric Tortuosity)$^{-2}$	0.8097	0.8917	0.8015	0.9076	0.8734	0.8301	0.9317	0.7011
Percolation Factor	0.9985	0.9997	0.9991	0.9999	0.9992	0.9985	0.9998	0.9832
Average feature size (µm)	2.173	4.042	2.071	2.537	4.244	4.552	4.130	3.050
Average bottleneck size (µm)	1.522	2.687	1.418	1.829	3.316	3.304	3.194	1.622
Constriction Factor	0.491	0.442	0.469	0.520	0.611	0.527	0.598	0.283

4. Solid-State Li-Ion Electrolyte with Template-based Porous Microstructure:

As an alternative to the tape-cast microstructures, porous garnet samples were fabricated by infiltrating an existing cellulose template with garnet sol gel solution and sintering the sample to burn away the template, leaving behind the sintered garnet with the original template microstructure.[61] The goal was to identify how the template-based garnet fabrication approach affected the resulting garnet microstructure and determine any advantages/disadvantages of the structure when compared to the tape-cast garnet structures.

4.1. Methods and Characterization:

4.1.1. Porous LLZO Fabrication:

Following Gong, *et al.*, Al-doped LLZO with the chemical composition of $Li_{6.28}Al_{0.24}La_3Zr_2O_{11.98}$ was prepared by dissolving stoichiometric amounts of 2.31 g $LiNO_3$ (99%; Alfa Aesar), 0.48 g $Al(NO_3)_3*9H_2O$ (98%; Alfa Aesar), 6.94 g $La(NO_3)_3*6H_2O$ (99.9%; Alfa Aesar), and 5.0 g Zirconium propoxide solution (70 wt.%; Sigma Aldrich) in 30-ml ethanol with 15 vol.% acetic acid. 30% excess $LiNO_3$ was added to compensate for lithium loss during the subsequent calcination procedure.[61] Cellulose templates were soaked in a 2.5 mol/L LLZO precursor solution for 24 h. The multi-scale porosity existing in the porous templates enabled homogenous impregnation by the LLZO precursor. Several soaked cellulose templates were stacked and dried, and calcination of the precursor impregnated templates was conducted under flowing oxygen at different temperatures to obtain garnet textiles.

4.1.2. X-ray Diffraction:

The crystalline phases present in several samples were characterized via x-ray diffraction (XRD) using a Bruker C2 Discover with 2D Detector operated at 40 kV and 40 mA. Phase identification was performed with Diffrac.Eva (Version 4, Bruker AXS) and lattice parameters were calculated using Topas (Version 5, Bruker AXS).

4.2. Results and Discussion: LLZO Phase:

4.2.1. XRD Results:

Figure 4.1 shows XRD patterns for the template-based LLZO sintered at maximum holding temperatures ranging from 700 °C to 900 °C with 30% excess Li-precursor. The XRD pattern for pure phase LLZO was also included for reference. The highest purity LLZO XRD pattern was obtained at 750 °C. 700 °C produced LLZO with some minor secondary phases, and temperatures from 800 °C and above showed increasing amounts of secondary phase as well as the formation of $La_2Zr_2O_7$. By 900 °C, no LLZO remained. This indicated the highly porous template-based LLZO microstructure was significantly affected by Li-loss as increased sintering temperature enhanced Li-volatilization from the sample. Based on this, 750 °C was selected for the maximum holding temperature for sintering the template-based LLZO sample.

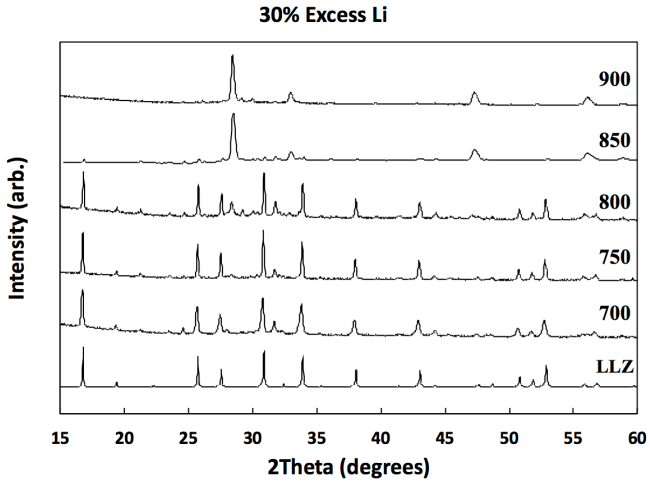

Figure 4.1: XRD patterns for sintered LLZO for different holding temperatures during sintering. The reference pattern for LLZO is included.

4.2.2. 3D FIB-SEM Analysis:

Figure 4.2 shows a BSE image of the cross-section of the epoxy-filled template-based LLZO sample after mechanical polishing, with the sintered LLZO appearing bright relative to the dark epoxy. The image showed the LLZO was highly porous and highlighted the layer-like microstructure of the template-based LLZO, which originated from the unique microstructure of the individual cellulose templates and from multiple templates stacked together in the un-sintered sample. The sample was approximately 50-60 μm thick and could be made thicker/thinner by using more/fewer soaked templates in the un-sintered stack. The LLZO microstructure appeared to be preferentially aligned with the horizontal axis of the image, due to the mesh-like nature of the original templates used. Still, the sintered sample remained intact when handled, indicating the successful development of sintered connections between the stacked template layers.

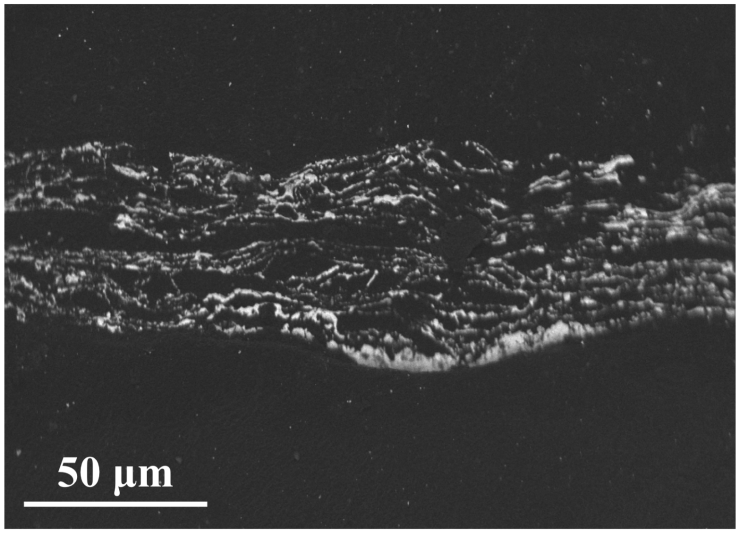

Figure 4.2: BSE image of cross-section of epoxy-filled template-based LLZO sample after mechanical polishing.

The 3D Tomography milling-and-imaging run produced 137 SE and BSE images of the FIB polished cross-sections. Figure 4.3 shows several of the angle-corrected BSE

images, cropped to remove artifacts and unusable portions of the image. The Pt protection layer was visible at the top with the milled triangular thickness reference mark, and the sintered LLZO appeared bright relative to the dark epoxy. The 3D FIB Tomography cross-sections revealed the sample microstructure was more complex than it initially appeared in the mechanically polished cross-section. Rather than parallel sheets, the microstructure appeared composed of thin membranes that formed a large array of "chambers" that varied in size and shape both across each image and between images. Moreover, these chambers were well filled by the epoxy indicating a highly connected network of pores within the template-based LLZO.

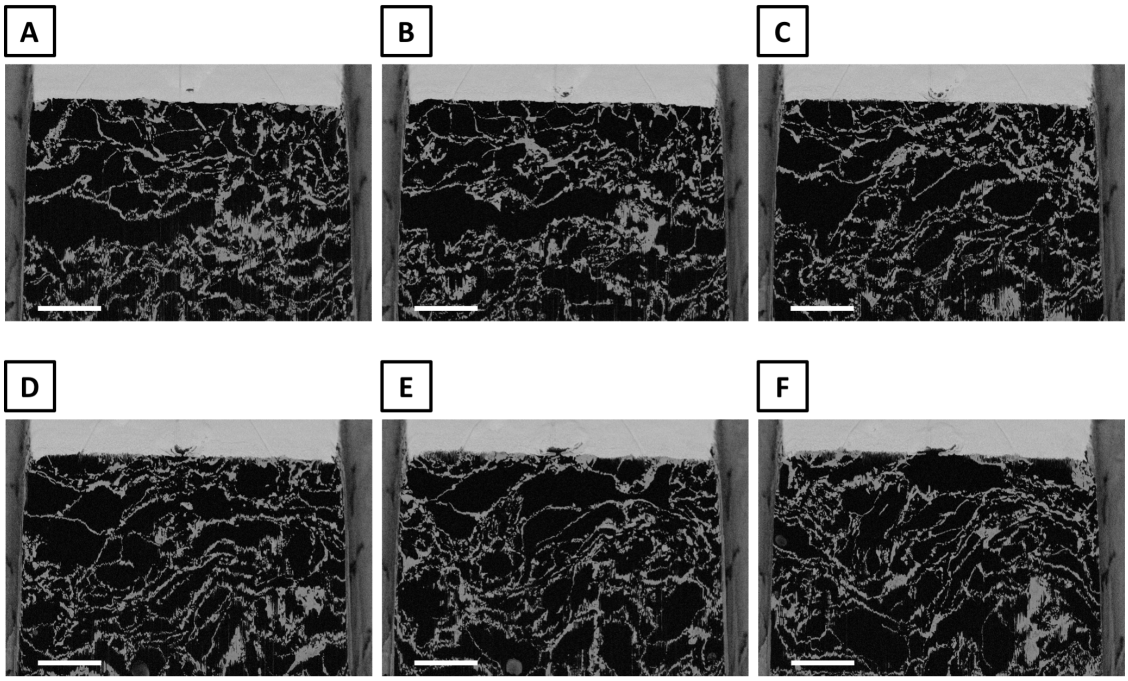

Figure 4.3: BSE images of FIB polished cross-section of epoxy-filled template-based LLZO sample, specifically A) Image 1, B) Image 25, C) Image 50, D) Image 75, E) Image 100, and F) Image 125. All scalebars are 25 μm.

The segmented and post-processed images were combined in the visualization program, Dragonfly (Object Research Systems), to reconstruct the 3D template-based LLZO microstructure (Figure 4.4). The horizontal axis of the 3D image region was the X-

axis, the vertical axis was the Y-axis, and the axis parallel to the milling direction was the Z-axis. For reference, the XY-plane was parallel to the plane of the templates and the templates were stacked along the Z-axis. Examining the 3D microstructure, it was clear the seemingly isolated "chambers" observed in the individual cross-sections were parts of larger pores that were actually all interconnected. At the same time, the LLZO membranes observed in the individual cross-sections were also part of larger 3D membranes that extended through the entire thickness of the image region and created a well-connected LLZO network.

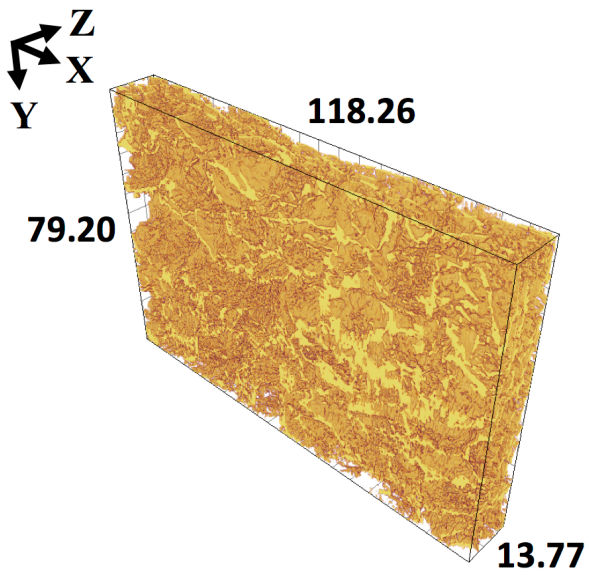

Figure 4.4: 3D reconstruction of the template-based LLZO sample from FIB Tomography image set. Reconstruction dimensions were in µm.

4.2.3. Volume, Volume Fraction, and Surface Area:

The volume, volume fraction, surface area, and surface-area-to-volume (SA/V) ratio for each phase in the template-based LLZO sample were calculated with Dragonfly and the results shown in Table 4.1. The template-based LLZO sample had a pore volume fraction of 78.98%. The LLZO phase had a significantly higher SA/V ratio than the pore

phase, likely due to the small thickness of the LLZO membranes in the 3D image region as compared to the much larger pores.

Table 4.1: Characterization of the 3D FIB Tomography image region of the template-based LLZO microstructure.

Dimensions (µm)	**Material**	**Phase Volume Fraction (%)**	**Volume V (µm^3)**	**Surface Area SA (µm^2)**	**SA/V (1/µm)**
118.26	LLZO	21.02	27,109.29	205,896.92	7.5951
79.20	Pore	78.98	101,829.13	205,896.92	2.0220
13.77					
	Totals	*100.00*	*128,938.42*	*411,793.85*	

Examining the phase volume fractions at different points along the X-, Y, and Z-axes (Figure 4.4), all axes showed some amount of variation but remained close to the mean value for the 3D image region. The Y-axis appeared the most homogenous, with the X-axis showing a small decrease in porosity from left to right across the 3D image region and the Z-axis showing a small increase in porosity from front to back. This was interesting given the Z-axis was parallel to the "vertical" axis of the sample during sintering, so any pore collapse should occur preferentially along the Z-axis and cause the LLZO phase to be more aligned along the XY-plane than the Z-axis. This should cause the pore collapse to manifest as high frequency oscillations in the phase volume fractions along the Z-axis, due to alternating layers of high and low porosity. Yet these oscillations were not present in Figure 4.4, strongly suggesting very little pore collapse occurred during sintering. This was likely due to the relatively low sintering temperature used for the template-based LLZO sample as compared to the much higher temperatures typical of sintering garnet pellets or even the LLCZN bilayers/trilayers.

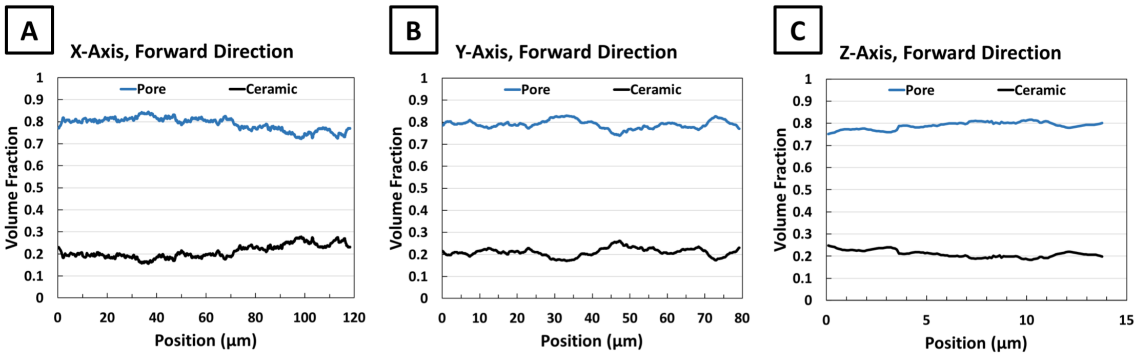

Figure 4.4: Volume fraction distributions along the X-, Y-, and Z-axes of the template-based LLZO sample (A-C).

4.2.4. Geometric Tortuosity:

Figure 4.5a-c shows 3D visualizations of the cumulative geometric tortuosity across the template-based LLZO sample when calculating along the forward directions of the X-, Y-, and Z-axes of the LLZO phase, with arrows denoting the calculation direction. The tortuosity began with an initial value of 1.0 (blue color), with early deviations from straight paths resulting in tortuosity quickly increasing above 2.0 (red color). As the calculations progressed across the 3D image region, the cumulative geometric tortuosity decreased and became more homogenous as local variations were smoothed over by global properties. This behavior was visible in the average and standard deviation of the cumulative geometric tortuosity when measured vs. propagation distance (Figure 4.5d-f). Based on the final cumulative geometric tortuosity values for the forward directions, the Z-axis had the highest tortuosity of 1.5618 +/- 0.2507, the Y-axis had a medium tortuosity of 1.1518 +/-0.0320, and the X-axis had the lowest tortuosity of 1.1196 +/- 0.0209. This pattern persisted when the forward and reverse directions were averaged together, resulting in a direction-averaged Z-axis tortuosity of 1.5454 +/- 0.2398, a Y-axis tortuosity of 1.1614 +/-0.0496, and an X-axis tortuosity of 1.1225 +/- 0.0208. The different tortuosity values of each axis indicated the microstructure was strongly anisotropic, with a low tortuosity XY-

plane and a high tortuosity Z-axis. This made sense based on the mesh-like nature of the cellulose textiles used to make the template-based LLZO sample.

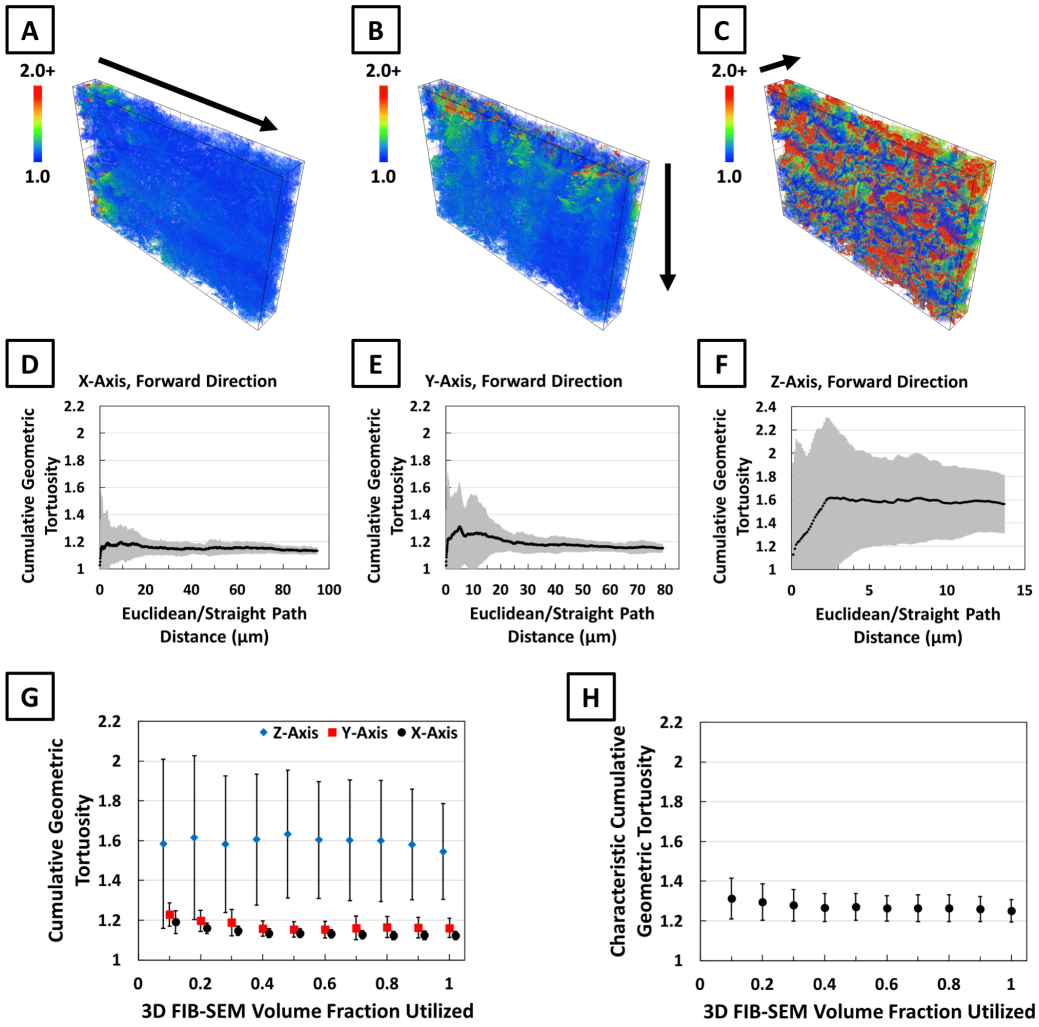

Figure 4.5: 3D visualization of the LLZO phase cumulative geometric tortuosity along the forward directions for the X-, Y-, and Z-axes of the template-based LLZO sample (A-C). Average LLZO phase cumulative geometric tortuosity and SD for the forward directions for the X-, Y-, and Z-axes of the template-based LLZO sample (D-F). Average LLZO phase cumulative geometric tortuosity and SD for the direction-averaged X-, Y-, and Z-axes, as well as overall cumulative tortuosity and SD (G-H).

To test the representativeness of the 3D image region, sub-volumes ranging from 10% to 90% of the full 3D image volume were extracted and the geometric tortuosity calculations repeated for each sub-volume. Figure 4.5g shows the direction-averaged results for each axis for the template-based LLZO sample. Significant variability was

expected between the small sub-volumes that would transition to more consistent values for larger sub-volumes. This behavior was most obvious in the X- and Y-axes, which reached stable values around the 70% sub-volume size. In contrast, the Z-axis showed consistent fluctuations throughout and actually started steadily declining above the 80% sub-volume size. Comparing the 100% volume and the 90% sub-volume tortuosity values, the X-, Y-, and Z-axes showed differences of 0.14%, 0.09%, and 2.28%, respectively. For reference, Tjaden, *et al*, observed differences of 7% between their 100% volume and their 90% sub-volume tortuosity values and concluded their 3D image volume was large enough to be representative.[128] Similarly, the template-based LLZO image region was deemed as representative of the overall sample. The X-, Y-, and Z-axes direction-averaged geometric tortuosity values were then combined into a single characteristic geometric tortuosity using Equation 2.12.[127] The results were plotted as a function of sub-volume size in Figure 4.5h. The characteristic tortuosity showed significantly less variability compared to the direction-averaged tortuosity values as sub-volume size increased, further supporting the earlier conclusion that the 3D image region was representative.

$$\tau_{characteristic} = \frac{3}{\frac{1}{\tau_x}+\frac{1}{\tau_y}+\frac{1}{\tau_z}} \tag{2.12}$$

Since Equation 1.3 utilized the inverse of tortuosity squared to calculate the M-factor, the characteristic geometric tortuosity squared was calculated. This meant the template-based LLZO characteristic tortuosity of 1.2505 corresponded to a tortuosity squared of 1.5638, an inverse tortuosity squared of 0.6395, and an effective conductivity reduction of 36.05% based on Equation 1.3. For reference, the template-based sample was 21.02% LLZO, reflecting an effective conductivity already reduced by 78.98% solely due

to reduced LLZO volume fraction in the sample. This meant the effect of tortuosity was relatively minor compared to the conductive phase volume fraction.

4.2.5. Percolation Factor:

The direction-averaged percolation factor for the X-, Y-, and Z-axes were shown for different sub-volume utilization sizes for the template-based LLZO sample (Figure 4.6a). All percolation factors were above 0.99, with 100% volumes producing values above 0.993. Given the percolation factors were very close to 1.0, it was highly likely the remaining "unconnected LLZO" were a combination of small spots of mislabeled LLZO in the pore phase and real LLZO particles connected to the LLZO microstructure at locations beyond the 3D image region boundaries. This was consistent with the LLZO phase being the only long-range solid present in the samples, so any truly isolated LLZO particles would separate from the bulk sample prior to epoxy infiltration. The X-, Y-, and Z-axes direction-averaged percolation factors were averaged into an overall percolation factor then plotted as a function of sub-volume size in Figure 4.6b. Similar to the characteristic geometric tortuosity, the overall percolation factor showed less variability and lower SD values than the direction-averaged percolation factors.

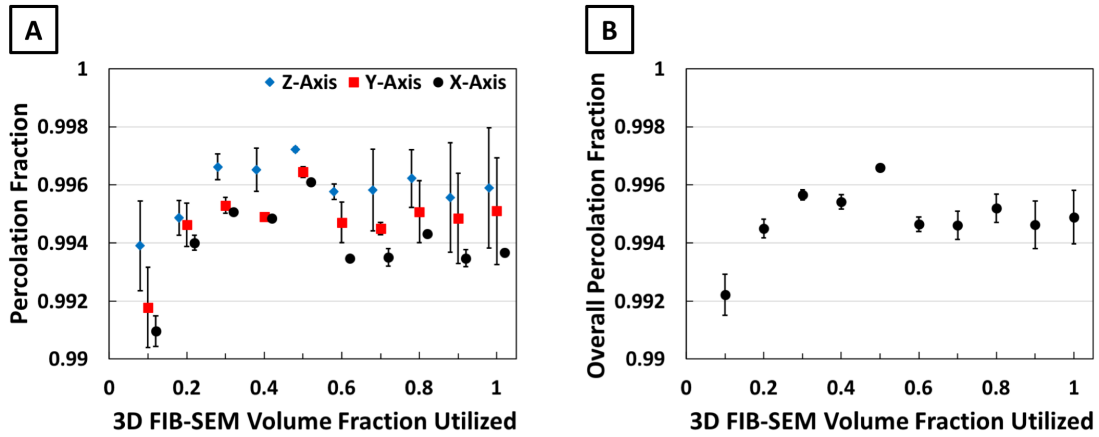

Figure 4.6: A) LLZO phase percolation factor and SD for the direction-averaged X-, Y-, and Z-axes for the template-based LLZO sample for different sub-volume sizes. B) overall sample percolation factor and SD for sample.

4.2.6. C-PSD, MIP-PSD, and Constriction Factor:

The cumulative coverage fraction c-PSD and average MIP-PSD results for the LLZO phase in the template-based LLZO sample were plotted together in Figure 4.7a, with the c-PSD results as a solid line and the corresponding MIP-PSD result as a dashed line. For both distribution curves, the cumulative coverage fraction of LLZO decreased as test sphere diameter increased and showed three distinct stages: an initial stage of high cumulative coverage fraction and near 0 slope; a "breakthrough" stage where the cumulative coverage fraction rapidly decreased; and a final stage of low cumulative coverage fraction and near 0 slope. The MIP-PSD curves decreased more drastically in the "breakthrough" stage than the c-PSD curves, showing how the bottlenecks quickly choked off access to much of LLZO structure. When the cumulative coverage fraction was converted to instantaneous coverage fraction (shown in Figure 4.7b), this behavior translated to narrow MIP-PSD peaks and broad c-PSD peaks. The c-PSD and MIP-PSD instantaneous coverage fraction curves both showed multiple peaks at different sphere sizes, corresponding to a concentration of features of that size. However, both curves

displayed a principle/maximum peak roughly positioned at the middle of the distribution. The MIP-PSD principle peak was at a smaller diameter than the c-PSD principle peak, in agreement with the idea that bottlenecks represent the narrowest parts of the contiguous LLZO microstructure.

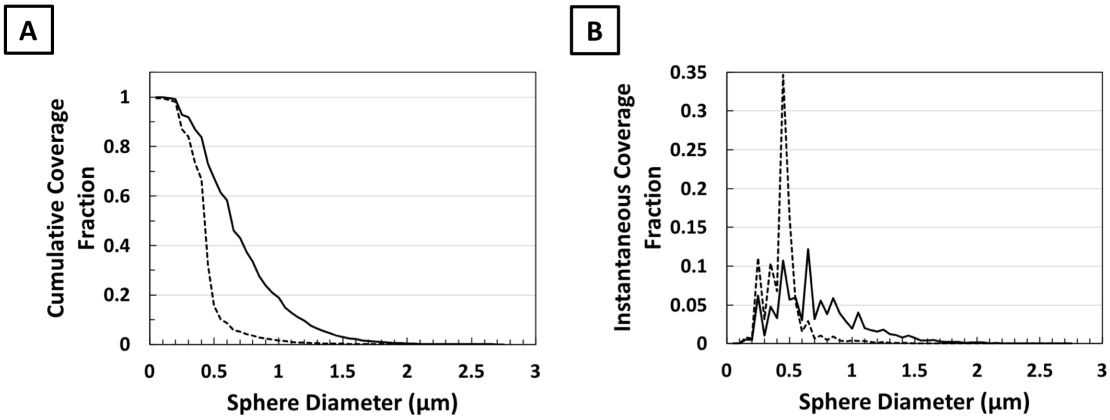

Figure 4.7: A) LLZO phase c-PSD (solid lines) and average MIP-PSD (dashed lines) for the template-based LLZO sample. B) instantaneous coverage distributions for c-PSD (solid lines) and average MIP-PSD (dashed lines).

Overall, the c-PSD gave a 50% coverage value of 0.634 µm and the MIP-PSD gave a 50% coverage value of 0.424 µm, corresponding to a constriction factor of 0.447 (Table 4.2). This meant that bottlenecks in the LLZO microstructure were responsible for reducing the effective conductivity of the sample by 55.3% overall. Examining the 50% coverage values of the MIP-PSD along the X-, Y-, and Z-axes, there was a slight increase in the LLZO bottleneck diameter from the lowest value of 0.417 µm along the X-axis to the highest value of 0.439 µm along the Z-axis. As a result, the constriction factors ranged from 0.433 to 0.479, a very narrow distribution, and showed that LLZO bottlenecks were essentially identical throughout the template-based LLZO sample despite the overall LLZO microstructure being very anisotropic.

Table 4.2: Summary of the LLZO phase 50% PSD Diameter, the 50% MIP-PSD diameters for the X-, Y-, and Z-axes, the overall 50% MIP-PSD diameter, and the resulting constriction factors.

50% PSD Diameter (µm)	50% MIP-PSD Diameter (µm)				Constriction Factor			
	X	Y	Z	Overall	X	Y	Z	Overall
0.634	0.417	0.424	0.439	0.424	0.433	0.446	0.479	0.447

4.2.7. M-Factor:

Thus far, this study examined the effects of LLZO phase fraction, constriction factor, geometric tortuosity, and percolation factor on the effective conductivity expected for the template-based LLZO sample. The reduction factors associated with each are summarized in Table 4.3, where it was clear the LLZO phase fraction had the greatest reduction effect on the effective conductivity, followed by the constriction factor and then the geometric tortuosity. The percolation factor had almost no effect due to the LLZO microstructure being virtually fully interconnected. The resulting M-factor for the microstructure was calculated using Equation 1.3 and was found to be 0.060, indicating the template-based LLZO sample had an effective conductivity 94.0% less than the intrinsic conductivity of the LLZO material. Due to the clear anisotropy of the template-based LLZO microstructure, it was necessary to examine these same reduction factors for each axis, with the results summarized in Table 4.4. Comparing the different axes, the constriction factor and percolation factor were virtually identical for all axes. In contrast, the X- and Y-axes had smaller geometric tortuosity values than the Z-axis, meaning the geometric tortuosity reduction factor for the X-and Y-axes axes was closer to 1.0 and the resulting M-factors were higher than the Z-axis M-factor. In fact, the Z-axis geometric tortuosity was so high the resulting tortuosity reduction factor was smaller than the

constriction factor, meaning that LLZO tortuosity had a more limiting effect than LLZO bottlenecks when examining the Z-axis. This was particularly concerning given the planar nature of similar cellulose templates means the primary conduction direction of the sintered stacks was along the Z-axis of the microstructure, the least conductive and most resistive direction of the sample based on these results.

Table 4.3: Summary of overall LLZO phase reduction factors of template-based microstructure.

	LLZO Phase Volume Fraction	**Constriction Factor**	**(Characteristic Geometric Tortuosity)$^{-2}$**	**Percolation Factor**	**M-factor**
Overall	0.2102	0.447	0.6395	0.9949	0.060

Table 4.4: Summary of LLZO phase reduction factors for the X-, Y-, and Z-axes of template-based microstructure.

	LLZO Phase Volume Fraction	**Constriction Factor**	**(Geometric Tortuosity)$^{-2}$**	**Percolation Factor**	**M-factor**
X-Axis (average)	0.2102	0.433	0.7937	0.9937	0.072
Y-Axis (average)	0.2102	0.424	0.7414	0.9951	0.069
Z-Axis (average)	0.2102	0.439	0.4187	0.9959	0.042

4.3. Results and Discussion: Pore Phase:

The M-factor of the pore phase was also analyzed to determine if the pores formed a highly connected network easily infiltrated by electrode material.

4.3.1. Geometric Tortuosity:

Figure 4.8a-c shows 3D visualizations of the pore phase cumulative geometric tortuosity calculated along the forward directions of the X-, Y-, and Z-axes for the template-based sample, with arrows denoting the calculation direction. While the solid LLZO phase tortuosity required a tortuosity visualization range of 1.0-2.0 (Figure 4.5), the pore phase tortuosity was significantly lower and thus only required a tortuosity visualization range of 1.0-1.5. The pore phase tortuosity appeared to homogenize more quickly along the X- and Y-axes than the Z-axis, and all axes homogenized faster than the corresponding tortuosity visualizations for the LLZO phase. Similar to the LLZO phase tortuosity, the forward direction for the Z-axis had the highest tortuosity of 1.0588 +/- 0.0474, the forward direction for the Y-axis had a medium tortuosity of 1.0248 +/- 0.0068, and the forward direction for the X-axis had the lowest tortuosity of 1.0226 +/- 0.0063 (Figure 4.8d-f). This pattern persisted when the forward and reverse directions were averaged together, resulting in a direction-averaged Z-axis tortuosity of 1.0570 +/- 0.0454, a Y-axis tortuosity of 1.0250 +/- 0.0070, and an X-axis tortuosity of 1.0225 +/- 0.0064. As observed from the 3D visualizations, the pore phase tortuosity was substantially lower than the LLZO tortuosity for all three axes. The pore phase was also somewhat anisotropic like the LLZO phase, with a low tortuosity XY-plane and a high tortuosity Z-axis. Given the

possibility that any pore collapse would occur preferentially along the Z-axis, this was expected.

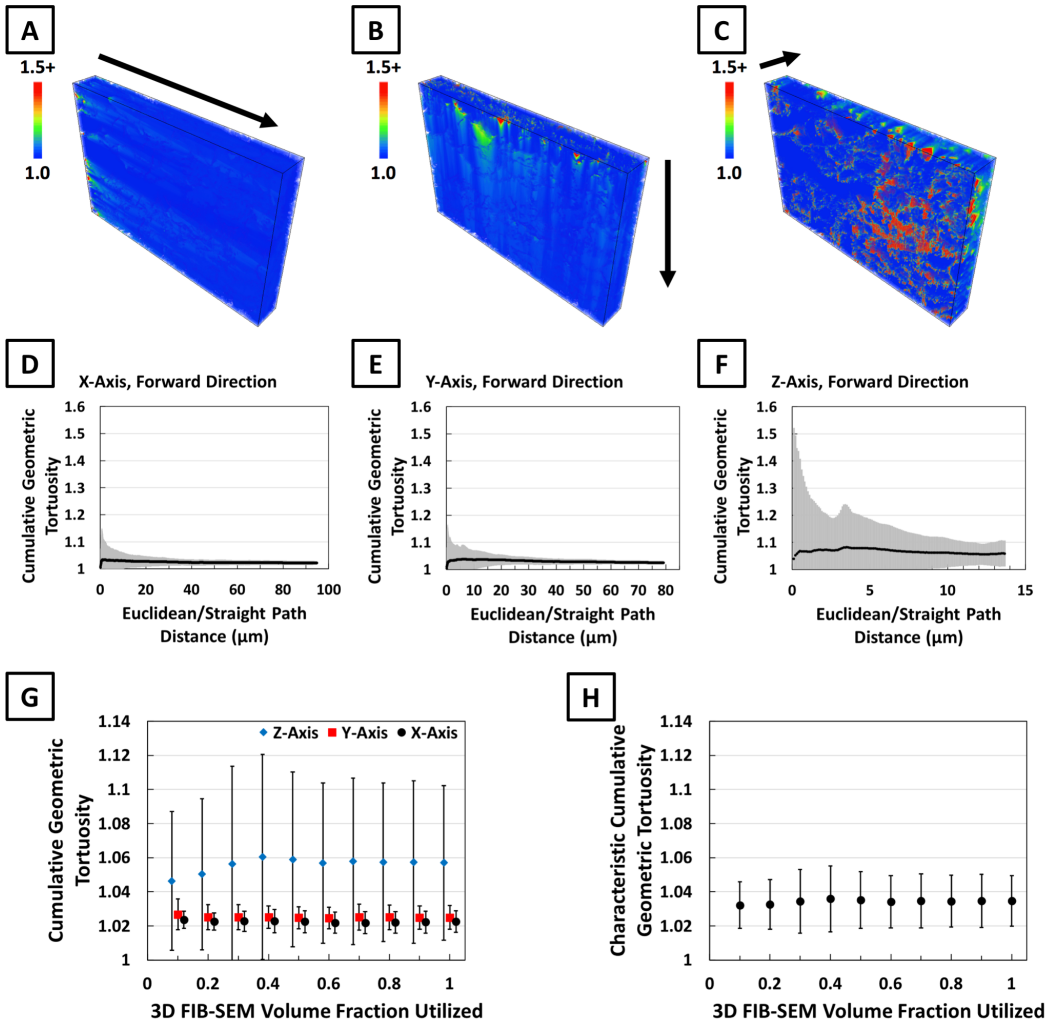

Figure 4.8: 3D visualization of the pore phase cumulative geometric tortuosity along the forward directions for the X-, Y-, and Z-axes of the template-based LLZO sample (A-C). Average pore phase cumulative geometric tortuosity and SD for the forward directions for the X-, Y-, and Z-axes of the template-based LLZO sample (D-F). Average pore phase cumulative geometric tortuosity and SD for the direction-averaged X-, Y-, and Z-axes, as well as overall cumulative tortuosity and SD (G-H).

Sub-volumes ranging from 10% to 90% of the full 3D image volume were extracted and the geometric tortuosity calculations repeated for the pore phase in each sub-volume. Figure 4.8g shows the direction-averaged results for each axis for the template-based LLZO sample. It was expected that significant variability would exist between the small

sub-volumes that transitioned to more consistent values for larger sub-volumes. This behavior was only obvious along the Z-axis, which reached stable values around the 50% sub-volume size. In contrast, the X- and Y-axes showed consistent tortuosity values for all sub-volume sizes. Comparing the 100% volume and the 90% sub-volume tortuosity values, the X-, Y-, and Z-axes showed differences of 0.03%, 0.01%, and 0.04%, respectively. As such, the template-based LLZO image region was deemed as representative of the pore phase in the overall sample. The X-, Y-, and Z-axes direction-averaged geometric tortuosity values were then combined into a single characteristic geometric tortuosity using Equation 2.12.[127] The results were plotted as a function of sub-volume size in Figure 4.8h. The characteristic tortuosity showed significantly less variability compared to the direction-averaged tortuosity values as sub-volume size increased, further supporting the earlier conclusion that the 3D image region was representative.

4.3.2. Percolation Factor:

The pore phase direction-averaged percolation factor for the X-, Y-, and Z-axes were shown for different sub-volume utilization sizes for the template-based LLZO sample (Figure 4.9a). All percolation factors for sub-volumes were above 0.9998, indicating the pore phase was either more connected than the LLZO phase or that the pore phase had fewer isolated/truncated voxels that the LLZO phase. The X-, Y-, and Z-axes direction-averaged percolation factors were averaged into an overall pore phase percolation factor and plotted as a function of sub-volume size in Figure 4.9b. Similar to overall pore phase geometric tortuosity, the overall pore phase percolation factor showed less variability and lower SD values than the direction-averaged percolation factors.

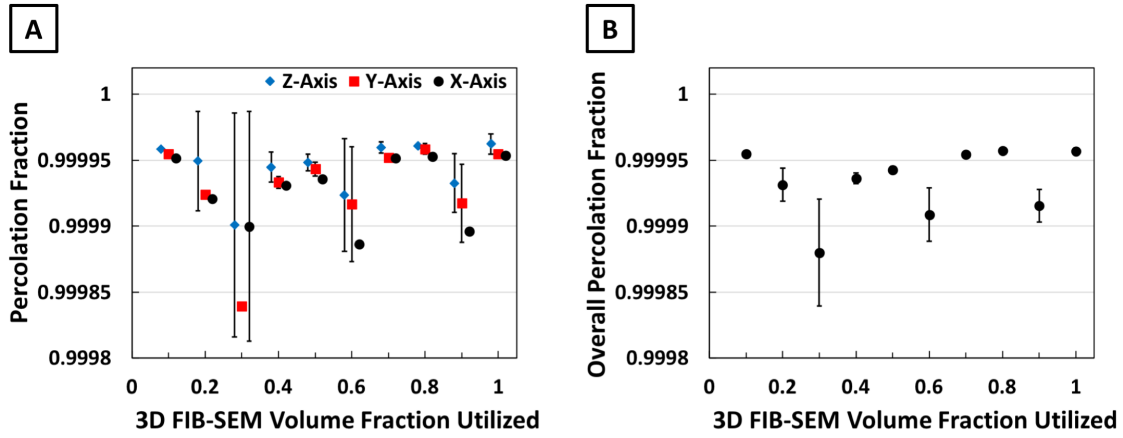

Figure 4.9: A) pore phase percolation factor and SD for the direction-averaged X-, Y-, and Z-axes for the template-based LLZO sample for different sub-volume sizes. B) overall sample percolation factor and SD for sample.

4.3.3. C-PSD, MIP-PSD, and Constriction Factor:

The cumulative coverage fraction c-PSD and average MIP-PSD results for the pore phase in the template-based LLZO sample were plotted together in Figure 4.10a, with the c-PSD results as a solid line and the corresponding MIP-PSD result as dashed lines. Immediately, it was clear the distribution curves extended to much larger sphere diameters than the corresponding curves for the LLZO phase. Moreover, the instantaneous coverage fraction curve for the c-PSD showed a broad peak that smoothly increased and gradually decreased as the test sphere size was increased, in contrast to the very narrow peak in the c-PSD curve for the LLZO phase (Figure 4.10b). The MIP-PSD curve had a similar appearance as the LLZO phase MIP-PSD curve, the only major difference being the corresponding sphere diameter of the peaks.

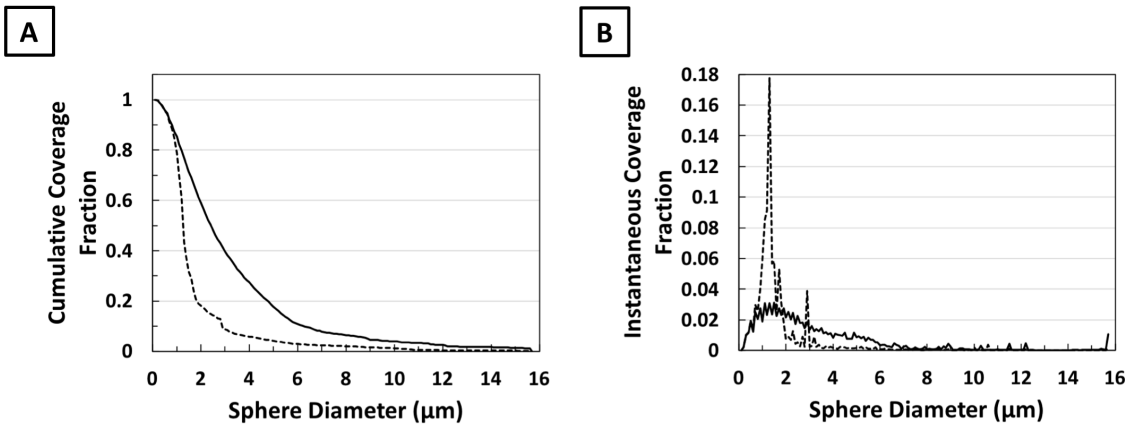

Figure 4.10: A) pore phase c-PSD (solid lines) and average MIP-PSD (dashed lines) for the template-based LLZO sample. B) instantaneous coverage distributions for c-PSD (solid lines) and average MIP-PSD (dashed lines).

Overall, the c-PSD gave a 50% coverage value of 2.417 µm and the MIP-PSD gave a 50% coverage value of 1.262 µm, corresponding to a constriction factor of 0.272. This meant the pore diameters were much larger than the LLZO diameters, but the pores were actually more relatively constricted by bottlenecks than the LLZO. The constriction factor of 0.272 meant that bottlenecks in the pore network would inhibit diffusion by 55.3% overall. Examining the 50% coverage values of the MIP-PSD along the X-, Y-, and Z-axes showed a slight increase in the pore bottleneck diameter from the lowest value of 1.255 µm along the X-axis to the highest value of 1.459 µm along the Z-axis (Table 4.5). As a result, the constriction factors ranged from 0.270 to 0.364, a wider range than displayed by the LLZO constriction factors for those axes. The higher constriction factor along the Z-axis was somewhat surprising given the Z-axis had the highest tortuosity, which should increase the lengths of conduction paths along the Z-axis and increase the effects of bottlenecks.

Table 4.5: Summary of the pore phase 50% PSD Diameter, the 50% MIP-PSD diameters for the X-, Y-, and Z-axes, the overall 50% MIP-PSD diameter, and the resulting constriction factors.

Name	50% PSD Diameter (µm)	50% MIP Diameter (µm)				Constriction Factor			
		X	Y	Z	Overall	X	Y	Z	Overall
Template-based LLZO	2.417	1.255	1.229	1.459	1.262	0.270	0.258	0.364	0.272

4.3.4. M-Factor:

Thus far, this study examined the effects of pore phase fraction, constriction factor, geometric tortuosity, and percolation factor on effective diffusion through the pore network of the template-based LLZO sample. The reduction factors associated with each are summarized in Table 4.6, showing the constriction factor had the greatest reduction effect on effective diffusion, followed by the pore phase fraction and then geometric tortuosity. The percolation factor had almost no effect at all due to the pore network being virtually fully interconnected. The resulting M-factor for the microstructure was calculated using Equation 1.3 and was found to be 0.201, indicating effective diffusion through the pore network of the template-based LLZO sample was 79.9% reduced. Due to the clear anisotropy of the template-based porous network, it was necessary to examine these same reduction factors for each axis, the results of which were summarized in Table 4.7. Comparing the different axes, the percolation factor was virtually identical for all axes. In contrast, the X- and Y-axes had smaller geometric tortuosity values than the Z-axis, meaning the geometric tortuosity reduction factor for the X-and Y-axes axes was closer to 1.0 and the resulting M-factors were higher than the Z-axis M-factor. This made sense given the cellulose template was preferentially oriented along the X-Y plane. At the same time, the X- and Y-axes had smaller constriction factors than the Z-axis, indicating bottlenecks were not uniformly distributed throughout the microstructure and more

obstructing within the X-Y plane. This was surprising given the straighter paths in the X-Y plane would be expected to increase bottleneck size relative to the feature size, and thus increase the constriction factor within the low tortuosity X-Y plane relative to the higher tortuosity Z-axis.

Table 4.6: Summary of overall pore phase reduction factors of template-based microstructure.

	Pore Phase Volume Fraction	**Constriction Factor**	**(Characteristic Geometric Tortuosity)$^{-2}$**	**Percolation Factor**	**M-factor**
Overall	0.7898	0.272	0.9342	1.0000	0.201

Table 4.7: Summary of pore phase reduction factors for the X-, Y-, and Z-axes of template-based microstructure.

	LLZO Phase Volume Fraction	**Constriction Factor**	**(Geometric Tortuosity)$^{-2}$**	**Percolation Factor**	**M-factor**
X-Axis (average)	0.7898	0.270	0.9565	1.0000	0.204
Y-Axis (average)	0.7898	0.258	0.9518	1.0000	0.194
Z-Axis (average)	0.7898	0.364	0.8950	1.0000	0.258

4.4. Implications for Batteries Utilizing Bilayer/Trilayer Garnet Electrolytes:

3D FIB Tomography was used to examine a template-based porous LLZO microstructure that was ~79% porosity, with the results of the LLZO and pore phases summarized in Table 4.8. The LLZO M-factor was 0.060 and the corresponding pore phase M-factor was 0.201, suggesting effective ionic conductivity of the LLZO structure was significantly reduced and diffusion through the pore network moderately obstructed. The LLZO microstructure was primarily limited by the low LLZO volume fraction, while the pore phase was primarily limited by bottlenecks resulting in a low constriction factor. Given the average pore feature and bottleneck sizes were significantly larger than the average LLZO features and bottleneck sizes, it was surprising the pore phase constriction factor was still much lower than the LLZO constriction factor. In contrast, the much lower tortuosity of the pore phase resulted in a tortuosity reduction factor much closer to 1.0 when compared to the LLZO phase.

Comparing the template-based LLZO sample results to the results for the tape-cast LLCZN samples, the template-based LLZO sample was by far the most porous microstructure examined. The tape-cast sample with the closest porosity to the template-based LLZO sample was the Porous 2 sample (56.67% porosity). The LLZO M-factor of the template-based LLZO sample was lower than the LLCZN M-factor of the Porous 2 sample due to the lower LLZO volume fraction of the template-based LLZO sample. However, the pore phase M-factor of the template-based LLZO sample was also lower than the pore phase M-factor of the Porous 2 sample, despite the template-based LLZO sample having a higher pore phase volume fraction. Examining Tables 3.4 and 4.8, the second biggest difference between the pore phases of the template-based LLZO sample and the

tape-cast Porous 2 sample was the Porous 2 sample pore phase had a much higher constriction factor. The tortuosity reduction factors being comparable resulted in the higher pore phase M-factor for the tape-cast Porous 2 sample. Still, constriction was the most significant obstacle to high M-factors in both electrolyte and pore phases of all samples examined. Based on these results, significant improvements are possible in electrolyte and pore phase performance if bottleneck sizes were increased relative to the feature sizes. Barring that, a microstructure with porosity between the Porous 1 sample (56.67% porosity) and the Porous 2 sample (40.58% porosity) would likely give similar M-factors for the solid-state electrolyte and the pore phase, a possibly ideal compromise between electrolyte effective conductivity and electrode infiltration/loading capacity.

Table 4.8: Summary of microstructural parameters for the LLZO phase and pore phase of the template-based LLZO.

	LLZO	**Pore**
M-factor	0.060	0.201
Phase Volume Fraction	0.2102	0.7898
Characteristic Geometric Tortuosity	1.2505	1.0346
(Characteristic Geometric Tortuosity)$^{-2}$	0.6395	0.9342
Percolation Factor	0.9949	1.0000
Average feature size (µm)	0.634	2.417
Average bottleneck size (µm)	0.424	1.262
Constriction Factor	0.447	0.272

5. Modeling Electrochemical Performance of 3D Microstructures:

Analyzing the M-factors and other structural parameters of the FIB Tomography microstructures identified that increasing microstructure porosity moderately improved electrode infiltration and loading while drastically decreasing electrolyte effective conductivity, thus increasing the overall porous layer ASR. As such, the best microstructure likely required an intermediate porosity (~45-50%) to balance the design goals of achieving a low ASR electrolyte and a high loading capacity pore network. Fortunately, the M-factor analysis of the solid-state electrolyte phase represented the highest ASR scenario for an operational battery, where electrodes remained at the external surfaces of the porous layer and Li-ions were transported across the entire porous microstructure. In a real battery, the electrode material is infiltrated into the pores and allows Li-ions to transport into/out of the garnet at all points on the electrode-electrolyte interface, so Li-ions only traverse fractions of the porous layer to reach the opposing electrode. This suggested the M-factor analysis would underestimate the actual effective ionic conductivity of the electrode-infiltrated electrolyte and thus overestimate the negative effects of the 3D porous microstructure on battery operation.

To determine the optimal porous microstructure for battery operation, we simulated the electric fields and charge transport through bilayer symmetric cells made of a dense layer digitally attached to the 3D FIB Tomography porous microstructures, with attached/infiltrated Li-metal electrodes. Similar approaches using 3D reconstructions and simulating the operational conditions of batteries successfully provided insight into the limitations faced by electrode materials in batteries utilizing liquid organic electrolytes.[148–150] Simulations of the bilayer symmetric cells should also provide a good understanding of

how the porous solid-state electrolyte microstructures would perform in real battery conditions.

5.1. Calculation Approach – Finite Difference Method:

5.1.1. Updating Individual Voxels:

The following derivation was adapted from Electromagnetic Fields and Energy by Haus and Melcher.[151] To calculate the static electric potential across a homogenous 3D electrolyte microstructure with an arbitrary surface, electrodes that applied fixed boundary potentials and acted as sources/sinks for current, and insulating surfaces that prevented current from entering/exiting the electrolyte, the Laplace equation was solved for all 3D voxels in the microstructure:

$$\nabla \cdot \vec{J} = \nabla \cdot \sigma \vec{E} = 0 \tag{5.1}$$

In Equation 5.1, the divergence of the 3D current density vector "J" or the divergence of the product of the electrolyte conductivity "σ" and the 3D electric field vector "*E*" must equal 0. Physically, this meant no sources/sinks for current density/electric field were present within the region being examined, so all current density/electric field entering the region must also exit the region. Since the 3D FIB Tomography microstructures were split into discrete voxels and only the electrodes were sources/sinks for current density, this meant the current density/electric field entering any electrolyte voxel must equal the amount exiting the voxel. Since the 3D electrolyte microstructure should be homogenous, this meant the electrolyte conductivity was uniform and could be eliminated from Equation 5.1 to yield a simpler version in Equation 5.2:

$$\nabla \cdot \vec{E} = 0 \tag{5.2}$$

This study focused on the static electric potential, meaning no time-varying fields were present and thus the electric field "E" was solely determined by the negative gradient of the scalar electric potential "φ":

$$\vec{\mathrm{E}} = -\nabla\varphi \tag{5.3}$$

Combining equations 5.2 and 5.3, we were left with the electric potential version of the Laplace equation:

$$\nabla^2\varphi = 0 \tag{5.4}$$

The term "$\nabla^2\varphi$" for a 3D microstructure composed of discrete voxels took on the following form when examining an arbitrary direction:

$$\nabla^2\varphi(x_0) = \frac{\varphi(x+1)+\varphi(x-1)-2\varphi(x_0)}{{l_x}^2} = \sum\frac{\varphi(x_i)-\varphi(x_0)}{{l_x}^2} \tag{5.5}$$

Extending this to include all three directions:

$$\begin{aligned}\nabla^2\varphi(x_0,y_0,z_0) = &\sum\frac{\varphi(x_i,y_0,z_0)-\varphi(x_0,y_0,z_0)}{{l_x}^2}\\ &+\sum\frac{\varphi(x_0,y_i,z_0)-\varphi(x_0,y_0,z_0)}{{l_y}^2}\\ &+\sum\frac{\varphi(x_0,y_0,z_i)-\varphi(x_0,y_0,z_0)}{{l_z}^2}\end{aligned} \tag{5.6}$$

To simplify the notation, this was rewritten as:

$$\nabla^2\varphi(x_0,y_0,z_0) = \sum\frac{\varphi_i-\varphi(x_0,y_0,z_0)}{{l_i}^2} = \sum\frac{\varphi_i}{{l_i}^2} - \varphi(x_0,y_0,z_0)\sum\frac{1}{{l_i}^2} \tag{5.7}$$

Equation 5.7 was valid when the nearest neighbors of a given voxel were either electrolyte or part of the electrodes with fixed potential. When one or more of the nearest neighbors are part of an insulating region/material, an additional boundary condition was necessary to prevent current from crossing the interface and flowing out of the electrolyte into the insulator:

$$\vec{n}\cdot\vec{J} = 0 \tag{5.8}$$

Here, “n” was the unit vector normal to the electrolyte microstructure surface that was considered insulated. The purpose of Equation 5.8 was to eliminate any components of the current density vector that would cause current to flow into the insulator. This type of condition was necessary in two cases: 1) at the parts of the 3D microstructure that intercepted the boundaries of the box enclosing the 3D reconstruction (considered insulating when periodic boundaries were not in use) and 2) when parts of the electrolyte surface were deliberately assigned to be insulating/next to insulating materials. Using previously discussed substitutions, Equation 5.8 became:

$$\vec{n} \cdot \nabla\varphi = 011 \tag{5.9}$$

This showed the gradient of the electric potential was parallel to “n” (i.e., normal to the insulating surface) must be forced to become 0, and the gradient perpendicular to “n” (i.e. parallel to the insulating surface) was left unchanged. Fortunately, implementing the insulating surface condition was fairly straightforward. To eliminate the gradient between the chosen electrolyte voxel and the neighboring voxel across the insulating surface, the neighboring voxel was given the same potential as the chosen electrolyte voxel. Looking back at the expanded expression for “$\nabla^2\varphi$” in Equation 5.6, making this change caused any of the six directions in the sum that involve an insulating neighbor to become 0. This was mathematically equivalent to adjusting the sum to exclude any of the six directions involving an insulating neighbor. With the insulating boundary condition properly accounted for, we used Equation 5.7 to solve the Laplace equation and arrive at Equation 5.10, the update condition for the electric potential of any electrolyte voxel in the 3D electrolyte microstructure:

$$\varphi(x_0, y_0, z_0) = \left. \sum \frac{\varphi_i}{{l_i}^2} \middle/ \sum \frac{1}{{l_i}^2} \right. \tag{5.10}$$

From Equation 5.10, it was clear the update condition changed the potential of the chosen electrolyte voxel to the average of the potentials of the neighboring voxels weighted by the square of the inverse of the distances between the voxels. In theory, Equation 5.10 could sequentially "scan" across the entire 3D microstructure, update the electric potential of all voxels, and then repeat this process until the calculated changes to the potential distribution fell below a user-defined relative threshold. In practice, this approach was extraordinarily slow because the true distribution was determined by the global boundary conditions of the 3D microstructure, while Equation 5.10 only examined the immediate local conditions of each voxel. As such, it would require an extremely long time for the effects of the boundary conditions to be propagated throughout the microstructure and converge the overall potential distribution to the true distribution.

5.1.2. Updating Blocks of Voxels Simultaneously:

A more efficient approach was to update the potentials of many voxels simultaneously. To do this, Equation 5.7 was rearranged to give it the following form:

$$\varphi(x_0, y_0, z_0) \sum \frac{1}{{l_i}^2} - \sum \frac{\varphi_i}{{l_i}^2} = 0 \tag{5.11}$$

Then the 2nd summation was separated to distinguish between neighbors that were part of the electrolyte and thus had potentials that needed updating ($\varphi_{i,update}$), and neighbors that were part of the electrode and thus had potentials that were fixed boundary conditions

($\varphi_{i,boundary}$). Moving the boundary condition terms to the opposite side of the equals sign yields Equation 5.12:

$$\varphi(x_0, y_0, z_0) \sum \frac{1}{{l_i}^2} - \sum \frac{\varphi_{i,update}}{{l_i}^2} = \sum \frac{\varphi_{i,boundary}}{{l_i}^2} \tag{5.12}$$

Considering the entire 3D microstructure, there was a version of Equation 5.12 for every voxel to be updated and thus many repeated references to each updatable voxel. All those equations must be solved in order to determine the true electric potential distribution of the microstructure, so this constituted a problem described by a set of linear equations. To solve this problem required defining the column vector "Φ" as the list of the potentials of all updatable voxels in the 3D microstructure; the column vector "b" as the list of the boundary condition values of the right side of Equation 5.12 associated with each voxel in vector "Φ" (a given term in vector "b" had a value of 0 if the corresponding term in vector "Φ" had no neighbors that were part of the electrode); and the square matrix "M" as the mathematical object that encoded the relationships on the left side of Equation 5.12 for all updatable voxels. This yielded the following linear equation:

$$\widehat{M}\overrightarrow{\Phi} = \vec{b} \tag{5.13}$$

In this form, Equation 5.13 described the Laplace equation relationships between all electrolyte voxels, the Laplace equation relationships with the fixed potential electrodes, and accounted for any insulating surfaces present. Solving Equation 5.13 for "Φ" produces the true electric potential distribution for the entire 3D electrolyte microstructure with the chosen boundary conditions. Ideally, Equation 5.13 would be solved in one calculation covering all the electrolyte voxels present in the 3D microstructure. However, if there are N electrolyte voxels to be updated, then the matrix "M" was NxN and thus had N^2 entries, which was often too many entries to be stored simultaneously in computer memory. A

typical way to overcome this limitation was to isolate blocks of the 3D microstructure, treating nearest neighbors of perimeter electrolyte voxels as fixed boundary conditions in addition to any global boundary voxels present in the block (electrode, insulating surface), iteratively solve Equation 5.13 for all updatable voxels in the block until block convergence was achieved, then repeat for blocks of the rest of the microstructure until global convergence was achieved. Once the true potential distribution was calculated, the potential was analyzed for a variety of relevant electrical properties, such as the local current/current density, the interfacial current/current density, the total battery current/current density, the total battery resistance/ASR, and the total battery overpotential.

5.2. Simulation of 3D FIB Tomography Microstructures – Results and Discussion:

Figure 5.1 shows 3D reconstructions of the template-based LLZO garnet porous microstructure and four different tape-cast LLCZN garnet porous microstructures, in order of decreasing porosity. As previously discussed, the template-based LLZO microstructure was composed of thin garnet membranes between large diameter pores, while the tape-cast LLCZN microstructure had comparatively large garnet particles and much smaller pores. The differences stemmed from using an existing structure for the garnet (the template-based LLZO) vs. building the structure using a random distribution of pore former spheres (the tape-cast LLCZN). The variety of microstructures and porosity made this group of samples a good test case for studying porous solid-state electrolytes.

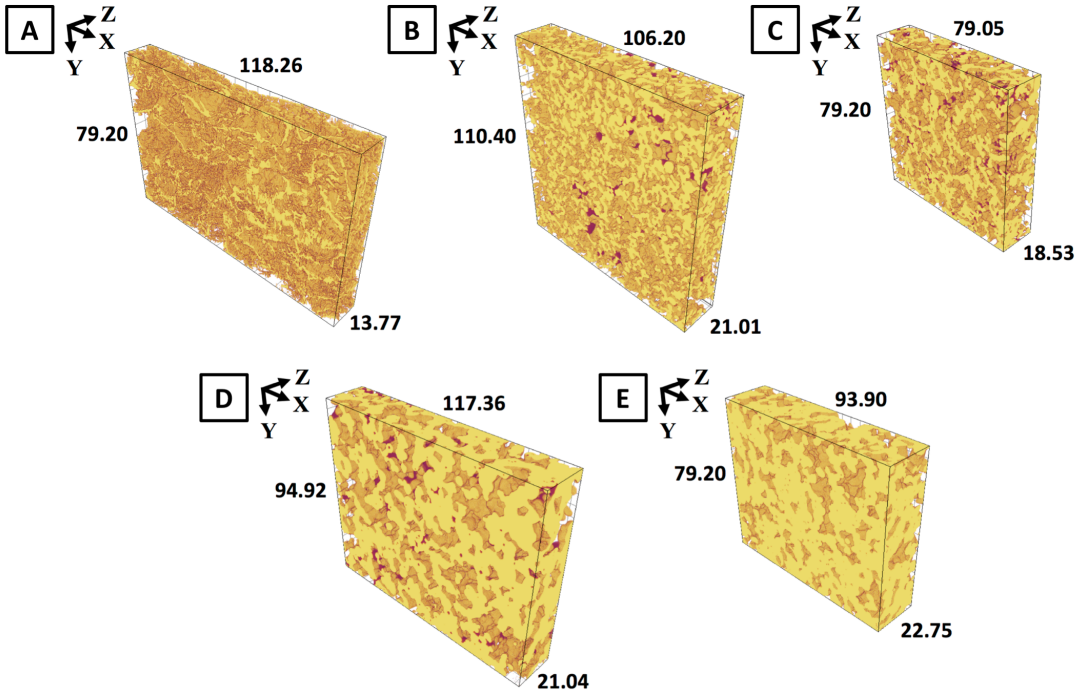

Figure 5.1: 3D reconstructions of A) template-based porous garnet ("Template"), and tape-cast porous garnet B) "Porous 1"; C) "Trilayer 1"; D) "Porous 2"; and E) "Porous 3". Garnet phase was yellow and secondary phase was red. The microstructures were in order of decreasing porosity. Reconstruction dimensions were in μm.

5.2.1. 3D Visualization of Simulation Results:

Using the 3D FIB Tomography microstructures as porous layers, we digitally created dense-porous bilayer symmetric cells by attaching a 5 µm thick dense layer to the porous layer, shown in Figure 5.2. The garnet electrolyte was shown in yellow, the pore space was filled with the positive electrode (red color), and a thin negative electrode (blue color) was attached to the planar surface of the dense layer. To focus on the garnet microstructure for these bilayers, any secondary phase was replaced by pore space. The electrodes were considered to be Li-metal, and since the electronic conductivity of Li-metal was many orders of magnitude higher than the ionic conductivity of garnet, the Li-metal electrodes were assumed to have uniform electric potentials identical to the potential of the corresponding current collector (grey color).

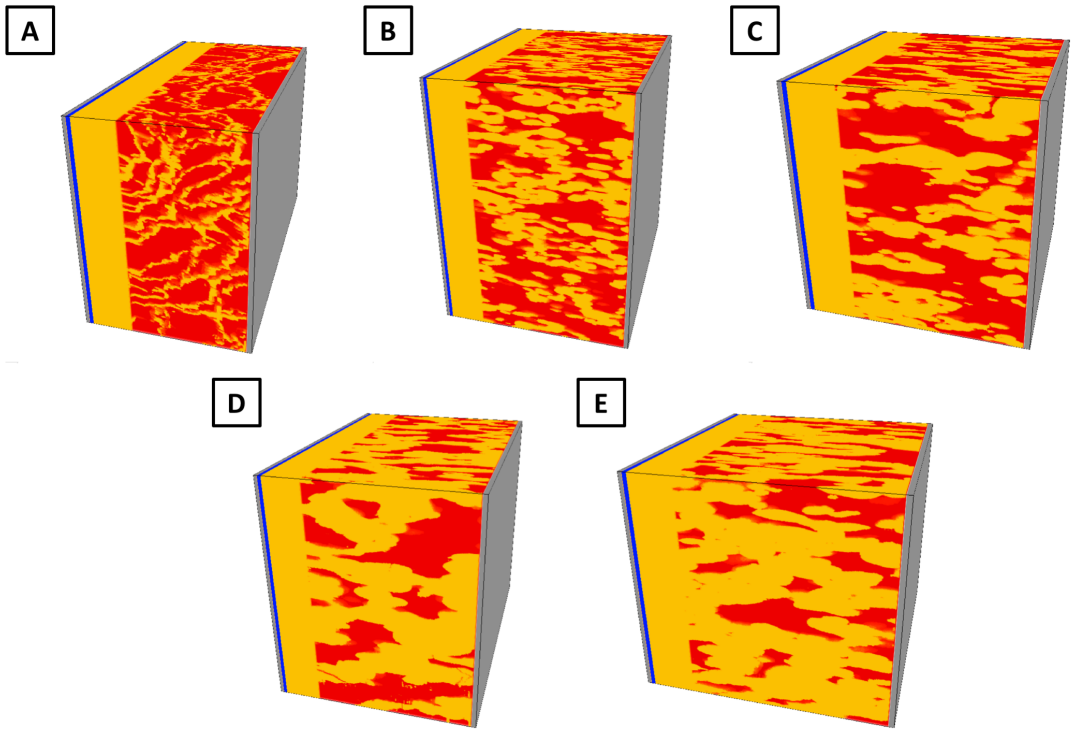

Figure 5.2: Schematic of FIB Tomography bilayer symmetric cells, created using of A) the Template microstructure, B) the Porous 1 microstructure; C) the Trilayer 1 microstructure; D) the Porous 2 microstructure; and E) the Porous 3 microstructure. The garnet electrolyte was yellow, the positive Li-metal electrode was red, the negative Li-metal electrode was blue, and the current collectors were grey. All visualizations were stretched by 3x along the Z-axis.

A potential difference of 1.0 V was applied across the bilayer (+0.5 V at the positive electrode, -0.5 V at the negative electrode), and the potential was iteratively relaxed until the desired level of convergence was achieved. Insulating boundary conditions were applied at the six planar boundaries around the region containing the bilayer structure. The details of the MATLAB implementation are given in Appendix F. Due to the large dimensions of the bilayers, the bilayers were divided into a number of overlapping sections and the set of sections along the "forward" direction (dense layer to porous layer) and along the "reverse" direction (porous layer to dense layer) were sequentially converged during each iteration. Figure 5.3 shows 3D visualizations of the simulated equilibrium potential distribution for the bilayers. Examining the distributions, the entire porous layer in each bilayer had the same potential of +0.5 V (white color) as the positive electrode, with only the dense layer showing any significant variation. The very high porosity Template bilayer (78.98% porosity) was the best example of this behavior. However, as the bilayer porosity decreased, more variation was observed in the electric potential in the dense layer. Examining the high porosity Porous 1 bilayer (56.67% porosity) and Trilayer 1 bilayer (56.03% porosity), the red region of the electric potential (~ 0.27-0.35 V) noticeably expanded towards locations on the dense layer surface that interfaced with the porous layer garnet. In the medium porosity Porous 2 bilayer (40.58% porosity), the red region of the electric potential expanded all the way to the dense layer surface and into parts of the porous garnet. This expansion into the porous layer was most extreme for the low porosity Porous 3 bilayer (26.45% porosity), where even the underlying electric potential within the dense layer was warped.

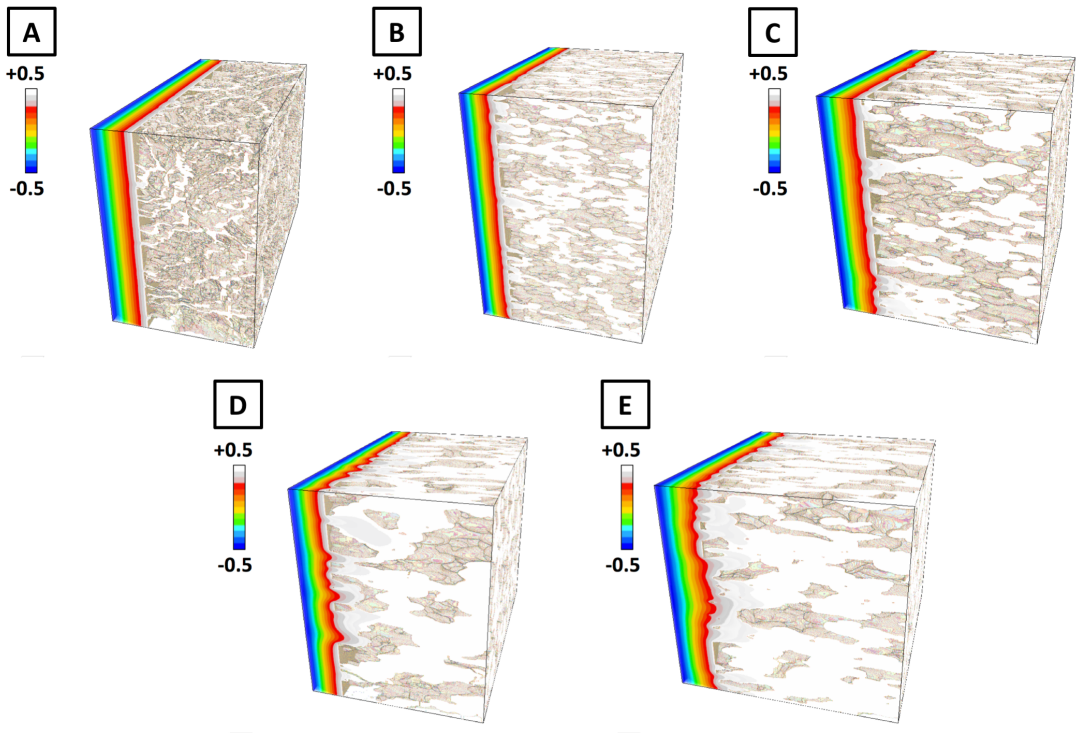

Figure 5.3: Simulated equilibrium electric potentials for bilayers created using of A) the Template microstructure, B) the Porous 1 microstructure; C) the Trilayer 1 microstructure; D) the Porous 2 microstructure; and E) the Porous 3 microstructure. Units are in Volts. All visualizations were stretched by 3x along the Z-direction.

The local electric field strength in the bilayers was calculated from the equilibrium electric potential distribution and the 3D visualizations of the results shown in Figure 5.4. The color bar scale units were in Volts/µm and ranged from 0 (blue) to the maximum cutoff of 150% of the average electric field strength at the negative Li electrode (white). This cutoff level ensured the average electric field strength at the dense layer-negative electrode interface always appeared red. As expected from the visible gradients in the electric potential distributions, the electric field strength was high in the dense layer (shown in red) and 0 in the majority of the porous layer (shown in blue). However, a small transition region was observed in the porous layer near the dense layer that transitioned from the high field strength of the dense layer to the 0-field strength of the rest of the porous garnet. Similar to the bilayer electric potential, the electric field distributions became more

complicated as the bilayer porosity decreased. Comparing the very high porosity Template bilayer (Figure 5.4a) to the high porosity Porous 1 and Trilayer 1 bilayers (Figure 5.4b, c), the reduced porosity caused the electric field transition region to extend further into the porous garnet. Moreover, the electric field strength decreased in the dense layer beneath the dense-porous garnet interfaces, and the electric field strength increased at the dense layer-electrode interfaces. In the medium porosity Porous 2 bilayer (Figure 5.4d), the electric field transition region extended even further into the porous garnet and large sections of the dense layer now had higher electric field strengths (white color) than the average field strength in the dense layer-negative electrode interface (red color). Interestingly, the low porosity Porous 3 bilayer (Figure 5.4e) looked very similar to the Porous 2 bilayer, in direct opposition to the expectation that the lower porosity would create even more extreme variations in the electric field distribution. Since current density was proportional to electric field strength, the electric field distributions showed that all the bilayers had high current density flowing through the dense layer and no current density flowing through the majority of the porous layer, with a thin transition region in the porous layer near the dense layer. These current density distributions resulted from the infiltration of the Li-metal electrodes into the pores. This infiltration allowed current to flow through the majority of the porous layer thickness as electronic current via the extremely high conductivity Li-metal, instead of ionic current via the comparatively low conductivity porous garnet. Near the dense layer, the electronic current quickly transformed to ionic current, as indicated by the transition region in the electric field strength distribution. This transformation created regions of very high current density, or “hot spots,” in the bilayer microstructure.

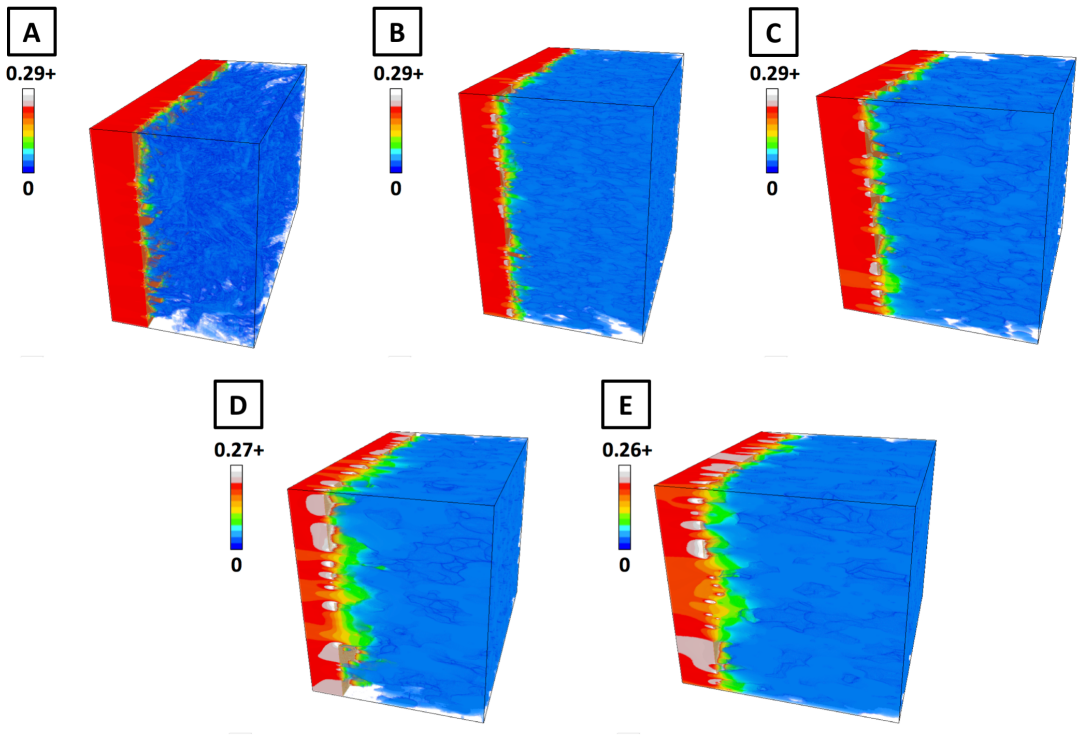

Figure 5.4: Simulated equilibrium electric fields for bilayers created using of A) the Template microstructure, B) the Porous 1 microstructure; C) the Trilayer 1 microstructure; D) the Porous 2 microstructure; and E) the Porous 3 microstructure. Units are in Volts/μm. The maximum cutoff of the color bar was set to 150% of the average electric field strength at the dense layer-negative electrode interface. All visualizations were stretched by 3x along the Z-direction.

5.2.2. Analysis of 2D Cross-Sections from 3D Visualization:

Given the potential consequences of high current density "hot spots" in a battery, further study was warranted on how the current density varied within the interior of the dense garnet and the porous garnet near the dense-porous interface. The magnitude of the ionic current density entering each voxel was calculated based on local electric field strength and a garnet intrinsic conductivity of 5×10^{-4} S/cm (well within the range of conductivities reported for LLZO-based garnets). Since real batteries and symmetric cells operate under fixed current conditions, the bilayer ionic current density distribution was normalized to give an average current density of 1 mA/cm^2 at the negative electrode/current collectors. Figures 5.5, 5.6, 5.7, 5.8, and 5.9 show the normalized ionic current density for

2D cross-sections of the dense layer at the dense-porous interface and the porous layer at distances of ~0.1 µm to ~0.5 µm from the dense layer for the Template, Porous 1, Trilayer 1, Porous 2, and Porous 3 bilayers, respectively. The porous layer cross-section ~0.1 µm from the dense layer was in direct contact with the dense layer. The color bar used has a maximum cutoff value of 1.5 mA/cm^2.

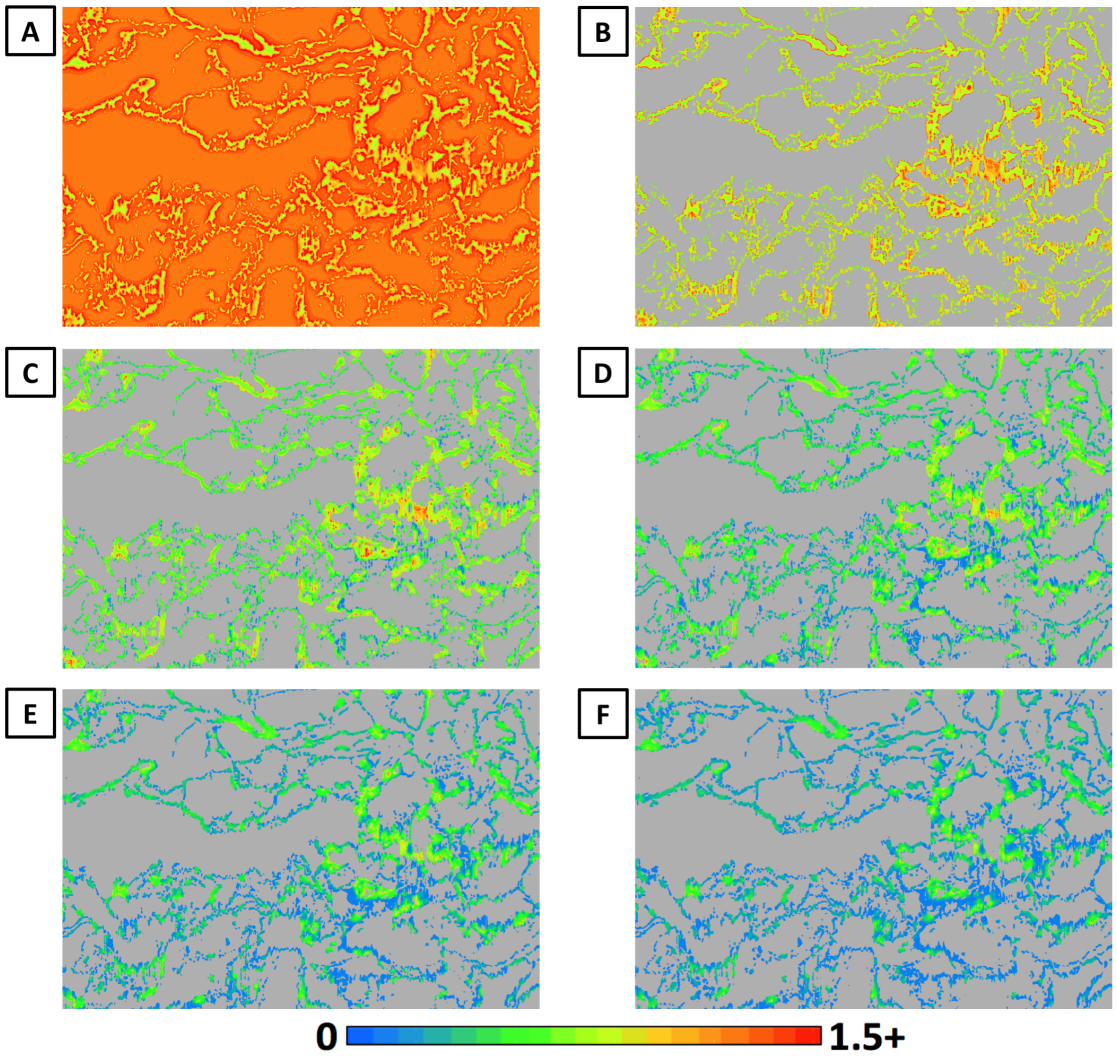

Figure 5.5: 2D cross-sections of normalized ionic current density in the Template bilayer at A) the dense-porous interface, and in the porous layer at distances of B) ~0.1µm, C) ~0.2 µm, D) ~0.3 µm, E) ~0.4 µm, and F) ~0.5 µm from the dense layer. Ionic current density was normalized to give 1.0 mA/cm2 at the negative electrode/current collectors.

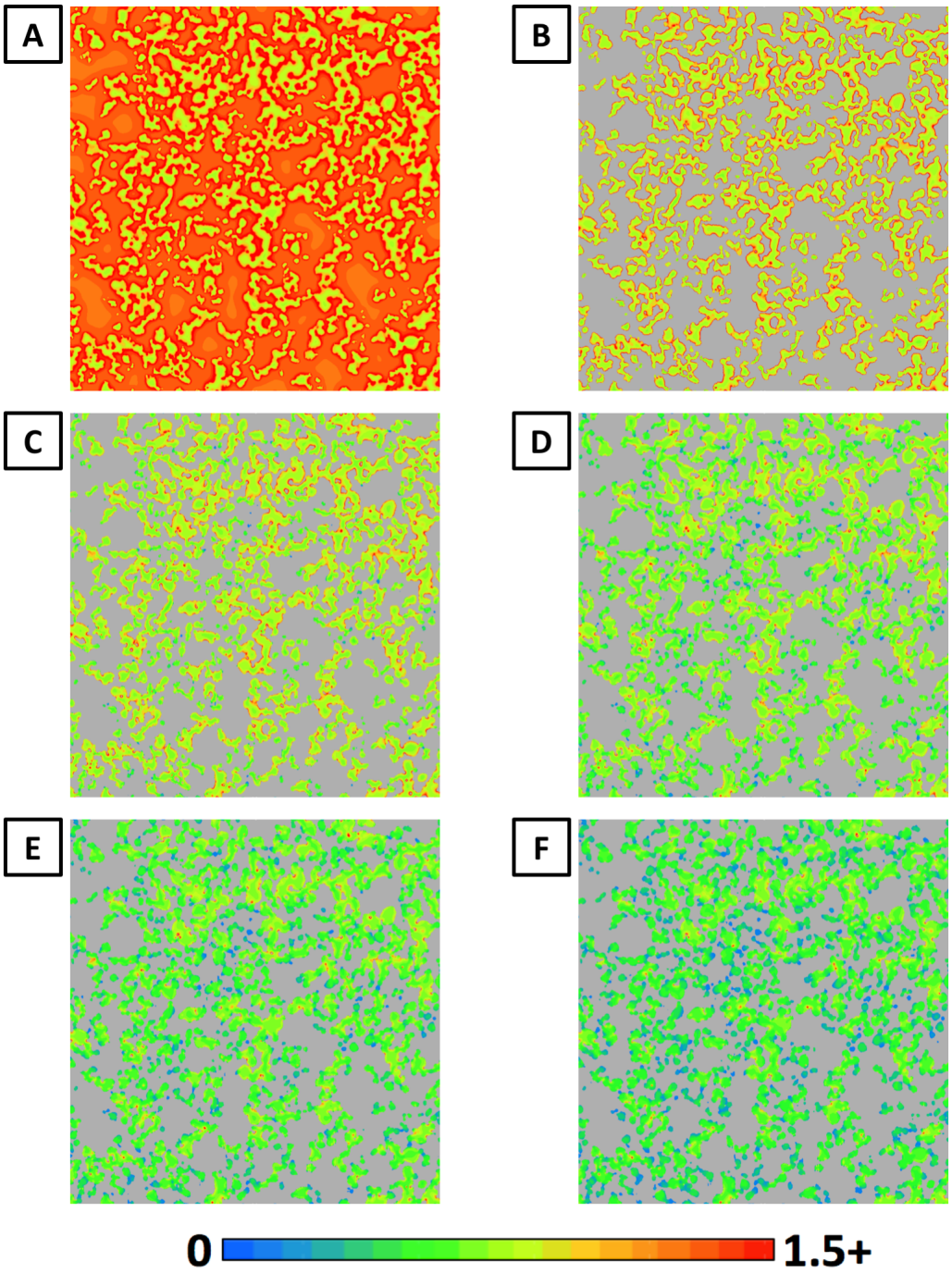

Figure 5.6: 2D cross-sections of normalized ionic current density in the Porous 1 bilayer at A) the dense-porous interface, and in the porous layer at distances of B) ~0.1µm, C) ~0.2 µm, D) ~0.3 µm, E) ~0.4 µm, and F) ~0.5 µm from the dense layer. Ionic current density was normalized to give 1.0 mA/cm2 at the negative electrode/current collectors.

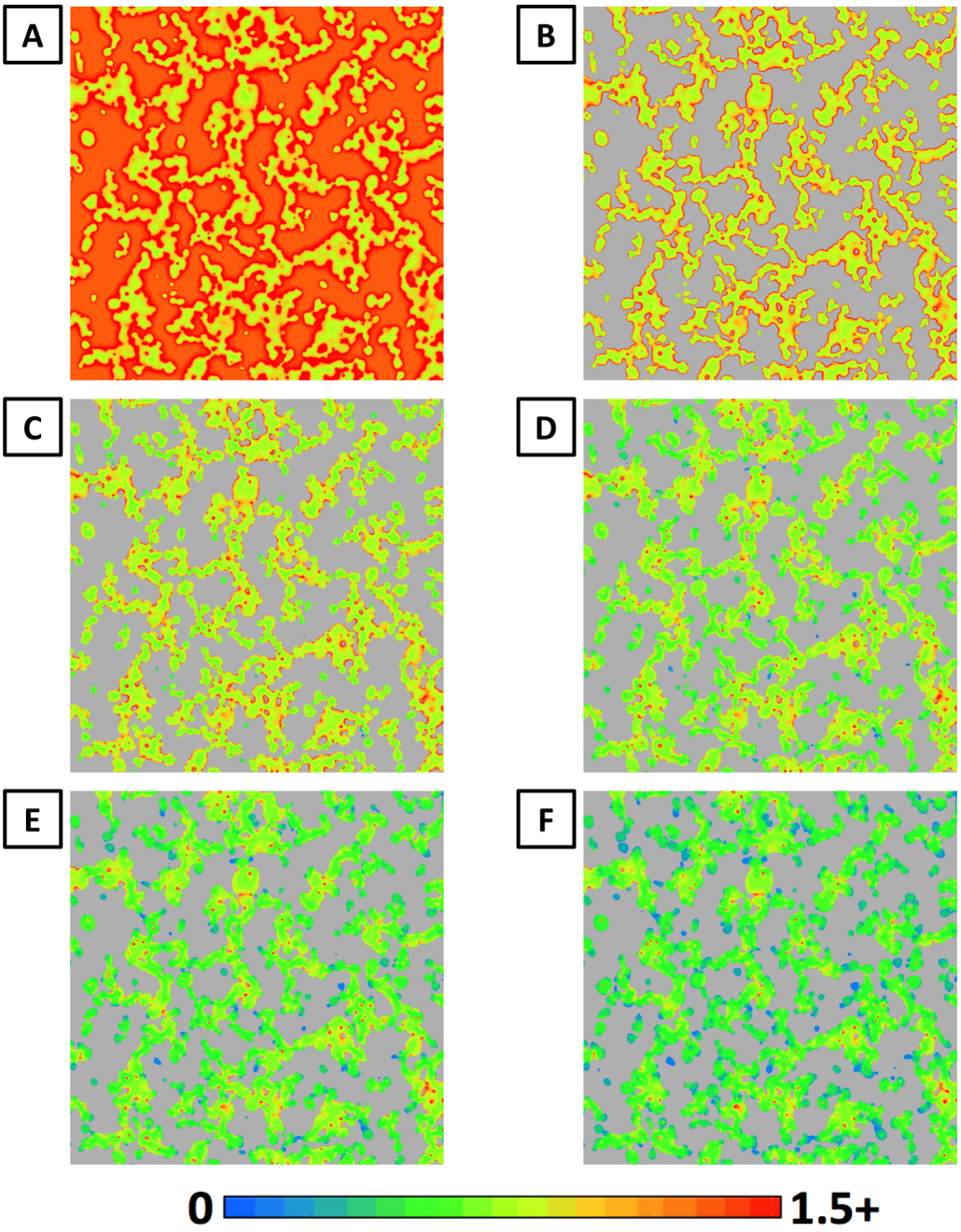

Figure 5.7: 2D cross-sections of normalized ionic current density in the Trilayer 1 bilayer at A) the dense-porous interface, and in the porous layer at distances of B) ~0.1µm, C) ~0.2 µm, D) ~0.3 µm, E) ~0.4 µm, and F) ~0.5 µm from the dense layer. Ionic current density was normalized to give 1.0 mA/cm2 at the negative electrode/current collectors.

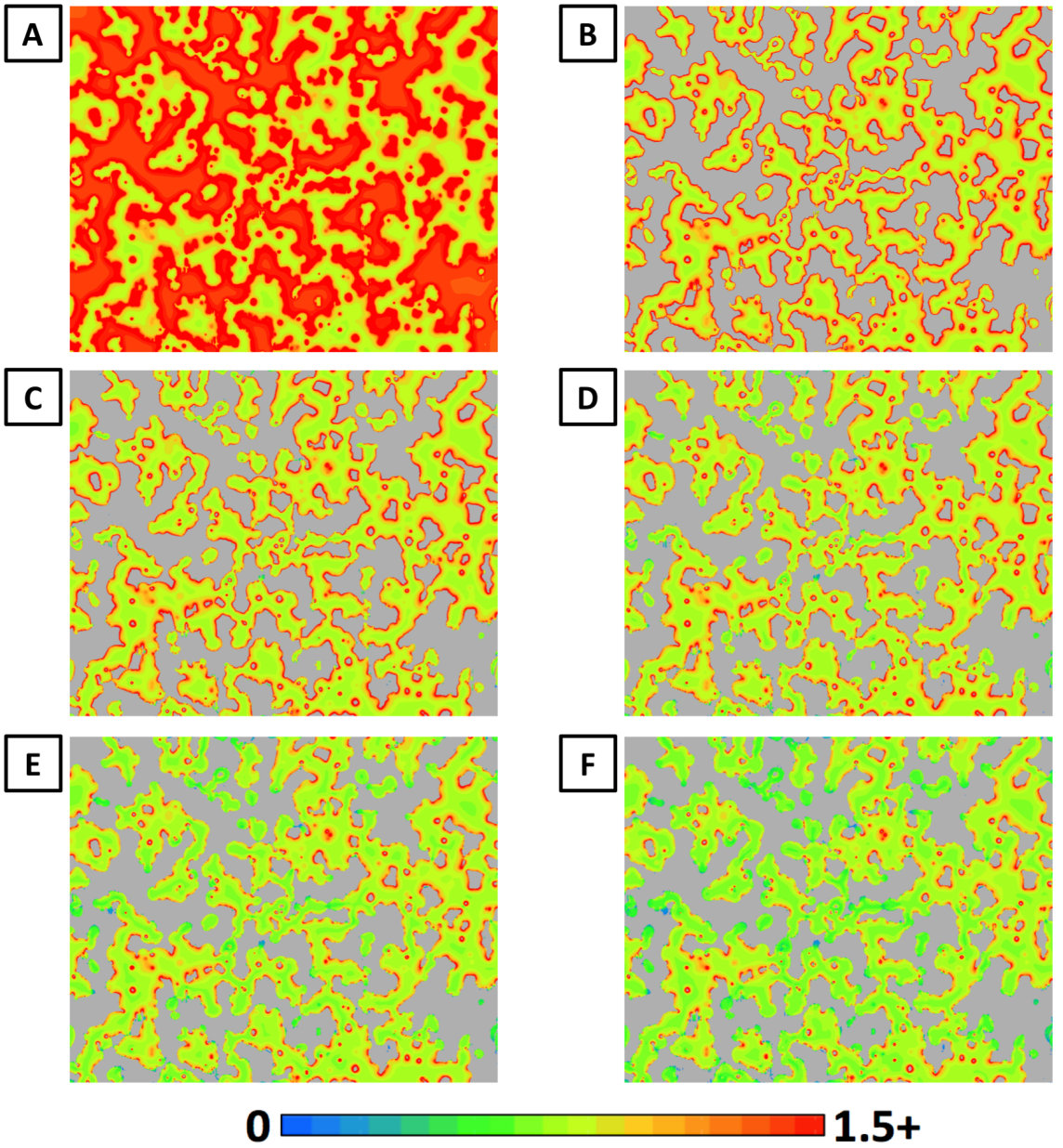

Figure 5.8: 2D cross-sections of normalized ionic current density in the Porous 2 bilayer at A) the dense-porous interface, and in the porous layer at distances of B) ~0.1µm, C) ~0.2 µm, D) ~0.3 µm, E) ~0.4 µm, and F) ~0.5 µm from the dense layer. Ionic current density was normalized to give 1.0 mA/cm2 at the negative electrode/current collectors.

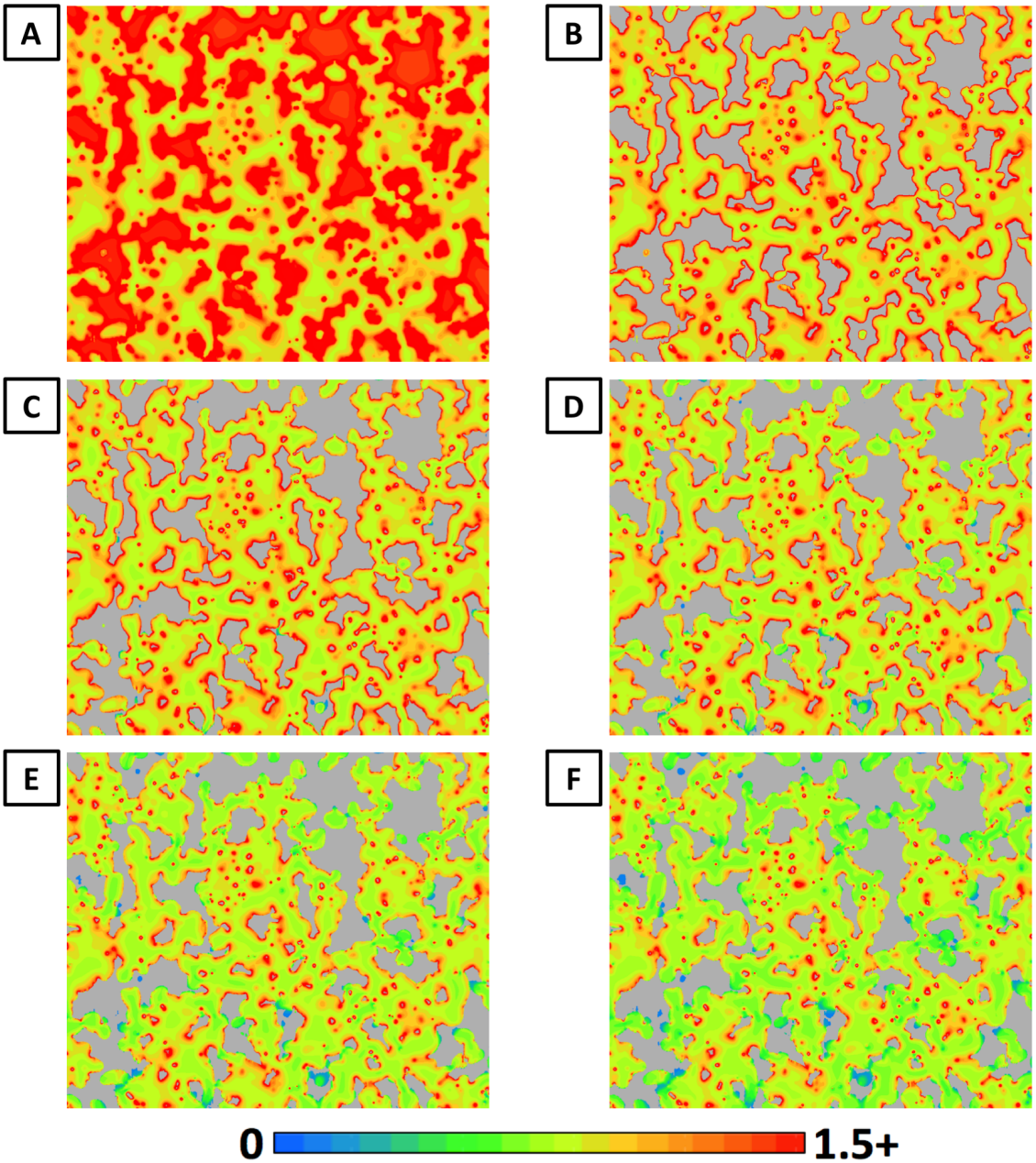

Figure 5.9: 2D cross-sections of normalized ionic current density in the Porous 3 bilayer at A) the dense-porous interface, and in the porous layer at distances of B) ~0.1µm, C) ~0.2 µm, D) ~0.3 µm, E) ~0.4 µm, and F) ~0.5 µm from the dense layer. Ionic current density was normalized to give 1.0 mA/cm2 at the negative electrode/current collectors.

Examining the cross-section of the dense layer at the dense-porous interface (Figures 5.5a, 5.6a, 5.7a, 5.8a, and 5.9a), there were large regions of ~1.0 mA/cm^2 ionic current density (orange color) and patches of lower ionic current density (yellow color)

surrounded by zones of high ionic current density (red color). The low ionic current density regions corresponded to interfaces between the dense garnet and the porous garnet, while the ~1.0 mA/cm^2 and higher current density regions corresponded to interfaces between the dense garnet and the positive Li electrode. This demonstrated the majority of ionic current was transferred from the positive Li electrode directly into the dense garnet, with only a relatively small amount of ionic current transported through the porous layer. The high ionic current density regions surrounding the dense-porous garnet interfaces extended further out from large dense garnet-porous garnet interfaces than small dense garnet-porous garnet interfaces. These high ionic current density regions and the high ionic current density at the porous garnet-electrode interfaces certainly qualified as "hot spots" in the bilayer microstructure and may prove problematic for bilayer operation. Examining the porous layer cross-sections for the Template microstructure (Figure 5.5b), the ionic current density in the porous garnet quickly decreased with increasing distance from the dense layer, consistent with earlier observation of a transition region in the electric field strength distribution. The porous garnet generally had low ionic current density in the garnet interior (yellow/green color) and a thin region of high ionic current density (red color) at the garnet surface/interface with the positive Li electrode (grey color). Regions of high ionic current density were present within the interior of the porous garnet particles, away from the garnet-electrode interface. Examining subsequent porous layer cross-sections (Figures 5.5c, d, e, f), seemingly interior parts of the garnet structure were actually at or close to the garnet surface along the Z-axis. This indicated high ionic current density was being transferred into the porous garnet from the electrode and propagated along the Z-axis.

Examining cross-sections of the remaining bilayers (Figures 5.6, 5.7, 5.8, and 5.9), similar patterns were seen of dense layer surfaces that were a mix of ~1.0 mA/cm^2 and low ionic current density regions surrounded by high current density regions corresponding to the dense garnet-porous garnet interfaces; high ionic current density at the porous garnet-electrode interfaces and lower ionic current density in the porous garnet interior; and ionic current density decreasing within the porous garnet with increasing distance from the dense layer. Comparing the very high porosity Template bilayer (Figure 5.5a) to the high porosity Porous 1 and Trilayer 1 bilayers (Figures 5.6a and 5.7a), decreasing porosity increased the overall ionic current density of the dense garnet-electrode interface. The increase in current density resulted from the high ionic current density regions near the dense garnet-porous garnet interfaces extending across a larger amount of the dense garnet-electrode interface area. The overall ionic current density of the dense garnet-electrode interface increased further when examining the medium porosity Porous 2 bilayer (Figure 5.8a), at which point all the dense garnet-electrode interface had ionic current densities above 1.0 mA/cm^2. The ionic current densities at the dense garnet-electrode interface of the low porosity Porous 3 bilayer (Figure 5.9a) were at or above the maximum cutoff of 1.5 mA/cm^2. At the same time, overall ionic current density in the porous garnet increased as bilayer porosity decreased (Figures 5.5b-f, 5.6 b-f, 5.7 b-f, 5.8 b-f, and 5.9 b-f), though the highest ionic current density regions in the porous garnet were still largely confined to near the porous garnet-electrode interface. The ionic current density in the interior of the porous garnet also increased as the porous layer porosity decreased, consistent with previous observations of the porous layer transition region increasing in size with decreasing porosity.

Based on the 2D cross-sections, it appeared the highest ionic current densities in the porous garnet were flowing through a thin sheath at the garnet surface and the interior of the porous garnet carried much lower ionic current density. To confirm this, histograms were calculated for the normalized ionic current densities of all garnet voxels, only interior garnet voxels away from the garnet-electrode interface, and only surface garnet voxels at the garnet-electrode interface. A bin width of 0.01 mA/cm^2 was used and the voxel counts plotted on a logarithmic scale. The results were shown in Figure 5.10 for the a) Template 1 bilayer, b) Porous 1 bilayer, c) Trilayer 1 bilayer, d) Porous 2 bilayer, and e) Porous 3 bilayer. In all the histograms, there were two principle peaks in the bilayer ionic current density at 0 mA/cm^2 and 1.0 mA/cm^2. For the overall garnet and interior garnet histograms, the 0 peak was due to the majority of the porous layer not transporting ionic current density, while the 1.0 peak was due to all ionic current density in the bilayer eventually flowing through the dense layer and smoothing out to 1.0 mA/cm^2. For the surface garnet histograms, the 0 peak was similarly due to the majority of the porous layer surface not being used to inject ionic current ionic into the porous garnet, while the 1.0 peak was due to the ionic current density flowing directly from the electrode into the dense layer. All three histograms also had garnet voxels with ionic current densities above 1.0 mA/cm^2, with the overall garnet and surface garnet histograms displaying maximum ionic current densities significantly higher than the maximum ionic current density in the interior garnet histograms. Both sets of maximums also increased as the bilayer porosity decreased. These patterns of increasing ionic current density with decreasing porosity were consistent with earlier observations in the 2D cross-sections. The surface garnet histogram also had a unique feature wherein the number of voxel decreased as ionic current density increased

above 0 mA/cm^2 and then the counts sharply increased at 1.0 mA/cm^2. In contrast, the interior garnet histogram smoothly decreased and then increased to the 1.0 peak. The difference originated from the high ionic current densities at the garnet interface spreading through the garnet interior and forming a smooth spectrum of lower ionic current densities. The greater number of interior garnet voxels meant the overall garnet histogram below the 1.0 peak and slightly above the 1.0 peak was dominated by the smoothed behavior of the interior garnet histogram.

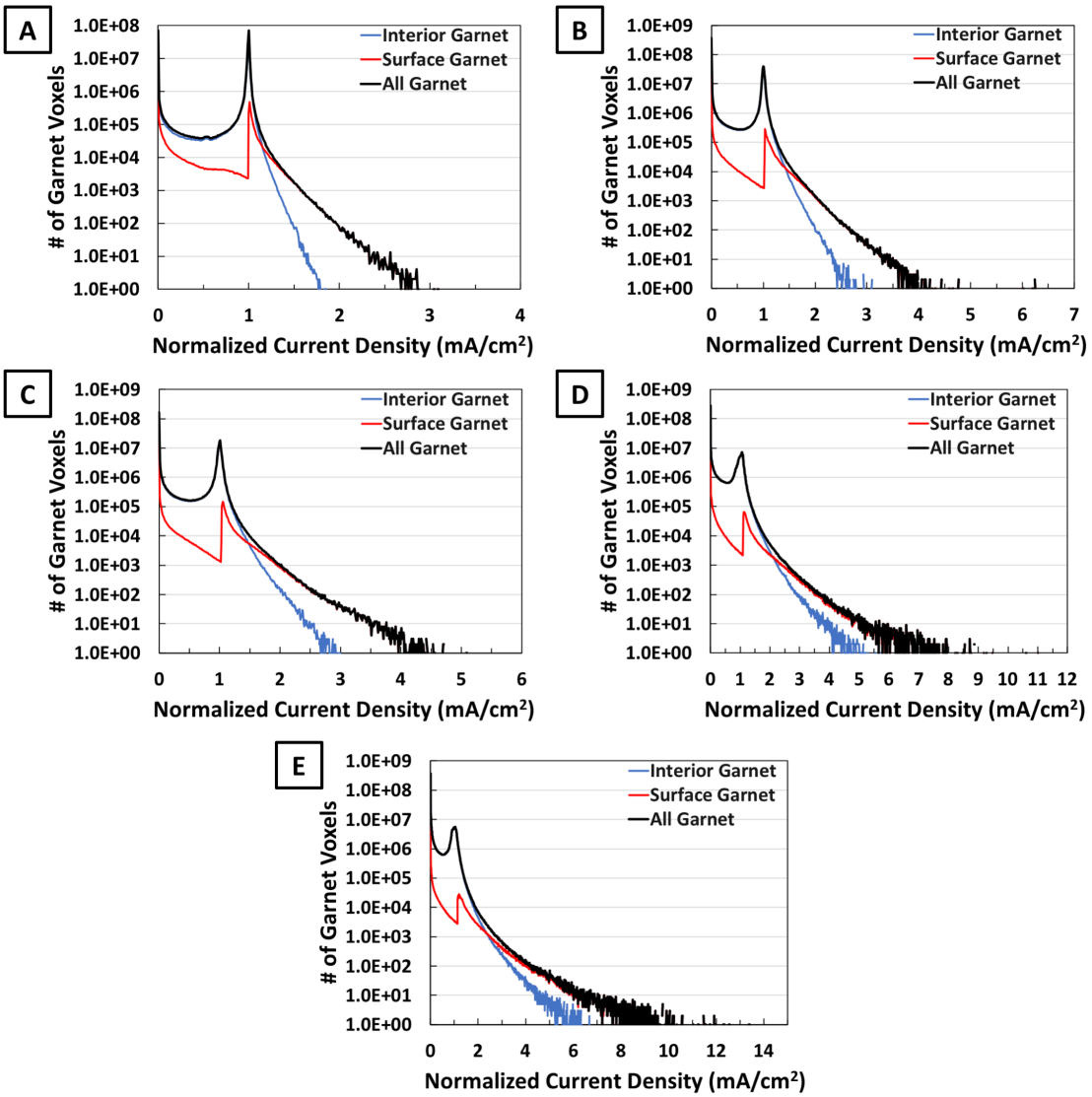

Figure 5.10: Histograms of the normalized current density of surface garnet voxels, interior garnet voxels, and all garnet voxels for A) the Template 1 bilayer, B) the Porous 1 bilayer, C) the Trilayer 1 bilayer, D) the Porous 2 bilayer, and E) the Porous 3 bilayer.

Table 5.1 shows the maximum ionic current density cutoff necessary to include 90%, 99%, 99.9%, and 99.99% of all garnet voxels, interior garnet voxels, and surface garnet voxels. 90% inclusion required a cutoff only slightly above 1 mA/cm^2 for all garnet and interior garnet voxels and below 0.5 mA/cm^2 for the surface garnet. This was due to the large number of dense garnet voxels with ionic current densities close to 1 mA/cm^2 and the majority of the garnet-electrode interface having 0 mA/cm^2 ionic current densities. 99%

inclusion required only a slightly increased ionic current density cutoff for all garnet and interior garnet voxels, while the ionic current density cutoff for the surface garnet voxels increased sharply. This indicated the tails above 1 mA/cm^2 were being drawn in and emphasized how the tail played a stronger role in the surface garnet histogram as there were fewer surface garnet voxels than interior garnet voxels. At 99.9% and 99.99% inclusion, all ionic current density cutoffs increased substantially as more of the distribution tail was included. Comparing the different bilayers, it was evident that an ionic current density cutoff of 1.5 mA/cm^2 would encompass a minimum of 99% and a maximum of nearly 99.99% of all garnet voxels for the bilayers being analyzed. This informed the decision to use a cutoff of 1.5 mA/cm^2 for the 2D cross-sections of the ionic current density.

Table 5.1: Maximum current density cutoff necessary to include 90%, 99%, 99.9%, and 99.99% of all garnet voxels, core garnet voxels, and surface garnet voxels of simulated 3D FIB Tomography bilayers.

		Maximum Current Density Cutoff to include X% of Voxels (mA/cm^2)			
		90%	**99%**	**99.9%**	**99.99%**
Template	*All Garnet*	1.00	1.04	1.21	1.54
	Interior Garnet	1.00	1.03	1.12	1.25
	Surface Garnet	0.02	1.24	1.48	1.87
Porous 1	*All Garnet*	1.01	1.10	1.36	1.85
	Interior Garnet	1.01	1.09	1.27	1.52
	Surface Garnet	0.06	1.34	1.92	2.55
Trilayer 1	*All Garnet*	1.02	1.11	1.41	1.96
	Interior Garnet	1.02	1.10	1.30	1.59
	Surface Garnet	0.41	1.45	2.10	2.96
Porous 2	*All Garnet*	1.05	1.22	1.66	2.52
	Interior Garnet	1.05	1.21	1.56	2.09
	Surface Garnet	0.41	1.77	2.97	4.61
Porous 3	*All Garnet*	1.01	1.23	1.71	2.77
	Interior Garnet	1.02	1.22	1.60	2.27
	Surface Garnet	0.25	1.89	3.52	6.03

5.2.3. Quantification of Bilayer Simulation Performance:

By combining the unnormalized ionic current densities at the current collectors with the 1.0 V potential difference applied across the bilayer, the ASR values of the different bilayers were calculated, plotted vs. porous layer porosity in Figure 5.11, and listed in Table 5.2. The bilayers ASR values were as low as 1.032 Ω-cm^2 for the very high porosity Template bilayer (78.98% porosity) and as high as 1.161 Ω-cm^2 for low porosity Porous 3 bilayer (26.45% porosity). This represented only a 12.5% increase in bilayer ASR despite a difference of over 50% porosity in the porous layers. In fact, above 56% porosity (i.e., the Template, Porous 1, and Trilayer 1 bilayers), the bilayer ASR showed very minor variations. It was only for lower porosity bilayers that the ASR began increasing notably and even that increase was small. All the dense layers were 5 μm thick and had an ASR of 1.000 Ω-cm^2 when isolated, so the porous layers contributed an additional ASR of 0.032 Ω-cm^2 for the very high porosity Template bilayer and 0.161 Ω-cm^2 for the low porosity Porous 3 bilayer. These small contributions were consistent with previous observations of substantial ionic current density in the dense garnet and significantly less ionic current density in the porous garnet, meaning the overall bilayer properties were dominated by the dense layer.

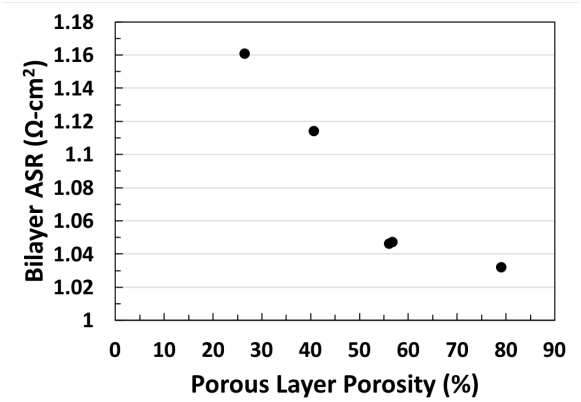

Figure 5.11: Bilayer Li symmetric cell ASR vs. porosity of the 3D FIB Tomography microstructures used for the porous layer.

Table 5.2: 3D FIB Tomography bilayer simulation results for porous layer (PL) porosity, bilayer ASR, porous layer 99.99% active region thickness, dense layer (DL) average normalized interfacial ionic current density, and maximum porous layer average normalized ionic interfacial current density. The electrode capacity of a 20 μm porous layer was also listed.

	PL Porosity (%)	Bilayer ASR (Ω-cm^2)	PL Active Region Thickness (μm)	DL Avg. Norm. Interfacial Current Density (mA/cm^2)	Max PL Avg. Norm. Interfacial Current Density (mA/cm^2)	Electrode capacity for 20 μm PL (mAhr/cm^2)
Template	78.98	1.032	2.01	1.070	0.884	3.257
Porous 1	56.67	1.048	4.30	1.179	1.416	2.337
Trilayer 1	56.03	1.046	4.97	1.187	1.580	2.311
Porous 2	40.58	1.114	11.41	1.355	2.099	1.673
Porous 3	26.45	1.161	11.94	1.490	2.219	1.091

To better understand how charge was transported at different positions in the bilayer, the bilayer was divided into 2D "slices" parallel to the XY-plane and the fraction of ionic current flowing through each 2D slice was calculated. This was accomplished by calculating the total normalized ionic current flowing in the garnet voxels in each 2D slice and dividing by the total normalized current flowing through the bilayer. The results were plotted vs. distance from the dense layer in Figure 5.12a. Immediately evident was the previous trends of ionic current fraction decreasing in the garnet microstructure as the

distance from the dense layer increased. The ionic current fraction decreased the quickest for the very high porosity Template bilayer, decreased slower for the high porosity Porous 1 and Trilayer 1 bilayers, decreased even more slowly for the medium porosity Porous 2 bilayer, and decreased the slowest for the low porosity Porous 3 bilayer. There were also jumps in the ionic current fraction when comparing the porous garnet cross-section immediately contacting the dense layer (shown as 0.1 μm) and the dense layer cross-section at 0 μm. These results were consistent with observations from the 3D visualizations of the electric field strength and 2D cross-sections of the normalized ionic current density. Notably, the size of the jump in the ionic current fraction decreased as the bilayer porosity decreased, revealing the ionic current was substantially redistributed to the porous garnet from the dense garnet in less porous bilayers. This indicated the reduced dense garnet-electrode interfacial area was unable to fully accommodate the battery ionic current despite previous observations of higher ionic current densities in the dense layer cross-section of less porous bilayers.

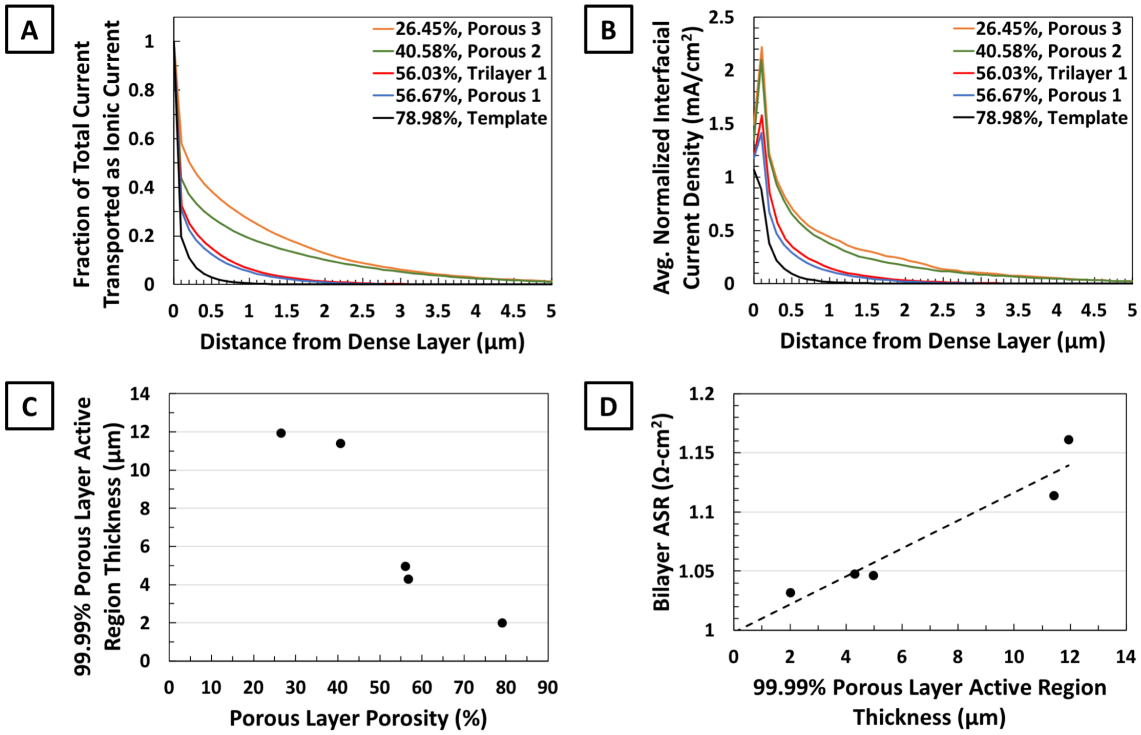

Figure 5.12: A) fraction of total current flowing through bilayer as ionic current vs. distance from the dense layer. B) average normalized interfacial current density vs. distance from the dense layer. C) 99.99% porous layer active region thicknesses vs. porous layer porosity. D) bilayer ASR vs. 99.99% porous layer active region thickness.

The average normalized current density transported across the garnet-electrode interface within each 2D slice of the bilayer was calculated and plotted vs. distance from the dense layer in Figure 5.12b. Similar to the previous observations, most of the active garnet-electrode interface was at the dense layer (distance of 0 µm) and parts of the porous layer close to the dense layer. At the same time, parts of the porous layer interface showed interfacial current densities greater than the 1.0 mA/cm^2 of the current collector, and the dense layer always showed interfacial current densities greater than 1.0 mA/cm^2. As the bilayer porosity decreased, an increasing amount of the garnet-electrode interface was utilized, and an increasing amount of that interface had interfacial current densities greater than 1.0 mA/cm^2. Figure 5.12b also showed the highest average interfacial current density

was generally observed in the porous garnet slice immediately contacting the dense layer, appearing as a spike in the plot. The dense layer generally had the second highest average interfacial current density. The average interfacial current density in the dense layer cross-section and the maximum average interfacial current density in the porous garnet cross-sections both increased as the porosity of the bilayer decreased (Table 5.2). This was likely due to a combination of the decreasing dense garnet-electrode interfacial area and the increasing garnet particle size, which both appeared to correspond to increasing amounts of high ionic current density voxels in the 2D cross-sections. As this was the average interfacial current density, combined with the long tails of the previously discussed histograms, together they indicated there were parts of the garnet-electrode interface with still higher interfacial current densities.

Quantifying the amount of the porous layer utilized in each bilayer started with defining the "porous layer active region thickness" as the distance from the dense layer into the porous layer that corresponded to the ionic current fraction dropping below 0.0001 (meaning 99.99% of total current in the bilayer was being transported by ionic current between this point and the dense layer). The results were plotted in Figure 5.12c, showing the very high porosity Template bilayer had the smallest active region thickness of 2.01 μm and the low porosity Porous 3 bilayer had the largest active region thickness of 11.94 μm, compared to total porous layer thicknesses of 13.77 μm and 22.75 μm, respectively. Plotting the bilayer ASR vs. the 99.99% active region thickness in Figure 5.12d showed the bilayer ASR generally increased linearly as the active region thickness increased, with minor scatter in the results likely due to variations in the porous microstructure. When a linear function was fitted to the data, the line intercepted the y-axis at a value of 0.998,

very close to the dense layer ASR of 1.000. This was consistent with the earlier discussion of the bilayer ASR being dominated by the dense layer properties, so decreasing the active region thickness, and thus decreasing the utilization of the higher ASR porous layer, would decrease the bilayer ASR towards the minimum ASR limit of the dense layer alone.

Alongside bilayer ASR and current density distributions, the electrode loading capacity of the bilayer was also a key parameter considered when determining the optimal bilayer microstructure. To this end, the areal capacity of the Li-metal electrode loaded into the pore network of each bilayer was calculated. However, the different thicknesses of the underlying 3D FIB Tomography microstructures meant that direct comparison was not possible. Fortunately, the transition regions of each porous layer were significantly smaller than the total porous layer thicknesses, suggesting that further increases to the porous layer thickness would not increase the bilayer ASR noticeably. This logically followed from the fact that less than 0.01% of current was transported as ionic current through the porous layer outside the active region, and any additional porous layer would be part of this "inactive" region. Thus, the ASR of the bilayers with variable thickness porous layers were used as proxies for the ASR of hypothetical bilayers with the same porous microstructures but identical porous layer thicknesses with minimal loss of accuracy. Based on this, the 3D FIB Tomography bilayer results were extrapolated to hypothetical bilayers with a 20 μm porous layer, since this was very close to the real porous layer thicknesses, and the resulting the Li-metal areal capacity was calculated (Table 5.2). The hypothetical very high porosity Template bilayer could be loaded with 3.257 mAhr/cm^2 of Li-metal when the pores were fully infiltrated compared to the 1.091 mAhr/cm^2 of the hypothetical low porosity Porous 3 bilayer (Figure 5.13a). Moreover, increasing the porosity of the porous layers also

decreased the amount of garnet mass in the bilayer. Given the much higher garnet density (5.1 g/cm^3) than the Li-metal (0.534 g/cm^3), this would give gravimetric capacities of 588.1 mAhr/g and 105.5 mAhr/g for the hypothetical very high porosity Template bilayer and the hypothetical low porosity Porous 3 bilayer, respectively, when only including the garnet and infiltrated Li-metal masses (Figure 5.13b).

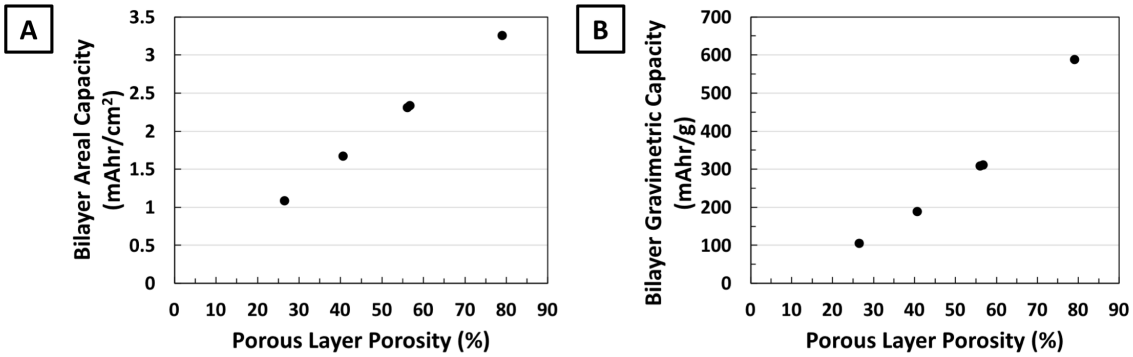

Figure 5.13: A) bilayer areal capacity for Li-metal infiltrated into 20 μm porous layer vs. porous layer porosity. B) bilayer gravimetric capacity for Li-metal infiltrated into 20 μm porous layer vs. porous layer porosity. Only the garnet mass and infiltrated Li metal mass were used.

5.2.4. Implications for Batteries Utilizing Bilayer/Trilayer Garnet Electrolytes:

The simulations of equilibrium electric potential, electric field, and ionic current density in fully infiltrated bilayer symmetric cells showed that in every meaningful way, a bilayer with a higher porosity porous layer would outperform a bilayer with a lower porosity porous layer. Specifically, increasing bilayer porosity caused the already low ASR to decrease further, reduced the ionic current densities within the bilayer garnet, reduced the interfacial current densities at the garnet-electrode interfaces, and increased the maximum electrode areal loading capacity. If we included the decreased electrolyte mass alongside the increased electrode loading capacity, the gravimetric capacity of a high porosity bilayer was dramatically higher than a low porosity bilayer. Based on these

patterns, the logical conclusion was that the dense layer alone was the best structure, since this would provide the minimum ASR and the minimum current densities due to having a 100% porosity "porous layer". However, the limited mechanical strength of the thin dense layer without the porous layer would require a thicker dense layer to maintain mechanical strength, which dramatically increases the ASR. Also, both thin and thick dense layers have difficulty utilizing high capacity electrodes such as Li-metal or sulfur since these electrodes change volume dramatically during cycling, risking loss of contact with the current collectors. The rigid structure of the porous garnet can contain the electrode in a more fixed volume and better maintain current collector contact. Thus, the high porosity bilayer structure was actually the best practical structure due to having near-dense layer ASR values and enough mechanical strength to remain intact during battery fabrication and cycling.

A clear goal of optimizing the bilayer structure is to decrease the current density, both within the garnet and at the garnet-electrode interfaces. The simplest approach was to continue increasing the porous layer porosity, but ultimately there is an upper porosity limit where the mechanical strength of the bilayer becomes compromised. An alternative approach is to fabricate the bilayer from 2 different electrolytes: the thin dense layer from LLZO-based garnet, and the porous layer from a higher conductivity material. This difference in conductivity reduces the added resistance/ASR for cycling through the porous layer and increases the thickness of the transition region in the porous layer while maintaining the same ASR. The total bilayer current then transfers into the bilayer electrolyte from the infiltrated electrodes across a larger interfacial area, thereby decreasing the interfacial current density. The higher porous layer conductivity may also cause the

current density within the porous electrolyte to become more homogenous and decrease overall garnet current density as well.

Crucially, the ability of the bilayer to defy the predictions of the earlier M-factor analysis and display near-dense layer ASR values for high porosity porous layers depended heavily on the ability of electrodes to interface with the dense layer directly. Any situation where the electrode does not contact the dense layer, such as failure to initially infiltrate or loss of contact during cycling, forces current transported via electronic current in the infiltrated Li-metal electrodes in the pores to be transported instead via ionic current in the porous layer. In that situation, the reduced effective conductivity of the porous layer garnet would substantially increase the bilayer ASR and garnet/interfacial current densities, with further increasing the bilayer porosity resulting in worsening performance. While wetting electrodes such as Li-metal and sulfur can likely infiltrate through the porous layer to the dense layer and use the dense garnet-electrode interface for primary current transport, non-wetting particle-based electrodes are much more likely to agglomerate and only partially infiltrate. Even if the non-wetting electrodes did infiltrate to the dense layer, the discrete nature of the electrode particles means that only particles contacting the dense layer operate in the ideal low ASR condition. The bulk of the particles would instead contact the porous layer and operate in high ASR conditions. For such a situation, a 2nd Li-ion conducting electrolyte infiltrated into the pores would provide a low ASR path for Li-ions to reach the dense layer that bypasses the high ASR porous garnet.

5.3. Simulation of Column-based Microstructures – Results and Discussion:

In studying the simulation results for bilayers using the 3D FIB Tomography microstructures, there are were questions remaining with consequences for application in real batteries: how much did the bilayer ASR increase when no dense garnet-electrode interface existed?; given the greater abundance of high current densities near larger porous garnet particle, would decreasing the particle size reduce overall current density and ASR?; and given that decreasing porosity also increased current densities and ASR, how did the effect of changing porosity compare to the effect of changing particle size? Answers to these questions were sought by simulating a series of artificial bilayer symmetric cells where the porous layers were composed of cylindrical columns (Figure 5.14). A primary benefit of this approach was the ability to control the microstructure of the bilayer layer by independently varying the nominal porous layer porosity, the column diameter, and the porous layer thickness/column height, while avoiding the confounding influences of tortuosity and bottlenecks. Moreover, the column-based bilayers could be reduced to the smallest repeat unit and periodic boundary conditions applied within the XY-plane to dramatically reduce the simulation time as compared to the simulation time necessary for the 3D FIB Tomography bilayers.

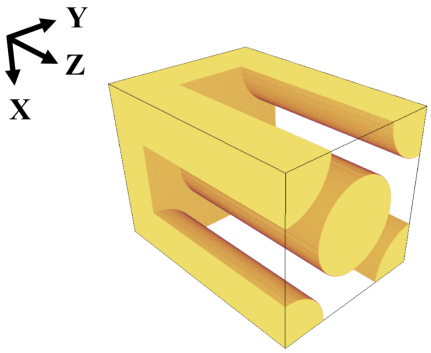

Figure 5.14: Repeat unit for simulating the column-based bilayer. Here, the dense layer was 5 μm thick and the porous layer was 20 μm thick, had a nominal porosity of 50%, and had 10 μm diameter columns.

5.3.1. 3D Visualization of Simulation Results:

Nine different column-based bilayers were created by varying the nominal porosity of the porous layer from 75% to 50% to 25% and varying the column diameter from 10 μm to 5 μm to 1 μm. The voxel size was set to 0.05 μm/voxel for the X-, Y-, and Z-axes to simplify calculations and ensure that even the 1 μm diameter columns were significantly larger than the voxels. The porosity was considered nominal as the discrete nature of voxels in the simulation caused the column surfaces to deviate from the ideal shapes of cylinders, making the actual porosity slightly different than the nominal value (Table 5.3). To provide comparable results to the 3D FIB Tomography bilayers, the dense layer was 5 μm thick, the porous layer was 20 μm thick, and the same intrinsic garnet conductivity of $5x10^{-4}$ S/cm was used. To provide visuals similar to the 3D FIB Tomography bilayers, the different repeat units were copied along the X- and Y-axes then truncated to give a bilayer with planar dense layer dimensions of 100 μm x 100 μm (Figure 5.15). Figure 5.16 shows the resulting bilayer symmetric cells, where the porous layers of the bilayers were 100% infiltrated with the positive Li-metal electrode (red color), and a thin negative Li-metal electrode (blue color) was attached to the planar surface of the dense layers. The electrolyte was shown in yellow and current collectors were shown in grey. A potential difference of 1.0 V was applied across the bilayer (+0.5 V at the positive electrode, -0.5 V at the negative electrode), and the potential in the bilayer was iteratively relaxed until the desired level of convergence was achieved. Periodic boundary conditions were applied within the XY plane to simulate a bilayer with infinite planar area. The details of the MATLAB implementation are given in Appendix F. Due to the small size of the column-based bilayer

repeat unit, the entire bilayer repeat unit was relaxed simultaneously so only one iteration was necessary.

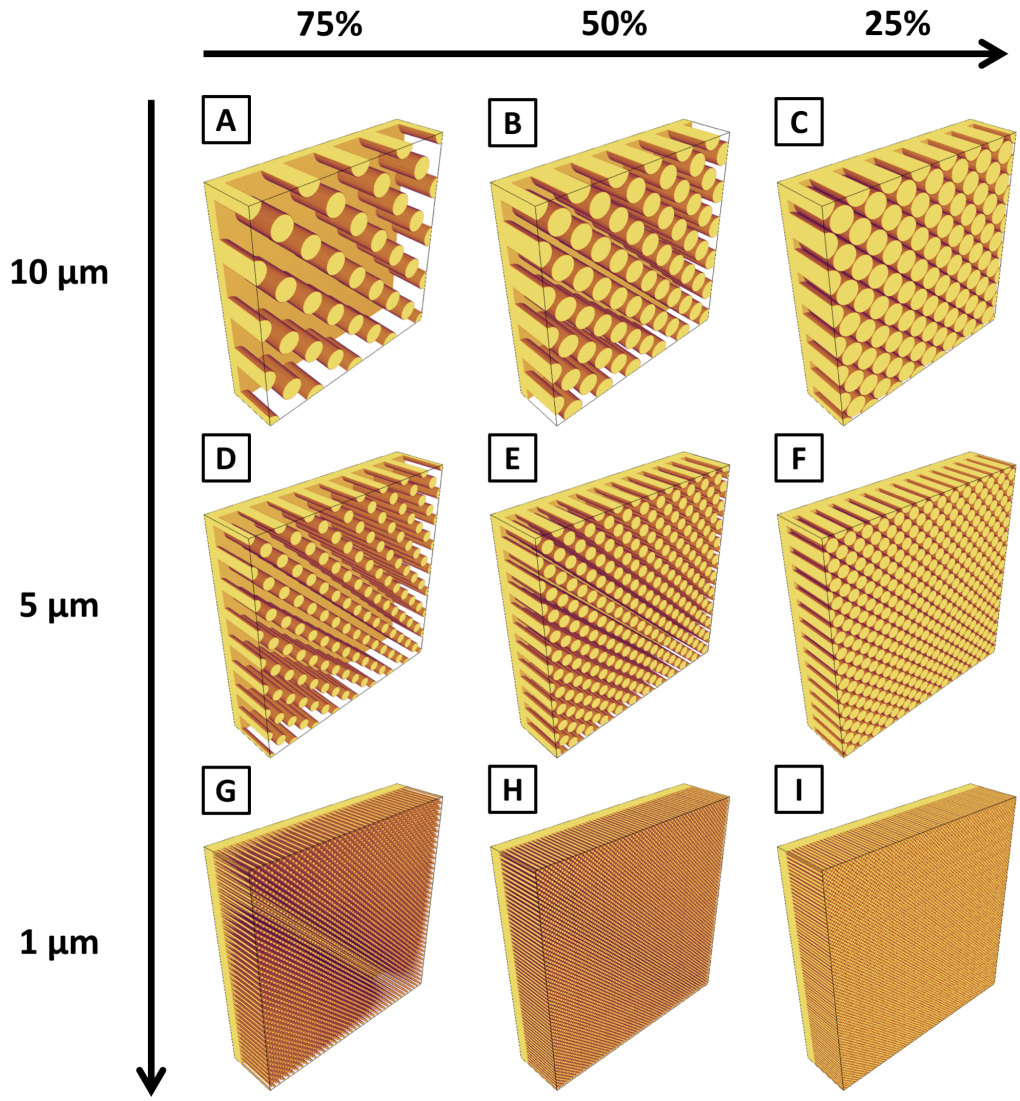

Figure 5.15: 100 µm x 100 µm x 25 µm (5 µm dense layer, 20 µm porous layer) column-based bilayers, showing the range of microstructures generated by varying the nominal porosity values (75%, 50%, and 25%) and column diameters (10 µm, 5 µm, and 1 µm).

Table 5.3: Actual porous layer porosity of column-based porous microstructures generated by varying nominal porosity values (75%, 50%, and 25%) and column diameters (10 µm, 5 µm, and 1 µm).

	Nominal Porosity		
Column diameter (µm)	**75%**	**50%**	**25%**
10	75.1	50.5	25.3
5	75.4	50.6	26.3
1	77.2	51.6	29.5

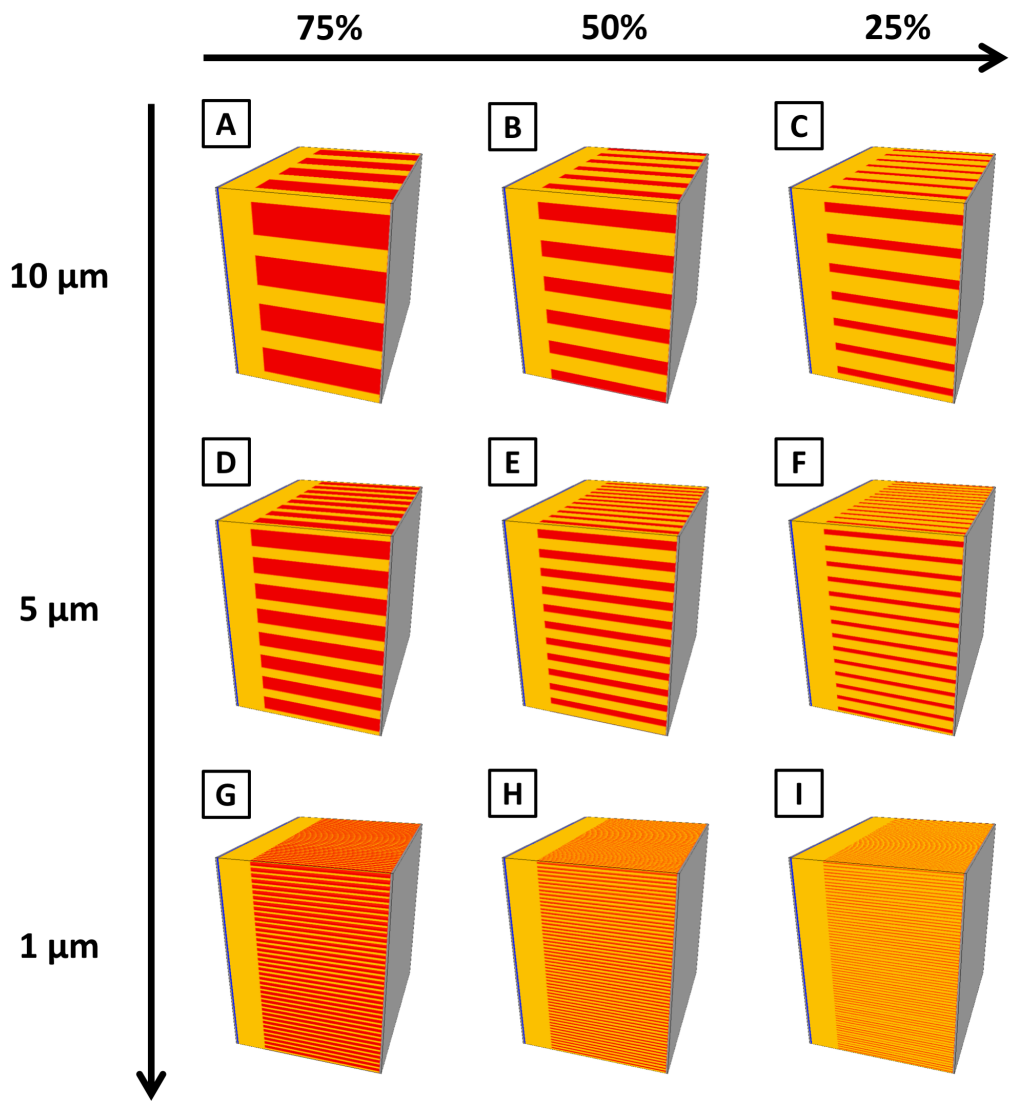

Figure 5.16: Schematic of column-based bilayer symmetric cells for range of nominal porosity values (75%, 50%, and 25%) and column diameters (10 µm, 5 µm, and 1 µm). The garnet electrolyte was yellow, the positive Li-metal electrode was red, the negative Li-metal electrode was blue, and the current collectors were grey. All visualizations were stretched by 3x along the Z-axis.

From the equilibrium electric potential distributions (not shown), the local electric field strength was calculated within each bilayer and shown in Figure 5.17, where the Z-axis was stretched by 3x for easier viewing. The maximum cutoff of the color bar was set to 150% of the average electric field strength at the dense layer-negative electrode interface, thereby ensuring that 0 electric field strength always appeared blue and the average electric field strength at the dense layer-negative electrode interface always

appeared red. The bilayers had regions of high electric field strength (red color) in the dense layer, 0 electric field strength (blue color) in the majority of the porous garnet, and a transition region in the porous garnet near the dense layer, similar to the 3D FIB Tomography bilayers. Notably, the size of the transition region decreased drastically as the column diameter was decreased for fixed porosity, while changing the bilayer porosity for fixed column diameter had little effect. Simultaneously, the presence of larger diameter columns reduced the electric field over large amounts of the dense layer beneath the dense-porous interface (orange/yellow color), due to the lower electric field within the columns relative to the majority of the dense layer. Interestingly, both the porosity and the column diameter appeared equally important for determining the dense garnet-electrode interfacial current densities and the overall dense layer current densities (i.e., the visible surface of the dense layer around the base of the columns). Looking at bilayers with nominal porosity of 75% (Figure 5.17a, d, g), the bilayer with 10 μm diameter columns had small rings of very high current density (white color) at the dense layer surface, while the bilayer with 5 μm diameter columns did not. For bilayers with the nominal porosity of 50% (Figure 5.17b, e, h), the high current density regions covered most of the dense layer surface for bilayers with 10 μm and 5 μm diameter columns, and the high current density region also extended into ~1/2 the dense layer thickness for the bilayer with 10 μm diameter columns. For bilayers with nominal porosity of 25% (Figure 5.17c, f, i), the high current density regions still appeared to cover most of the dense layer surface for bilayers with 10 μm and 5 μm diameter columns. The high current density region extended into ~2/3 the dense layer thickness for the bilayer with 10 μm diameter columns and a much smaller distance for the bilayer with 5 μm diameter columns. The features of the bilayers with 1 μm diameter

columns were too small to discern any reliable patterns regarding the dense layer surface, though the dense layer had an extremely uniform electric field distribution, in contrast to the bilayers with 10 µm and 5 µm diameter columns.

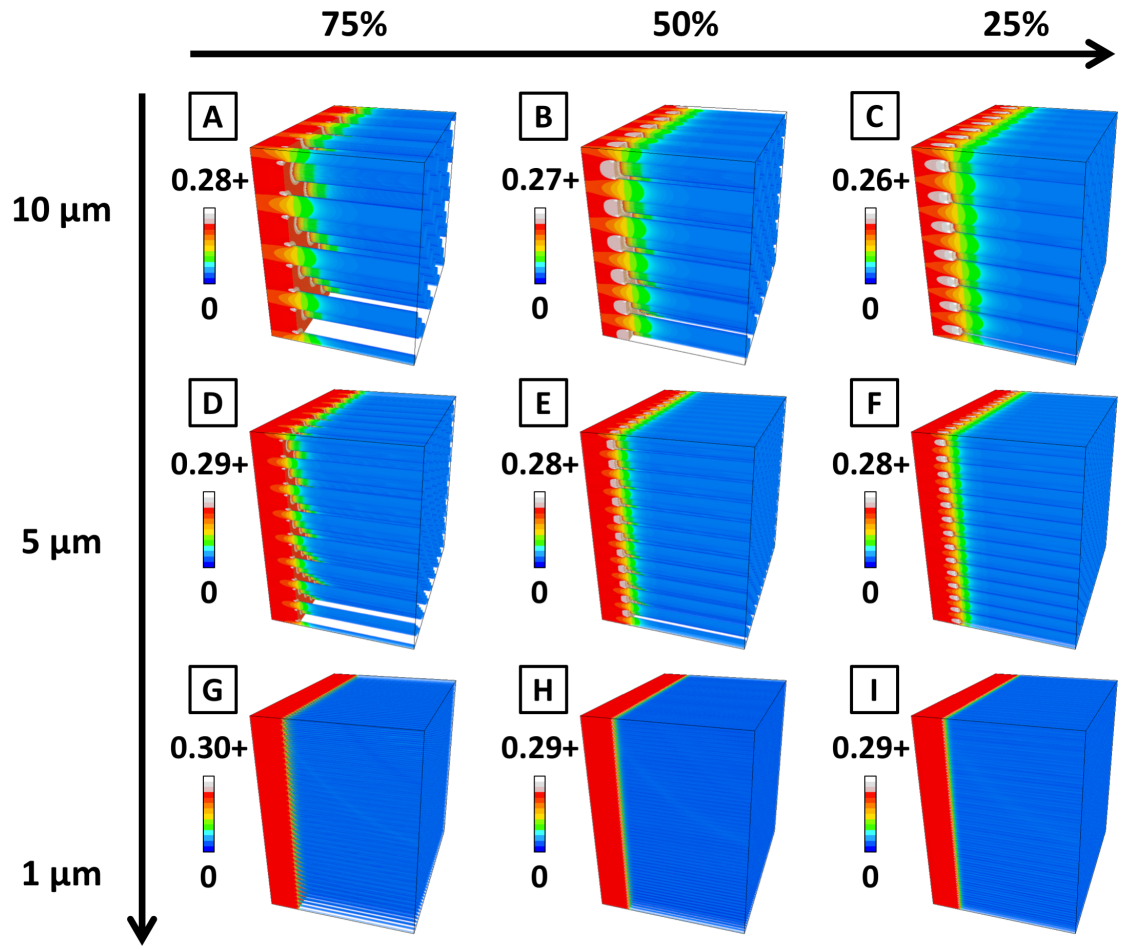

Figure 5.17: Simulated electric field for column-based bilayers for range of nominal porosity values (75%, 50%, and 25%) and column diameters (10 µm, 5 µm, and 1 µm). Units are Volts/µm. The maximum cutoff of the color bar was set to 150% of the average electric field strength at the dense layer-negative electrode interface. All visualizations were stretched by 3x along the Z-direction.

5.3.2. Analysis of 2D Cross-Sections from 3D Visualization – 100% Electrode Infiltration:

The magnitude of the ionic current density entering each voxel was calculated based on the local electric field strength and a garnet intrinsic conductivity of 5×10^{-4} S/cm. The bilayer ionic current density distribution was then normalized to give an average ionic

current density of 1 mA/cm^2 at the negative electrode/current collectors. Figure 5.18 shows the normalized ionic current density for 2D cross-sections of the dense layer at the dense-porous interface, and Figure 5.19 shows the normalized ionic current density for 2D cross-sections of the porous layer at a distance of 0.05 μm (the cross-section immediately contacting the dense layer). The color bar maximum cutoff was 1.5 mA/cm^2. To better see differences between the bilayers, the cross-sections were limited to the repeat units and the size of the repeat units adjusted for easier comparison. Examining Figure 5.18, the highest ionic current densities in the dense garnet cross-section were at the dense garnet-electrode interface (orange, red) and the lowest ionic current densities were at the dense-porous garnet interfaces (yellow, green), consistent with observations from the 3D FIB tomography bilayers. Also observed were similar regions of high ionic current density around the lower ionic current density regions of the dense-porous garnet interfaces for the 75% nominal porosity bilayers. These regions appeared the same size relative to the columns for all column diameters, meaning the high ionic current density regions were physically larger around larger columns. This supported the previous observations from the 3D FIB tomography bilayers. The overall dense garnet-electrode interfacial current density was lowest for the bilayer with 75% nominal porosity and 1 μm diameter columns and increased as the column diameters increased and as the nominal porosity decreased. However, the change in porosity increased the current density much more significantly than the change in the column diameter, as evidenced by the medium ionic current density (orange color) in the 75% porosity cross-sections being replaced by high ionic current density (red color) in the 25% porosity cross-sections. Increasing the column diameter also decreased the ionic current density at the center of the dense garnet-porous garnet

interfaces, indicating current was less able to fully propagate through the columns from the garnet-electrode interfaces. At the same time, decreasing the bilayer porosity increased the ionic current density throughout the dense-porous garnet interfaces, indicating that an increasing amount of current was directed through the columns rather than the dense garnet-electrode interface.

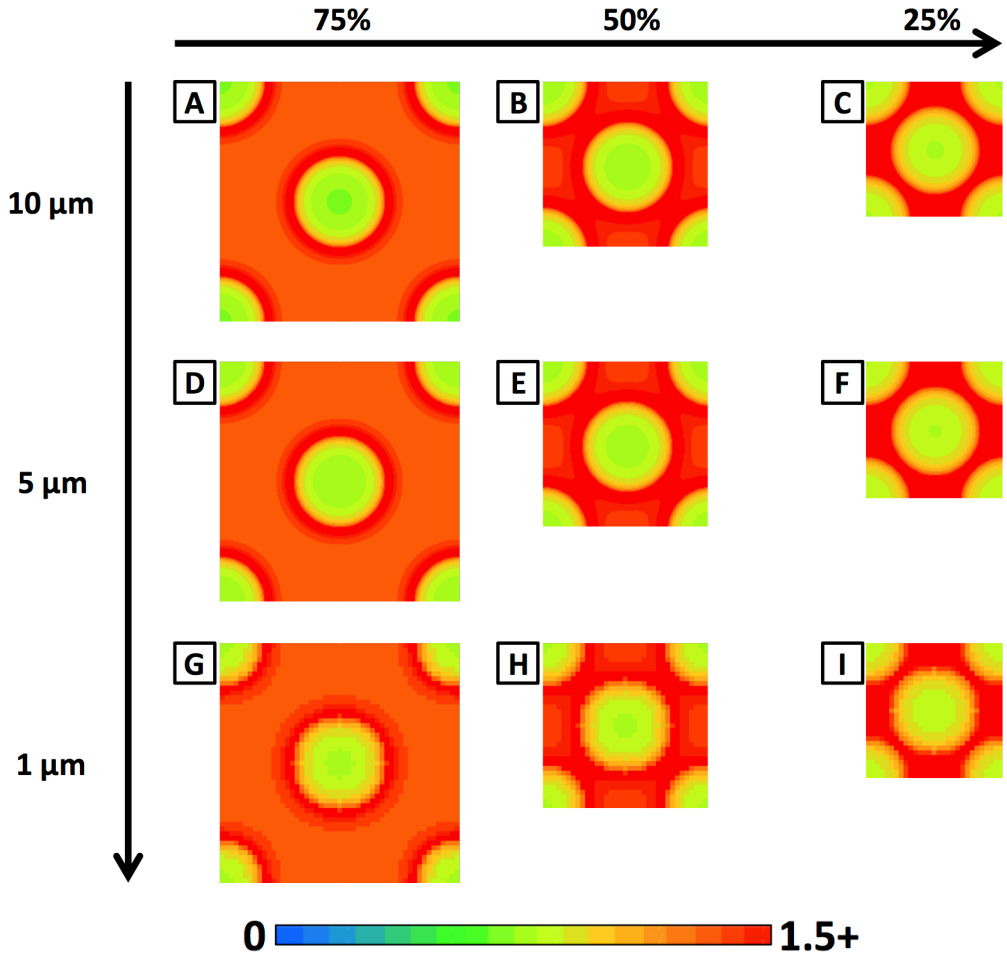

Figure 5.18: 2D cross-sections of the ionic current density in the dense garnet at the dense-porous interface for column-based bilayers over range of nominal porosity values (75%, 50%, and 25%) and column diameters (10 µm, 5 µm, and 1 µm).

Examining Figure 5.19, the highest ionic current densities in the porous garnet cross-section immediately next to the dense layer were at the porous garnet-electrode interface (orange, red), and the lowest current densities were at the center of the columns

(yellow, green), consistent with observations from the 3D FIB tomography bilayers. Similar to the high current ionic density regions in the dense garnet cross-section, the high ionic current density regions in Figure 5.19 appeared the same size relative to the columns for all column diameters, meaning the high ionic current density regions physically covered more of the porous garnet volume for the larger columns. In contrast to the dense garnet cross-section, there was no consistent effect of column diameter on the current density in the interior of the column. For 75% nominal porosity, the ionic current density increased and then decreased around the center of the column as column diameter increased. For both the 50% and 25% nominal porosity, the ionic current density around the column center initially decreased and then was constant as column diameter increased. Conversely, the overall ionic current density in the column clearly increased as the bilayer porosity decreased, consistent with earlier observations from the 3D FIB tomography bilayers.

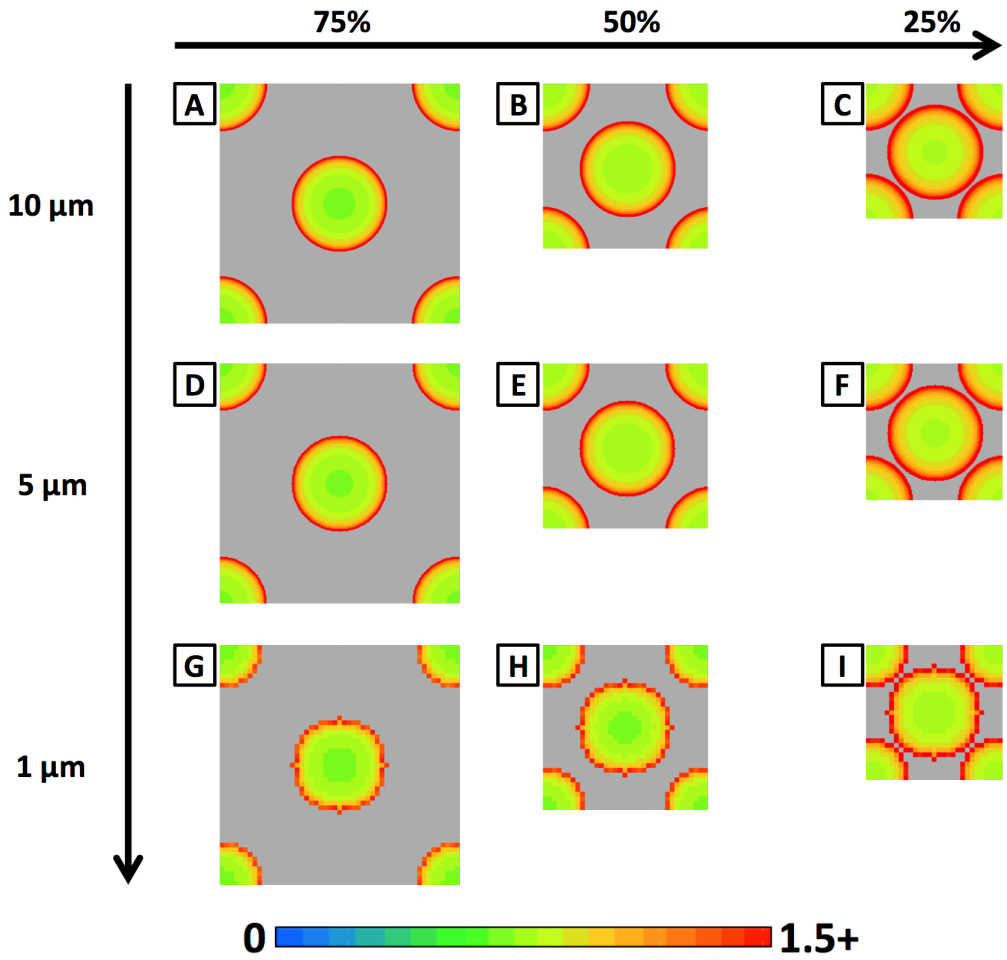

Figure 5.19: 2D cross-sections of the ionic current density at the porous garnet at the dense-porous interface for column-based bilayers over range of nominal porosity values (75%, 50%, and 25%) and column diameters (10 µm, 5 µm, and 1 µm).

5.3.3. Quantification of Bilayer Simulation Performance:

By combining the unnormalized ionic current densities at the current collectors with the 1.0 V potential difference applied across bilayer, we calculated the ASR values of the different column-based bilayers and plotted the results in Figure 5.20. For the bilayers with 1 µm diameter columns, the bilayer ASR increased from 1.01 to 1.03 Ω-cm^2 as the porosity decreased from 77.2% to 29.5% (actual porosity). For the bilayers with 5 µm diameter columns, the bilayer ASR increased from 1.03 to 1.09 Ω-cm^2 as the porosity decreased from 75.4% to 26.3%. For the bilayers with 10 µm diameter columns, the bilayer ASR

increased from 1.06 to 1.17 Ω-cm^2 as the porosity decreased from 75.1% to 25.3%. Comparing data sets, the bilayer ASR values linearly decreased as porosity increased and were projected to reach a minimum ASR of approximately 1.0 Ω-cm^2 when the porosity reached 100%, corresponding to the ASR of the dense layer alone. This was consistent with observations that the majority of current was transported by the dense layer, so increasing porosity would increase the dense garnet-electrode interfacial area and utilize less of the porous layer, decreasing ASR. The column diameter appeared to control the slope of the relation between the bilayer ASR and the porous layer porosity, with increasing column diameter resulting in a higher magnitude slope. This meant the effects of the column diameter were most significant at low porosity and much less significant at high porosity.

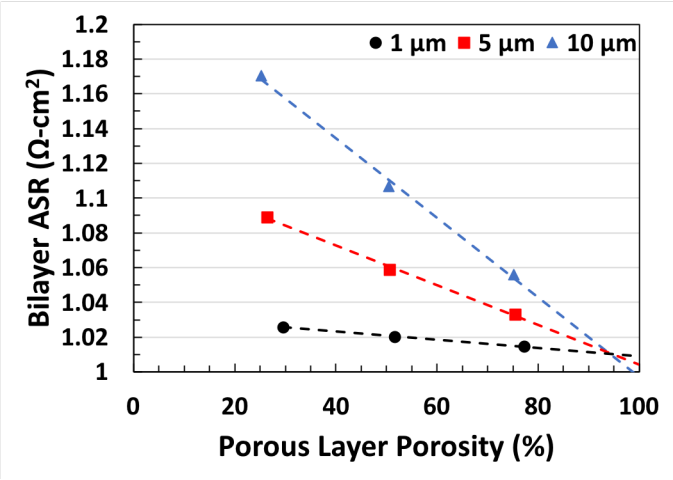

Figure 5.20: Column-based bilayer ASR vs. porous layer porosity, separated by column diameter.

The increased ASR associated with increasing column diameter was likely due to longer conduction pathways through the columns. As shown by Figure 5.19, the regions of high ionic current density in the porous layer became physically larger in larger columns. This meant that the underlying electric fields had propagated further towards the center of the column, and this was likely true even for 2D cross-sections of the porous layer further

from the dense layer. Since pathways of constant electric field must be continuous, this meant the conduction pathways between points on the porous garnet-electrode interface and the dense layer were elongated arcs predominantly parallel to the column axis, but with some components perpendicular to the column axis. The perpendicular components were stronger in the larger diameter columns to maintain the same electric field distribution relative to the larger, but still cylindrically-shaped, columns. Thus, the resulting pathways of constant current density also had stronger perpendicular components, extending the 3D conduction pathway length relative to the shortest possible Euclidean/straight path length. As porosity decreased, more current would flow through these longer conduction pathways and so bilayer ASR would increase faster for the large diameter columns than for the small diameter columns when examining the same porosity.

To better understand how charge was transported at different positions in the bilayer, we calculated the fraction of ionic current flowing through each 2D slice of the bilayer by calculating the total normalized ionic current flowing in the garnet voxels in each 2D slice and dividing by the total normalized current flowing through the bilayer. The results were plotted vs. distance from the dense layer in Figure 5.21 (a, c, e). The average normalized current density transported across the garnet-electrode interface was also calculated and plotted vs. distance from the dense layer in Figure 5.21 (b, d, f). The plots were split based on the column diameter (Figure 5.21 a and b = 1 μm, Figure 5.21 c and d = 5 μm, Figure 5.21 e and f = 10 μm) and the curves within each plot were further delineated by the porous layer porosity. Looking at the plots of ionic current fraction, the amount of the porous garnet actively transporting ionic current increased for all porosities as the column diameter increased.

This was due to the distribution of ionic current density within the columns scaling with column diameter, so larger diameter columns had more voxels with high current density and thus more total current was present within the column at a given distance from the dense layer. The ionic current fraction also jumped in value when transitioning from the porous garnet to the dense garnet, similar to observations of the ionic current fraction in the 3D FIB tomography bilayers. The jump appeared extremely similar for different column diameters and only noticeably decreased as porosity decreased. For the bilayer with nominal porosity of 75% and 1 μm diameter columns, the ionic current fraction reached a maximum of 15.47% in the porous layers, meaning 83.53% of total bilayer current was transported instead through the Li-metal electrodes and transferred directly to the dense layer garnet. As porosity decreased and more current was diverted to the porous garnet, that maximum ionic current fraction in the porous layer increased to 55.65% for the bilayer with nominal porosity of 25% and 10 μm diameter columns, meaning roughly equal amounts of current were transported through the Li-metal electrodes and through the porous garnet.

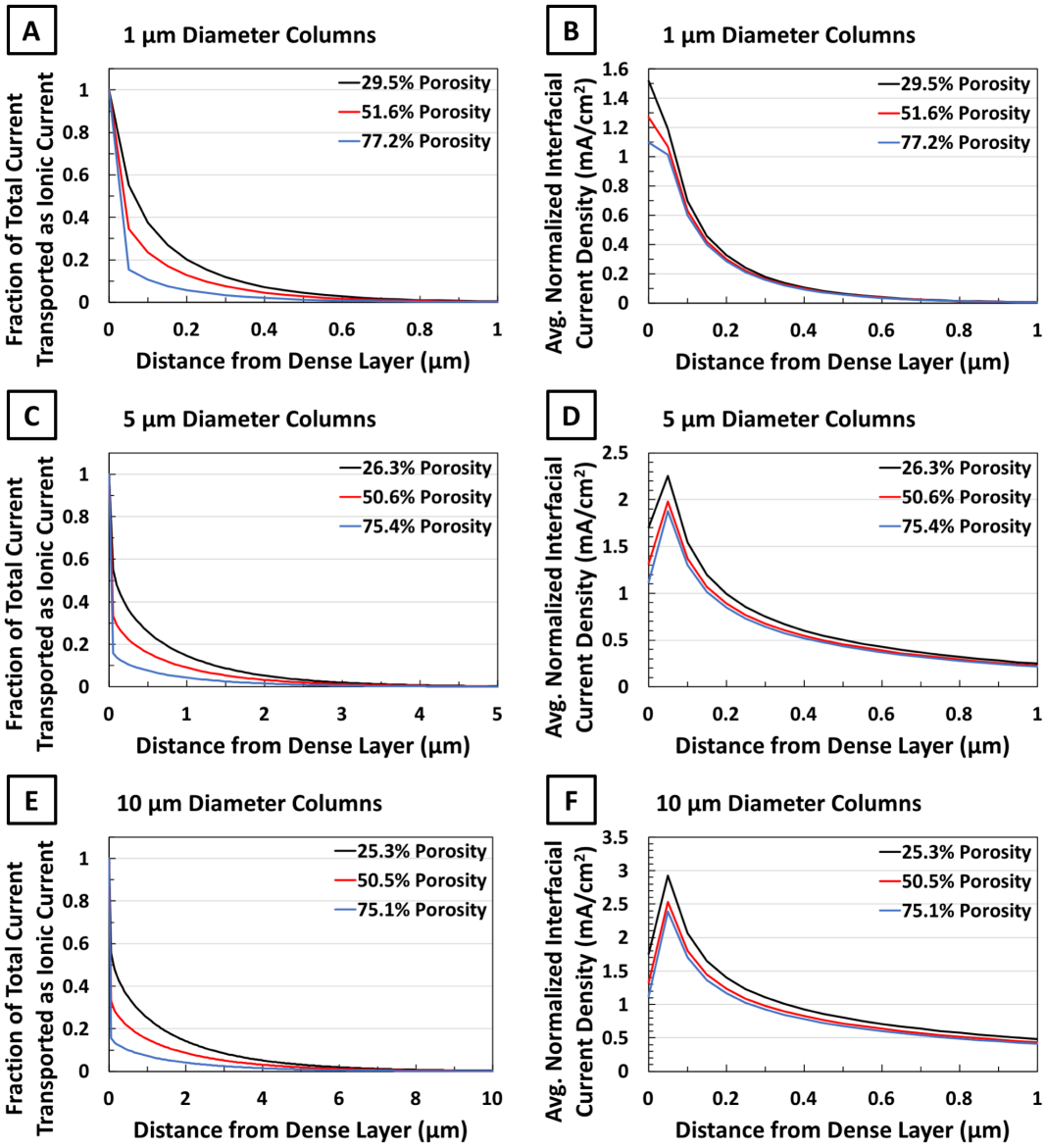

Figure 5.21: Fraction of total column-based bilayer current flowing as ionic current through the garnet (A, C, E) and the average interfacial current density magnitude (B, D, F) vs. distance from the dense layer. The plots were split based on the column diameter (A and B = 1 µm, C and D = 5 µm, E and F = 10 µm) and the curves within each plot were designated by the porous layer porosity.

Examining the average normalized current density transported across the garnet-electrode interface, the extent of the active garnet-electrode interface increased with increasing column diameter, consistent with trends in the ionic current fraction. Increasing the column diameter also significantly increased the interfacial current density in the

porous layer garnet and only marginally increased the interfacial current density at the dense layer. While decreasing the porous layer porosity had a similar effect, it was much less than the effects of increasing the column diameter. For the bilayer with 1 μm diameter columns, the dense layer displayed the highest average interfacial current density for all porosities, ranging from 1.10 mA/cm^2 for 75% nominal porosity to 1.52 mA/cm^2 for 25% nominal porosity. As the column diameter increased, the significant increase in the interfacial current density in the porous garnet created a spike in the curve when transitioning from the dense layer to the porous layer. This was consistent with the previous observations of increasing current densities in the porous garnet with increasing column diameter, which required increasing interfacial current density as the source of higher current density within the porous garnet. Similar behavior was observed in the bilayers using 3D FIB Tomography microstructures with lower porosity and higher porous garnet particle sizes.

To confirm the effects of the increased porous layer utilization on the bilayer ASR, the 99.99% porous layer active region thickness was calculated and plotted vs. porous layer porosity in Figure 5.22a, and the bilayer ASR was plotted vs. the 99.99% porous layer active region thickness in Figure 5.22b. However, the plots indicated the 99.99% active region thickness was very poorly correlated with porosity, given that the active region thickness did not approach 0 as porosity increased to 100%. The ASR was similarly observed to have very poor correlation to the active region thickness, with the data forming three distinct groupings that projected to ASR values far greater than 1.000 Ω-cm^2. This was in strong contrast to the 3D FIB Tomography bilayers, where the bilayer ASR showed a linear relationship to the porous layer active region thickness in Figure 5.12d. However,

the 3D FIB Tomography bilayers also showed a strong correlation between the active regions thickness and porosity (Figure 5.12c). Given that bilayer ASR was well-correlated with porosity while sporadically correlated with active region thickness, it appeared the 99.99% active layer thickness was likely over-estimating the relevant porous layer thickness and therefore porosity was a more reliable controlling variable for bilayer ASR. This also suggested the bilayer ASR was more strongly determined by bilayer transport near the dense layer than initially thought. To confirm, the dense layer average normalized interfacial current density and the porous layer maximum average normalized interfacial current density for the 3D FIB Tomography bilayers were plotted together in Figure 5.23a and plotted separately for the column-based bilayers in Figures 5.23b and c. For both sets of bilayers, the ASR was well-correlated with the dense layer average interfacial current density (indicated by linear intercepts close to 1.000 Ω-cm^2) and poorly coordinated with the porous layer maximum interfacial current density. The reason for correlation with one parameter but not the other was not immediately apparent, though it may indicate the bilayer ASR depended on ion transport in the entire transition region in the porous layer and not just the porous layer directly contacting the dense layer.

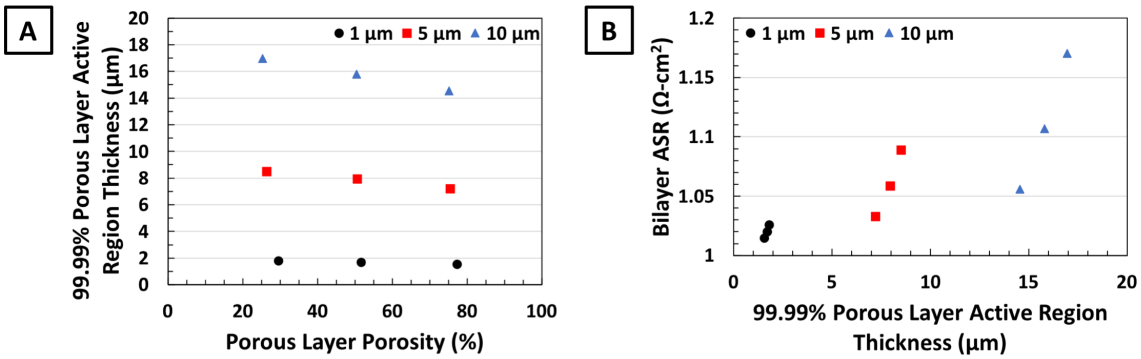

Figure 5.22: A) porous layer active region thicknesses vs. porous layer porosity. B) column-based bilayer ASR vs. porous layer active region thickness. Both plots were separated by column diameter.

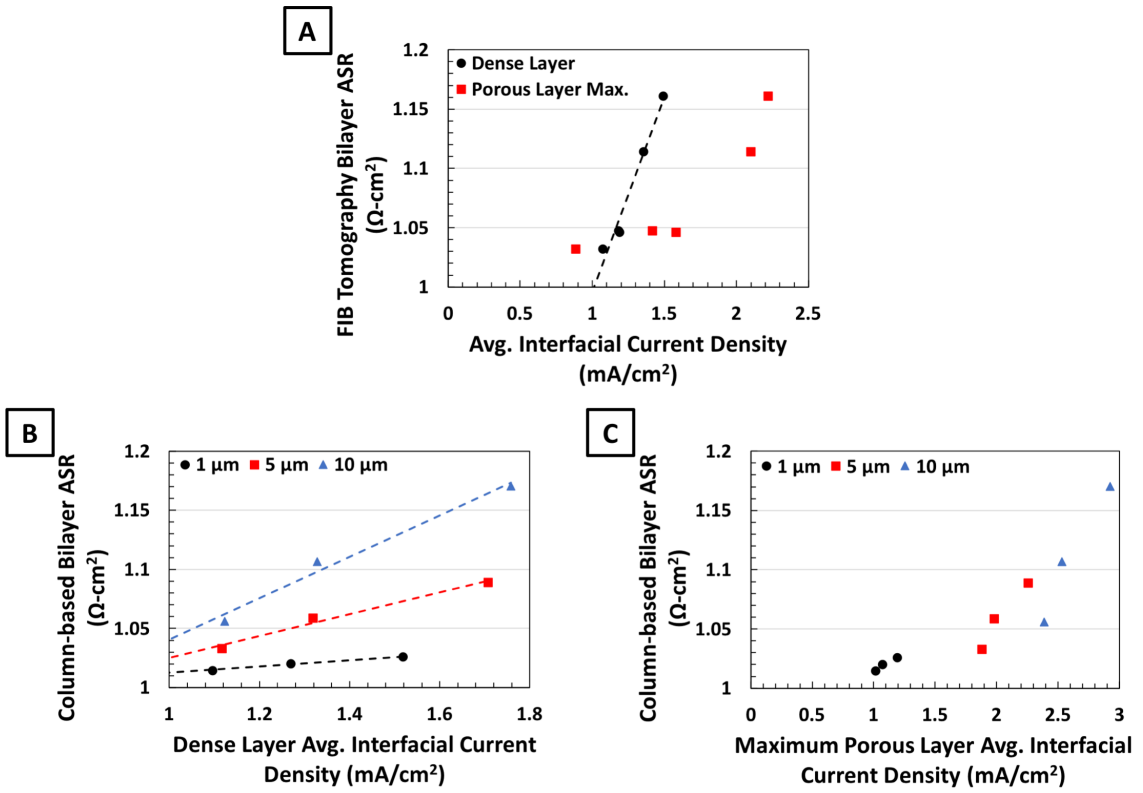

Figure 5.23: A) 3D FIB Tomography bilayer ASR vs. average normalized interfacial current density in the dense layer and the maximum in porous layer. Column-based bilayer ASR vs. B) average normalized interfacial current density in the dense layer and C) maximum average normalized interfacial current density in the porous layer.

5.3.4. Comparing Simulation Results for Column-based Bilayers and 3D FIB Tomography Bilayers:

In regarding the ASR, the very high porosity Template bilayer with 78.98% porosity was most similar to the column-based bilayer with 77.2% porosity and 1 µm dimeter columns, while the low porosity Porous 3 bilayer with 26.45% porosity was most similar to the column-based bilayer with 25.3% porosity and 10 µm dimeter columns. The distributions of ionic current fraction were also similar for these pairs of bilayers. Interestingly, the average normalized interfacial current density of the very high porosity Template bilayer and the 77.2% porosity, 1 µm dimeter column-based bilayer appeared very similar, while the low porosity Porous 3 bilayer had a noticeably smaller spike in the

interfacial current density curve than the 25.3% porosity, 10 μm dimeter column-based bilayer. This was unexpected given the 3D FIB Tomography microstructures had significant amounts of tortuosity and constricting bottlenecks that reduced the porous layer effective conductivity, which should concentrate the interfacial current density more in the porous layer cross-sections near the dense layer to minimize bilayer ASR. Examining Figure 5.9 again shows the low porosity Porous 3 bilayer had high ionic current density regions both at the porous garnet-electrode interface and the interior of the porous garnet, while the column-based bilayers only had high ionic current density regions at the porous garnet-electrode interfaces. This meant for the same porosity and same nominal transport distances through the porous layer, more of the porous garnet volume in the low porosity Porous 3 bilayer was utilized compared to the column-based bilayer, allowing interfacial current to spread over a wider area and reduce the porous layer interfacial current density. Based on these results, increasing porous layer porosity and decreasing porous layer particle size were the best approaches to decreasing bilayer ASR and interfacial current densities, with the possibility that engineering some tortuosity into the porous microstructure could further reduce interfacial current densities by improving access to the underutilized porous garnet interior.

5.3.5. Effect of Changing Porous Layer Thickness:

Based on observations that most of the porous layer was not utilized for transporting current, we previously theorized that increasing or decreasing the porous layer thickness would not alter the bilayer ASR so long as the porous layer remained thicker than the main active region of the porous layer. Given the estimates of the active region thickness were

likely too high, this suggested the relevant portion of the porous layer was extremely small for the column-based bilayers studied here. To determine if this was true, the equilibrium electric potential simulations were repeated on the column-based bilayers with porous layer thicknesses of 10 μm and 30 μm. Tables 5.4, 5.5, and 5.6 show the bilayer ASR values calculated for bilayers with 10 μm thick porous layers, bilayers with the original 20 μm thick porous layers, and bilayers with 30 μm thick porous layers, respectively. To within three decimal places, the ASR values for every combination of porosity and column diameters were identical across the different porous layer thickness. The ionic current fraction and interfacial current density distributions were also virtually identical across the different porous layer thickness. This confirmed the bilayer ASR was virtually independent of the porous layer thickness as long as it is thicker than the active porous layer thickness. Since practical bilayers for commercial use do not use porous layers less than 10 μm thick due to low electrode loading capacity, it was unnecessary to continue simulating porous layers with even thinner electrodes.

Table 5.4: Simulated column-based bilayer ASR for 10 μm thick porous layer, over the range of nominal porosity values (75%, 50%, and 25%) and column diameters (10 μm, 5 μm, and 1 μm).

	Nominal Porosity		
Column diameter (μm)	**75%**	**50%**	**25%**
10	1.056	1.107	1.170
5	1.033	1.059	1.089
1	1.015	1.020	1.026

Table 5.5: Simulated column-based bilayer ASR for 20 μm thick porous layer, over the range of nominal porosity values (75%, 50%, and 25%) and column diameters (10 μm, 5 μm, and 1 μm).

	Nominal Porosity		
Column diameter (μm)	**75%**	**50%**	**25%**
10	1.056	1.107	1.170
5	1.033	1.059	1.089
1	1.015	1.020	1.026

Table 5.6: Simulated column-based bilayer ASR for 30 μm thick porous layer, over the range of nominal porosity values (75%, 50%, and 25%) and column diameters (10 μm, 5 μm, and 1 μm).

Column diameter (μm)	Nominal Porosity		
	75%	**50%**	**25%**
10	1.056	1.107	1.170
5	1.033	1.059	1.089
1	1.015	1.020	1.026

5.3.6. Effect of 50% Electrode Infiltration:

Up to now, this work presented focused on the ideal case of the porous layer fully infiltrated by the Li-metal electrode and allowing current to transport directly from the Li-metal electrode to the dense layer. However, it is always possible the electrode will not fully infiltrate during initial battery fabrication or will lose contact with the dense layer during cycling. This is particularly relevant when considering the infiltration of non-wetting electrodes or particle-based electrodes, so investigating the effects of partial electrode infiltration is important. To that end, additional simulations were run on bilayers with electrodes infiltrated 50% of the distance from the top of the porous layer towards the dense layer. Figure 5.24 shows the resulting bilayer symmetric cells, where the porous layers of the bilayers were 50% infiltrated with the positive Li-metal electrode (red color), and a thin negative Li-metal electrode (blue color) was attached to the planar surface of the dense layers. The electrolyte was shown in yellow, current collectors were shown in grey, and the empty pores were shown in black.

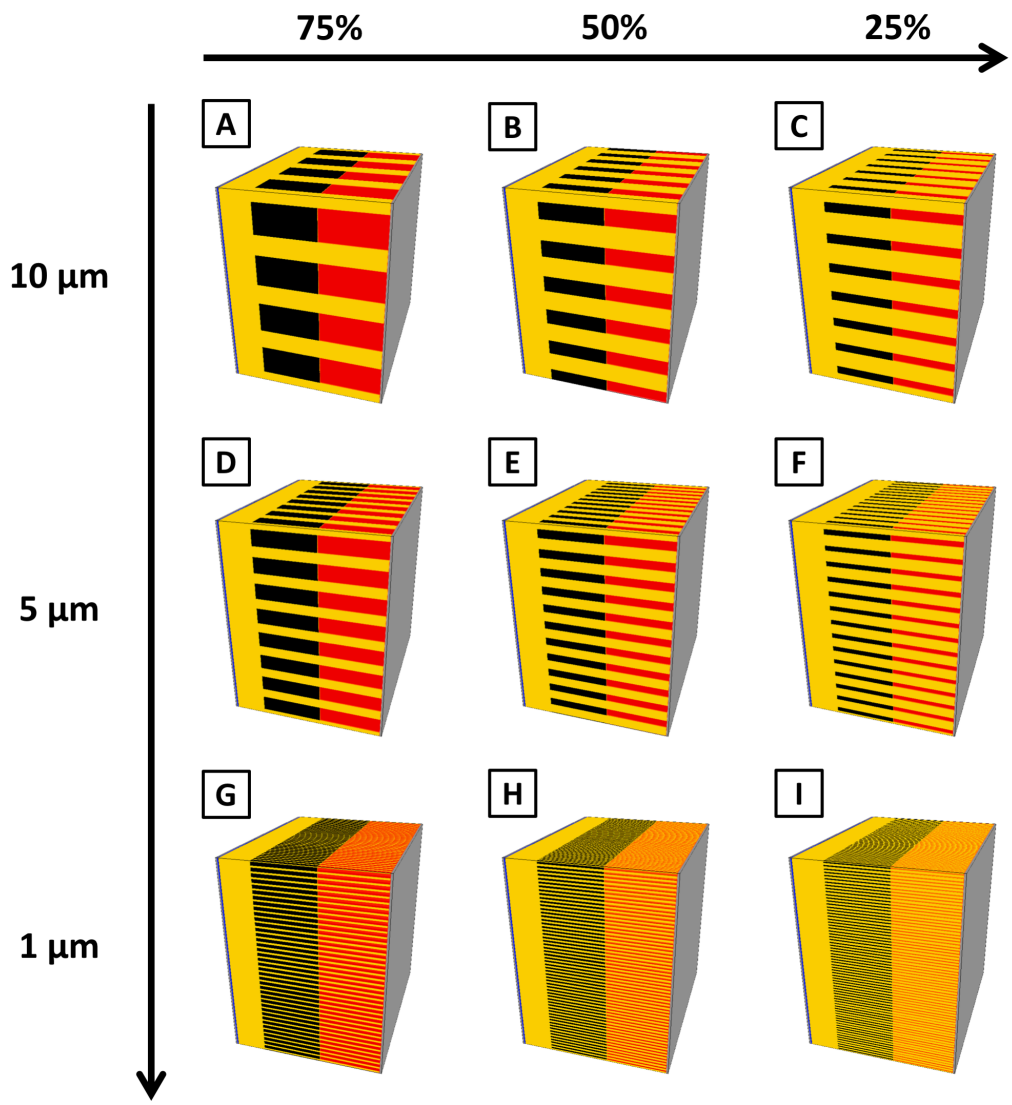

Figure 5.24: Schematic of 50% infiltrated column-based bilayer symmetric cells for range of nominal porosity values (75%, 50%, and 25%) and column diameters (10 µm, 5 µm, and 1 µm). The garnet electrolyte was yellow, the positive Li-metal electrode was red, the negative Li-metal electrode was blue, the current collectors were grey, and the empty pores were black. All visualizations were stretched by 3x along the Z-axis.

The local electric field strength was calculated within each 50% infiltrated bilayer and shown in Figure 5.25. The porous layer of each bilayer was divided into two regions: 1) a high field strength region at the maximum color bar cutoff corresponding to empty pores near the dense layer, and 2) a transition region of decreasing field strength corresponding to infiltrated pores far from the dense layer. This distribution originated

from the positive Li electrode ending before reaching the dense layer, forcing electronic current in the Li electrode to convert to ionic current in the porous garnet and transport solely as ionic current through the empty pore region. This also created high field strength zones at the dense garnet-porous garnet interface and the dense layer interior, since the high electric field in the porous layer transferred to the dense layer through a limited interfacial area. As porosity decreased for fixed column diameter, the size of the transition region in the porous layer decreased, the electric field strength in the empty pore region and the dense layer decreased relative to the color bar cutoff, and the dense layer electric field became more homogenous. As column diameter decreased for fixed porosity, the size of the transition region in the porous layer significantly decreased, the electric field strength in the empty pore region and the dense layer decreased relative to the color bar cutoff, and the dense layer electric field became more homogenous. This indicated the porous layer porosity and the column diameter were equally important for the determining electric field strength distribution in the 50% infiltrated bilayers.

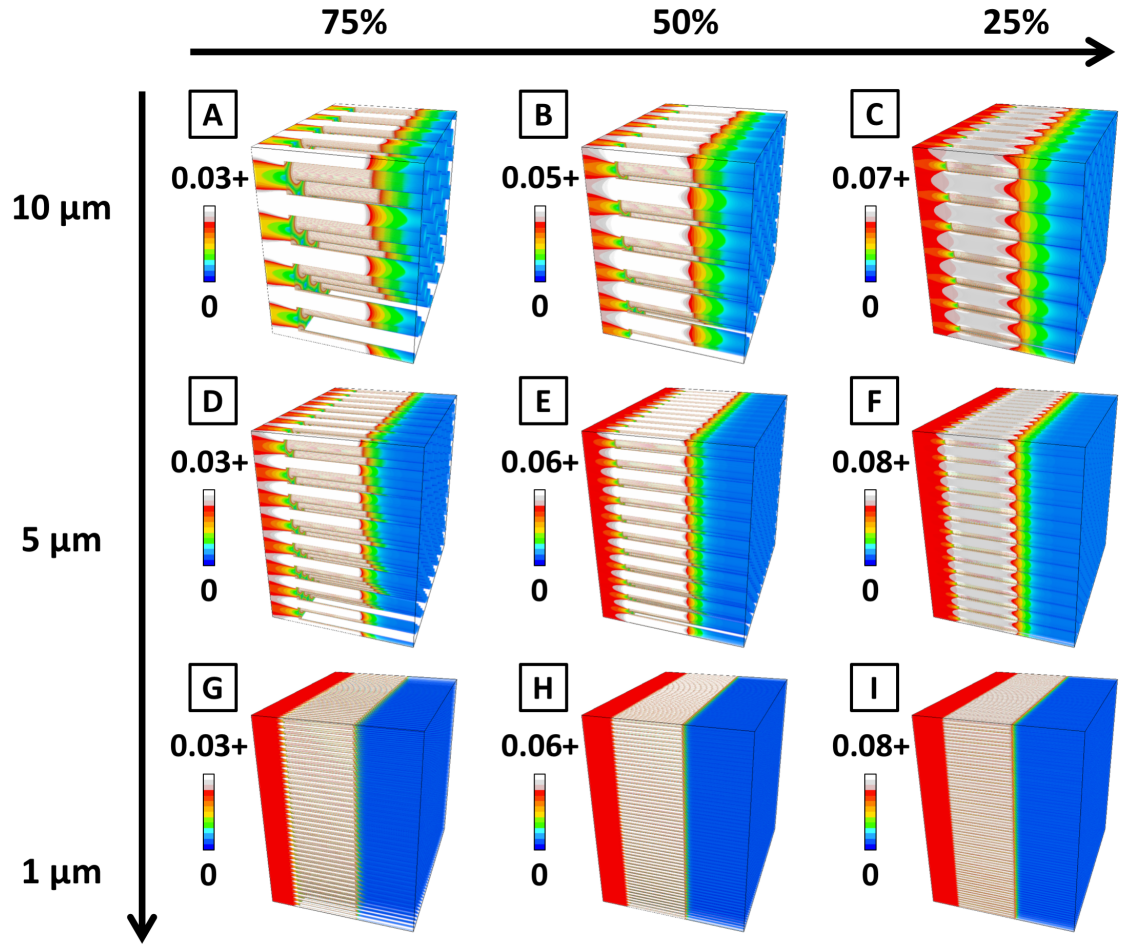

Figure 5.25: Simulated electric field for 50% infiltrated column-based bilayers for range of nominal porosity values (75%, 50%, and 25%) and column diameters (10 µm, 5 µm, and 1 µm). Units are Volts/µm. The maximum cutoff of the color bar was set to 150% of the average electric field strength at the dense layer-negative electrode interface. All visualizations were stretched by 3x along the Z-direction.

Figure 5.26 shows the ASR values for the 50% infiltrated bilayers for the previously discussed ranges of porosity and column diameters, as well as 10 µm, 20 µm, and 30 µm thick porous layers. The ASR of the 50% infiltrated bilayer increased with increasing porosity for all column diameters and porous layer thicknesses, in sharp contrast to the fully infiltrated bilayers that showed decreasing ASR with increasing porosity. The differences were due to the presence of the dense garnet-electrode interface in the fully infiltrated bilayers and the absence of that interface in the 50% infiltrated bilayers. The

lowest ASR was 2.474 Ω-cm^2 for 1 µm diameter columns, 25% nominal porosity, and 10 µm thick porous layer, and the highest ASR was 15.285 Ω-cm^2 for 10 µm diameter columns, 75% nominal porosity, and 30 µm thick porous layer. There was also a clear pattern of 50% infiltrated bilayer ASR increasing with increasing porous layer thickness, likely due to the increased distance the ionic current traveled through the porous garnet. Interestingly, increasing the column diameter generally increased the 50% infiltrated bilayer ASR, but the amount of increase was greater for higher porosity bilayers. Moreover, the difference in the ASR of a 50% infiltrated bilayer with 1 µm and 10 µm diameter columns became smaller as the porous layer thickness increased, with the 1 µm diameter columns giving a higher ASR than the 5 µm diameter columns for 30 µm thick porous layers and 75% nominal porosity. These observations and the similar appearances of the three plots suggested the 50% infiltrated bilayer ASR likely was a consistent function of the porous layer porosity and the rate the function scaled with porosity was affected by the column diameter. While this was similar to the fully infiltrated bilayers, the scaling rate of the function relating the 50% infiltrated bilayer ASR to porosity was also affected by porous layer thickness, which became a more dominant factor than column diameter as thickness was increased.

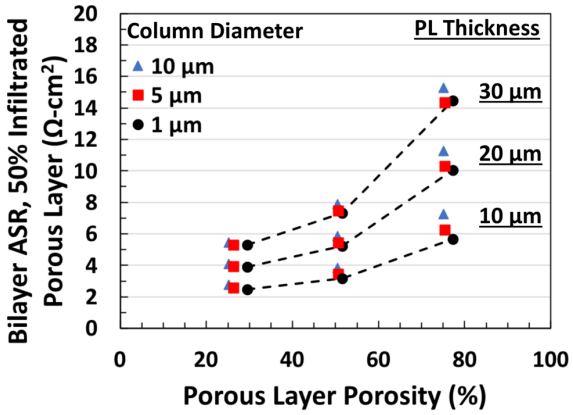

Figure 5.26: 50% infiltrated bilayer ASR for range of nominal porosity values (75%, 50%, and 25%), column diameters (10 µm, 5 µm, and 1 µm), and porous layer thicknesses (10 µm, 20 µm, and 30 µm).

Similar to the fully infiltrated bilayers, constant current density in the 50% infiltrated columns followed elongated arcs within parts of the columns with garnet-electrode interfaces that applied fixed boundary potentials. However, the lack of fixed boundary potential in the porous layer region with empty pores meant the current density spread out and became more homogenous within the column. After a long enough distance, the current density in the columns was uniform across the column cross-section, meaning all conduction pathways were virtually parallel to the column axis and following the minimum distance pathways. This homogenization of the current density became more complete and accounted for a larger fraction of the total column length as the porous layer thickness increased, which decreased the effect of column diameter on bilayer ASR.

To better observe the effects of the porous layer thickness, the column diameter was fixed at 10 μm and the 50% infiltrated bilayer ASR plotted for nominal porosities of 25%, 50%, and 75%, and porous layer thicknesses of 10, 20, and 30 μm in Figure 5.27. The 50% infiltrated bilayers ASR exhibited more consistent behavior than when plotting with different column diameters, displaying increasing ASR as porosity increased and consistently increasing ASR as the porous layer thickness increased. In fact, the ASR appeared to increase by fixed amounts when the porous layer thickness was increased, and the ASR changes were larger at higher porosity. Table 5.7 shows the 50% infiltrated bilayer ASR values for increasing porous layer thickness and increasing porosity, which showed the ASR changes were driven primarily by changes in porosity. Based on earlier discussion of conduction pathways through the columns, it was expected the increased ASR was largely due to increased length of the porous layer columns without infiltrated electrode, which accounted for half the total change in porous layer thickness, or 5 μm. Using the

ceramic fraction in the porous layer, geometric tortuosity of 1.0, constriction factor of 1.0, and percolation factor of 1.0, Equation 1.3 gave M-factors of 0.7475, 0.4954, and 0.2487 for the porous layers with column diameters of 10 µm and porosities of 25.25%, 50.46%, and 75.13%, respectively. The ASR was calculated for a 5 µm porous layer with the same intrinsic conductivity of 5 x 10^{-4} S/cm, modified by the M-factors, and recorded the results in Table 5.7. The actual ASR changes and the expected ASR change from adding 5 µm of porous layer without infiltrated electrode were in very good agreement, showing less than 0.4% differences.

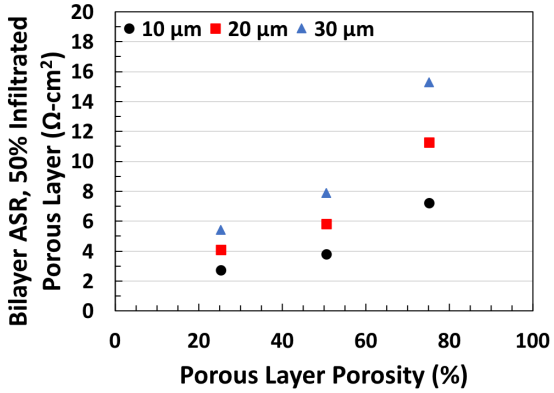

Figure 5.27: 50% infiltrated bilayer ASR vs. porous layer porosity, with column diameter fixed at 10 µm and the data delineated by porous layer thickness.

Table 5.7: Increase in simulated 50% infiltrated bilayer ASR for different changes in porous layer thickness and different porous layer porosities, as well as the ASR increase from adding 5 μm thick porous layer without infiltrated electrode. For all calculations, column diameter was fixed at 10 μm.

	Actual Porous Layer Porosity		
	25.25%	**50.46%**	**75.13%**
ASR increase from increasing porous layer thickness from 10 μm to 20 μm (Ω-cm^2)	1.341	2.024	4.035
ASR increase from increasing porous layer thickness from 20 μm to 30 μm (Ω-cm^2)	1.336	2.026	4.010
ASR increase from adding 5 μm of porous layer without infiltrated electrode (Ω-cm^2)	1.338	2.019	4.021

For the 50% infiltrated bilayer, the fraction of total current was plotted vs. distance from the dense layer in Figure 5.28 (a, c, e). The average normalized current density transported across the garnet-electrode interface was also plotted vs. distance from the dense layer in Figure 5.28 (b, d, f). The plots were split based on the porous layer thickness (A and B = 10 μm, C and D = 20 μm, E and F = 30 μm) and the curves within each plot were designated by the porous layer porosity. Examining the plots of total current fraction vs. distance from the dense layer, all plots showed current fractions of 1.0 between the dense layer and the end of the infiltration zone, after which the current fraction gradually decreased towards the top of the porous layer. For bilayers with 20 μm and 30 μm thick porous layers, the current fraction reached 0 at or before the top of the porous layer, while the bilayer with 10 μm thick porous layers reached a minimum current fraction of 0.095. Current fraction distribution was unaffected by the porous layer porosity, likely due to all current still flowing through the porous layer regardless of porosity. Examining the plots of average interfacial current density vs. distance from the dense layer, the interfacial

current density spiked at the end of the infiltration zone and gradually decreased towards the top of the porous layer. Increasing the sample porosity caused the interfacial current density of the spike and all points towards the top of the porous layer to increase. The maximum interfacial current densities were dramatically higher than the maximum interfacial current densities of the fully infiltrated bilayers, which only showed a maximum of 2.92 mA/cm^2. While the distribution was lengthened when the porous layer was made thicker, the shape of the distribution remained unchanged.

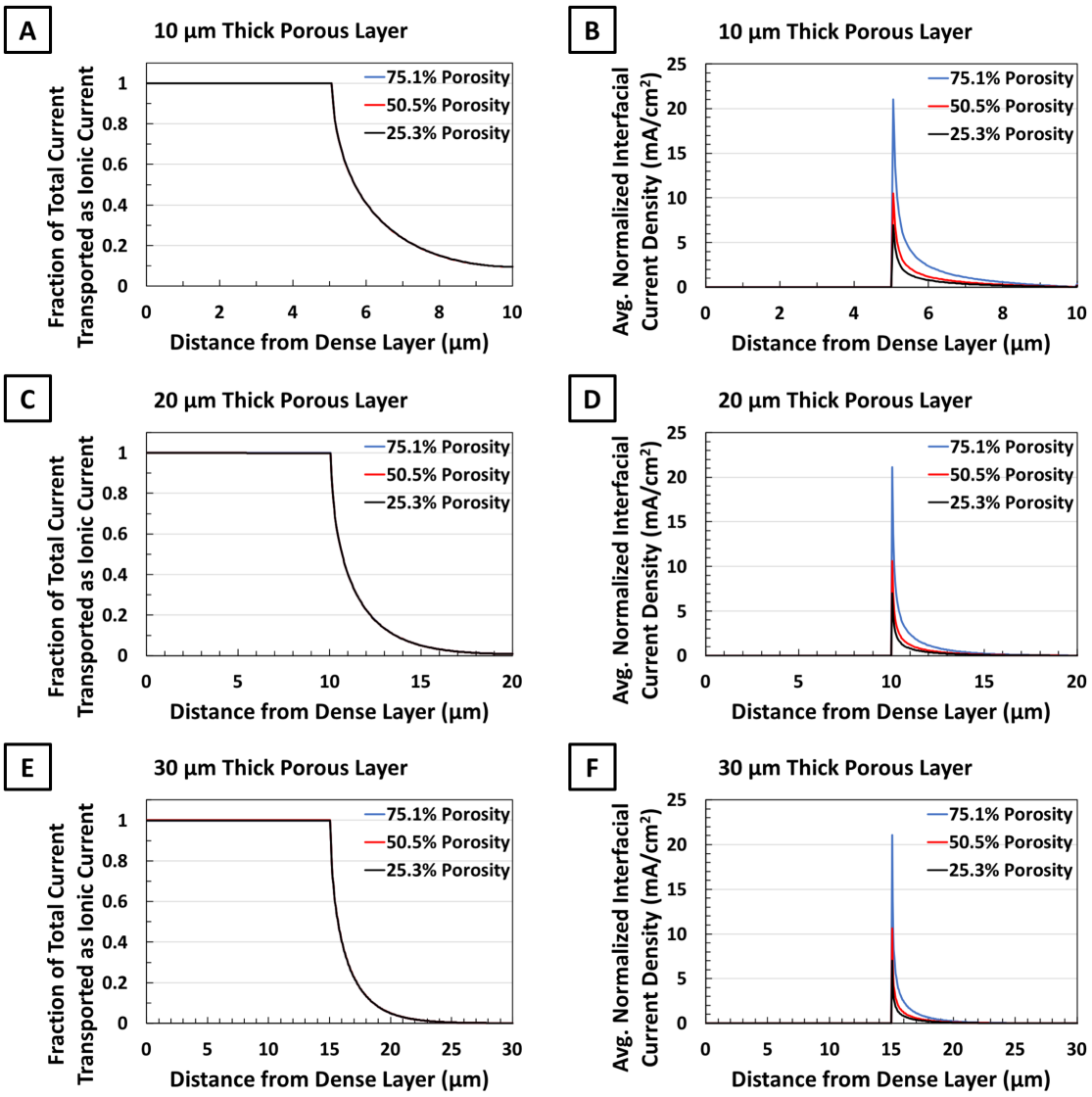

Figure 5.28: Fraction of total 50% infiltrated bilayer current flowing as ionic current through the garnet (A, C, E) and the average interfacial current density magnitude (B, D, F) vs. distance from the dense layer. The plots were split based on the porous layer thickness (A and B = 10 µm, C and D = 20 µm, E and F = 30 µm) and the curves within each plot were designated by the porous layer porosity.

5.3.7. Implications for Batteries Utilizing Bilayer/Trilayer Garnet Electrolytes:

Simulating the performance of Li-metal symmetric cell bilayers using column-based porous layers with varied microstructures helped answer several questions remaining from analyzing the bilayers using the 3D FIB Tomography microstructures. Fully infiltrated bilayers with porosities ranging from 25.3% to 77.2%, column diameters ranging

from 1 μm to 10 μm diameter, and porous layer thicknesses varying from 10 μm to 30 μm produced ASR's between 1.015 and 1.170 Ω-cm^2. The range of these ASR values was similar to the range of ASR values observed for the 3D FIB Tomography bilayers, demonstrating that low ASR was a universal feature of fully-infiltrated dense-porous bilayers. The porous layer porosity and the column diameter were both found to affect the bilayer ASR, with decreasing porosity linearly increasing bilayer ASR and increasing column diameter increasing the magnitude of the slope of the ASR-porosity relationship. Since the bilayer column diameter was essentially a proxy for the particle size of the porous garnet, this indicated that real porous garnet layers with high porosity and small garnet particle sizes would produce bilayers with the lowest ASR. The porosity had the greatest effect on the distribution of ionic current fraction near the dense layer, and a combination of porosity and column diameter determined the ionic current density in the garnet. This increased the list of benefits of using small porous garnet particle sizes and demonstrated the benefits of using high porosity porous layers to maximize the dense garnet-electrode interfacial area. The porous layer thickness did not have any noticeable effect on the bilayer, due to only the dense layer and a very small region of the porous layer being utilized for charge transport. Thus, the bilayer porous layer could be tailored to be thicker or thinner to match the desired electrode loading without the risk of radically increasing the bilayer ASR.

Simulations on 50%-infiltrated bilayers with porosities ranging from 25.3% to 77.2%, column diameters ranging from 1 μm to 10 μm diameter, and porous layer thicknesses varying from 10 μm to 30 μm produced ASR's between 2.754 and 15.285 Ω-cm^2. Increasing the porosity of the porous layer significantly increased the ASR of the

50%-infiltrated bilayers and dramatically increased the interfacial current densities at the porous garnet-electrode interface, with the maximum observed average interfacial current density reaching 21.07 mA/cm^2. Increasing the porous layer thickness also increased the ASR of the 50%-infiltrated bilayers but had no effect on the interfacial current densities. Increasing the column diameter increased the ASR of the 50%-infiltrated bilayers, though this change was the smallest relative to changing porosity or porous layer thickness. This was in stark contrast to the fully infiltrated bilayers, demonstrating the importance of achieving and maintaining full infiltration of the electrode in the porous garnet to fully benefit from the low resistance dense garnet-electrode interface. If full infiltration is not possible, then a 2nd electrolyte infiltrated between the electrode and the dense garnet layer would provide a low ASR pathway to transport Li-ions to the dense layer and bypass the high ASR porous layer garnet.

6. Conclusions and Future Outlook:

The research within this thesis investigated a range of potentially useful porous garnet electrolyte microstructures, with analysis of performance performed either experimentally via EIS measurements, theoretically via M-factor analysis, or theoretically via electrochemical simulations. Of note, simulations of dense-porous bilayer symmetric cells were found to be a superior tool for characterizing performance and provided significant insight into the granular details of charge transport within the garnet microstructure. From those insights, it was possible to identify microstructural trends likely to reduce bilayer ASR and improve overall performance metrics. A summary of these insights and conclusions is shown below, along with potential areas for future research.

6.1. Summary of Research Results:

6.1.1. Solid-State Li-Ion Electrolyte with Tape-Cast Porous Microstructure

Tape-cast porous LLCZN microstructures ranging from ~26% porosity to ~57% porosity were directly characterized using 3D FIB Tomography. The microstructures were reconstructed from the resulting image sets and analyzed for phase volume fraction, geometric tortuosity, constriction factor, and percolation factor. The microstructure factor, or M-factor, was then calculated to determine how much the porous microstructure inhibited ion transport by reducing the effective ionic conductivity of the porous garnet. The garnet and pore phases were found to be highly connected, providing percolation factors of nearly the maximum value 1.0 and showing that connectivity variations had minimal effect on the M-factor. Conversely, the M-factor was strongly dependent on the volume fraction of the phase being analyzed, followed by the constriction factor (or

bottleneck factor), and finally the geometric tortuosity. While surprising that the geometric tortuosity was the 3rd most important factor for ion transport, this was observed for all tape-cast samples across the porosity range. The LLCZN M-factor was found to reach a minimum of 0.160 for the highest porosity sample and a maximum of 0.410 for the lowest porosity sample, while the corresponding pore phase M-factor reach a maximum of 0.267 and a minimum of 0.052. This immediately demonstrated that an optimal tape-cast porous LLCZN microstructure requires balancing a high LLCZN M-factor (to minimize porous layer ASR) with a high pore phase M-factor (to ensure effective electrode infiltration). The relatively low values of the pore phase M-factor compared to the garnet M-factor suggested diffusion through the pore network was more easily affected by changes to the sample microstructure. While this was expected to only slightly affect the infiltration of wetting electrodes, non-wetting electrodes and particle-based electrodes are thought to greatly benefit from easier diffusion through the pore network. This suggested that maximizing the pore phase M-factor by increasing sample porosity would provide greater gains due to better infiltrated electrodes offsetting losses due to lower LLCZN effective conductivity and higher ASR. This was supported by higher porosity allowing for higher electrode loading while reducing electrolyte mass, thus facilitating higher battery energy density. Alternatively, increasing the diameters of bottlenecks within the garnet and pore phases would improve the M-factor and thus ion transport without requiring a penalty to the M-factor of the opposing phase, as was the case for changing the sample porosity.

To confirm the observed trends of decreasing M-factor with increasing sample porosity, we performed EIS measurements on a range of tape-cast porous LLCZN samples to measure the effective conductivity and used SEM images of polished, epoxy-filled cross-

sections to estimate the microstructure porosity. This "2D porosity" was found to be very close to the true "3D porosity" obtained from the 3D reconstructions of several microstructures. The effective ionic conductivity decreased exponentially as 2D porosity increased, similar to observations of the garnet M-factor decreasing exponentially with increasing 3D porosity. However, the theoretical effective conductivity values estimated from the M-factor values were consistently higher than the measured effective conductivity values. This suggested that bulk conductivity was also decreasing with increasing tape-cast sample porosity, with one possible explanation being enhanced Li-loss during sintering due to the increased garnet surface area of the higher porosity microstructures. This was further supported by XRD analysis of 2D porosity samples that showed nearly pure cubic phase LLCZN with some minor impurity peaks, indicating the decrease in sample conductivity was not due to LLCZN phase decomposition. The potential influence of higher sample surface area on bulk conductivity of tape-cast porous LLCZN samples emphasized the importance of carefully maintaining optimum sintering conditions when fabricating solid-state Li-ion electrolytes with significant microstructural porosity.

6.1.2. Solid-State Li-Ion Electrolyte with Template-based Porous Microstructure:

A cellulose fiber template was infiltrated with LLZO sol gel precursor solution and the infiltrated template was sintered to burn away the organic components. As a result, remaining sintered garnet adopted the same microstructure as the template fibers and was found to provide an extraordinarily high porosity of ~79%. The template-based porous LLZO microstructure was directly characterized using 3D FIB Tomography and the performance of the microstructure analyzed in a similar manner to the tape-cast garnet. The

template-based garnet M-factor was 0.060 and the corresponding pore phase M-factor was 0.201, suggesting that effective ionic conductivity of the garnet structure was significantly reduced and diffusion through the pore network was likely moderately obstructed. Transport through the garnet microstructure was primarily limited by the low LLZO volume fraction, while diffusion in the pore phase was primarily limited by bottlenecks that resulted in a low constriction factor. Given the average feature size and bottleneck size in the pore phase were significantly larger than in the garnet phase, it was surprising the pore phase constriction factor was much lower than the garnet constriction factor. In contrast, the much lower tortuosity of the pore phase resulted in a tortuosity reduction factor much closer to 1.0 when compared to the garnet phase. Notably, significant anisotropy was observed in the garnet phase tortuosity, with a low tortuosity plane and a high tortuosity direction normal to this plane. This was consistent with the expected orientation of the fibers within the cellulose template.

Comparing the template-based microstructure to the tape-cast microstructures, the template-based microstructure was by far the most porous microstructure examined in this work. By comparison, the tape-cast microstructures displayed a maximum porosity of 56.67%, though this was likely not the upper limit on porosity obtainable from future tape-cast microstructures. The garnet M-factor of the template-based microstructure was lower than the garnet M-factor of the highest porosity tape-cast microstructure, consistent with the trend of decreasing M-factor with decreasing volume fraction. However, the pore phase M-factor of the template-based microstructure was also lower than the pore phase M-factor of the highest porosity tape-cast microstructure. Comparing the different microstructures, the template-based microstructure pore phase was more constricted by bottlenecks than the

tape-cast microstructure pore phase for comparable geometric tortuosity values. This further supported the earlier conclusion that the garnet and pore phase performance could be significantly improved if the diameter of bottlenecks were increased relative to the average garnet/pore phase diameters. Barring that, a medium porosity microstructure (~40-55% porosity) appears to provide the ideal compromise between maximizing the garnet effective conductivity and maximizing electrode infiltration/loading capacity.

6.1.3. Simulation of 3D FIB Tomography Microstructures:

The previous M-factor analyses showed that high porosity garnet microstructures (>50%) had low effective conductivities and thus produce high resistance/ASR values. However, symmetric cell cycling in dense-porous garnet bilayers using Li-metal anodes infiltrated into porous garnet showed very low bilayer ASR and overpotentials. This suggested the M-factor analysis was overestimating the ASR due to the porous garnet, which was attributed to the M-factor describing Li-ion transport through the entire porous layer. In contrast, a full-infiltrated bilayer has the electrode interfacing directly with the dense layer, theoretically allowing most current to bypass the high ASR porous layer and flow directly into the low ASR dense layer. To test this, we digitally assembled dense-porous bilayer symmetric cells by attaching a 5 μm thick dense layer to a porous layer made of the 3D FIB Tomography microstructure. The pore space was filled with the positive electrode, a thin negative electrode was attached to the planar surface of the dense layer and a potential difference of 1.0 V was applied to the system. By simultaneously solving the Laplace equation for blocks of the bilayer, the equilibrium electric potential

distribution in the bilayer was iteratively solved. The local electric field and current densities were then calculated, which allowed for the calculation of the bilayer ASR.

The bilayers were found to have ASR values as low as 1.032 Ω-cm^2 for the highest porosity microstructure (i.e., the template-based porous garnet, 78.98% porosity) and as high as 1.161 Ω-cm^2 for the lowest porosity microstructure (i.e., the tape-cast porous garnet, 26.45% porosity). These results were similar to the bilayer/trilayer ASR values estimated from published symmetric cell cycling results and represented only a 12.5% increase in bilayer ASR despite a 50% difference in porous layer porosity. These low ASR values resulted from only a small region of the porous layer being actively utilized to transport charge while most charge transport occurred across the dense garnet-electrode interface. Increasing the porous layer porosity increased the dense garnet-electrode interfacial area, thus allowing more current to bypass the high ASR porous layer. The relative insensitivity of the fully-infiltrated bilayer to changes in the porous layer porosity was particularly encouraging, indicating well-infiltrated bilayers and trilayers with a range of porosities could provide ASR values close to the ASR of dense layers alone and fully benefit from using a thin dense layer instead of a thick dense pellet. The simulations also showed a bilayer with a higher porosity porous layer outperformed a bilayer with a lower porosity porous layer in other meaningful ways. Specifically, increasing the porous layer porosity reduced the current densities within the bilayer garnet, reduced the interfacial current densities at the garnet-electrode interfaces, and increased the maximum electrode areal loading capacity of the bilayer. If the decreased electrolyte mass is included along with increased electrode loading, the gravimetric capacity of a high porosity bilayer was dramatically higher than a low porosity bilayer. In theory, the best bilayer structure is a

dense layer alone, since this provides the minimum ASR, the minimum current density, and maximum "porosity" possible. However, the mechanical strength of such thin ceramic layers is limited, so a porous layer appears required to support the dense layer.

Of note was the ability of the bilayer to defy the predictions of the earlier M-factor analysis and display near-dense layer ASR values for high porosity, although this depended heavily on the electrode's ability to interface directly with the dense layer. Any situation where the electrode did not contact the dense layer (i.e., failure to initially infiltrate or loss of contact during cycling) forced the current flowing from the positive electrode to be transported entirely by the porous layer until reaching the dense layer, rather than largely transporting directly across the dense garnet-electrode interface. In that situation, the reduced effective conductivity of the porous layer was expected to substantially increase the bilayer ASR and garnet/interfacial current densities, with further increases in porosity resulting in worsening performance. While wetting electrodes will likely infiltrate through the porous layer to the dense layer and avoid this issue, infiltrating non-wetting electrodes or particle-based electrodes prone to agglomeration will depend strongly on the effective diffusivity of the pore phase network. Even if full infiltration is achieved, many electrode materials have far lower electronic and ionic conductivity values than Li-metal electrodes, which meant only the electrode contacting the dense layer would operate in the ideal low ASR condition, while the majority of the electrode instead will transfer Li-ions into the porous layer and operate in high ASR conditions. Additionally, the discrete nature of particle-based electrodes significantly inhibits current transport between neighboring electrode particles, resulting in a similar split between low ASR conditions for the electrode contacting the dense layer and high ASR conditions for the majority of the electrode

particles. For these situations, a second Li-ion conducting electrolyte infiltrated in the pores could quickly transport Li-ions from the electrodes to the dense layer and bypass the high ASR porous garnet.

6.1.3. Simulation of Column-based Microstructures:

Simulations of bilayers using the 3D FIB Tomography microstructures and predictions of effective conductivity from M-factor analyses of those microstructures emphasized the importance of fully infiltrating electrodes into the bilayer to facilitate low ASR transport from the electrode directly into the dense layer. Still, interest remained in understanding how varying aspects of the microstructure affect performance under full-infiltrated conditions and what changes occur with only partial infiltration. To answer these questions, simulations were run on a series of artificial bilayer symmetric cells where the porous layers were composed of non-contacting circular columns. This approach allowed for independent control of the microstructure by varying the nominal porous layer porosity, the column diameter, and the porous layer thickness/column height while avoiding the potentially confounding influences of tortuosity and bottlenecks. Moreover, the column-based bilayers could be reduced to the smallest repeat unit and periodic boundary conditions applied within the XY-plane to dramatically reduce the simulation time relative to the time necessary for the 3D FIB Tomography microstructures.

We used column-based bilayers nominal porosities in the porous layer ranging from 75% to 50% to 25%, the column diameters ranging from 10 μm to 5 μm to 1 μm, and porous layer thickness/column heights ranging from 10 μm to 20 μm and 30 μm. For fully infiltrated bilayers, the minimum ASR observed was 1.015 170 Ω-cm^2 for 1 μm diameter

columns and 75% nominal porosity, while the highest ASR observed was 1.170 Ω-cm^2 for 10 μm diameter columns and 25% nominal porosity. These ASR values were similar to the range of ASR values observed for bilayers using the 3D FIB Tomography microstructures, demonstrating that low ASR was a universal feature of fully-infiltrated dense-porous bilayers. Column diameter had the greatest effect on the bilayer ASR and the extent of the transition region in the porous layer between the high current density dense layer and the majority of the unutilized porous layer. Since the bilayer column diameter was essentially a proxy for the particle size of the porous garnet, this suggested that real porous garnet layers with small garnet particle sizes would produce bilayers with low ASR. The porosity had the greatest effect on the distribution of current near the dense layer, and a combination of porosity and column diameter determined the current density in the garnet. This increased the list of benefits of using small porous garnet particle sizes and demonstrated the benefits of using high porosity porous layers to maximize the dense garnet-electrode interfacial area. The porous layer thickness did not have any noticeable effect on the bilayer due to only the dense layer and a small region of the porous layer being utilized for charge transport. Thus, the bilayer porous layer could be tailored to be thicker or thinner to match the desired electrode loading without the risk of radically increasing the bilayer ASR.

Simulations on 50%-infiltrated bilayers with porosities ranging from 25.3% to 77.2%, column diameters ranging from 1 μm to 10 μm diameter, and porous layer thicknesses varying from 10 μm to 30 μm produced ASR's between 2.754 and 15.285 Ω-cm^2. In particular, increasing the porosity of the porous layer significantly increased the ASR of the 50%-infiltrated bilayers and dramatically increased the interfacial current densities at the porous garnet-electrode interface, with the maximum observed average

interfacial current density reaching 21.07 mA/cm^2. Increasing the porous layer thickness also increased the ASR of the 50%-infiltrated bilayers but had no effect on the interfacial current densities. Increasing the column diameter further increased the ASR of the 50%-infiltrated bilayers, though this change was the smallest relative to the changes due to changing porosity or porous layer thickness. This contrasted greatly to the fully infiltrated bilayers, demonstrating the importance of achieving and maintaining full infiltration of the electrode in the porous garnet to benefit fully from the low resistance dense garnet-electrode interface. If full infiltration was not possible, then a second electrolyte infiltrated between the electrode and the dense garnet layer could provide a low ASR pathway to transport Li-ions to the dense layer and bypass the high ASR porous layer garnet. Moreover, replacing the porous layer garnet with a porous layer of higher conductivity electrolyte may decrease interfacial and overall garnet current densities by increasing the transition region thickness and improving current density homogeneity within the porous electrolyte.

6.2. Future Work:

This work produced a number of findings that improve understanding of variable porosity solid-state Li-ion conducting electrolytes and support ongoing efforts to create all solid-state batteries utilizing these complex microstructures. Those findings also raise further questions and suggest several potential avenues for future research.

A clear extension of this work would involve characterizing the microstructures of a larger pool of porous solid-state electrolytes and determine the benefits and limitations of each, with the goal of identifying either the best microstructures or methods to improve existing ones. The striking differences between the largely isotropic tape-cast garnet and the anisotropic template-based garnet suggest possibilities of tailoring the porous structure to preferentially orient the pore and garnet networks along the Z-axis of the 3D microstructures (i.e., the direction that ionic current nominally flows), thus decreasing tortuosity and improving ion transport/electrode infiltration. 3D printing of garnet porous layers may lend itself to this approach, so characterizing 3D printed microstructures and comparing them to tape-cast and template-based structures could prove insightful. This work also showed that bottlenecks were substantial inhibitors of efficient ion transport through the porous layer, suggesting that reducing or eliminating bottlenecks within the porous microstructure could substantially improve porous layer effective conductivity. This may provide small improvements in fully infiltrated bilayers but yield more substantial improvements in partially-infiltrated bilayers or bilayers using discrete, particle-based electrodes.

The ability to simulate bilayer performance from artificial structures (such as the column-based porous layers) or real microstructures (such as 3D FIB Tomography

reconstructions) offers a wide array of opportunities for future work. Our investigations of bilayers 50%-infiltrated with Li-metal anodes showed bilayer ASR increased substantially with loss of contact with the dense layer. Further investigation of bilayer ASR for a range of electrode infiltration amounts is useful to identify how quickly the bilayer ASR increases as the infiltration amount decreases. This could reveal that the bulk of the increase was from the initial loss of contact with the dense layer (emphasizing the importance of maintaining the dense garnet-electrode interface or including a high conductivity intermediary electrolyte), or the decrease may be more drawn out (suggesting some loss of contact would still result in acceptable bilayer ASR values). A similar study based on the 3D FIB Tomography microstructures would reveal whether the effects of tortuosity and bottlenecks were important only for determining the porous layer effective conductivity or if these structural features have additional impacts on ASR, current density, and other metrics of bilayer performance. Extending the simulation to include different conductivity electrolytes supports testing the use of higher conductivity electrolytes in the porous layer as a possible way to reduce current densities. Additionally, charge transfer resistance at interfaces between different materials can be a significant source of ASR in a battery and was not covered in the studies presented in this thesis. Implementing charge transfer resistance into the bilayer simulations should increase the bilayer ASR and may also alter the distribution of current density across the garnet-electrode interface, potentially decreasing current densities within the bilayer.

A goal of potential research should include furthering collaboration with other research groups to expand the bilayer simulations to include more complex electrodes, such as electrode/binder/electronic conductor assemblies associated with electrically insulating

electrodes (e.g., LCO or sulfur). The symmetric cell simulations in this work provided substantial information regarding the performance of the solid-state garnet bilayers utilizing wetting Li-metal electrodes, so even greater breakthroughs are possible by studying how different electrode materials and electrode assemblies interact with the garnet bilayers. Given the prevalence of discrete, particle-based electrodes such as LCO and NMC (known to have poor electronic conductivity), simulating such systems could highlight possible limitations in solid-state batteries utilizing these electrodes and guide efforts to address those limitations. Extending the bilayer simulations from equilibrium, steady-state conditions to dynamic, time-dependent conditions could help describe the changes in an actively cycling bilayer battery. Such full cell simulations are technologically feasible, yet simulation studies are in early stages of investigating solid-state battery performance, especially for LLZO-based garnet electrolytes with complex structures. Collaboration, experience, and the capacity to simulate cycling behavior of full cells with complex solid-state electrolytes would greatly expand scientific understanding of a promising battery architecture and potentially have a lasting impact on energy storage and consumption in the world.

Appendix:

Appendix A: MATLAB Code used to Reduce Interface Artifacts and Curtain Artifacts in Segmented Images:

1. Import the segmented 2D/3D TIFF image(s) for the current sample and store in the raw 2D/3D image matrix, "Image".
2. Begin Part 1: interface artifact removal
    a. Assign value to user-defined variables: "maximum change length," "minimum contiguous particle size," "maximum gold expansion."
    b. Identify all contiguous pixels of each phase in the image (excluding pore phase).
        i. If each group of contiguous pixels had a pixel count less than/equal to "minimum contiguous particle size", then change that group to the average of the surrounding neighbors.
    c. Identify all contiguous gold phase pixels.
        i. Loop 1 start: expand gold phase into neighboring LLCZN and secondary phase to remove double layer coating artifact.
            1. Identify neighboring pixels around contiguous gold pixels.
            2. If neighboring pixels are LLCZN/secondary phase AND current loop iteration was less than/equal to the "maximum gold expansion", then change neighboring pixels to gold phase.
        ii. Loop 1 (Step 2.a.i) ends when loop iteration equals the "maximum gold expansion."
    d. Loop 2 start: split the image into row/column, identify contiguous pixels of each phase, and change each group of contiguous pixels to match neighboring pixels if that group has a length less than/equal to "minimum contiguous length."
        i. Select a row/column of the image and identify all contiguous phase pixels.
        ii. Identify the neighboring pixels of the contiguous phase.
        iii. If both neighboring pixels were the same AND the length of a given group of contiguous phase pixels was less than/equal to "minimum contiguous particle size," change the contiguous pixels to match the neighboring pixels.
        iv. Loop 2 (Step 2.f) ends when all rows and columns have been scanned across.
    e. Loop 3 start: split the image into row/column, identify contiguous secondary phase pixels, and remove secondary phase pixels based on neighboring pixels and whether length of contiguous secondary phase pixels is less than/equal to "maximum change length."
        i. Select a row/column of the image and identify all contiguous secondary phase pixels.
        ii. Identify the neighboring pixels of the contiguous secondary phase.

iii. If the length of a given group of contiguous secondary phase pixels was less than/equal to "maximum change length," remove/retain the secondary phase based on the neighboring pixels.
    1. If neighboring pixels were exactly 1 pore phase pixel and 1 LLCZN pixel, change the current group of contiguous secondary phase pixels to pore phase.
    2. If neighboring pixels were exactly 1 gold phase pixel and 1 LLCZN pixel, change the current group of contiguous secondary phase pixels to pore phase.
    3. If neighboring pixels were exactly 1 gold phase pixel and 1 pore pixel, change the current group of contiguous secondary phase pixels to pore phase.
    4. If neighboring pixels were exactly 2 pore phase pixels, change the current group of contiguous secondary phase pixels to pore phase.
    5. If neighboring pixels were exactly 2 LLCZN phase pixels, change the current group of contiguous secondary phase pixels to pore phase.

iv. Loop 3 (Step 3.g) ends when all rows and columns have been scanned across.

f. End Part 1: interface artifact removal

3. Begin Part 2: curtaining artifact removal (for 3D image sets only)
    a. Assign value to user-defined variables, "maximum 3D object size" and "maximum pore fraction."
    b. Identify all 3D contiguous secondary phase and filter out all identified objects that have less voxels than "maximum 3D object size."
    c. Loop 4 start: identify the remaining secondary phase in each image, find the corresponding pixels in the image before/after the current image, and remove secondary phase in current image based on what pixels are present in the "projection" in the neighboring images.
        i. In each 2D image in the 3D image set, identify all contiguous secondary phase.
        ii. Identify the row-column coordinates of pixels in each group of contiguous secondary phase in each image and locate pixels with the same coordinates in the next image after the current image.
        iii. Identify the fraction of LLCZN, secondary phase, and pore phase pixels in the "projected" region in the next image. If the fraction of pore phase is greater than "maximum pore fraction", then change the group of contiguous secondary phase in the current image to pore phase.
            1. Record whether secondary phase was removed during this step.
        iv. Repeat Step 3.d.i to Step 3.d.iii, this time projecting onto the image before the current image.
            1. Record whether secondary phase was removed during this step.

v. Loop 4 (Step 3.d) ends when no more secondary phase is removed during the most recent loop iteration.

d. End Part 2: curtaining artifact removal (for 3D image sets only)

4. Identify all contiguous pixels of each phase in the image (excluding pore phase).
    a. If each group of contiguous pixels had a pixel count less than/equal to "minimum contiguous particle size", then change that group to pore phase.
5. Save final 2D image/3D image set as TIFF, with "post-process" appended to name of original image name.

Appendix B: MATLAB Code Used to Calculate 2D Perimeter and 2D Perimeter/2D Area Ratio from Segmented Images:

1. Import the segmented and post-processed 2D TIFF image(s) for the current sample and store in the raw 2D image matrix, “Image”.
    a. Relabel any gold phase present as pore phase.
2. Assign the appropriate physical sizes to the pixel dimensions (pixel x-, y-direction size in nanometers/microns/etc.).
3. From the matrix “Image”, create a binary mask where voxels of the Chosen Phase are assigned values of 1 and all other voxels (Not-Chosen Phase) are assigned values of 0, creating the binary map “Chosen Phase”.
4. Identify all adjacent pixels that share a side with the “Chosen-Phase” pixels, which will be labeled as “Nearest-neighbors” pixels.
5. For each “Nearest-neighbors” pixel, identify how many “Chosen-Phase” pixels share a side with the current pixel and store in corresponding pixels in the “Shared Sides Count” matrix.
6. Sum up the values in the “Shared Sides Count” matrix to determine the total number of interface edge segments for all “Chosen-Phase” pixels and multiply this number by the physical size of each edge/pixel (in μm/pixel) to calculate the total “2D Perimeter” (measured in μm) of the chosen phase.
7. Count the number of “Chosen-Phase” pixels and multiply this number by the area of each pixel (in $\mu m^2/pixel^2$) to calculate the total “2D Area” of the chosen phase.
8. Divide the “2D Perimeter” by the “2D Area” to calculate the “2D Perimeter/Area Ratio” for the current phase.
    a. If multiple images were imported for the current image, calculate the mean and standard deviation of the “2D Perimeter”, “2D Area”, and “2D Perimeter/Area Ratio”.
9. Repeat Step 2 to Step 8 for all remaining phases.
10. Save the results.

Appendix C: MATLAB Code Used to Calculate Geometric Tortuosity Along the X-, Y-, and Z-directions of from 3D FIB Tomography Reconstruction, as well as Characteristic Geometric Tortuosity:

1. Import the segmented and post-processed 3D TIFF image set. These imported images are combined and stored in the raw 3D image matrix, "Image".
2. Assign the appropriate physical sizes to the voxel dimensions (voxel x-, y-, z-direction size in nanometers/microns/etc.).
3. From the matrix "Image", create a binary mask where voxels of the Chosen Phase are assigned values of 1 and all other voxels (Not-Chosen Phase) are assigned values of 0, creating the binary map "Chosen Phase".
4. Create the cumulative distance map "Distance" of the same size as the binary map "Chosen Phase", with all values of "Distance" initially set to 0.
5. Loop 1 start: calculate the shortest lengths for continuous paths from each of the 6 boundary planes surrounding the 3D image region (designated as the "Starting Plane") through the binary map "Chosen Phase" to the parallel boundary plane (designated as the "Ending Plane").
    a. Select 1 of the 6 boundary planes surrounding the 3D image region and designate it as the "Starting Plane," designate the opposite plane as the "Ending Plane," identify all "Chosen-Phase" voxels on the "Starting Plane" and label them as "Visited," and label all other "Chosen-Phase" voxels as "Usable".
    a. Set "Iteration" variable to 0.
    b. Loop 1.1 start: calculate the shortest lengths for continuous paths from the Starting Plane through the binary map "Chosen Phase" to the Ending Plane.
        i. Increase the value of the "Iteration" variable by 1.
        ii. Calculate the "Allowed Wave Propagation Distance" variable (D_{wave}) from the pixel size along the current direction ($\Delta d_{current}$), the current "Iteration" variable value, and the minimum pixel size value ($min[\Delta\, d_{x/y/z}]$) with the following equation:
            1. $D_{wave} = \Delta d_{current} + (Iteration - 1) * min\left[\Delta d_{x/y/z-axis}\right]$
        iii. Identify all "Usable" voxels that contact the faces, edges, or corners of any "Visited" voxels, and label these identified voxels as "Active".
        iv. Calculate the distance from each "Visited" voxel to the surrounding "Active" voxels, add these distances to the distance value in the cumulative distance map "Distance" that corresponds to the current "Visited" voxels to calculate the initial cumulative path length for each "Active" voxel, identify all instances of "Active" voxels that have initial cumulative path lengths less than the "Allowed Wave Propagation Distance", and make a list of these "Accepted Active" voxels.
        v. Identify all "Visited" voxels that contact the faces, edges, or corners of any "Accepted Active" voxels, calculate the distance from each "Accepted Active" voxel to the surrounding "Visited" voxels, add

these distances to the distance values in the cumulative distance map "Distance" that corresponds to the "Visited" voxels to calculate the updated cumulative path length for each "Accepted Active" voxel, identify the minimum updated cumulative path length and the corresponding "Visited" voxel for each "Accepted Active" voxel, and save the minimum cumulative path length for each "Accepted Active" voxel in the corresponding voxel in the cumulative distance map "Distance".

vi. Relabel all "Accepted Active" voxels as "Visited" voxels.

vii. Identify all "Visited" voxels that are not contacting "Usable" or "Active" voxels, and label these as "Complete".

viii. Loop 1.1 ends when all "Visited" voxels are re-labeled as "Complete".

b. For each "slice" of the 3D volume along the current propagation direction, divide the values in the cumulative distance map "Distance" by the Euclidean/straight path length to that "slice" to calculate the cumulative geometric tortuosity map "Tortuosity". Convert the values in the cumulative geometric tortuosity map "Tortuosity" into values ranging from 50-255 (with all tortuosity values above a cutoff being assigned values of 255), and export as a TIFF image.

c. For each "slice" of the 3D volume along the current propagation direction, gather the non-zero values in the cumulative geometric tortuosity map "Tortuosity", and calculate the average and standard deviation for the set of cumulative geometric tortuosity values for each "slice."

d. For the entire 3D image region, divide the number of "Complete" voxels by the number of "Chosen-Phase" voxels to determine the fraction of contiguous "Chosen-Phase" voxels that were processed during the run and label as the "Percolation Factor".

e. Save out lists of the cumulative geometric tortuosity and percolation factor for each "slice" of the 3D volume along the current propagation direction.

f. Loop 1 ends when all 6 directions have been analyzed.

6. Average the values for the "forward" and "reverse" directions for each axis to give a single cumulative geometric tortuosity value and percolation factor for the x-, y-, and z-axes. The standard deviation is recalculated for each. Save the results.

7. Calculate the characteristic geometric tortuosity and the average geometric tortuosity from the direction-averaged x-, y-, and z-axes cumulative geometric tortuosity. The standard deviation is recalculated for using error propagation. Save the results.

Appendix D: MATLAB Code Used to Calculate Continuous Particle Size Distribution (c-PSD) from 3D FIB Tomography Reconstruction:

1. Import the segmented and post-processed 3D TIFF image set. These imported images are combined and stored in the raw 3D image matrix, "Image".
2. Assign the appropriate physical sizes to the voxel dimensions (voxel x-, y-, z-direction size in nanometers/microns/etc.).
3. From the matrix "Image", create a binary mask where voxels of the Chosen Phase are assigned values of 1 and all other voxels (Not-Chosen Phase) are assigned values of 0, creating the binary map "Chosen Phase".
4. Loop 1 start: calculate a distance map that determines the distance between each Chosen Phase voxel and the closest Not-Chosen Phase voxel, saved as distance map "Distance".
    a. With Not-Chosen Phase voxels used as boundaries, apply the scanning approach described by Ref [141] generalized to 3D in order to efficiently calculate the distance between each Chosen Phase voxel and the nearest boundary, and store in the distance map "Distance".
    b. Loop 1 ends once all Chosen Phase voxels have been assigned a distance in the distance map "Distance".
5. Loop 2 start: for increasing sphere radii "R", filter the distance map "Distance" to accept all voxels with distances greater-than R and store as the binary map "Sphere Centers," dilate from the Sphere Centers through the binary map "Chosen Phase" create a new distance map "Dilation," and filter the distance map "Dilation" to accept all voxels with distances less-than-or-equal-to R and store as the binary map "Sphere Coverage".
    a. Select a sphere radius "R" and filter the distance map "Distance" to accept all voxels with distances greater-than R and store as the binary map "Sphere Centers", where accepted voxels have values of 1 and rejected voxels have values of 0.
    b. Loop 2.1 start: dilate from the Sphere Centers through the binary map "Chosen Phase" to create a new distance map "Dilation".
        i. With Sphere Center voxels used as boundaries, apply the scanning approach described by Ref [141] generalized to 3D in order to efficiently calculate the distance between each Chosen Phase voxel and the nearest boundary, and store in the distance map "Dilation".
        ii. Loop 2.1 ends once all Chosen Phase voxels have been assigned a distance in the distance map "Dilation".
    c. Filter the distance map "Dilation" to accept all voxels with distances less-than-or-equal-to R and store as the binary map "Sphere Coverage", where accepted voxels have values of 1 and rejected voxels have values of 0.
    d. Sum the binary map "Sphere Coverage" to calculate the total number of Sphere Coverage voxels and divide by the total number of Chosen Phase voxels to calculate the "Sphere Coverage Fraction" for the current sphere radius "R" and corresponding sphere diameter "D".
    e. Filter the distance map "Dilation" to accept all voxels with distances less-than-or-equal-to R+2x and store as the binary map "Updated Chosen

Phase", where x is the 3D diagonal distance between the center voxel of a 3x3x3 box and the corner voxel.

f. For the next iteration of Loop 2, replace the binary map "Chosen Phase" with the binary map "Updated Chosen Phase" in order to remove Chosen phase voxels that will fail the acceptance criteria for later iterations of the binary map "Sphere Coverage".

g. Loop 2 ends when the binary map "Sphere Centers" has no accepted voxels present.

6. From the list of sphere diameters "D" and "Sphere Coverage Fraction", use linear interpolation to calculate the sphere diameter for 50% sphere coverage ($d_{c\text{-}PSD,50}$).
7. Save the distributions and the 50% sphere coverage values.

Appendix E: MATLAB Code Used to Calculate Mercury Intrusion Porosimetry PSD (MIP-PSD) from 3D FIB Tomography Reconstruction:

1. Import the segmented and post-processed 3D TIFF image set. These imported images are combined and stored in the raw 3D image matrix, "Image".
2. Assign the appropriate physical sizes to the voxel dimensions (voxel x-, y-, z-direction size in nanometers/microns/etc.).
3. From the matrix "Image", create a binary mask where voxels of the Chosen Phase are assigned values of 1 and all other voxels (Not-Chosen Phase) are assigned values of 0, creating the binary map "Chosen Phase".
4. Loop 1 start: calculate a distance map that determines the distance between each Chosen Phase voxel and the closest Not-Chosen Phase voxel, saved as distance map "Distance".
    a. With Not-Chosen Phase voxels used as boundaries, apply the scanning approach described by Ref [141] generalized to 3D in order to efficiently calculate the distance between each Chosen Phase voxel and the nearest boundary, and store in the distance map "Distance".
    b. Loop 1 ends once all Chosen Phase voxels have been assigned a distance in the distance map "Distance".
5. Loop 2 start: for increasing sphere radii "R", filter the distance map "Distance" to accept all voxels with distances greater-than R and store as the binary map "Sphere Centers," create 6 binary maps "Accepted Sphere Centers" where accepted Sphere Center voxels are contiguous and connected to 1 of the 6 boundary planes surrounding the 3D image region, dilate from each of the 6 sets of Sphere Centers through the binary map "Chosen Phase" create new distance maps "Dilation," and filter the distance maps "Dilation" to accept all voxels with distances less-than-or-equal-to R and store as the binary maps "Sphere Coverage".
    a. Select a sphere radius "R" and filter the distance map "Distance" to accept all voxels with distances greater-than R and store as the binary map "Sphere Centers", where accepted voxels have values of 1 and rejected voxels have values of 0.
    b. Loop 2.1 start: for each of the 6 boundary planes surrounding the 3D image region, identify all Sphere Center voxels that are contiguous and connected to that boundary, store the Accepted Sphere Center voxels in the binary map "Sphere Center", dilate from the Sphere Centers through the binary map "Chosen Phase" create the distance map "Dilation," and filter the distance map "Dilation" to accept all voxels with distances less-than-or-equal-to R and store as the binary map "Sphere Coverage".
        i. Select 1 of the 6 boundary planes surrounding the 3D image region, identify all Sphere Center voxels that are contiguous and connected to that boundary, and store the Accepted Sphere Center voxels in the binary map "Sphere Center".
        ii. Loop 2.1.1 start: dilate from the Sphere Centers through the binary map "Chosen Phase" to create a new distance map "Dilation".
            1. With Sphere Center voxels used as boundaries, apply the scanning approach described by Ref [141] generalized to 3D

in order to efficiently calculate the distance between each Chosen Phase voxel and the nearest boundary, and store in the distance map "Dilation".

2. Loop 2.1.1 ends once all Chosen Phase voxels have been assigned a distance in the distance map "Dilation".

iii. Filter the distance map "Dilation" to accept all voxels with distances less-than-or-equal-to R and store as the binary map "Sphere Coverage", where accepted voxels have values of 1 and rejected voxels have values of 0.

iv. Sum the binary map "Sphere Coverage" to calculate the total number of Sphere Coverage voxels and divide by the total number of Chosen Phase voxels to calculate the "Sphere Coverage Fraction" for the current sphere radius "R" and corresponding sphere diameter "D".

v. Filter the distance map "Dilation" to accept all voxels with distances less-than-or-equal-to R+2x and store as the binary map "Updated Chosen Phase", where 2x is the 3D diagonal distance between the center voxel of a 3x3x3 box and the corner voxel.

i. For the next iteration of Loop 2, replace the binary map "Chosen Phase" with the binary map "Updated Chosen Phase" when analyzing the currently selected boundary plane in order to remove Chosen phase voxels that will fail the acceptance criteria for later iterations of the binary map "Sphere Coverage".

vi. Loop 2.1 ends when the binary map "Sphere Centers" has no accepted voxels present for the currently selected boundary plane.

c. Loop 2.1 ends when the binary map "Sphere Centers" has no accepted voxels present for any of the 6 boundary planes.

6. Average the distributions for parallel boundaries together to give a single distribution for each axis.
7. From the list of sphere diameters "D" and "Sphere Coverage Fraction", use linear interpolation to calculate the direction-averaged 50% sphere coverage for each axis ($d_{x\text{-axis,MIP-PSD,50}}$, $d_{y\text{-axis,MIP-PSD,50}}$, $d_{z\text{-axis,MIP-PSD,50}}$).
8. Average the average distributions for the 3 axes together to give a single distribution.
9. From the list of sphere diameters "D" and "Sphere Coverage Fraction", use linear interpolation to calculate the average 50% sphere coverage for the entire sample ($d_{MIP\text{-}PSD,50}$).
10. Save the distributions and the 50% sphere coverage values.

Appendix F: MATLAB Code Used to Calculate the Equilibrium Electric Potential within a 3D Electrolyte Microstructure with Arbitrary Electrode Geometry:

1. Designate the physical thickness of the dense layer, the % of the porous layer infiltrated with the positive electrode, the comparison threshold that determines when the loop calculating the equilibrium electric potential will end.
2. Import the segmented and post-processed 3D TIFF image set. These imported images are combined and stored in the raw 3D image matrix, "Image".
3. Assign the appropriate physical sizes to the voxel dimensions (voxel x-, y-, z-direction size in nanometers/microns/etc.).
4. For the 3 different directions, use the voxel dimensions to calculate the inverse voxel length squared for each direction and store in the list, "Inverse Voxel Length Squared".
5. From the matrix "Image", create a binary mask where voxels of the Chosen Phase are assigned values of 1 (referred to as Electrolyte voxels) and all other voxels (Pore voxels) are assigned values of 0, creating the binary map "Electrolyte Phase".
6. Create a matrix with the same X- and Y-dimensions as the matrix "Image", the Z-dimension equal to the number of dense layer voxels plus the Z-dimension of the matrix "Image," and label this the bilayer identity map, "Bilayer." For the dense layer portion, assign values of 1 to all voxels to label them as Electrolyte voxels and copy the binary map "Electrolyte Phase" into the porous layer portion.
7. Based on the % of porous layer infiltrated, assign values of 2 to the Pore voxels in the porous layer of the map "Bilayer" to label them as "Positive Electrode" voxels.
8. Along the Z-direction of the map "Bilayer", add a layer of Positive Electrode voxels in a new plane next to the top of the porous layer, and add a layer of voxels with values of 3 ("Negative Electrode") in a new plane next to the bottom of the dense layer. Pad the surfaces of the map "Bilayer" with 0's to prevent issues during later calculations.
9. Create a matrix of the same size as the map "Bilayer" to store the calculated electric potential values and call this the potential map "Electric Potential."
10. Based on the map "Bilayer", assign fixed potentials of +0.5 Volts and -0.5 Volts to all voxels in the map "Electric Potential" that correspond to Positive Electrode voxels and Negative Electrode voxels, respectively.
11. Based on the map "Bilayer" and the % of porous layer infiltrated, identify all voxels in the map "Electric potential" that correspond to Electrolyte voxels, select any Electrolyte voxels between the Negative Electrode voxels and the closest plane with Positive Electrode voxels, and assign a potentials gradient from -0.5 Volts to +0.5 Volts to these selected Electrolyte voxels. For all remaining Electrolyte voxels, assign potentials of +0.49 Volts.
12. Copy the map "Electric Potential" and store as a reference in the electric potential map "Previous Electric Potential".
13. Loop 1 start: alternating between the forward and reverse directions, select batches of consecutive planes in the map "Electric Potential", and solve the Laplace equation for Electrolyte voxels in each batch to update the electric potentials of the Electrolyte voxels. Compare the final updated map "Electric Potential" to the

previous iteration map “Previous Electric Potential”, calculate the average relative difference between the maps, and continue the loop until the average relative difference becomes smaller than the assigned threshold.

a. Create a list of the batches of consecutive planes along the forward direction of the map “Electric Potential”, ensuring that batches are as large as possible without exceeding the RAM limits of the computer. Batches are set to overlap with half of the neighboring batches.
b. Create a list of the batches of consecutive planes along the reverse direction of the map “Electric Potential”, ensuring that batches are as large as possible without exceeding the RAM limits of the computer. Batches are set to overlap with half of the neighboring batches.
c. Loop 1.1 start: alternating between the forward and reverse directions, select batches of consecutive planes in the map “Electric Potential” and solve the Laplace equation for Electrolyte voxels in each batch to update the electric potentials of the Electrolyte voxels.
    i. Select a batch of consecutive planes in the map “Electric Potential” and the map “Bilayer”.
    ii. Identify all Electrolyte voxels represented in the batch and store the indices for these voxels in the list “Electrolyte to Update”.
    iii. Identify all nearest neighbor voxels sharing faces with the Electrolyte voxels in the list “Electrolyte to Update” and store the coordinates of the neighboring voxels in the list “Nearest Neighbors”.
    iv. Using the list “Nearest Neighbors” and the map “Bilayer, check the identities of all nearest neighbor voxels and store in the list “Neighbor Identity List”.
    v. Find all Electrolyte voxels in the list “Neighbor Identity List”, identify any neighboring Electrolyte voxels that are outside the batch of consecutive planes, and assign values of 4 to these voxels in the list “Neighbor Identity List” to identify them as “Boundary Electrolyte” voxels.
    vi. Create an empty list of Laplace equation coefficients for the electrolyte voxels to be updated that is the same size as the list “Electrolyte to Update” and call this new list “Coefficient for Electrolyte to Update”.
    vii. For each Electrolyte voxel in the list “Electrolyte to Update”, check the corresponding nearest neighbors in the list “Neighbor Identity List” and find all neighbors with identify values greater than 0 (meaning they are Electrolyte, Electrode, or Boundary Electrolyte voxels). Sum the “Inverse Length Squared” values for the directions of these accepted neighbors relative to the chosen Electrolyte voxel and store the final value in the position of the list “Coefficient for Electrolyte to Update” corresponding to the chosen Electrolyte voxel.

viii. Create an empty list of Laplace equation coefficients for nearest neighbor voxels that is the same size as the list "Nearest Neighbors" and call this new list "Coefficient for Neighbors to Update".
ix. For each Electrolyte voxel in the list "Electrolyte to Update", check the list "Neighbor Identity List" and find all neighboring Electrolyte voxels (excluding Boundary Electrolyte voxels). Insert the "Inverse Length Squared" value for the direction of the neighboring Electrolyte voxel relative to the chosen "Electrolyte to Update" voxel into the positions of the list "Coefficient for Neighbors to Update" corresponding to each neighbor.
x. Create an empty list of Laplace equation boundary values for the electrolyte voxels to be updated that is the same size as the list "Electrolyte to Update" and call this new list "Boundary Values".
xi. For each Electrolyte voxel in the list "Electrolyte to Update", check the list "Neighbor Identity List" and find all neighboring Electrode and Boundary Electrolyte voxels. For the accepted voxels, look up the corresponding potentials in the map "Electric Potential", multiply each potential by the "Inverse Length Squared" value for the direction of the Electrode/Boundary Electrolyte voxel relative to the chosen Electrolyte voxel, sum the set of values, and store the final value in the position of the list "Boundary Values" corresponding to the chosen Electrolyte voxel.
xii. Create the empty, sparse list "Potentials to Update" that is the same size as the list "Electrolyte to Update" and insert the corresponding potential values from the map "Electric Potential."
xiii. Convert the list "Boundary Values" to a sparse format.
xiv. Loop 1.1.1 start: create the sparse, square matrix "Linear Equations" and fill all relevant positions with the coefficients of the Electrolyte voxels to update and the neighboring Electrolyte voxels to update.
    1. Create the empty, sparse, square matrix "Linear Equations" that has sides with the same length as the list "Electrolyte to Update". Create the empty, sparse list "Potentials to Update" that is the same size as the list "Electrolyte to Update". Convert the list "Boundary Values" to a sparse format.
    2. For each entry in the list "Coefficient for Electrolyte to Update", assign the value to the diagonal position of the square matrix "Linear Equations" such that the row of the diagonal position and the row of the entry in the list "Coefficient for Electrolyte to Update" are the same.
    3. For each entry in the list "Coefficient for Neighbors to Update", multiply the value by -1 and assign this value to the off-diagonal position of the square matrix "Linear Equations" such that the row of the off-diagonal position and the row of the entry in the list "Coefficient for Electrolyte to Update" are the same, and the column of the off-diagonal

position and the row of the neighboring Electrolyte voxel found in the list “Electrolyte to Update” are the same.

4. Loop 1.1.1 ends when all coefficients of the Electrolyte voxels to update and the neighboring Electrolyte voxels to update have been assigned.

xv. Use the “bicgstab” MATLAB function to take the square matrix “Linear Equations”, the list “Potentials to Update”, and the list “Boundary Values” as inputs, iteratively relax the electric potentials until the average relative difference of the batch becomes less than the assigned threshold divided by 2.

xvi. For the corresponding Electrolyte positions in the map “Electric Potential”, replaced the potentials with final values in the list “Potentials to Update”.

xvii. Loop 1.1 ends once all batches along the forward and reverse directions have been updated.

d. Compare the final updated map “Electric Potential” to the previous iteration map “Previous Electric Potential” and calculate the average relative difference between the maps.

e. Loop 1 ends when the average relative difference becomes smaller than the assigned threshold.

14. Save the final updated map “Electric Potential” and the map “Bilayer” to an external .mat file for future analysis

References:

1. Armand, M. & Tarascon, J.-M. Building better batteries. *Nature* **451,** 652–657 (2008).

2. Thackeray, M. M., Wolverton, C. & Isaacs, E. D. Electrical energy storage for transportation—approaching the limits of, and going beyond, lithium-ion batteries. *Energy Environ. Sci.* **5,** 7854 (2012).

3. Xu, K. Nonaqueous Liquid Electrolytes for Lithium-Based Rechargeable Batteries. *Chem. Rev.* **104,** 4303–4418 (2004).

4. Cheng, X.-B., Zhang, R., Zhao, C.-Z. & Zhang, Q. Toward Safe Lithium Metal Anode in Rechargeable Batteries: A Review. *Chem. Rev.* **117,** 10403–10473 (2017).

5. Zhang, S. S. A review on the separators of liquid electrolyte Li-ion batteries. *J. Power Sources* **164,** 351–364 (2007).

6. Brissot, C., Rosso, M., Chazalviel, J.-N. & Lascaud, S. Dendritic growth mechanisms in lithium/polymer cells. *J. Power Sources* **81–82,** 925–929 (1999).

7. Aurbach, D. *et al.* Design of electrolyte solutions for Li and Li-ion batteries: a review. *Electrochim. Acta* **50,** 247–254 (2004).

8. Lisbona, D. & Snee, T. A review of hazards associated with primary lithium and lithium-ion batteries. *Process Saf. Environ. Prot.* **89,** 434–442 (2011).

9. Wang, Q. *et al.* Thermal runaway caused fire and explosion of lithium ion battery. *J. Power Sources* **208,** 210–224 (2012).

10. Evarts, E. C. Lithium batteries: To the limits of lithium. *Nature* **526,** S93–S95 (2015).

11. Ouyang, M. *et al.* Low temperature aging mechanism identification and lithium deposition in a large format lithium iron phosphate battery for different charge profiles. *J. Power Sources* **286,** 309–320 (2015).

12. Aryanfar, A., Brooks, D. J., Colussi, A. J. & Hoffmann, M. R. Quantifying the dependence of dead lithium losses on the cycling period in lithium metal batteries. *Phys. Chem. Chem. Phys.* **16,** 24965–24970 (2014).

13. Wood, K. N. *et al.* Dendrites and Pits: Untangling the Complex Behavior of Lithium Metal Anodes through Operando Video Microscopy. *ACS Cent. Sci.* **2,** 790–801 (2016).

14. Julien, C. M. & Mauger, A. Review of 5-V electrodes for Li-ion batteries: status

and trends. *Ionics (Kiel).* **19,** 951–988 (2013).

15. Goodenough, J. B. & Park, K.-S. The Li-Ion Rechargeable Battery: A Perspective. *J. Am. Chem. Soc.* **135,** 1167–1176 (2013).

16. Mikhaylik, Y. V. & Akridge, J. R. Polysulfide Shuttle Study in the Li/S Battery System. *J. Electrochem. Soc.* **151,** A1969 (2004).

17. Hofmann, A. F., Fronczek, D. N. & Bessler, W. G. Mechanistic modeling of polysulfide shuttle and capacity loss in lithium–sulfur batteries. *J. Power Sources* **259,** 300–310 (2014).

18. Nayak, P. K. *et al.* Review on Challenges and Recent Advances in the Electrochemical Performance of High Capacity Li- and Mn-Rich Cathode Materials for Li-Ion Batteries. *Adv. Energy Mater.* **8,** 1702397 (2018).

19. Mohanty, D. *et al.* Structural transformation of a lithium-rich Li1.2Co0.1Mn0.55Ni0.15O2 cathode during high voltage cycling resolved by in situ X-ray diffraction. *J. Power Sources* **229,** 239–248 (2013).

20. Gilbert, J. A., Shkrob, I. A. & Abraham, D. P. Transition Metal Dissolution, Ion Migration, Electrocatalytic Reduction and Capacity Loss in Lithium-Ion Full Cells. *J. Electrochem. Soc.* **164,** A389–A399 (2017).

21. Zu, C.-X. & Li, H. Thermodynamic analysis on energy densities of batteries. *Energy Environ. Sci.* **4,** 2614 (2011).

22. Laboratory, A. N. Modeling the Cost and Performance of Lithium-Ion Batteries for Electric-Drive Vehicles Final Report. (2011).

23. Mankowski, P. J., Kanevsky, J., Bakirtzian, P. & Cugno, S. Cellular phone collateral damage: A review of burns associated with lithium battery powered mobile devices. *Burns* **42,** e61–e64 (2016).

24. National Transportation Safety Board. Aircraft Incident Report Auxiliary Power Unit Battery Fire Japan Airlines Boeing 787-8, JA829J Boston, Massachusetts January 7, 2013. 1–110 (2013).

25. Tarascon, J.-M. & Armand, M. Issues and challenges facing rechargeable lithium batteries. *Nature* **414,** 359–367 (2001).

26. Monroe, C. & Newman, J. The Impact of Elastic Deformation on Deposition Kinetics at Lithium/Polymer Interfaces. *J. Electrochem. Soc.* **152,** A396 (2005).

27. Porz, L. *et al.* Mechanism of Lithium Metal Penetration through Inorganic Solid Electrolytes. *Adv. Energy Mater.* **7,** 1701003 (2017).

28. Luo, W. *et al.* Transition from Superlithiophobicity to Superlithiophilicity of

Garnet Solid-State Electrolyte. *J. Am. Chem. Soc.* **138,** 12258–12262 (2016).

29. Richards, W. D., Miara, L. J., Wang, Y., Kim, J. C. & Ceder, G. Interface Stability in Solid-State Batteries. *Chem. Mater.* **28,** 266–273 (2016).

30. Bresser, D., Passerini, S. & Scrosati, B. Recent progress and remaining challenges in sulfur-based lithium secondary batteries – a review. *Chem. Commun.* **49,** 10545 (2013).

31. Knauth, P. Inorganic solid Li ion conductors: An overview. *Solid State Ionics* **180,** 911–916 (2009).

32. Xu, K. Electrolytes and Interphases in Li-Ion Batteries and Beyond. *Chem. Rev.* **114,** 11503–11618 (2014).

33. Park, M., Zhang, X., Chung, M., Less, G. B. & Sastry, A. M. A review of conduction phenomena in Li-ion batteries. *J. Power Sources* **195,** 7904–7929 (2010).

34. Takada, K. Progress and prospective of solid-state lithium batteries. *Acta Mater.* **61,** 759–770 (2013).

35. Murugan, R., Thangadurai, V. & Weppner, W. Fast lithium ion conduction in garnet-type Li(7)La(3)Zr(2)O(12). *Angew. Chem. Int. Ed. Engl.* **46,** 7778–7781 (2007).

36. Walker, C. W. Conductivity and Electrochemical Stability of Electrolytes Containing Organic Solvent Mixtures with Lithium tris(Trifluoromethanesulfonyl)methide. *J. Electrochem. Soc.* **143,** L80 (1996).

37. Dahbi, M., Ghamouss, F., Tran-Van, F., Lemordant, D. & Anouti, M. Comparative study of EC/DMC LiTFSI and LiPF6 electrolytes for electrochemical storage. *J. Power Sources* **196,** 9743–9750 (2011).

38. Thangadurai, V., Kaack, H. & Weppner, W. J. F. Novel Fast Lithium Ion Conduction in Garnet-Type Li 5 La 3 M 2 O 12 (M = Nb, Ta). *J. Am. Ceram. Soc.* **86,** 437–440 (2003).

39. Thangadurai, V. & Weppner, W. Li6ALa2Nb2O12 (A=Ca, Sr, Ba): A New Class of Fast Lithium Ion Conductors with Garnet-Like Structure. *J. Am. Ceram. Soc.* **88,** 411–418 (2005).

40. Huang, M. *et al.* Effect of sintering temperature on structure and ionic conductivity of Li7−xLa3Zr2O12−0.5x (x=0.5~0.7) ceramics. *Solid State Ionics* **204–205,** 41–45 (2011).

41. Lee, J.-M. *et al.* High lithium ion conductivity of Li7La3Zr2O12 synthesized by solid state reaction. *Solid State Ionics* **258,** 13–17 (2014).

42. Rangasamy, E., Wolfenstine, J. & Sakamoto, J. The role of Al and Li concentration on the formation of cubic garnet solid electrolyte of nominal composition Li 7La 3Zr 2O 12. *Solid State Ionics* **206,** 28–32 (2012).

43. Huang, M., Dumon, A. & Nan, C.-W. Effect of Si, In and Ge doping on high ionic conductivity of Li7La3Zr2O12. *Electrochem. commun.* **21,** 62–64 (2012).

44. Ahn, J. H., Park, S. Y., Lee, J. M., Park, Y. & Lee, J. H. Local impedance spectroscopic and microstructural analyses of Al-in-diffused Li7La3Zr2O12. *J. Power Sources* **254,** 287–292 (2014).

45. Wang, Y. & Lai, W. Phase transition in lithium garnet oxide ionic conductors Li7La3Zr2O12: The role of Ta substitution and H2O/CO2 exposure. *J. Power Sources* **275,** 612–620 (2015).

46. Thangadurai, V., Narayanan, S. & Pinzaru, D. Garnet-type solid-state fast Li ion conductors for Li batteries: critical review. *Chem. Soc. Rev.* **43,** 4714 (2014).

47. Ohta, S., Kobayashi, T. & Asaoka, T. High lithium ionic conductivity in the garnet-type oxide Li7-X La3(Zr2-X, NbX)O12 (X = 0-2). *J. Power Sources* **196,** 3342–3345 (2011).

48. Kihira, Y., Ohta, S., Imagawa, H. & Asaoka, T. Effect of Simultaneous Substitution of Alkali Earth Metals and Nb in Li7La3Zr2O12 on Lithium-Ion Conductivity. *ECS Electrochem. Lett.* **2,** A56–A59 (2013).

49. Cheng, L. *et al.* The origin of high electrolyte–electrode interfacial resistances in lithium cells containing garnet type solid electrolytes. *Phys. Chem. Chem. Phys.* **16,** 18294–18300 (2014).

50. Xia, W. *et al.* Reaction mechanisms of lithium garnet pellets in ambient air: The effect of humidity and CO2. *J. Am. Ceram. Soc.* **100,** 2832–2839 (2017).

51. Han, X. *et al.* Negating interfacial impedance in garnet-based solid-state Li metal batteries. *Nat. Mater.* **1,** (2016).

52. Chen, Z., Qin, Y., Amine, K. & Sun, Y.-K. Role of surface coating on cathode materials for lithium-ion batteries. *J. Mater. Chem.* **20,** 7606 (2010).

53. Martha, S. K. *et al.* Solid electrolyte coated high voltage layered–layered lithium-rich composite cathode: Li1.2Mn0.525Ni0.175Co0.1O2. *J. Mater. Chem. A* **1,** 5587 (2013).

54. Liu, N. *et al.* A Yolk-Shell Design for Stabilized and Scalable Li-Ion Battery Alloy Anodes. *Nano Lett.* **12,** 3315–3321 (2012).

55. Jin, Y. & Mcginn, P. J. Bulk solid state rechargeable lithium ion battery fabrication with Al-doped Li7La3Zr2O12 electrolyte and Cu0.1V2O5 cathode. *Electrochim.*

Acta **89,** 407–412 (2013).

56. Hitz, G. T. *et al.* High-rate lithium cycling in a scalable trilayer Li-garnet-electrolyte architecture. *Mater. Today* **22,** 50–57 (2019).

57. Fu, K. (Kelvin) *et al.* Three-dimensional bilayer garnet solid electrolyte based high energy density lithium metal–sulfur batteries. *Energy Environ. Sci.* **10,** 1568–1575 (2017).

58. Yang, C. *et al.* Continuous plating/stripping behavior of solid-state lithium metal anode in a 3D ion-conductive framework. *Proc. Natl. Acad. Sci.* 201719758 (2018). doi:10.1073/pnas.1719758115

59. Xu, S. *et al.* Three-Dimensional, Solid-State Mixed Electron–Ion Conductive Framework for Lithium Metal Anode. *Nano Lett.* acs.nanolett.8b01295 (2018). doi:10.1021/acs.nanolett.8b01295

60. Fu, K. (Kelvin) *et al.* Flexible, solid-state, ion-conducting membrane with 3D garnet nanofiber networks for lithium batteries. *Proc. Natl. Acad. Sci.* **113,** 7094–7099 (2016).

61. Gong, Y. *et al.* Lithium-ion conductive ceramic textile: A new architecture for flexible solid-state lithium metal batteries. *Mater. Today* **21,** 594–601 (2018).

62. McOwen, D. W. *et al.* 3D-Printing Electrolytes for Solid-State Batteries. *Adv. Mater.* **30,** 1707132 (2018).

63. van Brakel, J. & Heertjes, P. M. Analysis of diffusion in macroporous media in terms of a porosity, a tortuosity and a constrictivity factor. *Int. J. Heat Mass Transf.* **17,** 1093–1103 (1974).

64. Holzer, L. *et al.* Redox cycling of Ni–YSZ anodes for solid oxide fuel cells: Influence of tortuosity, constriction and percolation factors on the effective transport properties. *J. Power Sources* **242,** 179–194 (2013).

65. Wilson, J. R. *et al.* Three-dimensional reconstruction of a solid-oxide fuel-cell anode. *Nat. Mater.* **5,** 541–544 (2006).

66. Gostovic, D., Smith, J. R., Kundinger, D. P., Jones, K. S. & Wachsman, E. D. Three-Dimensional Reconstruction of Porous LSCF Cathodes. *Electrochem. Solid-State Lett.* **10,** B214 (2007).

67. Izzo, J. R. *et al.* Nondestructive Reconstruction and Analysis of SOFC Anodes Using X-ray Computed Tomography at Sub-50 nm Resolution. *J. Electrochem. Soc.* **155,** B504 (2008).

68. Shearing, P. R., Golbert, J., Chater, R. J. & Brandon, N. P. 3D reconstruction of SOFC anodes using a focused ion beam lift-out technique. *Chem. Eng. Sci.* **64,**

3928–3933 (2009).

69. Smith, J. R. *et al.* Evaluation of the relationship between cathode microstructure and electrochemical behavior for SOFCs. *Solid State Ionics* **180,** 90–98 (2009).

70. Iwai, H. *et al.* Quantification of SOFC anode microstructure based on dual beam FIB-SEM technique. *J. Power Sources* **195,** 955–961 (2010).

71. Gostovic, D., Vito, N. J., O'Hara, K. A., Jones, K. S. & Wachsman, E. D. Microstructure and Connectivity Quantification of Complex Composite Solid Oxide Fuel Cell Electrode Three-Dimensional Networks. *J. Am. Ceram. Soc.* **94,** 620–627 (2011).

72. Holzer, L. *et al.* Microstructure degradation of cermet anodes for solid oxide fuel cells: Quantification of nickel grain growth in dry and in humid atmospheres. *J. Power Sources* **196,** 1279–1294 (2011).

73. Cronin, J. S., Chen-Wiegart, Y. K., Wang, J. & Barnett, S. A. Three-dimensional reconstruction and analysis of an entire solid oxide fuel cell by full-field transmission X-ray microscopy. *J. Power Sources* **233,** 174–179 (2013).

74. Wang, H. *et al.* Mechanisms of Performance Degradation of (La,Sr)(Co,Fe)O 3-δ Solid Oxide Fuel Cell Cathodes. *J. Electrochem. Soc.* **163,** F581–F585 (2016).

75. Buqa, H., Goers, D., Holzapfel, M., Spahr, M. E. & Novák, P. High Rate Capability of Graphite Negative Electrodes for Lithium-Ion Batteries. *J. Electrochem. Soc.* **152,** A474 (2005).

76. Liu, X. H. *et al.* Size-Dependent Fracture of Silicon Nanoparticles During Lithiation. *ACS Nano* **6,** 1522–1531 (2012).

77. Lin, F. *et al.* Metal segregation in hierarchically structured cathode materials for high-energy lithium batteries. *Nat. Energy* **1,** 15004 (2016).

78. Manuel Stephan, A. Review on gel polymer electrolytes for lithium batteries. *Eur. Polym. J.* **42,** 21–42 (2006).

79. Fergus, J. W. Ceramic and polymeric solid electrolytes for lithium-ion batteries. *J. Power Sources* **195,** 4554–4569 (2010).

80. Tatsumisago, M., Nagao, M. & Hayashi, A. Recent development of sulfide solid electrolytes and interfacial modification for all-solid-state rechargeable lithium batteries. *J. Asian Ceram. Soc.* **1,** 17–25 (2013).

81. Shearing, P. R., Howard, L. E., Jørgensen, P. S., Brandon, N. P. & Harris, S. J. Characterization of the 3-dimensional microstructure of a graphite negative electrode from a Li-ion battery. *Electrochem. commun.* **12,** 374–377 (2010).

82. Ender, M., Joos, J., Carraro, T. & Ivers-Tiffée, E. Three-dimensional reconstruction of a composite cathode for lithium-ion cells. *Electrochem. commun.* **13,** 166–168 (2011).

83. Wilson, J. R., Cronin, J. S., Barnett, S. A. & Harris, S. J. Measurement of three-dimensional microstructure in a LiCoO2 positive electrode. *J. Power Sources* **196,** 3443–3447 (2011).

84. Ebner, M., Marone, F., Stampanoni, M. & Wood, V. Visualization and Quantification of Electrochemical and Mechanical Degradation in Li Ion Batteries. *Science (80-.).* **342,** 716–720 (2013).

85. Chen-Wiegart, Y. C. K., Liu, Z., Faber, K. T., Barnett, S. A. & Wang, J. 3D analysis of a LiCoO2-Li(Ni1/3Mn1/3Co1/3)O2Li-ion battery positive electrode using x-ray nano-tomography. *Electrochem. commun.* **28,** 127–130 (2013).

86. Komini Babu, S., Mohamed, A. I., Whitacre, J. F. & Litster, S. Multiple imaging mode X-ray computed tomography for distinguishing active and inactive phases in lithium-ion battery cathodes. *J. Power Sources* **283,** 314–319 (2015).

87. Giannuzzi, L. A. & Stevie, F. A. *Introduction to Focused Ion Beams: Instrumentation, Theory, Techniques and Practice*. (Springer US, 2005).

88. Orloff, J., Utlaut, M. & Swanson, L. *High Resolution Focused Ion Beams: FIB and its Applications: Fib and Its Applications: The Physics of Liquid Metal Ion Sources and Ion Optics and Their Application to Focused Ion Beam Technology*. (Springer US, 2003).

89. Stevie, F. A. *et al.* Applications of focused ion beams in microelectronics production, design and development. *Surf. Interface Anal.* **23,** 61–68 (1995).

90. Giannuzzi, L. A. & Stevie, F. A. A review of focused ion beam milling techniques for TEM specimen preparation. *Micron* **30,** 197–204 (1999).

91. Levi-Setti, R., Wang, Y. L. & Crow, G. Scanning ion microscopy: Elemental maps at high lateral resolution. *Appl. Surf. Sci.* **26,** 249–264 (1986).

92. Tomiyasu, B., Fukuju, I., Komatsubara, H., Owari, M. & Nihei, Y. High spatial resolution 3D analysis of materials using gallium focused ion beam secondary ion mass spectrometry (FIB SIMS). *Nucl. Instruments Methods Phys. Res. Sect. B Beam Interact. with Mater. Atoms* **136–138,** 1028–1033 (1998).

93. McDonnell, L. A. & Heeren, R. M. A. Imaging mass spectrometry. *Mass Spectrom. Rev.* **26,** 606–643 (2007).

94. Yabuuchi, N., Yoshii, K., Myung, S.-T., Nakai, I. & Komaba, S. Detailed Studies of a High-Capacity Electrode Material for Rechargeable Batteries, Li 2 MnO 3 −LiCo 1/3 Ni 1/3 Mn 1/3 O 2. *J. Am. Chem. Soc.* **133,** 4404–4419 (2011).

95. Sudraud, P. & Ben Assayag, G. Focused-ion-beam milling, scanning-electron microscopy, and focused-droplet deposition in a single microcircuit surgery tool. *J. Vac. Sci. Technol. B Microelectron. Nanom. Struct.* **6,** 234 (1988).

96. Zaefferer, S., Wright, S. I. & Raabe, D. Three-Dimensional Orientation Microscopy in a Focused Ion Beam–Scanning Electron Microscope: A New Dimension of Microstructure Characterization. *Metall. Mater. Trans. A* **39,** 374–389 (2008).

97. Holzer, L. Review of FIB-tomography. *Nanofabrication Using Focus. Ion Electron Beams Princ. Appl.* 410–435 (2011).

98. Taillon, J. A., Pellegrinelli, C., Huang, Y., Wachsman, E. D. & Salamanca-Riba, L. G. Improving microstructural quantification in FIB/SEM nanotomography. *Ultramicroscopy* **184,** 24–38 (2018).

99. Saif, T., Lin, Q., Butcher, A. R., Bijeljic, B. & Blunt, M. J. Multi-scale multi-dimensional microstructure imaging of oil shale pyrolysis using X-ray micro-tomography, automated ultra-high resolution SEM, MAPS Mineralogy and FIB-SEM. *Appl. Energy* **202,** 628–647 (2017).

100. Uchic, M. D., Holzer, L., Inkson, B. J., Principe, E. L. & Munroe, P. Three-Dimensional Microstructural Characterization Using Focused Ion Beam Tomography. *MRS Bull.* **32,** 408–416 (2007).

101. Lasagni, F., Lasagni, A., Holzapfel, C., Mücklich, F. & Degischer, H. P. Three Dimensional Characterization of Unmodified and Sr-Modified Al-Si Eutectics by FIB and FIB EDX Tomography. *Adv. Eng. Mater.* **8,** 719–723 (2006).

102. Goldstein, T. & Osher, S. The Split Bregman Method for L1-Regularized Problems. *SIAM J. Imaging Sci.* **2,** 323–343 (2009).

103. Cai, J., Dong, B., Osher, S. & Shen, Z. Image restoration: Total variation, wavelet frames, and beyond. *J. Am. Math. Soc.* **25,** 1033–1089 (2012).

104. Chang, Y., Fang, H., Yan, L. & Liu, H. Robust destriping method with unidirectional total variation and framelet regularization. *Opt. Express* **21,** 23307 (2013).

105. Fitschen, J. H., Ma, J. & Schuff, S. Removal of curtaining effects by a variational model with directional forward differences. *Comput. Vis. Image Underst.* **155,** 24–32 (2017).

106. Inkson, B. J., Steer, T., Mobus, G. & Wagner, T. Subsurface nanoindentation deformation of Cu-Al multilayers mapped in 3D by focused ion beam microscopy. *J. Microsc.* **201,** 256–269 (2001).

107. Munroe, P. R. The application of focused ion beam microscopy in the material

sciences. *Mater. Charact.* **60,** 2–13 (2009).

108. Schindelin, J. *et al.* Fiji: An open-source platform for biological-image analysis. *Nat. Methods* **9,** 676–682 (2012).

109. Lowe, D. G. Distinctive Image Features from Scale-Invariant Keypoints. *Int. J. Comput. Vis.* **60,** 91–110 (2004).

110. Lowe, D. G. (2004). United States Patent No. US 006711293B1. Retrived from https://patents.google.com/patent/US6711293B1/en.

111. Xiaolong Dai & Khorram, S. The effects of image misregistration on the accuracy of remotely sensed change detection. *IEEE Trans. Geosci. Remote Sens.* **36,** 1566–1577 (1998).

112. Buades, A., Coll, B. & Morel, J.-M. J.-M. A non-local algorithm for image denoising. *Comput. Vis. Pattern Recognition, 2005. CVPR 2005. IEEE Comput. Soc. Conf.* **2,** 60–65 vol. 2 (2005).

113. Arganda-Carreras, I. *et al.* Trainable Weka Segmentation: a machine learning tool for microscopy pixel classification. *Bioinformatics* **33,** 2424–2426 (2017).

114. Tjaden, B., Brett, D. J. L. & Shearing, P. R. Tortuosity in electrochemical devices: a review of calculation approaches. *Int. Mater. Rev.* **6608,** 1–21 (2016).

115. Clennell, M. Ben. Tortuosity: a guide through the maze. *Geol. Soc. London, Spec. Publ.* **122,** 299–344 (1997).

116. Zahn, R., Lagadec, M. F. & Wood, V. Transport in Lithium Ion Batteries: Reconciling Impedance and Structural Analysis. *ACS Energy Lett.* **2,** 2452–2453 (2017).

117. Landesfeind, J., Hattendorff, J., Ehrl, A., Wall, W. A. & Gasteiger, H. A. Tortuosity Determination of Battery Electrodes and Separators by Impedance Spectroscopy. *J. Electrochem. Soc.* **163,** A1373–A1387 (2016).

118. Sethian, J. a. Fast Marching Methods. *SIAM Rev.* **41,** 199–235 (1999).

119. Jørgensen, P. S., Ebbehøj, S. L. & Hauch, A. Triple phase boundary specific pathway analysis for quantitative characterization of solid oxide cell electrode microstructure. *J. Power Sources* **279,** 686–693 (2015).

120. Wiedenmann, D. *et al.* Three-dimensional pore structure and ion conductivity of porous ceramic diaphragms. *AIChE J.* **59,** 1446–1457 (2013).

121. Lindquist, W. B., Lee, S.-M., Coker, D. A., Jones, K. W. & Spanne, P. Medial axis analysis of void structure in three-dimensional tomographic images of porous media. *J. Geophys. Res. Solid Earth* **101,** 8297–8310 (1996).

122. Ebner, M. & Wood, V. Tool for Tortuosity Estimation in Lithium Ion Battery Porous Electrodes. *J. Electrochem. Soc.* **162,** A3064–A3070 (2014).

123. Shearing, P. R. *et al.* Multi Length Scale Microstructural Investigations of a Commercially Available Li-Ion Battery Electrode. *J. Electrochem. Soc.* **159,** A1023–A1027 (2012).

124. Promentilla, M. A. B., Sugiyama, T., Hitomi, T. & Takeda, N. Quantification of tortuosity in hardened cement pastes using synchrotron-based X-ray computed microtomography. *Cem. Concr. Res.* **39,** 548–557 (2009).

125. Cooper, S. J. *et al.* Microstructural Analysis of an LSCF Cathode Using In-Situ Tomography and Simulation. *Solid Oxide Fuel Cells 13* **57,** 2671–2678 (2013).

126. Holzer, L. *et al.* The influence of constrictivity on the effective transport properties of porous layers in electrolysis and fuel cells. *J. Mater. Sci.* **48,** 2934–2952 (2013).

127. Cooper, S. J. *et al.* Image based modelling of microstructural heterogeneity in LiFePO 4 electrodes for Li-ion batteries. *J. Power Sources* **247,** 1033–1039 (2014).

128. Tjaden, B., Finegan, D. P., Lane, J., Brett, D. J. L. & Shearing, P. R. Contradictory concepts in tortuosity determination in porous media in electrochemical devices. *Chem. Eng. Sci.* **166,** 235–245 (2017).

129. Shen, L. & Chen, Z. Critical review of the impact of tortuosity on diffusion. *Chem. Eng. Sci.* **62,** 3748–3755 (2007).

130. Petersen, E. E. Diffusion in a pore of varying cross section. *AIChE J.* **4,** 343–345 (1958).

131. Chen-Wiegart, Y. K. *et al.* Tortuosity characterization of 3D microstructure at nano-scale for energy storage and conversion materials. *J. Power Sources* **249,** 349–356 (2014).

132. Vivet, N. *et al.* 3D Microstructural characterization of a solid oxide fuel cell anode reconstructed by focused ion beam tomography. *J. Power Sources* **196,** 7541–7549 (2011).

133. Jørgensen, P. S., Hansen, K. V., Larsen, R. & Bowen, J. R. Geometrical characterization of interconnected phase networks in three dimensions. *J. Microsc.* **244,** 45–58 (2011).

134. Liu, Z. *et al.* Relating the 3D electrode morphology to Li-ion battery performance; a case for LiFePO4. *J. Power Sources* **324,** 358–367 (2016).

135. Finsterbusch, M. *et al.* High Capacity Garnet-Based All-Solid-State Lithium Batteries: Fabrication and 3D-Microstructure Resolved Modeling. *ACS Appl.*

Mater. Interfaces **10,** 22329–22339 (2018).

136. Michaels, A. S. Diffusion in a pore of irregular cross section—a simplified treatment. *AIChE J.* **5,** 270–271 (1959).

137. Currie, J. A. Gaseous diffusion in porous media. Part 2. - Dry granular materials. *Br. J. Appl. Phys.* **11,** 318–324 (1960).

138. Münch, B. & Holzer, L. Contradicting geometrical concepts in pore size analysis attained with electron microscopy and mercury intrusion. *J. Am. Ceram. Soc.* **91,** 4059–4067 (2008).

139. Stenzel, O., Pecho, O., Holzer, L., Neumann, M. & Schmidt, V. Predicting effective conductivities based on geometric microstructure characteristics. *AIChE J.* **62,** 1834–1843 (2016).

140. Diamond, S. Mercury porosimetry: An inappropriate method for the measurement of pore size distributions in cement-based materials. *Cem. Concr. Res.* **30,** 1517–1525 (2000).

141. Meijster, A., Roerdink, J. B. T. M. & Hesselink, W. H. in *Mathematical Morphology and its Applications to Image and Signal Processing* 331–340 (Kluwer Academic Publishers). doi:10.1007/0-306-47025-X_36

142. Gaiselmann, G. *et al.* Quantitative relationships between microstructure and effective transport properties based on virtual materials testing. *AIChE J.* **60,** 1983–1999 (2014).

143. Holzer, L. *et al.* Fundamental relationships between 3D pore topology, electrolyte conduction and flow properties: Towards knowledge-based design of ceramic diaphragms for sensor applications. *Mater. Des.* **99,** 314–327 (2016).

144. Garman, R. M. *Sintering Theory and Practice*. (John Wiley & Sons, Inc., 1996).

145. Rahaman, M. N. *Ceramic Processing and Sintering*. (CRC Press, 2003).

146. Li, Y., Han, J.-T., Wang, C.-A., Xie, H. & Goodenough, J. B. Optimizing Li+ conductivity in a garnet framework. *J. Mater. Chem.* **22,** 15357–15361 (2012).

147. Shin, D. O. *et al.* Synergistic multi-doping effects on the Li7La3Zr2O12 solid electrolyte for fast lithium ion conduction. *Sci. Rep.* **5,** 18053 (2016).

148. Wiedemann, A. H., Goldin, G. M., Barnett, S. A., Zhu, H. & Kee, R. J. Effects of three-dimensional cathode microstructure on the performance of lithium-ion battery cathodes. *Electrochim. Acta* **88,** 580–588 (2013).

149. Feinauer, J. *et al.* Stochastic 3D modeling of the microstructure of lithium-ion battery anodes via Gaussian random fields on the sphere. *Comput. Mater. Sci.* **109,**

137–146 (2015).

150. Kashkooli, A. G. *et al.* Multiscale modeling of lithium-ion battery electrodes based on nano-scale X-ray computed tomography. *J. Power Sources* **307,** 496–509 (2016).

151. Haus, Hermann A., and James R. Melcher, Electromagnetic Fields and Energy. (Massachusetts Institute of Technology: MIT OpenCourseWare). http://ocw.mit.edu (accessed 02 24, 2018). Also available from Prentice-Hall: Englewood Cliffs, NJ, 1989. ISBN: 9780132.